



UNIVERSITÀ
DI PAVIA

SCUOLA DI ALTA FORMAZIONE DOTTORALE
MACRO-AREA SCIENZE E TECNOLOGIE

Dottorato di Ricerca in Scienze della Terra e dell'ambiente

Marta Morana

**Structure and properties of crystalline inclusions
trapped in minerals**

Anno Accademico 2019-2020
Ciclo XXXIII

Coordinatore
Prof. Roberto Sacchi

Tutor
Prof. Matteo Alvaro

Co-tutor
Prof. Luca Bindi

Abstract

This thesis deals with the characterization of mineral inclusions by means of various non-destructive techniques. Two type of inclusions are analyzed: inclusions in diamonds and inclusions in metamorphic rocks, in particular the host-inclusion pair quartz in garnet. The work on inclusion in diamonds focuses on rare inclusions of magnetic minerals, such as iron oxides, and employs a multi-analytical approach: X-ray diffraction, Raman spectroscopy, magnetometry, and X-ray tomography. Magnetic properties can help in the identification of the composition of the inclusions and thus of the environment in which the host-inclusion system grew. X-ray tomography was employed to locate the inclusions in the samples, asses the presence of fractures, and support the identification of the phases. The characterization of the quartz-in-garnet pair is focused on the determination of the stress state of the inclusions and the influence of such stress on the structure and properties of the system. It is shown how to characterize the crystal structure of inclusions in-situ by means of X-ray diffraction. A thorough characterization of the polarized Raman scattering of quartz as a function of pressure and temperature was performed to guide the interpretation of the results from inclusions. The high-pressure Raman experiment verifies the validity of the approach based on the phonon-mode Grüneisen tensor to calculate the pressure in the inclusions, also for the E modes. Furthermore, it points out that strong multiphonon interactions can contribute to the stability of alpha-quartz at ambient conditions and provides new pressure calibrations. The heating experiment performed in situ by Raman spectroscopy shows that the quartz inclusion in garnet does not undergo the α - β phase transition. The comparison of the free and trapped crystal data clearly shows a different response to heating and the applied models cannot reproduce the experimental data. It can be shown that the disagreement between the data and the prediction is due to the elastic anisotropy of quartz, suggesting that at a new model taking into account elastic anisotropy is needed.

Contents

Acknowledgements	19
Preface	21
1 Introduction and theoretical background	25
1.1 Diamond: from deep Earth to outer space	25
1.2 Inclusions in metamorphic rocks	27
Part I Diamond: from inclusions to impact shock. Methodology and application to natural samples	
2 Multi-analytical characterization of Fe-rich magnetic inclusions in diamonds	37
2.1 Introduction	37
2.2 Samples and methods	40
2.2.1 XRD acquisitions	41
2.2.2 SRXTM scans	42
2.2.3 AGFM measurements	42
2.3 Results	43
2.3.1 XRD	43
2.3.2 SRXTM	45
2.3.3 AGFM	45
2.4 Discussion	51
2.5 Conclusions	54
3 Primary inclusion of magnetite and quartz in Consolidated African Selection Trust (CAST) diamonds from Akwatia, Ghana	59
3.1 Introduction	59
3.2 Materials and Methods	61
3.3 Results	63
3.4 Discussion	63

4	Impact shock origin of diamonds in ureilite meteorites	73
4.1	Introduction	73
4.2	Results	75
4.2.1	Samples	75
4.2.2	Micro XRD	78
4.3	Discussion	82
4.3.1	AhS 72 and AhS 209b	82
4.3.2	NWA 7983	83
4.3.3	Additional evaluation of proposed evidence for high static pressure	87
4.4	Conclusions	88
Part II Inclusions in metamorphic rocks: novel techniques and application to a case study		
5	Crystal structure of quartz inclusions in garnet	97
5.1	Introduction	97
5.2	Materials and methods	98
5.2.1	Samples	98
5.2.2	X-ray diffraction	100
5.3	Results and discussion	101
5.3.1	Quartz in air	101
5.3.2	Quartz inclusion	103
5.4	Conclusions and further developments	106
6	Quartz metastability at high pressure: what new can we learn from polarized Raman spectroscopy?	111
6.1	Introduction	111
6.2	Material and methods	113
6.3	Results and discussion	114
6.4	Conclusions	126
7	Raman scattering of a free quartz crystal at high temperature	129
7.1	Introduction	129
7.2	Materials and methods	130
7.3	Raman scattering at high temperature	132
7.4	Raman shifts and Grüneisen tensor components at high temperature	136

8	Raman scattering from a quartz inclusion at high temperature	147
8.1	Introduction	147
8.2	Materials and methods	148
8.3	Results	149
8.3.1	Determination of P_{inc}	150
8.3.2	Calculation of the temperature dependence of P_{inc}	153
8.3.3	Temperature dependence of Raman peak positions and widths	155
8.4	Discussion	162
8.5	Conclusions	168
9	Fossil subduction recorded by quartz from the coesite stability field	175
9.1	Introduction	175
9.2	Eclogite xenolith from the Mir pipe (Yakutia)	176
9.3	Determination of inclusion strains	177
9.4	Calculation of unique pressure and temperature of elastic equilibration	179
9.5	Eclogite xenoliths: magmatic or metamorphic?	181
10	Conclusions	187

Appendices

A	Spiridonovite, $(\text{Cu}_{1-x}\text{Ag}_x)_2\text{Te}$ ($x \approx 0.4$), a new telluride from the Good Hope Mine, Vulcan, Colorado (U.S.A.)	193
A.1	Introduction	193
A.2	Description and physical properties	194
A.3	Chemical data	195
A.4	X-ray crystallography	196
A.5	Results and Discussion	199
B	Exploring the role of halide mixing in lead-free BZA_2SnX_4 two dimensional hybrid perovskites	205
B.1	Introduction	205
B.2	Results and discussion	206
B.2.1	New 1D perovskite	219
B.3	Conclusions	223
B.4	Experimental section	224
B.4.1	Materials preparation	224
B.4.2	Optical spectroscopy	224

B.4.3	X-ray diffraction measurements	225
B.4.4	EDX analysis	225

List of Tables

2.1	Numerical values of: IRM remanence at zero field ($m_{\text{IRM}}(0)$), IRM at saturation field 0.15 T (sIRM), IRM coercive field (H_c^{bf}), as extrapolated from IRM/backfield curves (Figure 2.6); saturation magnetic moment (m_{sat}), remanent magnetic moment (m_r) and coercive field (H_c), as extrapolated from hysteresis loops (Figure 2.7), for the CAST2 diamonds reported in the first column.	48
3.1	Minerals identified in the inclusions in diamonds from Akwatia, Ghana, and occurrence of fractures. The first number of the samples' name refers to the host diamond, the second number to the inclusion.	64
3.2	Unit cell parameters of selected olivine inclusions	65
5.1	Parameters used for data collection of the quartz free crystal	100
5.2	Data quality of QZPD01 refinement	101
5.3	Bond lengths and displacement parameters for quartz and olive vs resolution	103
5.4	Refinement results for free quartz and inc6. See the main thext for the labels.	105
5.5	Unit cells of the free quartz and the inclusion	105
6.1	Mode symmetry, selection rules and reference peak positions of quartz at ambient conditions	116
6.2	Pressure dependence of the peak positions and FWHMs of the four A_1 modes. Reported uncertainties are from the spectral fitting.	117
6.3	Pressure dependence of the peak positions and FWHMs of four selected E modes. Reported uncertainties are from the spectral fitting.	118
6.4	Coefficients of the function $\omega_i(P)$	122
6.5	Pressure calibrations for the modes at 128, 206, 265, 464, 696, 809, 1080, 1161 cm^{-1}	123
7.1	Correlation diagram for α - and β -quartz	133

7.2	Temperature dependence of peak positions and FWHM for the 128-, 206-, 355 and 464-cm ⁻¹ modes and the 147-cm ⁻¹ two-phonon band in the $\bar{z}(xx)z$ scattering geometry. Reported uncertainties are from spectral fitting.	139
7.3	Temperature dependence of peak positions and FWHM for the 147-cm ⁻¹ two-phonon band, the 206-, 355 and 464- and 1080-cm ⁻¹ modes in the $\bar{y}(zz)y$ scattering geometry. Reported uncertainties are from spectral fitting	141
7.4	Strains calculated from unit-cell parameters from Carpenter et al. (1998) (A) and from the equation of state of quartz by Angel et al., (2017) (B)	142
8.1	Equation of state parameters for the three garnet endmembers almandine, grossular and pyrope. The model for compression is a Birch-Murnaghan equation of the 3 rd order, while the model for the thermal expansion is a Mie-Grüneisen-Debye equation	150
8.2	Equation of state parameters for quartz from (Angel et al., 2017a). The reported properties are not elastic properties of α -quartz but of the so-called bare phase, as defined in Angel et al. (2017a) and Carpenter et al. (1998).	151
8.3	Pressure calculated from Raman shift and strains through the Grüneisen tensor. Different combinations of modes are reported, used modes are marked with a star	151
8.4	Pressure using <i>EntraPT</i> . Different combinations of modes are reported, see Table 8.3 for the labels	152
8.5	Pressure in GPa from hydrostatic calibrations	152
8.6	P_{trap} calculated with <i>EosFitPinc</i> (Angel et al., 2017b) for almandine, grossular and pyrope using a P_{inc} of 0.3 GPa and T_{trap}	153
8.7	P_{inc} variation with temperature	154
8.8	Slopes $d\omega/dT$ from the linear fits up to 800 K for the free and trapped quartz	156
8.9	Temperature dependence of the peak positions and FWHMs of selected modes for the quartz inclusion and a free quartz crystals. Uncertainties are from spectral fitting	159
8.10	Calculated $(\Delta\omega)_i$ for the 128-, 206-, and 464-cm ⁻¹ modes	163
8.11	Calculated $(\Delta\omega)_{464}$ with a linear temperature contribution	166
9.1	Strains calculated for inclusions i3, i5, i6 and i7 (see figure 1) from micro-raman measurements, together with single-crystal x-ray diffraction data on inclusion i6 before and after subtracting the anisotropic relaxation	178

A.1	Reflectance values for spiridonovite.	195
A.2	Analytical data in wt.% for spiridonovite.	196
A.3	Observed and calculated X-ray powder diffraction data (d in Å) for spiridonovite; calculated diffraction pattern obtained with the atom coordinates and occupancies reported in Table A.5 (only reflections with $I_{rel} \geq 4$ are listed)	197
A.4	Crystal and experimental data for spiridonovite	198
A.5	Atoms, site-occupancy factors (s.o.f.), Wyckoff positions, atom coordinates and isotropic displacement parameters (Å ²) for spiridonovite	199
A.6	Selected bond distances (Å) for spiridonovite	199
A.7	Bond valence sums (v.u.) for spiridonovite	201
A.8	Minerals belonging to the Cu-Ag-Te system	201
B.1	Atomic coordinates in the structure of BZA ₂ SnI ₄ resolved from single crystal X-ray diffraction	207
B.2	Atomic coordinates in the structure of BZA ₂ SnBr ₄ resolved from single crystal X-ray diffraction	208
B.3	Atomic coordinates in the structure of BZA ₂ SnCl ₄ resolved from single crystal X-ray diffraction	209
B.4	Octahedral interatomic distances in the structure of BZA ₂ SnX ₄ .	211
B.5	Sn-X-Sn bond angles within the inorganic layer in the structure of BZA ₂ SnX ₄	211
B.6	Elemental composition of some selected samples probed by EDX, where x refers to BZA ₂ Sn(Br _x I _{1-x}) ₄ composition and X/Sn indicates the halide to Sn ratio, which is 4 for a full 2D composition. E.s.d. for the measurements is around 5%	212
B.7	Lattice parameters in Å of the BZA ₂ Sn(Br _x I _{1-x}) ₄ solid solution from powder X-ray diffraction in the same setting	213
B.8	Atomic coordinates in the structure of BZA ₃ Sn(Br _{0.3} I _{0.7}) ₅ resolved from single crystal X-ray diffraction	220
B.9	Comparison of lattice parameters (Å) of BZA ₃ Sn(Br _{0.3} I _{0.7}) ₅ obtained with different nominal composition	223

List of Figures

- 2.1 (a) Diamonds belonging to the CAST₂ series and optical images of: (b) CAST₂-1; (c) CAST₂-5; (d) CAST₂-13 samples chosen as examples. Diamonds show quite different shapes; inclusions are in most cases distinguishable by their dark-gray, black color. 41
- 2.2 Setup of (a) diffractometer and (b) AGFM used for crystallographic and magnetic characterization. Diamonds are mounted on a pin in the diffractometer and on a rod in the AGFM, indicated with arrows in the pictures 43
- 2.3 Sketch of the procedure followed to acquire IRM curves. Magnetic field H (the uniform, stronger field in the AGFM) is successively applied at increased values $H_1 < H_2 < \dots$ (solid lines) and subsequently removed (dashed lines). The corresponding components of the remanent magnetic moment (or of the magnetization) m_1, m_2, \dots , along the direction of H , are collected for each field value only after its removal. 44
- 2.4 Diffractograms identifying magnetic phases (magnetite – blue squares; magnesioferrite – red circles) in: (a) CAST₂-1; (b) CAST₂-6; (c) CAST₂-7 and (d) CAST₂-12 diamonds. Diffractograms related to non-magnetic inclusions are not reported. Inset in Figure 2.4a shows the pattern from an acquisition at fixed φ ; diffraction spots related to diamond are not shown. Phase identification performed with the HighScore software. 46
- 2.5 3D reconstructions of SRXTM images for: (a) CAST₂-1; (b) CAST₂-6; (c) CAST₂-7; (d) CAST₂-12 samples. Inclusions are clearly visible in brighter colors since composed by chemical elements heavier than carbon. Estimates of inclusions and diamonds sizes, expressed in μm units, are shown for arbitrary fixed sample orientations in orange and light-blue color, respectively. 47

- 2.6 IRM ($H \geq 0$) and backfield ($H \leq 0$) curves, acquired with the AGFM, on CAST2-1 (red squares), CAST2-6 (green circles), CAST2-7 (violet triangles) and CAST2-12 (orange diamonds) samples. Points describing the remanence at zero field $m_{\text{IRM}}(0)$ (best approximation of the NRM), the remanence at saturation sIRM, reached at 0.15 T for all samples, and the coercive field of remanence H_c^{bf} are indicated with arrows; corresponding values are reported in Table 2.1. 48
- 2.7 Hysteresis loops, acquired with the AGFM, on CAST2-1 (dash-dotted, green), CAST2-6 (solid, orange), CAST2-7 (dotted, blue) and CAST2-12 (dashed, pink) samples. The dimensionless magnetic moment is obtained by dividing m by m_{sat} values reported in Table 2.1. The diamagnetic contribution of diamonds, becoming relevant at $\mu_0 H \gg 0.2$ T (CAST2-1, -6 samples) or 0.5 T (CAST2-7, -12 samples), is not shown. A sample-dependent vertical offset due to instrumental noise has been subtracted from the curves. 49
- 2.8 2D FORC diagrams evaluated from full sets of FORCs acquired with the AGFM on: (a) CAST2-1; (b) CAST2-6; (c) CAST2-7; (d) CAST2-12 samples. FORC distribution values are expressed in dimensionless units as $\hat{\rho} = (H_0^2/m_0)\rho$, where ρ , H_0 and m_0 are defined in Sec. 2.3.3. Reversible contribution to $\hat{\rho}$, lying on the $H - H_{\text{rev}} = 0$ bisector, is not included 50
- 3.1 (a) 3D reconstructions of SRXTM images for CAST2-15; (b) SRXTM image of CAST2-15 showing a crack connecting the inclusion to the surface; (c) X-ray diffraction pattern from CAST2-15-1 highlighting the presence of magnetite and hematite 66
- 3.2 (a) 3D reconstructions of SRXTM images for CAST2-11; (b) SRXTM image of the inclusion CAST2-11-1; (c) X-ray diffraction pattern from CAST2-11-1 highlighting the presence of magnetite and quartz 68

- 4.1 Carbon masses in polished sections of AhS 209b and NWA 7983. (A) BEI of AhS 209b, showing elongated masses of carbon phases located along inferred primary silicate grain boundaries. (B) BEI of non-carbon-coated section of AhS 209b in low-vacuum mode (hence low contrast). (C) BEI of carbon-coated section of NWA 7983 in high-vacuum mode. Carbon masses in this sample tend to have elongated, blade-like morphology and internally show a structure of dark and light stripes parallel to the long edges of the carbon mass. Dark areas show only C, whereas lighter areas show C, Fe, and S peaks in EDS spectra. (D) Reflected light image of same area as in C. Highly reflective, high-relief stripes correlate with dark areas in BEI and are inferred to be diamond from their optical properties, as well as fluorescence under the electron beam. (E) Raman phase map of area in C and D. The intensity of the red color corresponds to the intensity of the diamond $\sim 1332\text{-cm}^{-1}$ band. The intensity of the blue color corresponds to the intensity of the graphite G band ($\sim 1575\text{ cm}^{-1}$). In nanodiamonds, the $\sim 1332\text{-cm}^{-1}$ band is broad, has low intensity, and is downshifted, making it difficult to detect. Thus, the Raman image is predominantly sensitive to large diamonds (red) while most nanodiamonds likely go undetected (Ferrari et al, 2004, Osswald et al. 2009). In this Raman image, nanodiamonds were detected only in a few areas, although XRD results indicate that they are present throughout the carbon mass. (F) Raman spectra of large diamonds (red) and nanodiamonds (black) from E

77

- 4.2 (A) The diffractogram (Left) and the diffraction image (Right) of the AhS 209b sample, analyzed by micro X-ray powder diffraction at the Paul Scherrer Institute, Villigen, Switzerland. In the diffractogram the most abundant phases found in the carbon-bearing aggregate, polycrystalline diamond, graphite, and iron metal are shown. (B) Diffraction image (Left) for a fragment of a carbon area in NWA 7983 (from an area that was dark in BEI), showing only diffraction spots typical of a monocrystalline diamond. This monocrystal must be at least $100\ \mu\text{m}$ (the size of the whole fragment removed along its longest dimension). We determined its unit-cell edge length, $a=3.569\ \text{\AA}$, typical of diamond. (C) Diffractogram (Left) and the diffraction image (Right) of another fragment of NWA 7983, this one from an area that was lighter in BEI. This sample was analyzed by the Rigaku-Oxford Diffraction Supernova kappa-geometry goniometer at the Department of Geoscience, University of Padova. In this fragment polycrystalline diamond, graphite, iron, cohenite, and a minor abundance of troilite are detected

80

- 4.3 (Left) A typical bright-field image of the AhS 72 sample, which shows diamond domains with size ranging from 20 to 150 nm. The corresponding electron diffraction image (Right) indicates that nanodiamonds are associated with graphite (see the ring at about 3.35 Å) and diamond with stacking faults, that is, lonsdaleite (see ring at about 2.18 Å), confirming the XRD results. The diffraction line indicators are represented by the (hkl) planes of diamond (indicated with the subscript “d”) and graphite (indicated with the subscript “g”) and give the spacing in angstroms. These images were obtained with a Philips CM200 transmission electron microscope. 82
- 5.1 (a) The sample TM90-1, the position of inc 6 and of the pin are marked in red. (b) Close-up of the quartz inclusion inc6 99
- 5.2 (a) Bond distances and B_{eq} vs resolution for quartz (b) Bond distances and B_{eq} vs resolution for olivine 102
- 5.3 Comparison of the results from different refinement. See the main text for the explanation of the labels. 104
- 6.1 Polarized spectra at ambient conditions in the experimental scattering geometries. The arrows indicate a two-phonon band around 147 cm^{-1} 113
- 6.2 Selected spectra at high pressure in the experimental scattering geometries. 115
- 6.3 Comparison between the measured pressure dependencies of the phonon wavenumbers and FWHMs (this study, open circles) with experimental data from (Schmidt and Ziemann (2000) (filled circles), simulated $\Delta\omega$ by DFT calculations at 0 K (squares) and predictions of the mode Grüneisen tensors (lines) (Murri et al. 2019). Uncertainties on peak positions and pressures for data from the current work are generally smaller than the symbol size. This also applies to subsequent figures unless the error bars are visible. A realistic estimate of the true precision can be obtained from the scatter of consecutive data points 120
- 6.4 Pressure dependence of the peak positions and FWHMs of the four A_1 modes. Dashed lines indicate the pressures of the equilibrium phase boundaries between quartz and coesite Bose and Ganguly (1995) and coesite and stishovite Zhang et al. (1996). Open symbols are data points collected on decompression. 121
- 6.5 Pressure dependence of the peak positions and FWHMs of selected E modes. Dashed lines indicate the pressures of the equilibrium phase boundaries between quartz and coesite Bose and Ganguly (1995) and coesite and stishovite Zhang et al. (1996). Open symbols are data points collected on decompression. 121

- 6.6 Phonon compressibilities of the four A_1 modes and well resolved E modes. Dashed lines indicate the pressures of the equilibrium phase boundaries between quartz and coesite Bose and Ganguly (1995) and coesite and stishovite Zhang et al. (1996) 121
- 6.7 LO-TO splitting of the 128- (LO+TO) (a), 264- (TO) and 265- (LO) (b), 394- (TO) and 403- (LO) (c), and 1161- (TO) and 1159- cm^{-1} [- 1] (LO) modes (d) 124
- 6.8 Phonon compressibilities of the 1161- (TO) and 1159- cm^{-1} (LO) modes 124
- 7.1 Crystal structure of quartz (S.G. $P3_121$) 130
- 7.2 Temperature dependence of the peak positions of: the 147- cm^{-1} two-phonon band (a) in the scattering geometries $\bar{z}(xx)z$, and the $\bar{y}(zz)y$ for the thickest and the thinnest sample (zz thin); the 206- (b) and the 464- cm^{-1} (c) in the scattering geometries $\bar{z}(xx)z$, $\bar{z}(yx)z$, $\bar{y}(xz)y$, and $\bar{y}(zz)y$ for the thickest and the thinnest sample (zz thin). Data from the geometries $\bar{z}(yx)z$, $\bar{y}(xz)y$, and $\bar{y}(zz)y$ for the thickest sample are from Murri et al. 2019. Dashed lines indicate the α - β transition temperature 131
- 7.3 Selected spectra upon increasing temperature in the $\bar{z}(xx)z$ scattering geometry 134
- 7.4 Temperature dependence of the peak positions and FWHMs of the 464- cm^{-1} (a) and 206- cm^{-1} (b) modes in the $\bar{z}(xx)z$ scattering geometry. Dashed lines indicate the α - β transition temperature 134
- 7.5 Temperature dependence of the peak positions and FWHMs of the two-phonon excitation around 147 cm^{-1} in the $\bar{z}(xx)z$ scattering geometry. Dashed lines indicate the α - β transition temperature 135
- 7.6 Temperature dependence of the peak positions and FWHMs of the mode around 128 cm^{-1} (a) and 355 cm^{-1} (b) in the $\bar{z}(xx)z$ scattering geometry. The E_1 mode in β -quartz corresponding to the E mode at 128 cm^{-1} is not allowed by polarization selection rule in this scattering geometry. Dashed lines indicate the α - β transition temperature 136
- 7.7 Experimental wavenumber changes of the Raman modes at 128, 206, 355, 464 cm^{-1} as a function of temperature; for the 206- cm^{-1} mode data from Murri et al. (2019) and from a thinner quartz cut are reported. Predicted trends calculated from Grüneisen tensor components from Murri et al. (2019) are shown as solid lines. The trend are calculated from unit-cell parameters from Carpenter et al. (1998) (a) and the equation of state of quartz by Angel et al. (2017b) (b) 138
- 8.1 Example Raman spectra from the quartz inclusion at various temperatures obtained subtracting the host spectra 149

- 8.2 Comparison of the pressure range employed in Schmidt and Ziemann (2000) and Morana et al. (2020). The hydrostatic calibration reported by Schmidt and Ziemann (2000) is drawn as a solid line 153
- 8.3 P-T diagram for quartz calculated with almandine and and pyrope as the host; the solid line represents the α - β phase transition boundary 154
- 8.4 Temperature dependence of the peak positions and FWHMs of selected modes for a free (red) and trapped quartz (black) 157
- 8.5 Temperature dependence of the peak positions of the 206- and 464- cm^{-1} modes in free (red) and trapped quartz (black) 158
- 8.6 Comparison between the calculated $\Delta\omega_i$ and the inclusion data 165
- 8.7 Comparison between the calculated $\Delta\omega_{464}$ not including pre-transition effects and the inclusion data 169
- 8.8 Comparison between the $\Delta\omega_i$ calculated with the isotherm slope from Schmidt and Ziemann (2000) and the inclusion data 169
- 8.9 (a) Temperature dependence of peak positions, widths and fractional intensities of the A_{1g} mode of garnet at $\sim 920 \text{ cm}^{-1}$ (b) Spectra at room temperature before run 1 and run 2 and spectrum of the recovered garnet fragment after run 2. A spectrum of nanocrystalline hematite is reported for reference 170
- 9.1 (A) Microphotography of a thin section (parallel polarized light) of eclogite xenolith from the Mir pipe (Yakutian kimberlites, Russia), where location of inclusions within the garnet host are highlighted (red box). (B) High-magnification microphotography of two inclusions highlighting the high degree of preservation of quartz crystals, absence of cracks, and back-transformation features. (C,D) In cross-polarized light images (same areas as shown in A and B), birefringence haloes around selected inclusions show the presence of significant residual stresses in the inclusions. (E) Reconstructed three-dimensional microtomography of the same cluster of inclusions as in B and D (colored) and the host (gray background), which demonstrates the absence of cracks and shows that only one inclusion (i6, blue) has a very complex shape, far from a sphere or ellipsoid, for which dedicated finite element model (FEM) calculation on its specific shape is mandatory 177

- 9.2 (A) Raman spectra measured on four inclusions of eclogite xenolith from the Mir pipe (Yakutian kimberlites, Russia) while still trapped in the host. a.u.—arbitrary units. (B) Residual strains (a/a_0 and c/c_0) on inclusions along a and c lattice (squares and circles, respectively) after correcting for anisotropic elastic relaxation are isotropic within estimated standard deviations. Dashed lines represent hydrostatic equations of state for a and c lattice for quartz. Two boundary values of inclusion pressure are given at corresponding V/V_0 value. (C) Plot with a and c lattice strains for quartz inclusions trapped in garnet as a function of temperature calculated as described in the Data Repository (see footnote 1). Dashed line is strain along c axis and solid line is strain along a axis. Shaded areas represent uncertainties on measurements. Intersection between lattice isomekes represents the unique condition of garnet elastic equilibration at the pressure and temperature that occurred under hydrostatic conditions. Ellipsoids represent correlation of uncertainties for the calculation of intersection between strains. Color coding is as in Figure 1 180
- 9.3 Schematic view of the area of Mir pipe (Yakutian kimberlites, Russia) and process from fossil subduction to elastic equilibration of garnet and subsequent exhumation during kimberlite ascent. Image not to scale. Abbreviations and color coding as in Figure 2. 181
- A.1 Scanning Electron Microscopy-BackScattered Electron (SEM-BSE) image of spiridonovite (SPI) associated with cameronite (CAM), rickardite (RIC), vulcanite (VUL) and tellurium (TEL) 195
- A.2 The crystal structure of spiridonovite. M (Cu,Ag) sites and Te atoms are given as white and black circles, respectively. The tetrahedral coordination of the M sites is shown as isolated polyhedra. The unit cell and the orientation of the structure are outlined 200
- B.1 Room temperature sketch as determined from single crystal diffraction for (a) BZA_2SnI_4 , (b) BZA_2SnBr_4 , and (c) BZA_2SnCl_4 . Sn atoms are depicted in red, halide in green, C in white and N in yellow 210
- B.2 (a) Photo of some of the samples synthesized by ball-milling; (b) room temperature XRD patterns of the samples of the $BZA_2Sn(Br_xI_{1-x})_4$ system; (c) lattice parameters of the samples reported in (b) keeping the setting of the I-member for simplicity 212
- B.3 (a) Absorption spectra of the $BZA_2Sn(Br_xI_{1-x})_4$ system; (b) trend of the band-gap as a function of x ; (c) PL measurements for the samples of the of the $BZA_2Sn(Br_xI_{1-x})_4$ system; (d) PL decay at the peak emission upon excitation at 375 nm 214

B.4	DFT calculations of electronic band structures for BZA_2SnX_4 ($X = I, Br, \text{ and } Cl$)	216
B.5	DFT calculations of total and partial density of states (PDOS) for BZA_2SnX_4 ($X = I, Br, \text{ and } Cl$)	217
B.6	Calculated charge density for BZA_2SnX_4 ($X = I, Br, \text{ and } Cl$) within the $[110]$ plane	218
B.7	XRD patterns of BZA_2SnI_4 (a) and BZA_2PbI_4 (b) as a function of time under laboratory-air exposure and UV-Vis spectra of BZA_2SnI_4 (c) and BZA_2PbI_4 (d) as a function of time under laboratory-air exposure	219
B.8	(a) Sketch of the crystal structure of $BZA_3Sn(Br_{0.3}I_{0.7})_5$ along the b -axis; (b) refinement of powder pattern of $BZA_3Sn(Br_{0.3}I_{0.7})_5$; (c) absorption spectra of the sample	222

Acknowledgements

I wish to thank my supervisors prof. Matteo Alvaro and prof. Luca Bindi for their constant guidance and support: it is mostly thanks to them if I started two PhDs and finished (maybe) at least one. I also had two "unofficial" supervisors, prof. Boriانا Mihailova and dr. Ross Angel, who greatly contributed to the work reported in this thesis sharing their experience and advice; I also had the honor and pleasure of being a guest in the laboratory of Boriانا in Hamburg. I express my gratitude to the people who had to review and manage my final reports and now this thesis: dr. Alberto Zanetti, prof. Costanza Bonadiman, prof. Fabrizio Nestola and Chiara Trabella. I would like to thank all the people involved in the TrueDepths project, in Pavia and beyond, for their support, friendship and never-ending efforts to turn me in a real geologist, even if I refuse to lick rocks. I will always be grateful to my family, my boyfriend and my friends for their support during this journey.

This project has been funded by TRUE DEPTHS ERC-StG n.714936 to Matteo Alvaro, M.I.U.R.-F.A.R.E-IMPACT n. R164WEJAHH to Matteo Alvaro, PRNA Commander PNRA18_00247 - A to Fabrizio Nestola.

Preface

The aim of this PhD Thesis is to study mineral inclusions by means of non-destructive techniques to identify and describe rock-forming processes and environments. This approach is applied to two important groups of mineral inclusions: inclusions in diamond and inclusions of quartz in garnet in metamorphic rocks. In the former case, an innovative characterization method, based on the combination of multiple techniques, allows to extract information on the growth environment of the host-inclusion pair without breaking the host diamond. In the latter case, this thesis work focuses on the effect of non-hydrostatic stress that might play a major role in subduction zones as deviation from lithostatic pressure.

During my PhD, I worked on different minerals and different host-inclusion systems, characterized by a combination of non-destructive techniques. The first part of my work was devoted to diamonds. As described in chapters 2 and 3, I characterized by means of X-ray diffraction and Raman spectroscopy inclusions in alluvial diamonds from Ghana, performing the measurements and interpreting the data. This information was combined with X-ray tomographic data collected at the TOMCAT beamline at the Paul Scherrer Institute, Villigen, Switzerland. Together with Dr. Marco Piazzì, I also performed magnetic measurements on some magnetic inclusions at INRIM in Turin. I also worked on the characterization of impact diamonds, performing X-ray diffraction measurements in-house at the Material Science beamline at the Paul Scherrer Institute, Villigen, Switzerland, as described in chapter 4. During the second part of my PhD I focused on inclusions in metamorphic rocks and in particular on the quartz in garnet host-inclusion system. Chapter 5 shows how I collected X-ray data from inclusions in situ using a micro source and synchrotron radiation at the XPress beamline at Elettra Sincrotrone, Basovizza, Italia. Together with Dr. Ross Angel, I developed a workflow to measure inclusions on the beamline, import and treat the data. I spent four months with an Erasmus Traineeship scholarship in the laboratory of Prof. Boriana Mihailova at the Mineralogisch-Petrographisches Institut, University of Hamburg, and the results obtained during this period abroad are summarized in chapters 6, 7, 8. There I performed Polarized Raman spectroscopy at high pressure and high temperature on free quartz crystals and on a quartz inclusion in garnet, and the spectral fittings. An example of application of this techniques

and methodologies is reported in chapter 9, to which I contributed the X-ray tomography data. During my PhD, I also worked on structure determination by X-ray diffraction and solved the structure of a new mineral and of two synthetic hybrid perovskites, as reported in the appendices.

This PhD thesis is organized as follows.

Chapter 1 provides a general introduction and a theoretical background to the study cases and techniques used in this thesis.

Part I is dedicated to inclusions in diamond and comprises three chapters. The first chapter is dedicated to the development of a multi-analytical methodology, while the following chapters provide two case studies that require a combination of different techniques and approaches.

Chapter 2 Multi-analytical characterization of Fe-rich magnetic inclusions in diamonds describes the development and validation of a new methodology to characterize Fe-rich magnetic inclusions in diamonds. This approach involves the use of non-conventional and non-destructive techniques, such as magnetometry, to identify the mineral phases in the inclusions and derive information on growth conditions, such as oxygen fugacity. This chapter was published as an article in *Diamond and Related Materials* Volume 98, October 2019.

Chapter 3 Primary inclusion of magnetite and quartz in Consolidated African Selection Trust (CAST) diamonds from Akwatia, Ghana deals with the application of non-destructive techniques to a rare and unusual set of diamonds from Akwatia, Ghana. It focuses on the time of formation of iron oxide inclusions with respect to the host diamond.

Chapter 4 provides another example of a case study requiring a combination of multiple techniques to investigate a rock-forming environment characterized by non-hydrostatic stress, such as shocked meteorites. In particular, it describes diamonds from ureilites and discuss their origin either from static high pressure or impact shock.

Part II is dedicated to quartz inclusions in garnet from metamorphic rocks and how to characterize the effect of non-hydrostatic stress on such inclusions. The characterization is performed in situ by means of X-ray diffraction and Raman spectroscopy at ambient and high temperature. This approach lies in the framework of elastic geobarometry that exploits the difference in the elastic properties between the host and inclusion minerals to back-calculate the pressure of entrapment. Part II comprises four chapters, including an example of application of a combination of non-destructive techniques and elastic geobarometry to derive the pressure of entrapment of a quartz inclusion in garnet.

Chapter 5 describes the effect of the confinement within the host on the crystal structure of the trapped minerals. It also describes a methodology to collect X-ray data from inclusions in situ using a micro source and synchrotron radiation to obtain reliable cell parameters, and thus strains, and collect intensity data for structure refinement. The method is validated against Density Functional Theory calculations.

Chapter 6 Quartz metastability at high pressure: what new can we learn from polarized Raman spectroscopy? provides a comprehensive characterization of quartz Raman scattering under hydrostatic condition at high pressure to provide a standard reference to interpret data from inclusions and validate the use of the Grüneisen tensor approach to derive the strain and stress from Raman measurements. This chapter was published as an article in *Physics and Chemistry of Minerals*, volume 47, 2020.

Chapter 7 describes the response of the Raman scattering of quartz to high temperature, describing how the $\alpha - \beta$ phase transition can be detected and analyzed by means of Raman spectroscopy. The chapter provides fundamental information to interpret in situ heating experiments on host-inclusion systems.

Chapter 8 describes the characterization of a quartz inclusion in garnet that was studied in situ at high temperature by means of Raman spectroscopy. Characterizing the temperature dependence of the Raman scattering of quartz and garnet shows how the host and inclusion are influenced by heating and that the alpha-beta quartz phase transition does not occur in the inclusion.

Chapter 9 reports the application of elastic geobarometry and the techniques used in this thesis to quartz inclusions in a garnet from the Mir Kimberlite pipe. This chapter was published as a research article in *Geology*, volume 48, 2020.

Chapter 10 Conclusions summarizes the main results of this thesis and highlights possible future developments.

Appendices A and B are dedicated to one of the techniques used in this thesis, X-ray diffraction, and its application to determine crystal structures. Two examples are reported: a new mineral and synthetic hybrid perovskites. These appendices were published in *Minerals*, volume 3, 2019, and *Journal of Material Chemistry A*, volume 8, 2020.

1 Introduction and theoretical background

Mineral inclusions are minerals trapped within larger crystals during either their formation or their re-crystallization. Inclusions are ubiquitous in rocks, since any mineral can in principle trap and preserve the phases present in their growth environment. From the moment of their entrapment, inclusions are isolated from most of the physico-chemical changes affecting rocks at depth and can thus provide insights about the formation of the host crystal, the protoliths and P-T paths of metamorphic rocks. This thesis is focused on two large groups of inclusions: inclusions in diamond and inclusions in metamorphic rocks.

1.1 DIAMOND: FROM DEEP EARTH TO OUTER SPACE

Diamond is one of the most interesting and sought-after minerals, thanks to its physical properties and its economic value. From the geological point of view, diamond has additional value, since it grows at depths from 130 to 700 km, and is one of the oldest geological material known (e.g. Shirey et al., 2013). Since diamond is chemically inert, the inclusions within are protected and can reach unaltered the Earth's surface. As a consequence, mineral inclusions in diamond provide pristine samples from regions of the Earth that we cannot access directly, over a wide range of geological times. It is thus not surprising that studies on mineral inclusions in diamonds have played a fundamental role in our understanding of where and when their diamond hosts form. The first studies were purely descriptive (e.g. Stutton, 1921), till X-ray diffraction was introduced to identify unambiguously the trapped minerals. The seminal work by Mitchell and Giardini (1953) was followed by a series of more systematic studies on inclusions in diamonds from Russia (Orlov, 1977) and South Africa (Harris et al., 1967). In the late Sixties studies of diamond inclusions flourished thanks to the development of new approaches and technologies. Criteria of identification were developed (Harris, 1968a, 1968b), mostly focusing on a key aspect: the time of formation of the inclusions with respect to the diamond. Inclusions in diamonds are classified as protogenetic, syngenetic or epigenetic, whether their formation preceded, accompanied or followed crystallization of their host diamonds. The traditional criterion to identify the time of formation is the observation of the morphology of the included crystals. In fact, inclusions showing a cubo-octahedral morphology, irrespective

of their crystal system, were thought to grow at the same time as diamond, which could impose its morphology. Analogously, protogenetic inclusions were supposed to show a shape determined by their own crystal system. From the technological point of view, the introduction of the electron microprobe, which allowed to perform chemical analyses on the inclusions despite their small dimensions (e.g. Meyer, 1968; Sobolev et al., 1969), was a turning point for quantitative analysis of diamond inclusions. This allowed to conduct a systematic characterization of inclusions in diamond, including the compilation of large databases (Stachel & Harris, 2008), that led to understand that minerals included in lithospheric diamonds are associated to rock types characteristic of the mantle roots beneath ancient cratons. In particular, three suites, peridotitic eclogitic, and websteritic, are related to the main mantle source rocks and account for 65%, 33%, and 2% of diamonds worldwide. The use of the electron microprobe also allowed to estimate the condition of pressure and temperature of last equilibration from non-touching pairs of different mineral species included in diamond, such as garnet and olivine (O'Neill & Wood, 1979), garnet and clinopyroxene (Krogh, 1988), garnet and orthopyroxene (Brey & Köhler, 1990; Harley, 1984). However, these well-established approaches have recently shown some limitations. Firstly, the imposition of morphology has been proven to fail in the case of olivine inclusions that were identified as protogenetic, despite their cubo-octahedral morphology (Milani et al., 2016; Nestola et al., 2014). Furthermore, geothermobarometric estimates rely on the occurrence of certain mineral pairs assumed to be in equilibrium, and require the extraction of the inclusions from the diamond host. On the contrary, non-destructive techniques can be applied to have further insights on the time and conditions of formation of the host-inclusions pair. Tomographic analyses can detect the presence of fractures that suggest a late alteration for the inclusions, while X-ray diffraction can identify not only the minerals comprising the inclusions, but also epitaxial growth relationships between the inclusions and the host diamond through crystallographic orientation relationships (Milani et al., 2016; Nestola et al., 2014; Nimis et al., 2019). Elastic geobarometry represents a non-destructive alternative to chemical thermobarometry. In this methodology, the difference in elastic properties between the host and the inclusion is used to derive the entrapment pressure and can be applied also to monomineralic inclusions, since it does not rely on the assumption of equilibrium between mineral pairs. More details on elastic geobarometry will be given in the following sections. Recent studies on diamond inclusions often employ a combination of techniques and can also be coupled with theoretical calculations (e.g. Anzolini et al., 2019). An approach involving multiple techniques is particularly useful in the case of rare inclusions, poorly characterized and of unknown paragenesis, such as the iron oxides inclusions described in Chapters 2] and 3.

Diamonds do not only grow in deep Earth. In fact, diamond can also form as

a result of meteorite impacts on the Earth's surface when shock waves generate dynamically high pressures. Notable examples of impact sites where diamonds were found are the Popigai impact structure in Russia (Koeberl et al., 1997), and the Nördlinger Ries in Germany (Goresy et al., 2001). Diamonds also occur as nanometric (Lewis et al., 1987) presolar dust grains of interstellar origin, and as component of meteorites. The first meteorites where diamonds were found are ureilites (e.g. Yerofeyev & Lachinov, 1888), a class of ultramafic meteorites known to contain relatively large amount of carbon as graphite, diamond and lonsdaleite (Mittlefehldt et al., 1998; Vdovykin, 1970). The formation process of diamond in these meteorites is still unclear and three main hypotheses are debated. Firstly, diamonds in ureilites may form in an analogous way as terrestrial diamond grows: under static high-pressure conditions in the interior of the ureilite parent body (Urey, 1956). Alternatively, they may form by shock conversion of graphite as a result of some impact, such as the one that caused the catastrophic breakup of their parent body (Lipschutz, 1964). A third hypothesis suggests that diamond may form at low pressure in the solar nebula by chemical vapor deposition (Fukunaga et al., 1987). Formation by impact shock has long been the most widely accepted hypothesis, but has been recently questioned by Miyahara et al. (2015), who supported the formation either by chemical vapor deposition or static high pressure conditions, and Nabiei et al. (2018), who stated that diamonds in ureilites formed under static high pressure conditions in a parent body of the same size as Mercury or Mars. This controversy is addressed in Chapter 4, where three diamond-bearing ureilite fragments, two from the Almahata Sitta polymict ureilite (Jenniskens et al., 2009) and one from the NWA 7983 (Ruzicka et al., 2015) main group ureilite, are thoroughly characterized.

1.2 INCLUSIONS IN METAMORPHIC ROCKS

Mineral inclusions play a fundamental role in the study of metamorphic rocks. In fact, the discovery of coesite as inclusions in garnet from Dora-Maira, Italy (Chopin, 1984), and in clinopyroxene from the Western Gneiss Region of Norway (Smith, 1984), together with inclusions of microdiamonds in garnet from the Kokchetav massif, Kazakhstan (Sobolev & Shatsky, 1990), led to a new field of metamorphic petrology called ultrahigh-pressure metamorphism. Different theories have been developed to explain the presence of ultrahigh-pressure phases in crustal rocks, such as subduction of continental crust to depths of more than 100 km in collisional orogens (Spear et al., 2016), tectonic overpressure (Schmalholz & Podladchikov, 2014), local overpressurization at the grain scale (Tajčmanová et al., 2015), and confined melting (Vrijmoed et al., 2009). In this context, mineral inclusions can be of great interest, since they can provide insights on the condition of pressure, temperature and depth in which the host grew. As in the case of diamond inclusions, the composition of inclusions trapped during growth

have long been used to derive pressure and temperature conditions, but elastic geobarometry is emerging as an alternative method that does not require equilibrium between the minerals, but relies on difference in elastic properties. Since elastic processes are reversible by definition, any convenient path in P–T space can be used for calculations of elastic stresses. A common choice is the isomeke, a line along which the fractional volume change of the host and inclusion does not change (Rosenfeld & Chase, 1961). The slope of an isomeke is given by:

$$\left(\frac{\partial P}{\partial T}\right) = \frac{\alpha_I - \alpha_H}{\beta_I - \beta_H} \quad (1.1)$$

thus depends on the difference between the thermal expansion coefficients of the inclusion and host, $(\alpha_I - \alpha_H)$, and in volume compressibilities $(\beta_I - \beta_H)$. it is possible to define an entrapment isomeke that goes through the P–T conditions of entrapment and the P and T points at which the inclusion remains at the same pressure as the external pressure. This specific isomeke divides the P–T space into two regions: one where the pressure in the inclusion will be higher than the external pressure on the host, and, conversely, another one where the pressure in the inclusion will be lower than the external pressure on the host. As a consequence the inclusions will be over- or under-pressured, with respect to the external pressure. This condition is determined by the bulk modulus defined as:

$$K = -V \frac{\partial P}{\partial V} = \frac{1}{\beta} \quad (1.2)$$

In particular, when the the host moves from the entrapment isomeke of dP_{ext} , the pressure change in the inclusion is given by:

$$dP_{inc} = \frac{K_{inc}}{K_{host}} dP_{ext} \quad (1.3)$$

As a consequence, for a soft inclusion in a stiff host with $K_{inc} < K_{host}$ the pressure will be between the external pressure and the pressure of the entrapment isomeke, thus the inclusion will be over-pressured and will show a remanent pressure $P_{inc} > P_{ext} \approx 0$, while it will be at room pressure in the opposite case of $K_{inc} > K_{host}$. Till the system lies on the entrapment isomeke, the pressure of the inclusion can be calculated from the equations of state of the two minerals, giving the so called P_{thermo} . However, as soon as the system leaves the entrapment isomeke, along which by definition $P_{host} = P_{inc} = P_{ext}$, P_{thermo} will become different from the external pressure, causing a instantaneous elastic relaxation ΔP_{relax} of the host-inclusion boundary that lowers the pressure difference between the inclusion and the external pressure. These concepts can be applied on real host-inclusion systems. The first step is the determination of the remanent pressure P_{inc} while the host is at room conditions from X-ray diffraction or Raman spectroscopy data. Then, P_{inc} is used to calculate ΔP_{relax} and P_{thermo} (Angel et al., 2017)

that are in turn used to derive the entrapment isomeke at room temperature. Combining it with the equations of state of the two minerals allows to calculate the entrapment isomeke and the pressure of entrapment P_{trap} . However, this approach is limited by few underlying assumptions. First, the inclusion is assumed to be spherical and to fill completely the void in the host. The inclusion and the host are also supposed to be under the same hydrostatic stress at the entrapment. Finally, both phases are considered elastically isotropic. Finite elements modeling allows to quantify and take in to account the inclusion shape (Mazzucchelli et al., 2018) and other effects such as the proximity to the external surface (Campomenosi et al., 2018). The assumption of elastic isotropy is indeed the most problematic, since minerals, as any other crystals, are inherently anisotropic. As a consequence, the inclusion-host boundary will always impose deviatoric stress on the trapped mineral. Recently, Bonazzi et al. (2019) showed that calculating P_{inc} and P_{trap} from an hydrostatic calibration of Raman shifts leads to unreliable results in the case of strains significantly different from those associated to hydrostatic conditions. Instead of using an hydrostatic calibration, the strains can be calculated from the phonon-mode Grüneisen tensor, since the fractional change in the wavenumber $\frac{-\Delta\omega^m}{\omega_0^m}$ of a phonon mode m as a result of a strain ε is given by the following relationship:

$$\frac{-\Delta\omega^m}{\omega_0^m} = \gamma^m : \varepsilon \quad (1.4)$$

where γ^m is the phonon-mode Grüneisen tensor (Angel et al., 2019). The strains can then be used to calculate P_{inc} applying the elastic tensor of the mineral of interest. It is worth noting that X-ray diffraction allows to directly obtain the strains from the comparison of the measured unit cell parameters of the inclusion with respect to those of a free crystal.

From this brief introduction, it is clear that elastic geobarometry require a detailed characterization of the elastic properties and high pressure response of the minerals of interest. This is the aim of Chapters 6 and 7, where a thorough description of the high pressure and high temperature Raman scattering of quartz and a validation against experimental data of the Grüneisen tensor approach are provided. Another important aspect to consider is the influence of deviatoric stress. The response of crystal structures to the application of non-hydrostatic stress is still poorly characterized, since it is difficult to generate and control it during experiments. In this respect, host-inclusion pairs can act as model systems, as in Chapters 5 and 8, where the effect of non-hydrostatic stress upon increasing temperature and of the confinement within the host on the crystal structure of quartz inclusions are described. Finally, an example of application of elastic geobarometry to estimate the conditions of entrapment is reported in Chapter 9.

REFERENCES

- Angel, R. J., Mazzucchelli, M. L., Alvaro, M., & Nestola, F. (2017). EosFit-Pinc: A simple GUI for host-inclusion elastic thermobarometry. *American Mineralogist*, *102*(9), 1957–1960.
- Angel, R. J., Murri, M., Mihailova, B., & Alvaro, M. (2019). Stress, strain and Raman shifts. *Zeitschrift für Kristallographie - Crystalline Materials*, *234*(2), 129–140. <https://doi.org/10.1515/zkri-2018-2112>
- Anzolini, C., Nestola, F., Mazzucchelli, M. L., Alvaro, M., Nimis, P., Gianese, A., Morganti, S., Marone, F., Campione, M., Hutchison, M. T., & Harris, J. W. (2019). Depth of diamond formation obtained from single periclase inclusions. *Geology*, *47*(3), 219–222.
- Bonazzi, M., Tumiati, S., Thomas, J. B., Angel, R. J., & Alvaro, M. (2019). Assessment of the reliability of elastic geobarometry with quartz inclusions. *Lithos*, *350–351*, 105201. <https://doi.org/10.1016/j.lithos.2019.105201>
- Brey, G., & Köhler, T. (1990). Geothermobarometry in four-phase lherzolites II. New thermobarometers, and practical assessment of existing thermobarometers. *Journal of Petrology*, *31*(6), 1353–1378.
- Campomenosi, N., Mazzucchelli, M. L., Mihailova, B., Scambelluri, M., Angel, R. J., Nestola, F., Reali, A., & Alvaro, M. (2018). How geometry and anisotropy affect residual strain in host-inclusion systems: Coupling experimental and numerical approaches [Publisher: De Gruyter Section: American Mineralogist]. *American Mineralogist*, *103*(12), 2032–2035. <https://doi.org/10.2138/am-2018-6700CCBY>
- Chopin, C. (1984). Coesite and pure pyrope in high-grade blueschists of the Western Alps: A first record and some consequences. *Contributions to Mineralogy and Petrology*, *86*(2), 107–118.
- Fukunaga, K., Matsuda, J.-i., Nagao, K., Miyamoto, M., & Ito, K. (1987). Noble-gas enrichment in vapour-growth diamonds and the origin of diamonds in ureilites. *Nature*, *328*(6126), 141–143.
- Goresy, A. E., Gillet, P., Chen, M., Künstler, F., Graup, G., & Stähle, V. (2001). In situ discovery of shock-induced graphite-diamond phase transition in gneisses from the Ries Crater, Germany. *American Mineralogist*, *86*(5–6), 611–621.
- Harley, S. L. (1984). An experimental study of the partitioning of Fe and Mg between garnet and orthopyroxene. *Contributions to Mineralogy and Petrology*, *86*(4), 359–373.
- Harris, J. (1968a). Recognition of diamond inclusions. 1. Syngenetic mineral inclusions. *Industrial Diamond Review*, *28*(334), 402.
- Harris, J. (1968b). Recognition of diamond inclusions. 2. Epigenetic mineral inclusions. *Industrial Diamond Review*, *28*(335), 458.

- Harris, J., Henrique, R., & Meyer, H. (1967). Orientation of silicate mineral inclusions in diamonds. *Crystal Growth*, 7, 118–123.
- Jenniskens, P., Shaddad, M., Numan, D., Elsir, S., Kudoda, A., Zolensky, M., Le, L., Robinson, G., Friedrich, J., Rumble, D., et al. (2009). The impact and recovery of asteroid 2008 TC 3. *Nature*, 458(7237), 485–488.
- Koeberl, C., Masaitis, V. L., Shafranovsky, G. I., Gilmour, I., Langenhorst, F., & Schrauder, M. (1997). Diamonds from the Popigai impact structure, Russia. *Geology*, 25(11), 967–970.
- Krogh, E. J. (1988). The garnet-clinopyroxene Fe-Mg geothermometer—a reinterpretation of existing experimental data. *Contributions to Mineralogy and Petrology*, 99(1), 44–48.
- Lewis, R. S., Ming, T., Wacker, J. F., Anders, E., & Steel, E. (1987). Interstellar diamonds in meteorites. *Nature*, 326(6109), 160–162.
- Lipschutz, M. E. (1964). Origin of diamonds in the ureilites. *Science*, 143(3613), 1431–1434.
- Mazzucchelli, M. L., Burnley, P., Angel, R. J., Morganti, S., Domeneghetti, M. C., Nestola, F., & Alvaro, M. (2018). Elastic geothermobarometry: Corrections for the geometry of the host-inclusion system [Publisher: GeoScience-World]. *Geology*, 46(3), 231–234. <https://doi.org/10.1130/G39807.1>
- Meyer, H. O. (1968). Chrome pyrope: an inclusion in natural diamond. *Science*, 160(3835), 1446–1447.
- Milani, S., Nestola, F., Angel, R., Nimis, P., & Harris, J. (2016). Crystallographic orientations of olivine inclusions in diamonds. *Lithos*, 265, 312–316. <https://doi.org/10.1016/j.lithos.2016.06.010>
- Mitchell, R. S., & Giardini, A. A. (1953). Oriented olivine inclusions in diamond. *American Mineralogist*, 38(1-2), 136–138.
- Mittlefehldt, D. W., McCoy, T. J., Goodrich, C. A., & Kracher, A. (1998). Non-chondritic meteorites from asteroidal bodies. *Reviews in Mineralogy and Geochemistry*.
- Miyahara, M., Ohtani, E., El Goresy, A., Lin, Y., Feng, L., Zhang, J.-C., Gillet, P., Nagase, T., Muto, J., & Nishijima, M. (2015). Unique large diamonds in a ureilite from Almahata Sitta 2008 TC₃ asteroid. *Geochimica et Cosmochimica Acta*, 163, 14–26.
- Nabiei, F., Badro, J., Dennenwaldt, T., Oveisi, E., Cantoni, M., Hébert, C., El Goresy, A., Barrat, J.-A., & Gillet, P. (2018). A large planetary body inferred from diamond inclusions in a ureilite meteorite. *Nature communications*, 9(1), 1–6.
- Nestola, F., Nimis, P., Angel, R., Milani, S., Bruno, M., Prencipe, M., & Harris, J. (2014). Olivine with diamond-imposed morphology included in diamonds. Syngensis or protogenesis? *International Geology Review*, 56(13), 1658–1667. <https://doi.org/10.1080/00206814.2014.956153>

- Nimis, P., Angel, R. J., Alvaro, M., Nestola, F., Harris, J. W., Casati, N., & Marone, F. (2019). Crystallographic orientations of magnesiochromite inclusions in diamonds: what do they tell us? *Contributions to Mineralogy and Petrology*, 174(4), 29. <https://doi.org/10.1007/s00410-019-1559-5>
- O'Neill, H. S. C., & Wood, B. (1979). An experimental study of Fe-Mg partitioning between garnet and olivine and its calibration as a geothermometer. *Contributions to Mineralogy and Petrology*, 70(1), 59–70.
- Orlov, I. L. (1977). *The mineralogy of the diamond*. John Wiley & Sons.
- Rosenfeld, J. L., & Chase, A. B. (1961). Pressure and temperature of crystallization from elastic effects around solid inclusions in minerals? *American Journal of Science*, 259(7), 519–541. <https://doi.org/10.2475/ajs.259.7.519>
- Ruzicka, A., Grossman, J., Bouvier, A., Herd, C. D., & Agee, C. B. (2015). The meteoritical bulletin, no. 102. *Meteoritics & Planetary Science*, 50(9), 1662–1662.
- Schmalholz, S. M., & Podladchikov, Y. (2014). Metamorphism under stress: The problem of relating minerals to depth. *Geology*, 42(8), 733–734.
- Shirey, S. B., Cartigny, P., Frost, D. J., Keshav, S., Nestola, F., Nimis, P., Pearson, D. G., Sobolev, N. V., & Walter, M. J. (2013). Diamonds and the geology of mantle carbon. *Reviews in Mineralogy and Geochemistry*, 75(1), 355–421. <https://doi.org/10.2138/rmg.2013.75.12>
- Smith, D. C. (1984). Coesite in clinopyroxene in the caledonides and its implications for geodynamics. *Nature*, 310(5979), 641–644.
- Sobolev, N. V., Lavrent'ev, Y. G., Pospelova, L. N., & Sobolev, V. C. (1969). Chrome pyropes from Yakutian diamonds. *Doklady Akademii Nauk SSSR*, 180(1), 162–+.
- Sobolev, N. V., & Shatsky, V. S. (1990). Diamond inclusions in garnets from metamorphic rocks: A new environment for diamond formation. *Nature*, 343(6260), 742–746.
- Spear, F. S., Pattison, D. R., & Cheney, J. T. (2016). The metamorphosis of metamorphic petrology. *The web of geological sciences: Advances, impacts, and interactions II*. Geological Society of America. [https://doi.org/10.1130/2016.2523\(02\)](https://doi.org/10.1130/2016.2523(02))
- Stachel, T., & Harris, J. (2008). The origin of cratonic diamonds- constraints from mineral inclusions. *Ore Geology Reviews*, 34(1), 5–32. <https://doi.org/10.1016/j.oregeorev.2007.05.002>
- Stutton, J. (1921). Inclusions in diamond from South Africa. *Mineralogical Magazine and Journal of the Mineralogical Society*, 19(94), 208–210.
- Tajčmanová, L., Vrijmoed, J., & Moulas, E. (2015). Grain-scale pressure variations in metamorphic rocks: Implications for the interpretation of petrographic observations. *Lithos*, 216, 338–351.
- Urey, H. C. (1956). Diamonds, meteorites, and the origin of the solar system. *The Astrophysical Journal*, 124, 623.

- Vdovykin, G. (1970). Ureilites. *Space Science Reviews*, 10(4), 483–510.
- Vrijmoed, J. C., Podladchikov, Y. Y., Andersen, T. B., & Hartz, E. H. (2009). An alternative model for ultra-high pressure in the svartberget fe-ti garnet-peridotite, western gneiss region, norway. *European Journal of Mineralogy*, 21(6), 1119–1133.
- Yerofeyev, M., & Lachinov, P. (1888). The meteorite from Novo-Urei village. *Zap. Mineral. Ova.*, 24.

Part I Diamond: from inclusions to impact shock. Methodology
and application to natural samples

2 Multi-analytical characterization of Fe-rich magnetic inclusions in diamonds

This chapter was published as an article in *Diamond and related materials* as:

Piazzì, M., Morana, M., Coisson, M., Marone, F., Campione, M., Bindi, L., Jones, A. P., Ferrara, E., and Alvaro, M. (2019). Multi-analytical characterization of Fe-rich magnetic inclusions in diamonds. *Diamond and Related Materials*, 98, 107489.
<https://doi.org/10.1016/j.diamond.2019.107489>

ABSTRACT

Magnetic mineral inclusions, as iron oxides or sulfides, occur quite rarely in natural diamonds. Nonetheless, they represent a key tool not only to unveil the conditions of formation of host diamonds, but also to get hints about the paleointensity of the geomagnetic field present at times of the Earth's history otherwise not accessible. This possibility is related to their capability to carry a remanent magnetization dependent on their magnetic history. However, comprehensive experimental studies on magnetic inclusions in diamonds have been rarely reported so far. Here we exploit X-ray diffraction, Synchrotron-based X-ray Tomographic Microscopy and Alternating Field Magnetometry to determine the crystallographic, morphological and magnetic properties of ferrimagnetic Fe-oxides entrapped in diamonds coming from Akwatia (Ghana). We exploit the methodology to estimate the natural remanence of the inclusions, associated to the Earth's magnetic field they experienced, and to get insights on the relative time of formation between host and inclusion systems. Furthermore, from the hysteresis loops and First Order Reversal Curves we determine qualitatively the anisotropy, size and domain state configuration of the magnetic grains constituting the inclusions.

2.1 INTRODUCTION

Natural diamonds can provide unique information on the composition and formation processes of the Earth's interior as well as about many fundamental phenomena involved in the geological history of our planet, as for example fluids diffusion into the continental lithosphere (Bulanova, 1995; Haggerty, 1986; Stachel

& Harris, 2009; Stachel & Luth, 2015; Tappert & Tappert, 2011). This distinctive feature is related to diamond capability of traveling long distances inside the Earth, from the depth of strata where they were formed, moving towards the surface without being subjected to cracks or breakages. However, it is quite difficult to recover directly from diamonds valuable information about their ages and the pristine thermodynamic conditions and chemico-physical environment present during their growth, because they act as chemically inert materials. In most cases, these conditions and environments are traced back by characterizing and analyzing the properties of mineral inclusions they entrapped (Harris, 1993; Shirey et al., 2013; Stachel & Harris, 2008), which can reach us almost unaltered thanks to the shielding action of diamonds. For the purpose of restoring this information, many experimental techniques (Anzolini et al., 2018; Liu et al., 1990; Nasdala et al., 2003; Nestola et al., 2016a; Nestola et al., 2016b) and numerical tools have been developed in the last years allowing to identify the mineral phases composing the inclusions and to relate, by means of analytical equations of state, their crystalline properties to the depth, pressure and temperature of their ancient nucleation and growth processes (Angel et al., 2015a; Angel et al., 2014; Angel et al., 2015b; Milani et al., 2015). A key aspect that should be carefully addressed to avoid incorrect conclusions on this topic is the ascertainment of the time of formation of the inclusion with respect to the time of formation of the host diamond. Syngenetic inclusions, contrary to proto- and epigenetic ones, are indeed the only ones providing us with accurate information about the environment of growth of the diamonds since they nucleate simultaneously with their host. Some criteria, developed quite recently and looking at the relative lattice orientation between the host and the inclusion structures (Nestola et al., 2017; Nestola et al., 2014; Nimis et al., 2019) or at the presence of fractures into diamonds (Bulanova et al., 1996; Meyer & McCallum, 1986), rather than at the morphology imposed by the host only (Harris, 1968), resulted to be effective in distinguishing between the proto-/syngenetic and the epigenetic class of inclusions.

In this context, very few studies have been reported so far about the magnetic properties of mineral inclusions found either in kimberlitic diamonds (Clement et al., 2008), in carbonados (Fitzgerald et al., 2006; Kletetschka et al., 2000) or in mixtures of kimberlite-source polycrystalline diamonds and carbonados (Collinson, 1998). These inclusions have been identified as iron sulfides (pyrrhotite) entrapped in the deeper parts of the diamonds by Clement et al. (2008) and as iron oxides (magnetite) for the kimberlite-source polycrystalline diamonds studied in Ref. Collinson, 1998, while Fitzgerald et al. (2006) and Kletetschka et al. (2000) have evidenced that the magnetic carriers responsible for the detected ferromagnetic signals are present at the surface or in open pores, rather than in the bulk of the examined carbonados. This kind of inclusions is able to carry a natural remanent magnetization (NRM) which represents a signature of the geomagnetic field they have been subjected to along their history. Therefore, magnetic inclusions can

be regarded as geological objects of great interest since they might bring useful data about the growth conditions of the host system (Gilder et al., 2011) and, at the same time, about the paleointensity of the geomagnetic field present in key geological eras, which would be otherwise not accessible. It is worth noting that the latter information may be hindered if the inclusion has strong magnetic anisotropy, as for example may happen when dealing with pyrrhotite (Clement et al., 2008). In particular, the work by Clement et al. (2008) offers a complete study about the magnetic characterization of pyrrhotite inclusions entrapped in eleven diamonds of millimeter size coming from the Orapa kimberlite mine in Botswana. The authors propose an experimental procedure to ascertain the main magnetic properties of the inclusions based on: (i) progressive alternating field demagnetization and isothermal remanent magnetization (IRM) measurements, aimed at establishing the natural remanent magnetization carried by the system; (ii) thermal demagnetization measurements, with the purpose of determining the Curie temperature of the inclusions and their possible chemical alteration due to heating processes; (iii) hysteresis loops acquisition at different orientations, to investigate the coercive field, remanence and potential magnetic anisotropy present in the system. The presence of quite regular shapes and distinct features in their diamonds allowed the authors to perform a visual identification of the inclusions. When present, such distinct features, as for example cleavage planes and well visible fractures connected to the diamond surface and surrounding the inclusions, allows also to visually distinguish epigenetic inclusions from proto-/syngenetic ones. Unfortunately, in some cases natural diamonds do not show these clear features and other analytical tools (e.g. optical microscopy, X-ray diffraction, ...) are required to clearly identify the inclusions and to determine their properties. As shown by Clement et al. (2008), thermal demagnetization can help in identifying magnetic minerals through their Curie temperatures, but this process may bring to undesired chemical alteration of the pristine inclusions. Furthermore, the identification of a magnetic mineral only through thermal demagnetization can be hard when dealing with multiple magnetic inclusions, characterized by similar Curie temperatures, within a single diamond.

In this work we thus suggest an experimental procedure allowing to partially overcome the above mentioned difficulties and we apply it to investigate the crystallographic, morphological and magnetic properties, not accessible by optical and visual means alone, of iron oxides inclusions entrapped in a series of single-crystal diamonds coming from Akwatia (Ghana). This procedure exploits several non-destructive, efficient and relatively fast techniques detailed in Sec. 2.2, i.e. X-ray diffraction (XRD), Synchrotron-based X-ray Tomographic Microscopy (SRXTM) and Alternating Gradient Field Magnetometry. In particular, XRD allows to determine the crystal structure of the inclusions in a repeatable way without altering them (Angel et al., 2016; Nestola et al., 2012; Nestola et al., 2011; Pearson et al., 2014), while SRXTM is performed to establish which inclusions

can be regarded as epigenetic by searching for the potential presence of fractures connecting them to the surface all along the diamond interiors (Nimis et al., 2016). SRXTM allows also to give a reasonable estimate of the linear size, volume and shape of the host-inclusion system, which is an important piece of information to determine more precisely the magnetization of the inclusions or to perform numerical calculations. Finally, Alternating Gradient Field Magnetometry measurements represent a quick and enough sensitive tool to investigate the magnetic properties of the system. These properties may provide further constraints when attempting to unveil the thermodynamic conditions of growth of the inclusions, because of the pressure-temperature dependence of the magnetic response of any material with magnetic order. In Sec. 2.3 we present the experimental results obtained, while in Sec. 2.4 we propose their possible interpretation. Sec. 2.5 is finally devoted to draw conclusions, proposing also some possible routes for future works on this topic.

2.2 SAMPLES AND METHODS

The series of diamonds investigated in our study, labelled as CAST2 (Figure 2.1a) and provided us as a courtesy of Dr. H. J. Milledge from the University College of London, were collected in the Birim River valley of Akwatia, in Ghana, in 1960-1970. Unfortunately, it was not possible to recover the exact orientation of the samples when they were extracted from the deposit, since alluvial diamonds are randomly oriented in the alluvial valley. 15 diamonds of the series, clearly showing the presence of inclusions, have been selected through optical microscopy for subsequent measurements. Selected diamonds show quite different shapes (Figure 2.1b, 2.1c, 2.1d), from clearly octahedral to irregular habit, and range in size between ~ 0.5 mm and 1.5 mm. Inclusions appear in most cases dark-gray or black in color, although a clear identification of their distinctive features is made difficult by the many reflexes present in diamonds and by the unclean surface.

To identify the mineral phases present as inclusions, estimate their sizes and unveil the possible presence of fractures in the diamond host, all samples have been analyzed combining XRD and SRXTM. 4 diamonds (CAST2-1, -6, -7, -12) containing inclusions that we could identify as magnetic have also been chosen to undergo magnetic characterization with an Alternating Gradient Force Magnetometer (AGFM) (Flanders, 1988), by acquiring IRM and backfield curves, and complete hysteresis loops and First Order Reversal Curves (FORCs). The masses of the samples have been measured to be 0.48 mg, 2.32 mg, 1.27 mg, 1.85 mg, respectively, with an uncertainty of $\sim 2\%$. The combined knowledge of these magnetic features should be sufficient for determining with high enough accuracy the natural remanent magnetization of the inclusions and to interpret their magnetic behaviour in terms of the magnetic granulometry (single- or multi-domain state) of their particles. Such interpretation, combined with the appreciation of

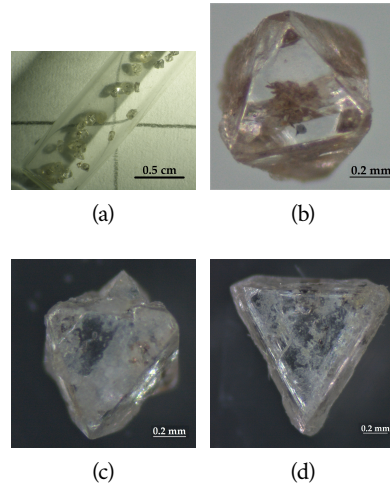


Figure 2.1. (a) Diamonds belonging to the CAST2 series and optical images of: (b) CAST2-1; (c) CAST2-5; (d) CAST2-13 samples chosen as examples. Diamonds show quite different shapes; inclusions are in most cases distinguishable by their dark-gray, black color..

magnetic anisotropy, could permit to evaluate the intensity of the geomagnetic field to which inclusions have been subjected to. This comparison actually goes beyond the scope of the present paper and will be the subject of future works.

2.2.1 XRD acquisitions

XRD measurements have been performed with a Rigaku-Oxford Supernova single-crystal diffractometer. The instrument mounts a Dectris Pilatus3 R 200K-A detector and it is equipped with a molybdenum microfocus source ($\lambda_{\text{Mo}} \approx 0.71 \text{ \AA}$) and 4-circles K geometry. Diamonds were attached on brass pins with wax and mounted on a goniometer head allowing for centering the crystal onto the incoming X-ray beam (Figure 2.2a) and φ scans of few degrees, usually $\sim 40^\circ\text{--}50^\circ$ in steps of 0.5° , have been performed around each selected inclusion. The most significant frames acquired in each scan have been first corrected by masking the diffraction spots corresponding to the host diamond and then integrated with CrysAlis^{Pro} software (Rigaku Oxford Diffraction, 2006), and finally merged together by summing them up with the help of HighScore software (Degen et al., 2014).

2.2.2 SRXTM scans

Synchrotron radiation absorption-based tomographic microscopy has been performed at the TOMCAT-Xo2DA beamline at the Swiss Light Source facility of the Paul Scherrer Institut (Stampanoni et al., 2006). 2D radiographic projections of the samples have been collected by setting the X-ray beam energy to 20 keV and by using: (i) a 5.8 μm thick LSO:Tb scintillator; (ii) an Optique Peter high-resolution microscope accommodating 10x, 20x and 40x Olympus UPLAPO objectives; and (iii) a high sensitive, low noise, large field-of-view pco.Edge 5.5 optical camera, featuring a sensor size of 2560×2160 pixels with a pitch size of 6.5 μm . Tomographic volumes have been reconstructed at the facility by means of a highly optimized software based on Fourier transform algorithms (Marone & Stampanoni, 2012). Obtained 3D reconstructed volumes consist of 2160 slices each, with a spatial resolution of $\sim 0.5 \mu\text{m}$ – $2 \mu\text{m}$ depending on the objective used. Reconstructed 3D images have been subsequently post-processed with Thermo Scientific™ Avizo™ software to get an estimate of the shape, size and volume of the diamonds and their inclusions.

2.2.3 AGFM measurements

Magnetic characterization of inclusions, as detected in XRD measurements, has been performed with a Lake Shore Cryotronics MicroMag 2900 AGFM. The instrument allows to measure the scalar component of the magnetic moment of a specimen, along the direction of an applied, uniform field H , with a nominal sensitivity of 10^{-11} A m^2 and a resolution that in our acquisitions varied between $\sim 10^{-11} \text{ A m}^2$ and $\sim 2.5 \times 10^{-11} \text{ A m}^2$ depending on the sample. The uniform and constant flux intensity of the applied field $\mu_0 H$, with $\mu_0 = 4\pi \cdot 10^{-7} \text{ Wb}/(\text{A m})$ being the permeability of vacuum, can vary in the range $(-2.2, 2.2) \text{ T}$ in minimum steps of $\sim 0.05 \times 10^{-3} \text{ T}$, although the flux intensity of the field needed in our experiments to achieve magnetic saturation of the samples did not exceed 1 T. Throughout the measurements, specimens have been centered into the gap of the 2-probes electromagnet generating H by means of a rod mounted on a piezoelectric sensor (Figure 2.2b). Acquisitions have been performed by applying a weak, non-uniform, alternating field H_{ac} in the x -direction longitudinal to H and setting $\partial H_{ac}/\partial x = 1.5 \text{ T/m}$.

For each selected diamond we acquired IRM and backfield curves, major hysteresis loops and full sets of FORCs. As schematically depicted in Figure 2.3, IRM curves are obtained by measuring the remanent magnetic moment of the sample $m_{\text{IRM}}(H)$ after application and subsequent removal of increasing fields H , starting from $H = 0$. It is worth noting that since $m_{\text{IRM}}(0)$, i.e. the first point of the IRM curve, depends on the entire magnetic history experienced by the sample prior to any magnetic treatment and it is irreversibly cancelled after

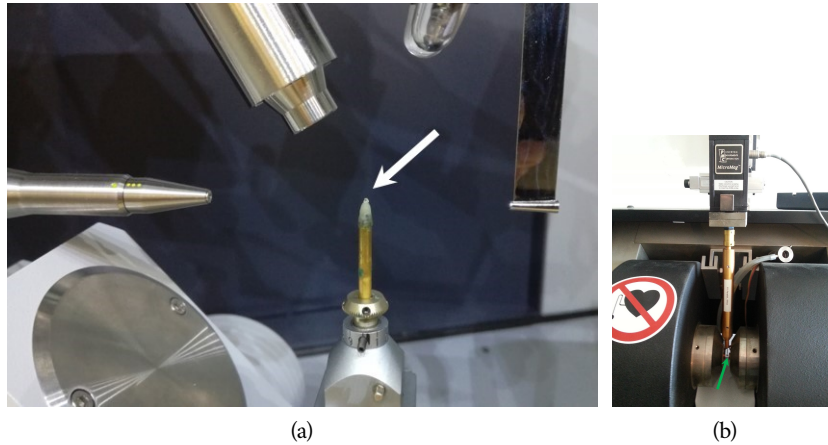


Figure 2.2. Setup of (a) diffractometer and (b) AGFM used for crystallographic and magnetic characterization. Diamonds are mounted on a pin in the diffractometer and on a rod in the AGFM, indicated with arrows in the pictures.

measurement, its acquisition is a crucial step and it has to be accomplished prior to any other measurements or treatments of the samples. Backfield curves are acquired similarly to IRM ones but in this case decreasing the applied field from the saturating value downward to $H = 0$, applying then small reverse, negative fields of increasing absolute intensity, and finally going back to $H = 0$, when the value of the remanent moment is measured. FORCs represent a full set of minor branches, lying inside the unique major hysteresis loop characterizing a given system, collected with a conventional procedure. Starting from the positive saturation field H_{sat} , above which the magnetic moment is essentially constant, the magnetic field H is decreased down to a reversal point $-H_{\text{sat}} \leq H_{\text{rev}} \leq H_{\text{sat}}$ and then increased up again to H_{sat} . Magnetic moment (or magnetization) values $m(H; H_{\text{rev}})$ are recorded along the ascending branch of the loop $H_{\text{sat}} \rightarrow H_{\text{rev}} \rightarrow H_{\text{sat}}$, therefore at all magnetic fields $H_{\text{rev}} \leq H \leq H_{\text{sat}}$.

2.3 RESULTS

2.3.1 XRD

The XRD analysis shows that the inclusions in the 15 selected diamonds comprise different mineral phases, that are present as both single crystal and polycrystalline material. Only in two samples, CAST2-4 and CAST2-8, no magnetic phases have been detected, while in the others both magnetic and non-magnetic phases were present. Among the non-magnetic minerals, single-crystal olivine has been identified in most inclusions, while the presence of single-crystal quartz and garnet has

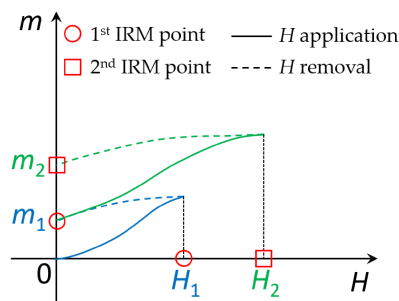


Figure 2.3. Sketch of the procedure followed to acquire IRM curves. Magnetic field H (the uniform, stronger field in the AGFM) is successively applied at increased values $H_1 < H_2 < \dots$ (solid lines) and subsequently removed (dashed lines). The corresponding components of the remanent magnetic moment (or of the magnetization) m_1, m_2, \dots , along the direction of H , are collected for each field value only after its removal.

been more sporadically detected. Focusing on magnetic phases, in most inclusions they have been identified as magnetite (Fe_3O_4) or magnesioferrite (MgFe_2O_4), which are ferrimagnetic materials, and in few cases as hematite ($\alpha\text{-Fe}_2\text{O}_3$), a canted antiferromagnet. In particular, the latter, if present, has been always found in a mixture with magnetite/magnesioferrite. Furthermore, all Fe-rich phases generally appeared as powders and only in one diamond (CAST2-7) single-crystal magnetite has also been detected. Finally, it is important to note that magnetite and magnesioferrite have very similar lattice parameters and spinel structure, reflected in similar XRD patterns that make nearly impossible their separated identification especially if investigated as inclusions in diamonds (e.g. Angel & Nestola, 2016). For this reason, in what follows we will refer indistinctly to magnetite or magnesioferrite whenever this kind of phase is involved.

In particular, for our purposes a promising sample shall contain a unique magnetic phase, not necessarily derived from a single inclusion, in order to surely identify the source of the magnetic signal. The additional presence of non-magnetic minerals does not constitute a problem as they would only contribute with a weak diamagnetic response superimposed to that of the diamond, that is why diffractograms related to non-magnetic inclusions present in the samples are not reported here. According to the above reasoning, CAST2-1 represents the most interesting diamond in the suite, since it contains a unique polycrystalline magnetic phase, as clearly shown from the rings present in the pattern reported in the inset of Figure 2.4a. Beyond the CAST2-1 diamond, we have selected three more samples, i.e. CAST2-6, CAST2-7 and CAST2-12, to perform magnetic characterization. They contain multiple inclusions, some of them comprising only non-magnetic phases, while others possessing also a magnetic character. Diffrac-

tograms corresponding to the magnetic inclusions present in the 4 diamonds are reported in Figure 2.4 and show that all the inclusions have been identified as magnetite or magnesioferrite.

2.3.2 SRXTM

3D reconstructions of the tomographic projections for the four diamonds selected for magnetic characterization are shown in Figure 2.5. Estimates of the linear sizes of both inclusions and diamonds are reported for some arbitrarily chosen sample orientation. From these estimates we can conclude that the inclusion size ranges approximately between 100 μm and 700 μm , while the diamond size is $\sim 0.5\text{ mm} - 1.5\text{ mm}$, in agreement with the outcomes of optical microscopy analysis (see Figure 2.1). A careful analysis of 2D tomographic slices through the reconstructed volume of the four diamonds allowed us to conclude that only the CAST2-1 inclusion is fully entrapped into the diamond, while the inclusions in the other three diamonds are connected to the external surroundings being therefore epigenetic with respect to the host. Another possible explanation for the appearance of fractures can arise whenever the inclusions have higher compressibility with respect to the host and thus expand in volume more than diamond, when travelling towards the Earth's surface. In such a case, inclusions may also be proto- or syngenetic with respect to the host diamond even in presence of fractures.

2.3.3 AGFM

IRM curves have been first acquired on CAST2-1, -6, -7 samples, while backfield curves have been later collected on CAST2-6, -7 and -12 samples. Resulting curves are shown in Figure 2.6, while $m_{\text{IRM}}(0)$ and saturation m_{IRM} (sIRM) values, the latter reached for all samples at 0.15 T, are listed in Table 2.1. The same table reports also the values of the coercivity of remanence H_c^{bf} , which identify on each backfield curve the magnetic fields for which $m_{\text{bf}}(H_c^{\text{bf}}) = 0$.

After IRM and backfield curves, major hysteresis loops reporting the detected magnetic moment m as a function of the uniform applied field H have been acquired for all the four samples and are displayed in Figure 2.7. In the loops, the magnetic moment is expressed in dimensionless units by dividing the scalar component m measured with the AGFM by the saturation moment m_{sat} , which represents the value of m reached at the saturation field H_{sat} introduced in Sec. 2.2.3. For $H \geq H_{\text{sat}}$, hysteresis loops show a characteristic plateau and no further magnetization processes due to domain wall motion, spin rotation or spin reversal, occur anymore so that m remains essentially constant. In the present case, m_{sat} values have been chosen as the maximum reached by m for each sample and are reported in Table 2.1. The values of the remanent magnetic

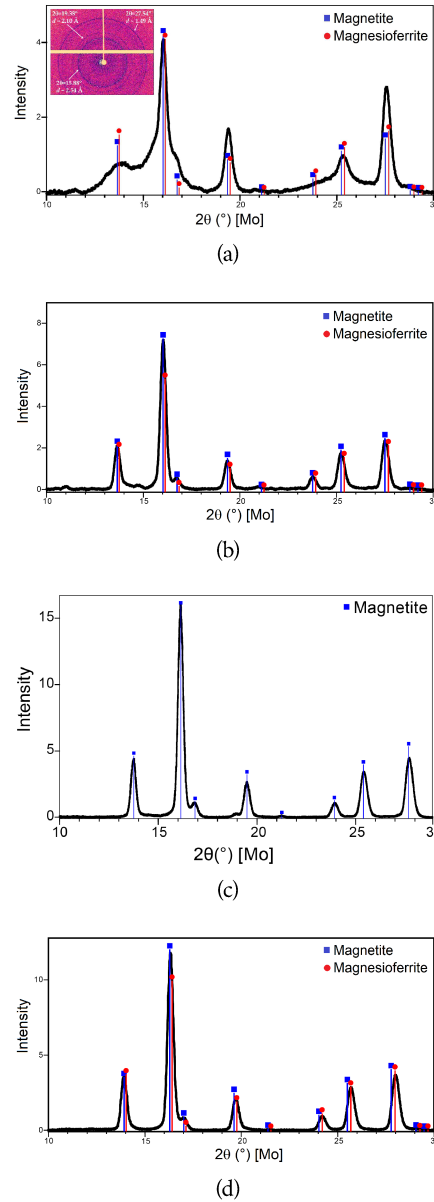


Figure 2.4. Diffractograms identifying magnetic phases (magnetite – blue squares; magnesioferrite – red circles) in: (a) CAST₂-1; (b) CAST₂-6; (c) CAST₂-7 and (d) CAST₂-12 diamonds. Diffractograms related to non-magnetic inclusions are not reported. Inset in Figure 2.4a shows the pattern from an acquisition at fixed φ ; diffraction spots related to diamond are not shown. Phase identification performed with the HighScore software..

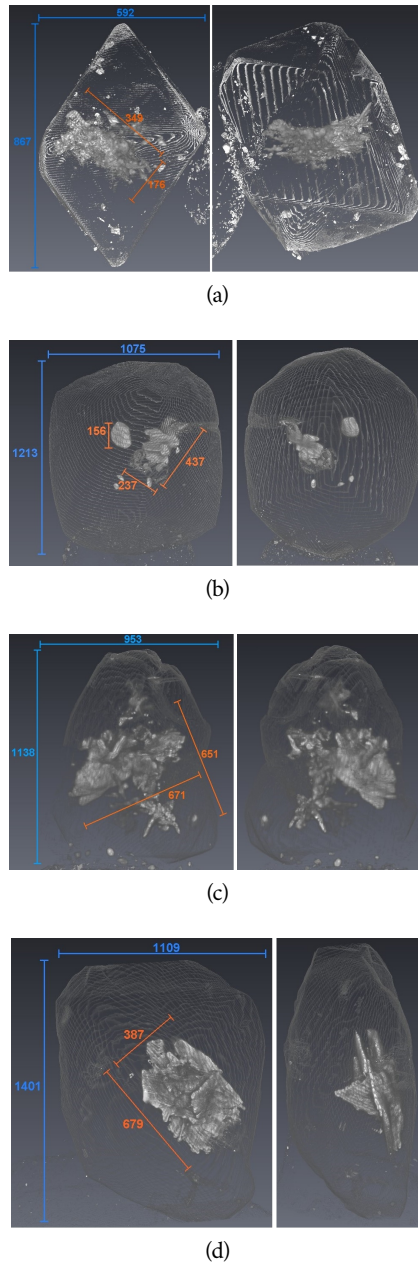


Figure 2.5. 3D reconstructions of SRXTM images for: (a) CAST2-1; (b) CAST2-6; (c) CAST2-7; (d) CAST2-12 samples. Inclusions are clearly visible in brighter colors since composed by chemical elements heavier than carbon. Estimates of inclusions and diamonds sizes, expressed in μm units, are shown for arbitrary fixed sample orientations in orange and light-blue color, respectively..

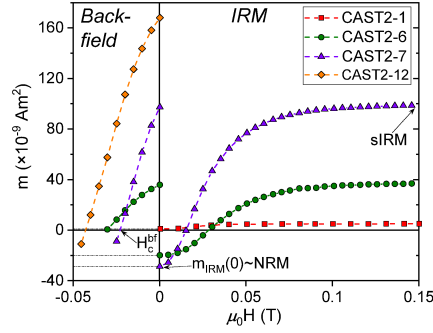


Figure 2.6. IRM ($H \geq 0$) and backfield ($H \leq 0$) curves, acquired with the AGFM, on CAST2-1 (red squares), CAST2-6 (green circles), CAST2-7 (violet triangles) and CAST2-12 (orange diamonds) samples. Points describing the remanence at zero field $m_{\text{IRM}}(0)$ (best approximation of the NRM), the remanence at saturation sIRM, reached at 0.15 T for all samples, and the coercive field of remanence H_c^{bf} are indicated with arrows; corresponding values are reported in Table 2.1.

Sample	IRM/backfield parameters			Hysteresis parameters		
	$m_{\text{IRM}}(0)$ [$\times 10^{-9}$ A m 2]	sIRM [$\times 10^{-9}$ A m 2]	$\mu_0 H_c^{\text{bf}}$ [T]	m_{sat} [$\times 10^{-9}$ A m 2]	m_r [$\times 10^{-9}$ A m 2]	$\mu_0 H_c$ [T]
CAST2-1	1	5	//	27	5	0.006
CAST2-6	-20	37	-0.031	112	35	0.020
CAST2-7	-29	99	-0.023	541	98	0.012
CAST2-12	60	168	-0.043	510	174	0.026

Table 2.1. Numerical values of: IRM remanence at zero field ($m_{\text{IRM}}(0)$), IRM at saturation field 0.15 T (sIRM), IRM coercive field (H_c^{bf}), as extrapolated from IRM/backfield curves (Figure 2.6); saturation magnetic moment (m_{sat}), remanent magnetic moment (m_r) and coercive field (H_c), as extrapolated from hysteresis loops (Figure 2.7), for the CAST2 diamonds reported in the first column..

moment $m_r = m(H = 0)$ and of the coercive field H_c at which $m(H_c) = 0$, as extrapolated from the curves, are also reported in Table 2.1. We notice that sIRM and m_r values can be considered equal within the uncertainty value, as expected since sIRM can be identified with the usual remanence associated to a major complete hysteresis loop of a magnetic material.

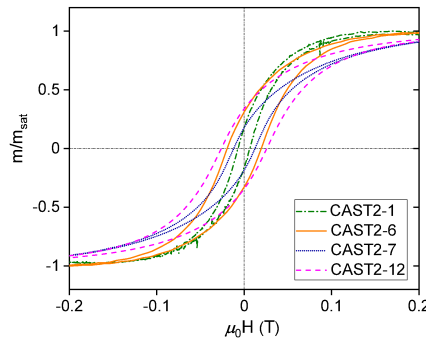


Figure 2.7. Hysteresis loops, acquired with the AGFM, on CAST2-1 (dash-dotted, green), CAST2-6 (solid, orange), CAST2-7 (dotted, blue) and CAST2-12 (dashed, pink) samples. The dimensionless magnetic moment is obtained by dividing m by m_{sat} values reported in Table 2.1. The diamagnetic contribution of diamonds, becoming relevant at $\mu_0 H \gg 0.2$ T (CAST2-1, -6 samples) or 0.5 T (CAST2-7, -12 samples), is not shown. A sample-dependent vertical offset due to instrumental noise has been subtracted from the curves..

Finally, full sets of FORCs have been collected for the four samples as detailed in Sec. 2.2.3 and after their acquisition FORC diagrams have been evaluated as 2D contour plot of the 3D function $\rho(H, H_{\text{rev}}) = -\partial^2 m / (\partial H \partial H_{\text{rev}})$, known as FORCs distribution. For the evaluation of ρ various numerical methods have been developed, as described in Pike et al. (1999) and Roberts et al. (2000). Resulting 2D FORC diagrams are reported in Figure 2.8 where, for a better comparison, ρ values have been expressed in dimensionless units as $\hat{\rho}(H, H_{\text{rev}}) = (H_0^2 / m_0) \rho(H, H_{\text{rev}})$. In the previous relation H_0 is a characteristic magnetic field that, for all samples, we set equal to the saturation field of the IRM curves, i.e. $\mu_0 H_0 = 0.15$ T, while m_0 is a characteristic magnetic moment that we fixed equal to the saturation value m_{sat} of the hysteresis loop of each sample reported in Table 2.1. Finally, we notice that the reversible contribution to $\hat{\rho}$ due to the points $m(H_{\text{rev}}; H_{\text{rev}})$, lying on the descending branch of the major hysteresis loop, is not included into the diagrams. Indeed, $\hat{\rho}$ is correctly evaluated only for $H > H_{\text{rev}}$ because its definition involves second derivatives, and hence the reversible contribution to $\hat{\rho}$ must be added, when necessary, by making proper ansatz about its analytical behaviour Pike (2003).

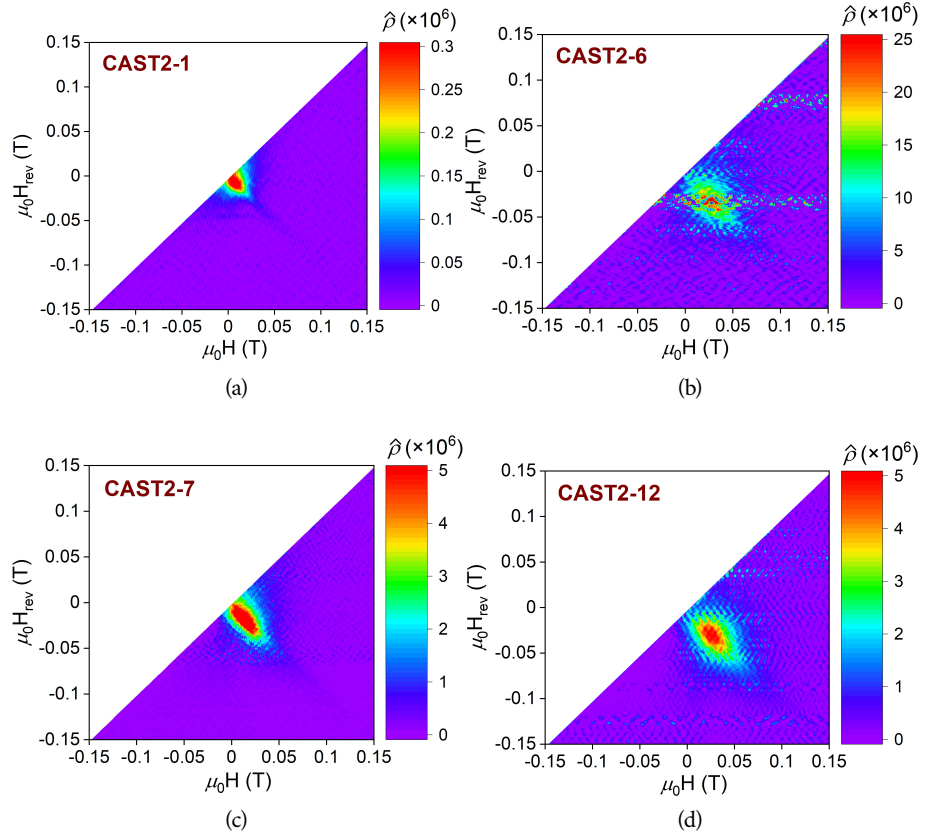


Figure 2.8. 2D FORC diagrams evaluated from full sets of FORCs acquired with the AGFM on: (a) CAST2-1; (b) CAST2-6; (c) CAST2-7; (d) CAST2-12 samples. FORC distribution values are expressed in dimensionless units as $\hat{\rho} = (H_0^2/m_0)\rho$, where ρ , H_0 and m_0 are defined in Sec. 2.3.3. Reversible contribution to $\hat{\rho}$, lying on the $H - H_{rev} = 0$ bisector, is not included.

2.4 DISCUSSION

The combination of XRD, SRXTM and magnetic data we acquired allows to develop the following crystallographic, inner-structural and physical picture about the inclusions present in the four diamonds we investigated. All samples contain one magnetic phase, in some cases comprised in more than one inclusion for each diamond, that XRD allows to determine as a polycrystalline iron oxide, restricting the possibilities to magnetite or magnesioferrite. Furthermore, microtomography shows that only the CAST2-1 diamond has a fully entrapped and isolated inclusion, while the other samples have fractures connecting the external surface to the embedded magnetic oxides. Therefore, CAST2-1 is the only sample that may comprise a proto- or syngenetic inclusion, although its sheet-like shape is similar to that of the inclusions found in the fractured diamonds (Figure 2.5). The knowledge of the saturation magnetic moment of the samples m_{sat} from AGFM measurements, combined with estimates of the volume of the magnetic inclusions V_{mag} as extrapolated from SRXTM data, can then provide useful insights to distinguish between magnetite and magnesioferrite phases. Indeed, these two Fe-rich spinels have different saturation magnetization $M_{\text{sat}} = m_{\text{sat}}/V_{\text{mag}}$ due to the substitution of Mg for Fe^{2+} in the octahedral B sites and, partially, for Fe^{3+} in the tetrahedral A sites of magnetite (pp. 178–180 Cullity & Graham, 2009). For the CAST2-1 sample, the analysis of tomographic data has shown that the volume of the diamond alone is $V_{\text{diam}} \approx 1227.8 \times 10^{-13} \text{ m}^3$, the volume of non-magnetic phases possibly present in negligible amount inside the diamond and of fractures is $V_{\text{fract}} \approx 3.2 \times 10^{-13} \text{ m}^3$, while the magnetic phase comprised in the inclusion has volume $V_{\text{mag}} \approx 0.6 \times 10^{-13} \text{ m}^3$. This means that the volume of the whole sample is $V_{\text{CAST2-1}} = V_{\text{diam}} + V_{\text{fract}} + V_{\text{mag}} \approx 1231.6 \times 10^{-13} \text{ m}^3$ and that the magnetic inclusion volume V_{mag} is about 0.05% of $V_{\text{CAST2-1}}$. By combining V_{mag} with the $m_{\text{sat}} = 27 \times 10^{-9} \text{ A m}^2$ value reported in Table 2.1, we obtain an estimate of the saturation magnetization at room temperature for the CAST2-1 inclusion which is $M_{\text{sat}} \approx 486 \times 10^3 \text{ A/m}$. Since the reported M_{sat} values at 293 K for magnetite and magnesioferrite are $480 \times 10^3 \text{ A/m}$ and $120 \times 10^3 \text{ A/m}$ respectively (Cullity & Graham, 2009, p. 183), we can conclude that CAST2-1 inclusion is most probably magnetite. Similar reasoning may be applied to the inclusions within the other samples in order to identify more precisely the magnetic phase composing them.

Magnetic signals detected with the AGFM by collecting IRM/backfield curves, hysteresis loops and FORCs show a quite complex behaviour making the development of a fully comprehensive physical interpretation quite difficult. IRM curves (Figure 2.6) remarkably show that $m_{\text{IRM}}(0)$ values are different from zero in all the samples, meaning that they all carry a detectable NRM. This important outcome, holding as long as the exposure to magnetic fields other than the Earth's one H_{GMF} can be ruled out as in our case, can provide interesting information on the amplitude of H_{GMF} at the time of formation of the inclusions, since the

time history of H_{GMF} influences the NRM recorded by the samples. It is worth pointing out that information about the declination and inclination of H_{GMF} is instead not available from the kind of inclusions and measurements here proposed, because of the random orientation that the diamonds we have investigated had in the alluvial valley at the time of their eruption and subsequent extraction. As a second remark, $m_{\text{IRM}}(0)$ and sIRM values span more than one order of magnitude. Indeed, $m_{\text{IRM}}(0)$ is about 10^{-9} A m^2 for CAST2-1 sample and of the order of 10^{-8} A m^2 for CAST2-6 and CAST2-7 samples. The same circumstance occurs for sIRM values, that vary between $\sim 5 \times 10^{-9} \text{ A m}^2$ for CAST2-1 and $\sim 1 \times 10^{-7} \text{ A m}^2$ for CAST2-7 samples. Various reasons may explain the observed quite large variations. The most obvious one is that inclusions comprise different magnetic materials, but it does not apply to the samples here investigated because of the XRD results. Another possibility is that magnetic inclusions vary in size and volume from sample to sample and microtomographic images (Figure 2.5) show that we can rely on these differences to partially explain the different outcomes in the IRM behaviour. A final possibility, applying as well in our case, can be that the magnetic moment of a specimen is a vector quantity, but the AGFM is able to perform only scalar measurements. Understanding which of the last two reasons play a major role in each sample we have investigated is a challenging task deserving specific consideration in future works.

Hysteresis loop reflect the main properties of a magnetic system, as its magnetic anisotropy, magnetic susceptibility, coercive forces and saturation magnetization (Bertotti, 1998; Cullity & Graham, 2009), while the shape of FORCs diagrams shed light on the microscopic magnetic configuration of the particles composing a system, which is particularly interesting when dealing with natural samples as mineral inclusions in host diamonds or rocks (Pike et al., 1999; Roberts et al., 2000). In particular, hysteresis is a complex phenomenon strictly related in our samples to the their magnetic granulometry, i.e. the relative distribution of superparamagnetic, single-domain, or multi-domain magnetic particles according to the composition, size and geometry of the included Fe-based crystallites (magnetite or magnesioferrite), whose associated magnetization vectors can have varied amplitudes pointing in different directions with relaxation times mainly depending on their size. Detailed descriptions of such processes can be found in many textbooks devoted to the subject (Bertotti, 1998; Dunlop & Özdemir, 1997). The loops we acquired on our samples (Figure 2.7) can offer a qualitative information about the magnetic anisotropy and the microgranulometry of the inclusions, encompassed in their behaviour close to the saturation field H_{sat} and to the coercive field H_c . The behaviour of the loops close to saturation is known to be closely dependent on an intrinsic factor, the magnetic anisotropy, with systems having lower uniaxial anisotropy constant K being characterized by lower H_{sat} values (pp. 218–222 Cullity & Graham, 2009; Stoner & Wohlfarth, 1948, for a detailed explanation) . According to this general observation and by assuming to

deal with inclusions characterized by an effective uniaxial anisotropy constant K_{eff} , encompassing both the effects of their crystal structure and of the strains, dislocations, defects induced by the host diamond, we can conclude that CAST2-1 and CAST2-6 diamonds ($\mu_0 H_{\text{sat}} \approx 0.2$ T) shall most probably have lower K_{eff} with respect to CAST2-7 and CAST2-12 samples ($\mu_0 H_{\text{sat}} \approx 0.5$ T). Similarly, the behaviour of the hysteresis close to H_c gives insights about an extrinsic factor which is the grain size of the magnetic particles composing the inclusions. In this case, it is known that the higher the coercivity is, the lower the grain size of the particles and more crystal defects are most probably present in the system (pp. 360–364 Cullity & Graham, 2009; Kneller & Luborsky, 1963; Luborsky, 1961). Then, by looking at the H_c values reported in Table 2.1, we can conclude that CAST2-6 and CAST2-12 inclusions shall comprise finer grains with respect to CAST2-1 and CAST2-7 samples, respectively. To get more quantitative results, models of hysteresis must be developed to relate H_c values to extrinsic parameters such as the grain size of the particles.

The symmetry of the FORC diagrams (Figure 2.8) around the $H_{\text{rev}} + H = 0$ axis is to be expected for magnetic systems, due to the symmetry of ascending and descending branches of the hysteresis loops around the origin ($H = 0, M = 0$), i.e. $M_{\text{desc}}(-H) = -M_{\text{asc}}(H)$ with M_{asc} (M_{desc}) being the magnetization value evaluated on the ascending (descending) branch of the loop. The shape of the diagrams, appearing in all the cases slightly spread out in the $H - H_{\text{rev}} = 0$ direction, is due to the presence of single-domain magnetic particles with not negligible local interactions among them, as exhaustively explained in Pike et al. (1999) and Roberts et al. (2000). It is worth mentioning that when the particles crystallize at different times, the presence of such coupling makes it more difficult to establish at which point the NRM they carry can be ascribed to the action of the Earth's magnetic field. In particular, we see from Figure 2.8 that local coupling plays a bigger role in CAST2-6 and CAST2-12 inclusions with respect to CAST2-1 and CAST2-7 ones, since the contour plots of the former samples show less sharp peaks. It is noteworthy that FORC diagrams did not evidence negative peaks usually associated to interactions among different magnetic objects, or inclusions, in the analyzed systems. Finally, the position of the ρ distribution peaks, defined as the point $(\bar{H}, \bar{H}_{\text{rev}})$ at which the contour plot reaches its maximum, provides an estimate of the mean value \bar{H}_c of the distribution of coercive fields and energy barriers that are associated to each magnetic particle of the inclusion. By expressing the peak position as $H_{\text{peak}} = (\bar{H} - \bar{H}_{\text{rev}}) / 2$, we can again gather the samples into two groups: on the one side we have CAST2-1 and CAST2-7 samples, having $\mu_0 H_{\text{peak}} \approx 0.006$ T and 0.017 T respectively, while on the other side there are CAST2-6 and CAST2-12 samples, with peaks values at $\mu_0 H_{\text{peak}} \approx 0.029$ T and 0.026 T respectively. The difference in H_{peak} values can be ascribed in our case to variations in the grain size and in the orientation of the magnetization within the particles belonging to the various samples. The latter explanation and

the extrapolated $\bar{H}_c \sim H_{\text{peak}}$ values are in agreement with the H_c estimates reported in Table 2.1.

2.5 CONCLUSIONS

In the present paper we have proposed an efficient, non-destructive experimental methodology to determine the inner structure, the crystallographic and the magnetic properties of inclusions entrapped in a series of natural diamonds. The methodology is based on the use of XRD, SRXTM and AGFM techniques and has the potential to be successfully applied to any host-inclusion system of mm/sub-mm size comprising magnetic phases with magnetic moments higher than $\sim 10^{-9}$ A m². It allows to build up a qualitatively comprehensive and robust picture of the main chemico- and geophysical features of the samples under investigation.

In particular, for the four diamonds we selected in our study, we have shown that magnetic inclusions comprise polycrystalline iron oxides having ferrimagnetic spinel structure identified as magnetite or magnesioferrite. We have demonstrated the presence of fractures connecting the inclusions to the diamond surface in all but one samples, thus suggesting that this kind of inclusions are epigenetic and probably formed because of pre-existing Fe-rich fluids that percolated through the cracks and diffused within diamonds. We have shown that all the inclusions carry a non zero NRM and we have interpreted the rich picture arising from the FORC diagrams by assuming that the inclusions are composed of locally interacting single-domain particles. Finally, we have distinguished the samples according to the different behaviour observed in their hysteresis loops, by relating the latter to both intrinsic and extrinsic factors represented by the magnetic anisotropy and the grain size of the particles. The comparison of experimental data with proper models of magnetic hysteresis is needed to derive more quantitative conclusions on this topic.

ACKNOWLEDGMENTS

This project has received funding from the European Research Council (ERC) under the European Union's Horizon 2020 research and innovation programme (grant agreement No. 714936 for the project TRUE DEPTHS to M. Alvaro). MA has also been funded by the FARE MIUR n. R164WEJAHH for the project IMPACT.

We acknowledge the Paul Scherrer Institut, Villigen, Switzerland for provision of synchrotron radiation beamtime at the TOMCAT beamline of the SLS.

REFERENCES

- Angel, R. J., Alvaro, M., Nestola, F., & Mazzucchelli, M. L. (2015a). Diamond thermoelastic properties and implications for determining the pressure of formation of diamond-inclusion systems. *Russ. Geol. Geophys.*, *56*, 211.
- Angel, R. J., Mazzucchelli, M. L., Alvaro, M., Nimis, P., & Nestola, F. (2014). Geobarometry from host-inclusion systems: the role of elastic relaxation. *Am. Miner.*, *99*, 2146.
- Angel, R. J., Milani, S., Alvaro, M., & Nestola, F. (2016). High-quality structures at high pressure? Insights from inclusions in diamonds. *Z. Kristall.*, *231*, 467.
- Angel, R. J., & Nestola, F. (2016). A century of mineral structures: how well do we know them? *Am. Miner.*, *101*, 1036.
- Angel, R. J., Nimis, P., Mazzucchelli, M. L., Alvaro, M., & Nestola, F. (2015b). How large are departures from lithostatic pressure? Constraints from host-inclusion elasticity. *J. Metamorph. Geol.*, *33*, 801.
- Anzolini, C., Prencipe, M., Alvaro, M., Romano, C., Vona, A., Lorenzon, S., Smith, E. M., Brenker, F. E., & Nestola, F. (2018). Depth of formation of super-deep diamonds: Raman barometry of CaSiO₃-walsstromite inclusions. *Am. Miner.*, *103*, 69.
- Bertotti, G. (1998). *Hysteresis in Magnetism - For Physicists, Materials Scientists, and Engineers*. Academic Press.
- Bulanova, G. P. (1995). The formation of diamond. *J. Geochem. Explor.*, *53*, 1.
- Bulanova, G. P., Griffin, W. L., Ryan, C. G., Shestakova, O. Y., & Barnes, S.-J. (1996). Trace elements in sulfide inclusions from Yakutian diamonds. *Contrib. Mineral. Petrol.*, *124*, 111.
- Clement, B. M., Haggerty, S., & Harris, J. (2008). Magnetic inclusions in diamonds. *Earth Planet. Sci. Lett.*, *267*, 333.
- Collinson, D. W. (1998). Magnetic properties of polycrystalline diamonds. *Earth Planet. Sci. Lett.*, *161*, 179.
- Cullity, B. D., & Graham, C. D. (2009). *Introduction to Magnetic Materials* (2nd). John Wiley & Sons.
- Degen, T., Sadki, M., Bron, E., König, U., & Nénert, G. (2014). The HighScore suite. *Powder Diffr.*, *29*, S13.
- Dunlop, D. J., & Özdemir, Ö. (1997). *Rock Magnetism - Fundamentals and frontiers*. Cambridge University Press.
- Fitzgerald, C. B., Venkatesan, M., Douvalis, A. P., & Coey, J. M. D. (2006). Magnetic properties of carbonado diamonds. *J. Magn. Magn. Mater.*, *300*, 368.
- Flanders, P. J. (1988). An alternating-gradient magnetometer. *J. Appl. Phys.*, *63*, 3940.
- Gilder, S. A., Egli, R., Hochleitner, R., Roud, S. C., Volk, M. W., Le Goff, M., & de Wit, M. (2011). Anatomy of a pressure-induced, ferromagnetic-to-paramagnetic transition in pyrrhotite: Implications for the formation pressure of diamonds. *J. Geophys. Res.*, *116*, B10101.

- Haggerty, S. E. (1986). Diamond genesis in a multiply-constrained model. *Nature*, 320, 34.
- Harris, J. W. (1968). The recognition of diamond inclusions. Part 1: Syngenetic mineral inclusions. *Ind. Diam. Rev.*, 28, 402.
- Harris, J. W. (1993). The geology of diamond: time and depth profiles from inclusions [Proceedings of the 3rd International Conference on the New Diamond Science and Technology – Diamond 1992 (Heidelberg, Germany, 1992), edited by P. K. Bachmann, A. T. Collins, M. Seal]. *Diam. Relat. Mat.*, 2, 75.
- Kletetschka, G., Taylor, P. T., Wasilewski, P. J., & Hill, H. G. M. (2000). Magnetic properties of aggregate polycrystalline diamond: implications for carbonado history. *Earth Planet. Sci. Lett.*, 181, 279.
- Kneller, E. F., & Luborsky, F. E. (1963). Particle Size Dependence of Coercivity and Remanence of Single-Domain Particles. *J. Appl. Phys.*, 34, 656.
- Liu, L.-g., Mernagh, T. P., & Jaques, A. L. (1990). A mineralogical Raman spectroscopy study on eclogitic garnet inclusions in diamonds from Argyle. *Contrib. Mineral. Petrol.*, 105, 156.
- Luborsky, F. E. (1961). Development of Elongated Particle Magnets. *J. Appl. Phys.*, 32, S171.
- Marone, F., & Stampanoni, M. (2012). Regridding reconstruction algorithm for real time tomographic imaging. *J. Synchrot. Radiat.*, 19, 1029.
- Meyer, H. O. A., & McCallum, M. E. (1986). Mineral Inclusions in Diamonds from the Sloan Kimberlites, Colorado. *J. Geol.*, 94, 600.
- Milani, S., Nestola, F., Alvaro, M., Pasqual, D., Mazzucchelli, M. L., Domeneghetti, M. C., & Geiger, C. A. (2015). Diamond-garnet geobarometry: The role of garnet compressibility and expansivity. *Lithos*, 227, 140.
- Nasdala, L., Brenker, F. E., Glinnemann, J., Hofmeister, W., Gasparik, T., Harris, J. W., Stachel, T., & Reese, I. (2003). Spectroscopic 2D-tomography: Residual pressure and strain around mineral inclusions in diamonds. *Eur. J. Mineral.*, 15, 931.
- Nestola, F., Alvaro, M., Casati, M. N., Wilhelm, H., Kleppe, A. K., Jephcoat, A. P., Domeneghetti, M. C., & Harris, J. W. (2016a). Source assemblage types for cratonic diamonds from X-ray synchrotron diffraction. *Lithos*, 265, 334.
- Nestola, F., Cerantola, V., Milani, S., Anzolini, C., McCammon, C., Novella, D., Kuppenko, I., Chumakov, A., Rüffer, R., & Harris, J. W. (2016b). Synchrotron Mössbauer Source technique for *in situ* measurement of iron-bearing inclusions in natural diamonds. *Lithos*, 265, 328.
- Nestola, F., Jung, H., & Taylor, L. A. (2017). Mineral inclusions in diamonds may be synchronous but not syngenetic. *Nat. Commun.*, 8, 14168.
- Nestola, F., Merli, M., Nimis, P., Parisatto, M., Kopylova, M., De Stefano, A., Longo, M., Ziberna, L., & Manghnani, M. (2012). *In situ* analysis of garnet

- inclusion in diamond using single-crystal x-ray diffraction and x-ray micro-tomography. *Eur. J. Mineral.*, 24, 599.
- Nestola, F., Nimis, P., Angel, R. J., Milani, S., Bruno, M., Prencipe, M., & Harris, J. W. (2014). Olivine with diamond-imposed morphology included in diamonds. Syngeneisis or protogeneisis? *Int. Geol. Rev.*, 56, 1658.
- Nestola, F., Nimis, P., Ziberna, L., Longo, M., Marzoli, A., Harris, J. W., Manghnani, M. H., & Fedortchouk, Y. (2011). First crystal-structure determination of olivine in diamond: Composition and implications for provenance in the Earth's mantle. *Earth Planet. Sci. Lett.*, 305, 249.
- Nimis, P., Alvaro, M., Nestola, F., Angel, R. J., Marquardt, K., Rustioni, G., Harris, J. W., & Marone, F. (2016). First evidence of hydrous silicic fluid films around solid inclusions in gem-quality diamonds. *Lithos*, 260, 384.
- Nimis, P., Angel, R. J., Alvaro, M., Nestola, F., Harris, J. W., Casati, N., & Marone, F. (2019). Crystallographic orientations of magnesiochromite inclusions in diamonds: what do they tell us? *Contrib. Mineral. Petrol.*, 174, 29.
- Pearson, D. G., Brenker, F. E., Nestola, F., McNeill, J., Nasdala, L., Hutchison, M. T., Matveev, S., Mather, K., Silversmit, G., Schmitz, S., Vekemans, B., & Vincze, L. (2014). Hydrous mantle transition zone indicated by ringwoodite included within diamond. *Nature*, 507, 221.
- Pike, C. R. (2003). First-order reversal-curve diagrams and reversible magnetization. *Phys. Rev. B*, 68, 104424.
- Pike, C. R., Roberts, A. P., & Verosub, K. L. (1999). Characterizing interactions in fine magnetic particle systems using first order reversal curves. *J. Appl. Phys.*, 85, 6660.
- Rigaku Oxford Diffraction. (2006). CrysAlis^{Pro} [Oxford Diffraction Ltd. (Abingdon, Oxfordshire, England)].
- Roberts, A. P., Pike, C. R., & Verosub, K. L. (2000). First-order reversal curve diagrams: A new tool for characterizing the magnetic properties of natural samples. *J. Geophys. Res.*, 105(B12), 28461.
- Shirey, S. B., Cartigny, P., Frost, D. J., Keshav, S., Nestola, F., Nimis, P., Graham Pearson, D., Sobolev, N. V., & Walter, M. J. (2013). Diamonds and the Geology of Mantle Carbon. In R. M. Hazen, A. P. Jones, & J. A. Baross (Eds.), *Carbon in Earth* (p. 355). Mineralogical Society of America – Geochemical Society.
- Stachel, T., & Harris, J. W. (2008). The origin of cratonic diamonds – Constraints from mineral inclusions. *Ore Geol. Rev.*, 34, 5.
- Stachel, T., & Harris, J. W. (2009). Formation of diamond in the Earth's mantle. *J. Phys.: Condens. Matter*, 21, 364206.
- Stachel, T., & Luth, R. W. (2015). Diamond formation – Where, when and how? *Lithos*, 220-223, 200.
- Stampanoni, M., Groso, A., Isenegger, A., Mikuljan, G., Chen, Q., Bertrand, A., Henein, S., Betemps, R., Frommherz, U., Böhler, P., Meister, D., Lange, M.,

- & Abela, R. (2006). Trends in synchrotron-based tomographic imaging: the SLS experience. In U. Bonse (Ed.), *Developments in X-Ray Tomography V* (p. 63180M). SPIE, Bellingham.
- Stoner, E. C., & Wohlfarth, E. P. (1948). A mechanism of magnetic hysteresis in heterogeneous alloys. *Phil. Trans. R. Soc. A*, 240, 599.
- Tappert, R., & Tappert, M. C. (2011). *Diamonds in Nature - A Guide to Rough Diamonds*. Springer.

3 Primary inclusion of magnetite and quartz in Consolidated African Selection Trust (CAST) diamonds from Akwatia, Ghana

3.1 INTRODUCTION

Diamond is among the most studied materials, due to its physical properties, but natural diamonds have further geological relevance since they provide extraordinary information from the deepest, and otherwise inaccessible, regions of our planet. In fact, natural diamonds can contain mineral inclusions that were trapped during their formation at depth and act as windows on the Earth's interior, providing fundamental insights on the composition of the deep Earth and global geo-dynamics. As such, the study of inclusions in diamonds is crucial to improve our understanding of the formation and evolution of the solid Earth through geological times and, as a consequence, the geological processes shaping the Earth's surface and impacting the environment. Inclusion bearing diamonds have been studied for many decades, leading to extraordinary discoveries regarding, for example, the recycling of oceanic plates to the lower mantle (Nestola et al., 2018; Walter et al., 2011) the hydrous nature of the deep Earth (Jean et al., 2016; Novella et al., 2015; Palot et al., 2016; Pearson et al., 2014; Taylor et al., 2016) and the nature of deep mantle melt/fluids, (e.g. Navon et al., 1988; Weiss et al., 2015). A crucial aspect of the study of inclusions in diamond is to understand the time of formation of the inclusions with respect to the time of diamond growth, a highly debated topic since the late 60s (Harris, 1968a, 1968b) which is still not set today (Jacob et al., 2016; Nestola et al., 2019; Nestola et al., 2017; Thomassot et al., 2009). According to their time of formation, inclusions formed before, during and after the diamond growth are classified as protogenetic, syngenetic and epigenetic, respectively. This knowledge is of paramount importance, since inclusions entrapped at different times provide information on various time scaling, related to distinct growth conditions and environments. In this context, iron oxides inclusions are potentially of great interest, because of their iron content that could be used to infer the oxygen fugacity conditions in which they grew (e.g. McCammon et al., 1997), but are rare and often difficult to classify in terms of both time of formation and paragenesis. Magnetite ($\text{Fe}^{2+}\text{Fe}_2^{3+}\text{O}_4$), in particular, is a rare inclusion of un-

known paragenesis, that has been found in various localities worldwide. In some specimens magnetite has been clearly identified as a secondary mineral, where, for example, it was found in an exposed cavity in a diamond from Blufontein, South Africa, (Spencer, 1924-12). Furthermore, magnetite inclusions in diamonds from the Sloan Kimberlite, Colorado (Meyer & McCallum, 1986) were reported to exhibit a composition analogous to late stage spinels in kimberlite, as reported, suggesting a secondary origin. Magnetite inclusions can also show evidence of interaction with the external environment through cracks in host (Bulanova et al., 1996) or appear as a rim of epigenetic oxidation around native iron (Sobolev et al., 1981), as seen in diamonds from Yakutia, Russia. In some of the reported findings, the identification of iron oxides as epigenetic minerals is not so clear. Magnetite inclusions from the Sloan diatremes of the Colorado-Wyoming state line Kimberlite district, for example, were compositionally homogeneous, but did not show the primary morphological characteristics normally attributed to syngeneses and were mostly associated with fractures to the diamond surface (Otter, 1989). Sometimes, it was even impossible to identify a paragenesis; this is the case for two inclusions of magnetite in diamonds from the Dokolwayo kimberlite, Swaziland, since an inclusion was found to be pure, while the other one contained TiO_2 , MgO and two inclusions of titanite (Daniels & Gurney, 1999). A similarly uncertain case is found in diamonds from the Monastery mine, South Africa, where some magnetite inclusions were clearly identified as syngenetic, but for most of the oxide samples it was difficult to assess the nature of their setting within the diamond (Moore, 1986). These magnetite inclusions identified as syngenetic were mostly associated with primary sulphides and very chemically pure, in agreement with previous studies where magnetite was classified as syngenetic (Harris, 1968a; Prinz et al., 1975). The recovery of iron oxides associated with primary inclusions, such as sulphides and silicates, suggest that they might be primary minerals rather than secondary phases. In the case of sulphides, the occurrence of coronae of nanocrystalline magnetite around a pyrrhotite inclusion, recently discovered in a diamond from Orapa, Botswana, suggest that the oxidation of pyrrhotite to magnetite might act as a trigger of diamond precipitation in the upper mantle (Jacob et al., 2016). Magnetite was also found associated to ferroprecipitate in diamonds from the São Luiz alluvial deposit, Brazil (Hutchison, 1997; Wirth et al., 2014). In the same Brazilian province of Juina magnetite was found as a single inclusion, embedded in the graphite matrix, in association with calcite (Kaminsky et al., 2009), and associated with iron carbides, native iron, graphite (Kaminsky & Wirth, 2011). Syngenetic magnetite has been related to the eclogitic paragenesis in the case of inclusions from Guaniamo, Guyana shield, Venezuela (Sobolev et al., 1998) and Rio Soriso, Juina, Brazil (Sobolev et al., 1998). However, magnetite was also reported as a primary nanoinclusion associated with Fe,Sn oxides in diamonds from the Samotkan' placer, Ukraine. Fe,Sn oxides were found to be also associated to primary inclusions, such as olivine and pyroxene of

the peridotitic association, suggesting that these oxides may be primary, as metal captured by diamond from the melt, that was later oxidized upon increasing fO_2 , or secondary, which grew from fluids (Kvasnytsya & Wirth, 2009). Magnetite was also reported to be associated with enstatite in diamonds with no detectable surface cracks from Arkansas (Pantaleo et al., 1979). Another occurrence of magnetite associated with a silicate was reported in Madwui, Tanzania (Stachel et al., 1998). Two magnetite crystals were extracted from the diamond, which did not display any optically visible external fractures, and had an almost identical in composition with SiO_2 , Cr_2O_3 , MnO , and CuO being the only impurities, as reported in Table 2 in Stachel et al. (1998), and with very low concentrations of TiO_2 , MgO , both below detection limit, and Al_2O_3 . Notably, these compositions are different from the magnetites that are interpreted to be epigenetic (Meyer & McCallum, 1986). In conclusion, it is clear from the review above that the origin of magnetite inclusions in diamonds is still enigmatic and that some of the traditional methodologies applied to identify the time of formation of the inclusions can lead to inconclusive results in the case of iron oxides. In this study a rare set of 14 diamonds from Akwatia, Ghana, where various inclusions of magnetite are found in association with silicate minerals, was investigated by means of single crystal X-ray diffraction, synchrotron-based X-ray tomographic microscopy (SRXTM) and Raman spectroscopy. These techniques were used to identify the minerals included in the diamonds and determine the possible presence of fractures through the host. The new data are used to provide new insights into the genesis and origin of iron oxides inclusions in diamonds.

3.2 MATERIALS AND METHODS

The study was focused on a suite of 14 diamonds from the Judith Milledge collection, originally obtained from Consolidated African Selection Trust (CAST), the major mining company in Ghana from 1924 to 1972 operating in Akwatia, Birim river valley. The diamonds have size ranging from 0.5 to 2 mm, with slightly octahedral or irregular shapes.

The original report classified this suite of sample as “slightly magnetic”. Silicates inclusions in diamond from the Birim field have been previously characterised (Stachel & Harris, 1997). Inclusion-bearing diamonds were classified as peridotitic with olivine as the most abundant phase (81%), together with minor pyrope, chromite, enstatite, chromian augite. According to this study, Akwatian diamonds come from a chemically more enriched and deeper diamond source than commonly observed. Their inclusions are characterised by unusually low Mg/Fe ratios with respect to harzburgite inclusions worldwide. In particular, the chromites show $Fe^{2+}/(Fe^{2+}+Mg)$ higher than usual and low recalculated ferric iron [$Fe^{3+}/(Fe^{3+}+Fe^{2+})\cdot 100$], suggesting a growth environment more reduced than usual. Since there are no known diamondiferous kimberlites in Ghana, the source

of Ghanaian diamonds remains to be identified. The small size of the specimens and the lack of abrasion suggest that such diamonds have not been transported a great distance Appiah et al., 1996. However, there are various theories regarding the source of Ghana's diamonds. It might have been deformed during tectonism and lie beneath the Voltaian Basin northeast of the Birim Basin. Alternatively, it might be a diamondiferous komatiite or a metamorphosed kimberlite. Finally, the source could lie within turbidites of the Tarkwaian sequences (Markwitz et al., 2016, and references therein). In the Birim valley, alluvial deposits lie on the Proterozoic rocks as a consequence of long-term Mesozoic domal tectonic uplift and subsequent erosion and accumulation (Teuw et al., 1991).

Single crystal X-ray diffraction analysis were performed using a Rigaku Oxford Diffraction XtaLAB SuperNova diffractometer installed at the *Fiorenzo Mazzi* Experimental Mineralogy Laboratory at the Department of Earth and Environmental Sciences, University of Pavia. The instrument is equipped with a 4-axis Kappa goniometer, Mo micro-source X-ray tube, a Dectris Pilatus3 R 200 K-A detector and a video microscope. Sample were mounted on a pin and inclusions were centred optically, using the video microscope. The diffraction patterns were acquired in transmission mode, varying only the phi angle, usually 40° – 50° in steps of 0.5° . The software CrysAlis Pro ("CrysAlisPro Software system", 2018) was used to perform both the measurement and the data reduction. For polycrystalline phases the data reduction requires various steps. First, the frames containing diffraction rings were identified. On each of these frames the single crystals reflections from the host diamond or other included phases were masked, and the image integrated to obtain a diffraction pattern. The resulting patterns were merged and were used for phase identification in the software HighScore (Degen et al., 2014). Diffraction data from one sample (#11) were also collected at the Material Science Beamline at the Swiss Light Source, Paul Scherrer Institute. Information regarding the beamline setup and analytical conditions can be found in Willmott et al. (2013).

Raman spectroscopy was also employed to assess the X-ray diffraction results and in particular to identify mineral phases contained in the smaller inclusions, that could not be measured by X-ray diffraction. The spectra were collected on a Horiba LabRAM HR Evolution spectrometer equipped on Symphony CCD detector cooled with liquid nitrogen also installed at the *Fiorenzo Mazzi* Experimental Mineralogy Laboratory, using an objective with magnification of 100x. Raman spectra were excited by the 532 nm line of a Nd-Yag laser. The spectrometer was calibrated to the silicon Raman peak at 520.5 cm^{-1} . The laser power on the sample surface was kept below 20 mW, to avoid laser-induced oxidation of the sample during the experiment.

The diamonds were investigated by synchrotron-based X-ray tomographic microscopy (SRXTM) at the TOMCAT beamline at the Swiss Light Source (SLS) (Stampanoni et al., 2006) to locate the inclusions in the diamonds and to assess the presence of possible fractures in the surrounding of the inclusions. Measurements were performed at 20 keV with two different magnifications: 10x to characterize the whole sample and 40x to have a close-up on the inclusions. A total of 2001 X-ray radiographs were acquired for each sample. The Gridrec algorithm (Marone & Stampanoni, 2012) was used for the reconstruction, with a pixel size of $0.65 \mu\text{m}$ and $0.1625 \mu\text{m}$ for the 10x and 40x magnifications respectively. Reconstructed 3D images have been post-processed using Thermo Scientific™ Avizo™ software.

3.3 RESULTS

Four diamonds from the same collection (CAST2-1, -6, -7, -12) were analyzed by Piazzzi et al. (2019). In this contribution, the authors applied a multi-analytical procedure to characterize the samples, including the magnetic properties of iron oxides inclusions. Five diamonds (CAST2-2, -3, -5, -14, -15) contained inclusions consisting of a mixture of polycrystalline magnetite and hematite (Fe_2O_3); in some cases it was not possible to distinguish between magnetite and magnesioferrite ($\text{MgFe}_2^{3+}\text{O}_4$), since they have the same space group ($Fd\bar{3}m$ No. 227), similar lattice parameters and chemical composition. It has been shown that magnetic properties can guide the identification (Piazzzi et al., 2019). In fact, the volume of the inclusion calculated from the tomographic scan can be used to predict the saturation magnetization associated to that volume of magnetite or magnesioferrite, through the relationship $M_{sat} = m_{sat}/V_{mag}$, where M_{sat} is the saturation magnetization, m_{sat} is the experimentally determined magnetic moment and V_{mag} is the volume of the magnetic inclusion obtained from the segmentation of the tomographic data. Then, the calculated value can be compared with reported values of M_{sat} to identify the composition of the inclusion. However, this method can only be applied when there is only one magnetic inclusion in the host and with accurate estimations of both the volume and the . A careful inspection of the SRXTM images of these samples clearly show that inclusions containing hematite are all connected to the surface by fractures. Sample CAST2-11 is of particular interest since it contains only one inclusion that was found to comprise a mixture of magnetite and hematite. Strikingly, this diamond does not show any fractures and the inclusion is completely trapped within the host. The experimental results are summarized in Table 3.1.

3.4 DISCUSSION

Iron oxide inclusions rarely occur as single crystals of well-defined morphology, but mostly as porous aggregates, lamellae or rims. As such, it is difficult if not

Table 3.1. Minerals identified in the inclusions in diamonds from Akwatia, Ghana, and occurrence of fractures. The first number of the samples' name refers to the host diamond, the second number to the inclusion. .

Inclusion	Mineral	Fractures to the surface
CAST2-1-1	magnetite	No
CAST2-2-1	magnetite+hematite	Yes
CAST2-2-3	Olivine	No
CAST2-3-2	Olivine, magnetite/Mgferrite+hematite	Yes
CAST2-4-2	Olivine	No
CAST2-4-3	Olivine	No
CAST2-4-5	Olivine	No
CAST2-4-6	Olivine	No
CAST2-5-1	Magnetite+hematite	Yes
CAST2-5-2	Olivine, magnetite+hematite	Yes
CAST2-5-3	Olivine	No
CAST2-5-4	Olivine	No
CAST2-5-5	Olivine	No
CAST2-5-6	Olivine	No
CAST2-6-1	magnetite/Mgferrite	Yes
CAST2-7-1	magnetite	Yes
CAST2-9-1	magnetite/Mgferrite	No
CAST2-11-1	magnetite, quartz	No
CAST2-12-1	magnetite/Mgferrite	Yes
CAST2-13-1	Olivine	No
CAST2-13-3	Olivine	No
CAST2-14-1	magnetite/Mgferrite+hematite	Yes
CAST2-14-2	Olivine	No
CAST2-14-3	Olivine	No
CAST2-15-1	Magnetite+hematite	Yes
CAST2-16-1	magnetite	Yes
CAST2-16-2	Olivine	No

Table 3.2. Unit cell parameters of selected olivine inclusions.

Sample name	<i>a</i> (Å)	<i>b</i> (Å)	<i>c</i> (Å)	<i>V</i> (Å) ³
CAST2-2-3	4.812(6)	10.351(15)	5.99(5)	298(2)
CAST2-3-2	4.796(6)	10.401(12)	6.056(6)	302.1(6)
CAST2-4-2	4.816(5)	10.344(10)	6.079(6)	302.8(5)
CAST2-4-3	4.8086(8)	10.320(2)	6.0497(11)	300.21(9)
CAST2-5-2	4.810(2)	10.327(5)	6.043(2)	300.1(2)
<i>F</i> ₀₈₀ (Nestola et al., 2011)	4.7711(2)	10.2623(7)	6.0080(3)	294.17(3)
<i>F</i> ₀₉₂ (Nestola et al., 2011)	4.7630(2)	10.2276(6)	5.9925(2)	291.92(2)

impossible to apply any of the typical approaches used to identify syngenetic inclusions, such as the imposition of the diamond morphology on the inclusions (Harris, 1968a) and the evaluation of epitaxy and reciprocal host-inclusion orientation (Nestola et al., 2014; Nimis et al., 2019). Alternatively, indications on the time of formation of the inclusions may be inferred by the presence of fractures. Since magnetite inclusions were suggested to precipitate from fluids entering along cracks into diamond (e.g. Bulanova et al., 1996), the absence of cracks connecting the inclusion to the surface of the diamond can be considered a diagnostic criterion of syngenesity. Thus, the identification of fractures can be used as indicator of the origin of these inclusions and shed light on their environment of formation. The investigated inclusions containing hematite are all connected to the surface, suggesting that hematite is most probably an epigenetic product. This is not surprising considering the high oxidation state of Fe in this mineral that suggest relatively oxidizing conditions (Lagoeiro, 1998). An example is reported in Fig 3.1, showing a fracture clearly connecting the inclusion to the surface, together with its diffraction pattern indicating the presence of hematite.

Sample 11 contains only one inclusion, that in the SRXTM images appears as a complex aggregate (Fig. 3.2). Interestingly, this inclusion does not show any fractures, excluding secondary alterations and epigenesis. X-ray diffraction data show that the inclusion comprises quartz and magnetite, and quartz occurs both as single crystals and as powder. This occurrence is similar to the previously described magnetite inclusions from Madwui, Tanzania (Stachel et al., 1998) that showed a distribution of silica resulting from the exsolution from a magnetite that was originally homogeneous and high in SiO₂. The experimental results by Woodland and Angel (2000) could provide an explanation for the occurrence of such sample, since they showed that significant solid solution of Fe₂SiO₄ in magnetite can indeed occur at moderate pressures and temperatures. In light of this data, the silica lamellae could have been originated through exsolution of Fe₂SiO₄ in magnetite due to decompression. Furthermore, the unit-cell param-

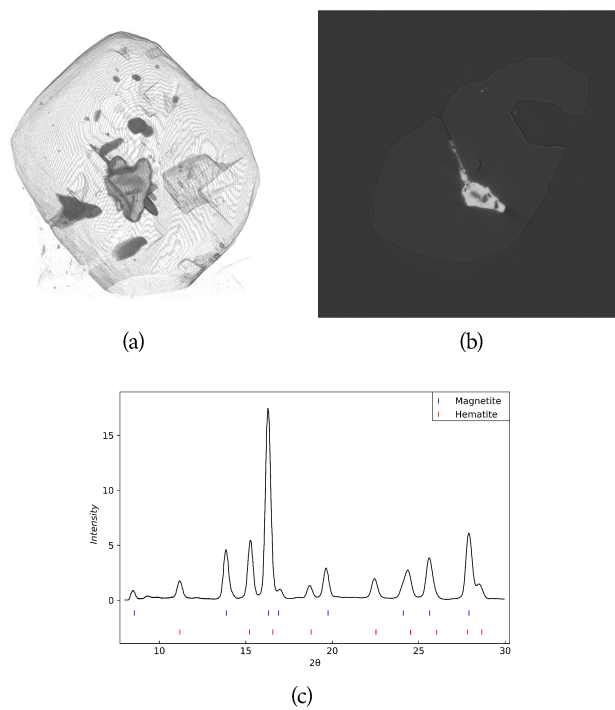
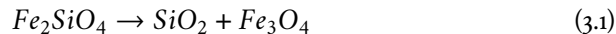


Figure 3.1. (a) 3D reconstructions of SRXTM images for CAST2-15; (b) SRXTM image of CAST2-15 showing a crack connecting the inclusion to the surface; (c) X-ray diffraction pattern from CAST2-15-1 highlighting the presence of magnetite and hematite.

eters of olivines in inclusion CAST2-2-3, -3-2, -4-2, -4-2, 5-2 are larger than the parameters of Fo₉₂, a common composition of olivine inclusions in diamonds (Table 5.5). These larger cell parameters might be due to a higher iron content. An higher amount of fayalite could justify the presence of quartz and magnetite as the results of the reaction:



However, such claim should be strengthened by microprobe measurements to assess the actual composition and further occurrences of similar inclusions. It is worth noting diamonds and inclusions such the ones described in this chapter have been long overlooked. A careful characterization of rare inclusions in diamonds is still partially missing and might give new and unexpected insights on the Earth's mantle.

REFERENCES

- Appiah, H., Norman, D. I., & Kuma, J. S. (1996). The diamond deposits of ghana. *Africa Geoscience Review*, 3, 261–272.
- Bulanova, G. P., Griffin, W. L., Ryan, C. G., Shestakova, O. Y., & Barnes, S.-J. (1996). Trace elements in sulfide inclusions from yakutian diamonds. *Contributions to Mineralogy and Petrology*, 124(2), 111–125. <https://doi.org/10.1007/s004100050179>
- CrysAlisPro software system* (Version 1.171.40.19). (2018). Wroclaw, Poland, Rigaku Oxford Diffraction.
- Daniels, L., & Gurney, J. (1999). Diamond inclusions from the dokolwayo kimberlite, swaziland. *Proceedings of theVIIth International Conference*, 1, 134–139.
- Degen, T., Sadki, M., Bron, E., König, U., & Nénert, G. (2014). The highscore suite. *Powder Diffraction*, 29(S2), S13–S18.
- Harris, J. (1968a). Recognition of diamond inclusions. 1. Syngenetic mineral inclusions. *Industrial Diamond Review*, 28(334), 402.
- Harris, J. (1968b). Recognition of diamond inclusions. 2. Epigenetic mineral inclusions. *Industrial Diamond Review*, 28(335), 458.
- Hutchison, M. T. (1997). *Constitution of the deep transition zone and lower mantle shown by diamonds and their inclusions* (Doctoral dissertation). University of Edinburgh.
- Jacob, D. E., Piazzolo, S., Schreiber, A., & Trimby, P. (2016). Redox-freezing and nucleation of diamond via magnetite formation in the earth's mantle. *Nature Communications*, 7(1). <https://doi.org/10.1038/ncomms11891>

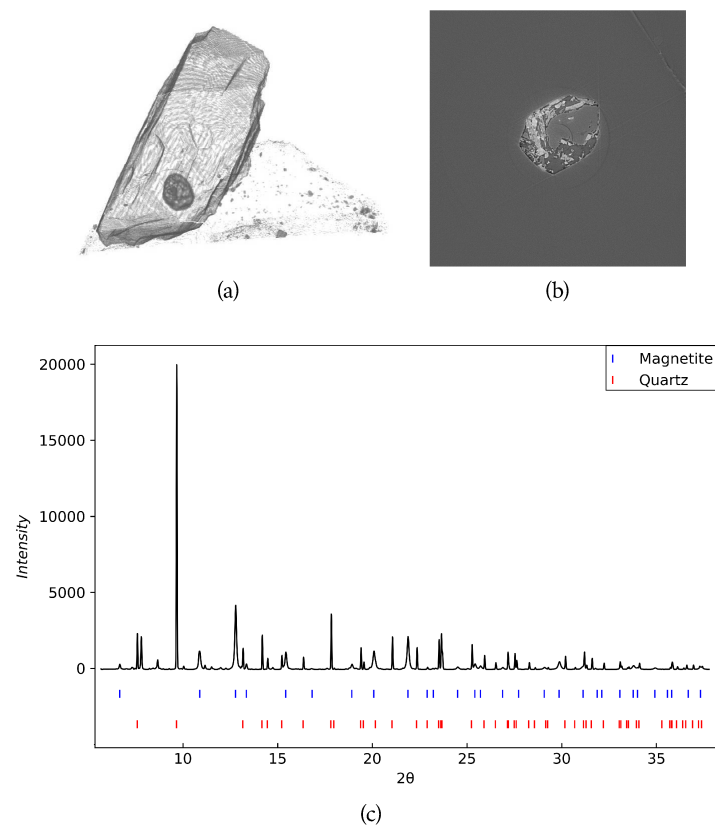


Figure 3.2. (a) 3D reconstructions of SRXTM images for CAST₂₋₁₁; (b) SRXTM image of the inclusion CAST₂₋₁₁₋₁; (c) X-ray diffraction pattern from CAST₂₋₁₁₋₁ highlighting the presence of magnetite and quartz.

- Jean, M. M., Taylor, L. A., Howarth, G. H., Peslier, A. H., Fedele, L., Bodnar, R. J., Guan, Y., Doucet, L. S., Ionov, D. A., Logvinova, A. M., Golovin, A. V., & Sobolev, N. V. (2016). Olivine inclusions in siberian diamonds and mantle xenoliths: Contrasting water and trace-element contents. *Lithos*, *265*, 31–41. <https://doi.org/10.1016/j.lithos.2016.07.023>
- Kaminsky, F., Wirth, R., Matsyuk, S., Schreiber, A., & Thomas, R. (2009). Nyerereite and nahcolite inclusions in diamond: Evidence for lower-mantle carbonatitic magmas. *Mineralogical Magazine*, *73*(5), 797–816. <https://doi.org/10.1180/minmag.2009.073.5.797>
- Kaminsky, F. V., & Wirth, R. (2011). IRON CARBIDE INCLUSIONS IN LOWER-MANTLE DIAMOND FROM JUINA, BRAZIL. *The Canadian Mineralogist*, *49*(2), 555–572. <https://doi.org/10.3749/canmin.49.2.555>
- Kvasnytsya, V. M., & Wirth, R. (2009). Nanoinclusions in microdiamonds from neogenic sands of the ukraine (samotkan' placer): A TEM study. *Lithos*, *113*(3), 454–464. <https://doi.org/10.1016/j.lithos.2009.05.019>
- Lagoeiro, L. E. (1998). Transformation of magnetite to hematite and its influence on the dissolution of iron oxide minerals. *Journal of Metamorphic Geology*, *16*(3), 415–423. <https://doi.org/10.1111/j.1525-1314.1998.00144.x>
- Markwitz, V., Hein, K. A. A., & Miller, J. (2016). Compilation of west african mineral deposits: Spatial distribution and mineral endowment. *Precambrian Research*, *274*, 61–81. <https://doi.org/10.1016/j.precamres.2015.05.028>
- Marone, F., & Stapanoni, M. (2012). Regridding reconstruction algorithm for real-time tomographic imaging. *Journal of Synchrotron Radiation*, *19*(6), 1029–1037. <https://doi.org/10.1107/S0909049512032864>
- McCammon, C., Hutchison, M., & Harris, J. (1997). Ferric iron content of mineral inclusions in diamonds from são luiz: A view into the lower mantle. *Science*, *278*(5337), 434–436. <https://doi.org/10.1126/science.278.5337.434>
- Meyer, H. O. A., & McCallum, M. E. (1986). Mineral inclusions in diamonds from the sloan kimberlites, colorado. *The Journal of Geology*, *94*(4), 600–612. <https://doi.org/10.1086/629062>
- Moore, R. O. (1986). *A study of the kimberlites, diamonds and associated rocks and minerals from the monastery mine, south africa. volume 1: Text* (Doctoral dissertation). Department of Geochemistry, University of Capetown.
- Navon, O., Hutcheon, I. D., Rossman, G. R., & Wasserburg, G. J. (1988). Mantle-derived fluids in diamond micro-inclusions. *Nature*, *335*(6193), 784–789. <https://doi.org/10.1038/335784a0>
- Nestola, F., Jacob, D. E., Pamato, M. G., Pasqualetto, L., Oliveira, B., Greene, S., Perritt, S., Chinn, I., Milani, S., Kueter, N., Sgreva, N., Nimis, P., Secco, L., & Harris, J. W. (2019). Protogenetic garnet inclusions and the age of diamonds. *Geology*, *47*(5), 431–434. <https://doi.org/10.1130/G45781.1>
- Nestola, F., Korolev, N., Kopylova, M., Rotiroti, N., Pearson, D. G., Pamato, M. G., Alvaro, M., Peruzzo, L., Gurney, J. J., Moore, A. E., & Davidson, J. (2018).

- CaSiO₃ perovskite in diamond indicates the recycling of oceanic crust into the lower mantle. *Nature*, 555(7695), 237–241. <https://doi.org/10.1038/nature25972>
- Nestola, F., Nimis, P., Angel, R., Milani, S., Bruno, M., Prencipe, M., & Harris, J. (2014). Olivine with diamond-imposed morphology included in diamonds. Syngeneses or protogenesis? *International Geology Review*, 56(13), 1658–1667. <https://doi.org/10.1080/00206814.2014.956153>
- Nestola, F., Nimis, P., Ziberna, L., Longo, M., Marzoli, A., Harris, J. W., Manghnani, M. H., & Fedortchouk, Y. (2011). First crystal-structure determination of olivine in diamond: Composition and implications for provenance in the Earth's mantle. *Earth Planet. Sci. Lett.*, 305, 249.
- Nestola, F., Jung, H., & Taylor, L. A. (2017). Mineral inclusions in diamonds may be synchronous but not syngenetic. *Nature Communications*, 8, 14168. <https://doi.org/10.1038/ncomms14168>
- Nimis, P., Angel, R. J., Alvaro, M., Nestola, F., Harris, J. W., Casati, N., & Marone, F. (2019). Crystallographic orientations of magnesiochromite inclusions in diamonds: what do they tell us? *Contributions to Mineralogy and Petrology*, 174(4), 29. <https://doi.org/10.1007/s00410-019-1559-5>
- Novella, D., Bolfan-Casanova, N., Nestola, F., & Harris, J. W. (2015). H₂O in olivine and garnet inclusions still trapped in diamonds from the siberian craton: Implications for the water content of cratonic lithosphere peridotites. *Lithos*, 230, 180–183. <https://doi.org/10.1016/j.lithos.2015.05.013>
- Otter, M. L. (1989). *Diamonds and their mineral inclusions from the sloan diatremes of the colorado-wyoming state line kimberlite district, north america*. (Doctoral dissertation). University of Cape Town.
- Palot, M., Jacobsen, S. D., Townsend, J. P., Nestola, F., Marquardt, K., Miyajima, N., Harris, J. W., Stachel, T., McCammon, C. A., & Pearson, D. G. (2016). Evidence for h₂o-bearing fluids in the lower mantle from diamond inclusion. *Lithos*, 265, 237–243. <https://doi.org/10.1016/j.lithos.2016.06.023>
- Pantaleo, N. S., Newton, M. G., Gogineni, S. V., Melton, C. E., & Giardini, A. A. (1979). Mineral inclusions in four arkansas diamonds; their nature and significance. *American Mineralogist*, 64(9), 1059–1062.
- Pearson, D. G., Brenker, F. E., Nestola, F., McNeill, J., Nasdala, L., Hutchison, M. T., Matveev, S., Mather, K., Silversmit, G., Schmitz, S., Vekemans, B., & Vincze, L. (2014). Hydrous mantle transition zone indicated by ringwoodite included within diamond. *Nature*, 507(7491), 221–224. <https://doi.org/10.1038/nature13080>
- Piazzzi, M., Morana, M., Coisson, M., Marone, F., Campione, M., Bindi, L., Jones, A. P., Ferrara, E., & Alvaro, M. (2019). Multi-analytical characterization of Fe-rich magnetic inclusions in diamonds. *Diamond and Related Materials*, 98, 107489. <https://doi.org/10.1016/j.diamond.2019.107489>

- Prinz, M., Mansoni, D. V., Hlava, P. F., & Keil, K. (1975). 51 - INCLUSIONS IN DIAMONDS: GARNET LHERZOLITE AND ECLOGITE ASSEMBLAGES. In L. H. Ahrens, J. B. Dawson, A. R. Duncan, & A. J. Erlank (Eds.), *Physics and chemistry of the earth* (pp. 797–815). Pergamon. <https://doi.org/10.1016/B978-0-08-018017-5.50055-9>
- Sobolev, N. V., Yefimova, E. S., Channer, D. M. D., Anderson, P. F. N., & Barron, K. M. (1998). Unusual upper mantle beneath guianamo, guyana shield, venezuela: Evidence from diamond inclusions. *Geology*, *26*(11), 971. [https://doi.org/10.1130/0091-7613\(1998\)026<0971:UUMBGG>2.3.CO;2](https://doi.org/10.1130/0091-7613(1998)026<0971:UUMBGG>2.3.CO;2)
- Sobolev, N., Efimova, E., & Pospelova, L. (1981). Native iron in diamonds of yakutia and its paragenesis. *Geologiya i Geofizika (Soviet Geology and Geophysics)*, *22*(12), 25–29.
- Spencer, L. J. (1924-12). An inclusion of magnetite in diamond. *Mineralogical Magazine and Journal of the Mineralogical Society*, *20*(107), 245–247. <https://doi.org/10.1180/minmag.1924.020.107.01>
- Stachel, T., & Harris, J. W. (1997). Syngenetic inclusions in diamond from the birim field (ghana)-a deep peridotitic profile with a history of depletion and re-enrichment. *Contributions to Mineralogy and Petrology*, *127*(4), 336–352.
- Stachel, T., Harris, J. W., & Brey, G. P. (1998). Rare and unusual mineral inclusions in diamonds from mwadui, tanzania. *Contributions to Mineralogy and Petrology*, *132*(1), 34–47. <https://doi.org/10.1007/s004100050403>
- Stampanoni, M., Groso, A., Isenegger, A., Mikuljan, G., Chen, Q., Bertrand, A., Henein, S., Betemps, R., Frommherz, U., Böhler, P., Meister, D., Lange, M., & Abela, R. (2006). Trends in synchrotron-based tomographic imaging: The SLS experience. *Developments in X-Ray Tomography V*, *6318*, 6318oM. <https://doi.org/10.1117/12.679497>
- Taylor, L. A., Logvinova, A. M., Howarth, G. H., Liu, Y., Peslier, A. H., Rossman, G. R., Guan, Y., Chen, Y., & Sobolev, N. V. (2016). Low water contents in diamond mineral inclusions: Proto-genetic origin in a dry cratonic lithosphere. *Earth and Planetary Science Letters*, *433*, 125–132. <https://doi.org/10.1016/j.epsl.2015.10.042>
- Teeuw, R. M., Thomas, M. F., & Thorp, M. B. (1991). Geomorphology applied to exploration for tropical placer deposits. *Alluvial mining* (pp. 458–480). Elsevier Science for Institute of Mining; Metallurgy London.
- Thomassot, E., Cartigny, P., Harris, J., Lorand, J., Rollion-Bard, C., & Chaussidon, M. (2009). Metasomatic diamond growth: A multi-isotope study (^{13}C , ^{15}N , ^{33}S , ^{34}S) of sulphide inclusions and their host diamonds from jwaneng (botswana). *Earth and Planetary Science Letters*, *282*(1), 79–90. <https://doi.org/10.1016/j.epsl.2009.03.001>
- Walter, M. J., Kohn, S. C., Araujo, D., Bulanova, G. P., Smith, C. B., Gaillou, E., Wang, J., Steele, A., & Shirey, S. B. (2011). Deep mantle cycling of oceanic

- crust: Evidence from diamonds and their mineral inclusions. *Science*. <https://doi.org/10.1126/science.1209300>
- Weiss, Y., McNeill, J., Pearson, D. G., Nowell, G. M., & Ottley, C. J. (2015). Highly saline fluids from a subducting slab as the source for fluid-rich diamonds. *Nature*, 524(7565), 339–342. <https://doi.org/10.1038/nature14857>
- Willmott, P. R., Meister, D., Leake, S. J., Lange, M., Bergamaschi, A., Böge, M., Calvi, M., Cancellieri, C., Casati, N., Cervellino, A., Chen, Q., David, C., Flechsig, U., Gozzo, F., Henrich, B., Jäggi-Spielmann, S., Jakob, B., Kalichava, I., Karvinen, P., ... Wulschleger, R. (2013). The materials science beamline upgrade at the swiss light source. *Journal of Synchrotron Radiation*, 20(5), 667–682. <https://doi.org/10.1107/S0909049513018475>
- Wirth, R., Dobrzhinetskaya, L., Harte, B., Schreiber, A., & Green, H. (2014). High-fe (mg, fe) inclusion in diamond apparently from the lowermost mantle. *Earth and Planetary Science Letters*, 404, 365–375. <https://doi.org/10.1016/j.epsl.2014.08.010>
- Woodland, A. B., & Angel, R. J. (2000). Phase relations in the system fayalite-magnetite at high pressures and temperatures. *Contributions to Mineralogy and Petrology*, 139(6), 734–747. <https://doi.org/10.1007/s004100000168>

This chapter was accepted for publication on *Proceedings of the National Academy of Sciences* and published online as:

Nestola F., Goodrich C.A., Morana M., Barbaro A., Jakubek R.S., Christ O., Brenker F.E., Domeneghetti M.C., Dalconi M.C., Alvaro M., Fioretti A.M., Litasov K.D., Fries M.D., Leoni M., Casati N.P. M., Jenniskens P. and Shaddad M.H. (2020). Impact shock origin of diamonds in ureilite meteorites. *Proceedings of the National Academy of Sciences*

ABSTRACT

The origin of diamonds in ureilite meteorites is a timely topic in planetary geology as recent studies have proposed their formation at static pressures >20 GPa in a large planetary body, like diamonds formed deep within Earth's mantle. We investigated fragments of three diamond-bearing ureilites (two from the Almahata Sitta polymict ureilite and one from the NWA 7983 main group ureilite). In NWA 7983 we found an intimate association of large monocrystalline diamonds (up to at least 100 μm), nanodiamonds, nanographite, and nanometric grains of metallic iron, cohenite, troilite, and likely schreibersite. The diamonds show a striking texture pseudomorphing inferred original graphite laths. The silicates in NWA 7983 record a high degree of shock metamorphism. The coexistence of large monocrystalline diamonds and nanodiamonds in a highly shocked ureilite can be explained by catalyzed transformation from graphite during an impact shock event characterized by peak pressures possibly as low as 15 GPa for relatively long duration (on the order of 4 to 5 s). The formation of "large" (as opposed to nano) diamond crystals could have been enhanced by the catalytic effect of metallic Fe-Ni-C liquid coexisting with graphite during this shock event. We found no evidence that formation of micrometer(s)-sized diamonds or associated Fe-S-P phases in ureilites require high static pressures and long growth times, which makes it unlikely that any of the diamonds in ureilites formed in bodies as large as Mars or Mercury.

4.1 INTRODUCTION

The origin of diamonds in ureilite meteorites is a highly controversial topic among planetary geologists with three main hypotheses being debated: 1) formation by

impact shock conversion from graphite (Hezel et al., 2008; Le Guillou et al., 2010; Lipschutz, 1964; Lorenz et al., 2019; Nakamuta & Aoki, 2000; Nakamuta et al., 2016; Ross et al., 2011) formation at low pressure in the solar nebula by chemical vapor deposition (Fukunaga et al., 1987; Matsuda et al., 1991; Matsuda et al., 1995), and 3) formation at high static pressures in a planetary-sized body (Miyahara et al., 2015; Nabiei et al., 2018; Urey, 1956). Ureilites form the second largest group of achondrites. They are ultramafic rocks mainly composed of olivine and pyroxene, with interstitial carbon, metal, and sulfide phases (Berkley et al., 1980; Goodrich, 1992; Goodrich et al., 2015; Goodrich et al., 2004; Mittlefehldt et al., 1998; Vdovykin, 1970). They represent the mantle of a partially differentiated parent body (the ureilite parent body, or UPB) that experienced igneous processing at temperatures up to 1200 to 1300 °C (Mittlefehldt et al., 1998). The UPB was catastrophically disrupted by a major impact before it had completely cooled, with ureilites being derived from daughter bodies that reassembled in the aftermath of the disruption (Downes et al., 2008; Goodrich et al., 2015; Goodrich et al., 2004; Herrin et al., 2010). Carbon abundances are notably high in ureilites, ranging up to 8.5 wt % (Cloutis et al., 2010; Goodrich et al., 2015), with the carbon occurring principally as graphite (Mittlefehldt et al., 1998). In ureilites of very low shock level (based on shock indicators in the silicates), the graphite occurs as millimeter-sized euhedral (blade-shaped or tabular) crystals showing prominent (0001) cleavage, closely associated with Fe, Ni metal, and sulfides (Berkley and Jones, 1982; Treiman and Berkley, 1994). Diamonds have not been reported in the lowest-shock samples (Nakamuta & Aoki, 2000; Wacker, 1986). Most ureilites, however, are shocked to various degrees and in these samples the graphite areas, though still having external blade-shaped morphologies, are internally polycrystalline (Mittlefehldt et al., 1998). Diamonds and lonsdaleite [diamond with stacking faults and twinning defects (Murri et al., 2019)] occur embedded in these areas, constituting a volumetrically minor (thus disproportionately illustrious) component of ureilites. Although the presence of diamonds in these meteorites was reported more than a century ago, the process by which the diamonds formed has been hotly debated and is still controversial. The first hypothesis on the origin of diamond in ureilites dates back to 1956, when Urey (1956) proposed that diamonds may form under static high-pressure conditions in the interior of large meteorite parent bodies. A few years later, in his seminal work on diamonds from the Goalpara and Novo Urei ureilites, Lipschutz (1964) proposed that diamonds in ureilites were formed by shock conversion of graphite, a hypothesis that has been supported by many subsequent studies (Hezel et al., 2008; Le Guillou et al., 2010; Lorenz et al., 2019; Nakamuta & Aoki, 2000; Nakamuta et al., 2016; Ross et al., 2011). A third hypothesis that has been discussed is that diamonds in ureilites formed at low pressure in the solar nebula by chemical vapor deposition (Fukunaga et al., 1987; Matsuda et al., 1991; Matsuda et al., 1995). Recent work on the Almahata Sitta (AHS) polymict ureilite (Miyahara et al., 2015; Nabiei et al., 2018) reported the presence of large

diamonds (with inclusions of chromite and Fe-S-P phases) in a ureilitic clast and suggested that such diamonds could only be formed at static pressures higher than 20 GPa. This would imply either that the UPB was similar in size to Mercury or Mars (Nabiei et al., 2018), or that diamonds in ureilites are exogenous to the UPB (Desch et al., 2019). In order to provide insight into the origin of diamonds in ureilites, we investigated carbon phases in two ureilitic stones from AhS, samples AhS 209b and AhS 72, and also the NWA7983 main group ureilite (Jenniskens et al., 2009), by single-crystal micro X-ray diffraction (XRD) both in-house at the University of Padova (all three samples) and using synchrotron radiation at Paul Scherrer Institute, Villigen, Switzerland (AhS samples only). In addition, micro-Raman spectroscopy was performed on several carbon areas in NWA 7983 at ARES (Astromaterials Research and Exploration Science), Johnson Space Center, NASA, Houston, TX. Our results cast reasonable doubt on purported evidence for formation of ureilitic diamonds under high static pressures and provide strong evidence for their formation by impact shock at pressure peaks possibly as low as 15 GPa.

4.2 RESULTS

4.2.1 Samples

AhS 209b and 72 are two stones from the AhS meteorite, which fell in the Nubian desert in 2008 (Goodrich et al., 2015; Herrin et al., 2010; Horstmann & Bischoff, 2014; Jenniskens et al., 2009; Shaddad et al., 2010). They are fine-grained, porous ureilites showing various degrees of “impact smelting” and shock metamorphism as previously described for fine-grained AhS ureilites and a few main group ureilites (Berkley, 1986; Warren & Rubin, 2010). Olivine areas in AhS 209b are completely mosaicized. They consist of aggregates of ~5- to 20- μm -sized equigranular tiles (adopting the terminology of Warren and Rubin, 2010) with tiny amounts of interstitial pyroxene and Si+Al-rich glass, which are inferred to represent recrystallized versions of originally ~0.5- to 1-mm-sized primary grains (e.g. Berkley, 1986; Warren and Rubin, 2010). The olivine largely preserves a typical ureilite olivine core composition of Fo~79, except in reduction rims near inferred original grain boundaries and/or carbon areas. Reduction rim compositions range up to Fo~93. Pigeonitic pyroxene areas in AhS 209b also show complete mosaicism with extensive in situ reduction and porosity. They consist of aggregates of ~5- to 10- μm -sized subhedral to anhedral grains, with varying amounts of interstitial Ca-enriched pyroxenes and Si-Al-enriched glass. Pores and small grains of metal and sulfide among the pyroxene grains are common. The pyroxene tiles show reverse zoning. Cores are reduced (core Mg#s up to ~93) relative to inferred primary compositions (~Mg# 81, such as would have been in equilibrium with Fo~79 olivine in a typical lower-shock ureilite) with varying Wo contents (~2 to 8). Pyroxene

textures such as these were described by Warren and Rubin (2010) in several main group and AhS ureilites and attributed to “impact smelting” (concomitant melting and chemical reduction by carbon) of originally larger primary pigeonite grains. Elongated masses of carbon phases and metal grains are dispersed throughout the sample, commonly occurring along inferred primary silicate grain boundaries (Fig. 9.1A and B).

The fragment of AhS 72 that we examined is dominated by olivine and shows a higher degree of shock metamorphism than 209b. Olivine is completely recrystallized to ~1- to 20- μm -sized equigranular (anhedral to subhedral) grains in a groundmass (of varying proportions relative to the amount of olivine) of pyroxene. The olivine grains are highly reduced (Fo~99) and nearly free of inclusions, suggesting recrystallization from a melt (or at least at very high temperatures) under highly reducing conditions. Interstitial pyroxene compositions range from Wo 0.8 to Wo 34 and are also reduced (Mg# 88 to 99). Pores, masses of carbon phases (~20 to hundreds of micrometers), and grains of metal are abundant throughout the section. The NWA 7983 meteorite was found in 2013 in Morocco. The stone has a total mass of 424.3 g and was classified as a main group ureilite (Ruzicka et al., 2015). The original description noted that the meteorite was extremely resistant to cutting and polishing and suggested that diamond was abundant (Ruzicka et al., 2015), and our work confirms this. We studied four polished sections of NWA 7983. A polished thick section with an area of about 2 cm² was used for scanning electron microscopy (SEM) observations (not carbon-coated) followed by microXRD. Three polished thin sections were used for optical microscopy and additional SEM observations (both carbon-coated and not carbon-coated). NWA 7983 consists mainly of olivine, minor pyroxene, and ~6 vol % masses of carbon phases. Metal, Fe-oxides/hydroxides (presumed terrestrial replacements of metal), troilite, and Cr-rich sulfides occur cross-cutting silicates and as blebs. The olivine shows a high degree of shock metamorphism, with textures similar to those in AhS 72. All olivine areas are either mosaiced with ~2- to 12- μm -sized euhedral tiles and very minor interstitial feldspathic material, or recrystallized to ~1- to 20- μm -sized equigranular (anhedral to subhedral) grains in a groundmass of minor pyroxene. The degree of reduction of the olivine varies greatly. Some areas (inferred original grains) are dominantly Fo 82 to 83, which may be close to the primary composition, while others are strongly reduced with Fo ~90 to 98. The interstitial pyroxenes vary in Wo from ~2 to 33 and Mg# ~84 to 92. Elongated masses of carbon phases, as well as metal \pm sulfide grains (wholly or partly altered to terrestrial Fe-hydroxides), are dispersed throughout the sample. Similar to AhS 72, the degree of re-crystallization of the silicates is so high that the outlines of primary silicate grain boundaries are difficult to discern. The carbon masses typically occur as elongated (blade-shaped), internally layered structures of up to 1 mm in length and 300 μm in width (Fig. 9.1C–E). In one of the sections that we studied, such blades form a nearly continuous vein ~1 cm long. In reflected light,

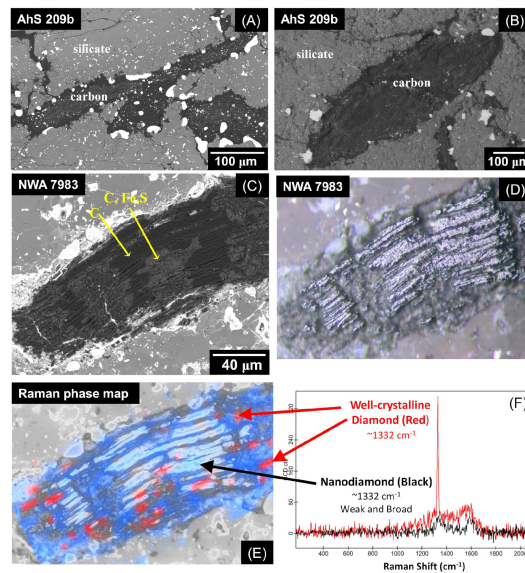


Figure 4.1. Carbon masses in polished sections of AhS 209b and NWA 7983. (A) BEI of AhS 209b, showing elongated masses of carbon phases located along-inferred primary silicate grain boundaries. (B) BEI of non-carbon-coated section of AhS 209b in low-vacuum mode (hence low contrast). (C) BEI of carbon-coated section of NWA 7983 in high-vacuum mode. Carbon masses in this sample tend to have elongated, blade-like morphology and internally show a structure of dark and light stripes parallel to the long edges of the carbon mass. Dark areas show only C, whereas lighter areas show C, Fe, and S peaks in EDS spectra. (D) Reflected light image of same area as in C. Highly reflective, high-relief stripes correlate with dark areas in BEI and are inferred to be diamonds from their optical properties, as well as fluorescence under the electron beam. (E) Raman phase map of area in C and D. The intensity of the red color corresponds to the intensity of the diamond $\sim 1332\text{-cm}^{-1}$ band. The intensity of the blue color corresponds to the intensity of the graphite G band ($\sim 1575\text{ cm}^{-1}$). In nanodiamonds, the $\sim 1332\text{-cm}^{-1}$ band is broad, has low intensity, and is downshifted, making it difficult to detect. Thus, the Raman image is predominantly sensitive to large diamonds (red) while most nanodiamonds likely go undetected (Ferrari et al, 2004, Osswald et al. 2009). In this Raman image, nanodiamonds were detected only in a few areas, although XRD results indicate that they are present throughout the carbon mass. (F) Raman spectra of large diamonds (red) and nanodiamonds (black) from E.

the carbon masses contain elongated, highly reflective, high-relief stripes that are parallel to the external morphology of the carbon mass in the long dimension and are inferred to be diamond, based on their optical properties and fluorescence under an electron beam (Fig. 9.1D). Some of these contain structures that resemble 111 crystal faces of octahedral diamonds. In back-scattered electron images (BEI), the carbon masses also show a striped appearance (parallel to the external morphology of the carbon mass), which is defined by light and dark areas (Fig. 9.1C). The lighter areas contain numerous tiny, bright grains of what appears to be metallic Fe and Fe-sulfides, based on energy-dispersive X-ray spectroscopy (EDS) spectra showing peaks for C, Fe, and S. The darker areas appear to be largely free of inclusions and have EDS spectra showing only C. Based on fluorescence under the electron beam, diamonds are abundant in both the light and the dark areas. In general, the high-reflectance, high-relief areas observed in reflected light correspond closely to the darker areas in BEI (Fig. 9.1C and D). None of the samples studied in this work shows any high-pressure polymorphs of olivine such as wadsleyite and ringwoodite, even in veins or fractures where we specifically searched for them by micro-Raman spectroscopy.

4.2.2 *Micro XRD*

Using reflected light and/or back-scattered electron images of thick sections that were not carbon-coated we located carbon areas for micro XRD in the three samples. We gently removed portions of such carbon areas and analyzed them by micro XRD.

AhS 72 and AhS 209b

The sections of carbon materials removed from the AhS 209b and AhS 72 samples were two irregularly shaped grains of 320 μm and 380 μm , respectively, along their longest dimension. Synchrotron radiation micro XRD showed that these two fragments are both composed mainly of diamonds, graphite and metallic iron (minor troilite was also detected). Fig. A.2A shows the X-ray diffractogram and the diffraction image of the AhS209b fragment. As demonstrated by the diffraction rings (rather than individual diffraction spots), the sample is polycrystalline. A similar observation was made for the AhS 72 sample. Diffraction line profile analysis (Delhez et al., 1982) using the High Score Plus software package (Panalytical) was applied to estimate the crystallite size of the carbon phases. The results show that diamonds in both AhS 209b and AhS 72 are nanometric with crystal size of 17 to 19 nm for AhS 209b and 18 to 25 nm for AhS 72. However, both of the AhS samples show a typical feature of diamond stacking faults (see the shoulder of the 2.06 Å peak of diamond in Fig. A.2A) and in order to take into account any defects in diamond and eventually graphite (which shows a significant peak

asymmetry and broadening) not considered in the previous profile analysis, we performed a further profile analysis by using DIFFaX+ software (Leoni et al., 2004), which provides more reliable results for defect-bearing powder materials. This revealed that the samples are characterized by two diamond domain sizes: smaller domains are on average 3 to 12 nm, whereas the larger ones are larger than 50 nm; for sizes >100 nm, diffraction is no longer reliable for the determination of size and defects in materials. The average graphite crystal size was estimated to be 20 nm. These analyses indicate that in the AhS ureilite fragments studied here diamonds are nanometric with an average size of about 25 nm.

NWA 7983

The BEI observations described above revealed that the carbon masses in NWA 7983 show distinct internal stripes of dark and light areas (Fig. 9.1C and D), correlating with stripes of high reflectance and high relief and low reflectance and low relief (respectively) in reflected light. We removed fragments from both dark and light areas within five different carbon masses and investigated them by micro XRD in-house. The XRD images of dark areas in several of the carbon masses (e.g., Fig. A.2) showed no evidence of diffraction rings but only diffraction spots typical of monocrystals. Based on the sizes of the removed fragments, the monocrystals that we investigated ranged from ~20 to at least 100 μm in size (longest dimensions). The diffraction image for the largest monocrystal that we observed is shown in Fig. A.2B. The unit-cell edge length that we determined for this crystal is $a=3.569 \text{ \AA}$, typical of cubic diamond. The absence of evidence for any other phases in the diffractogram of this crystal (or similar ones that we analyzed) is consistent with the observations from EDS analyses in the SEM that only C was detected in dark areas of the carbon masses in this sample. In other fragments removed from dark areas, the diffractograms showed the simultaneous presence of diffraction spots (indicating single crystal diamonds) and diffraction rings, indicating that in some of the darker areas large diamond monocrystals are intimately intermixed with nanodiamonds on a scale below that detectable in reflected light or BEI imaging. The diffraction results for fragments removed from the lighter carbon areas (as seen in BEI) in NWA 7983 yielded results very similar to those obtained on the AhS ureilite fragments. Fig. A.2C shows that such areas are polycrystalline and mainly composed of diamond, graphite, cohenite (ideally Fe_3C), troilite, and minor metallic iron, consistent with EDS spectra showing the presence of Fe and S in addition to C in such areas. The small shoulder at higher d-spacing (e.g., 2.18 \AA) with respect to the main peak of diamond at 2.06 \AA is characteristic of lonsdaleite as already observed for the AhS 209b and AhS 72 samples. The profile analysis for polycrystalline diamonds in both the light areas and the dark areas indicates that the polycrystalline diamond is nanometric and even smaller than diamonds in the AhS fragments with a size of 9 nm. Although

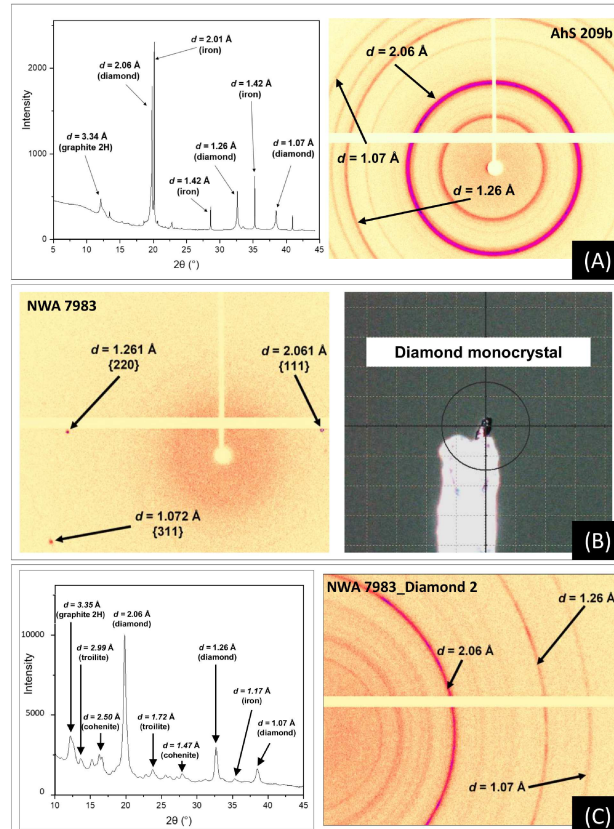


Figure 4.2. (A) The diffractogram (Left) and the diffraction image (Right) of the AhS 209b sample, analyzed by micro X-ray powder diffraction at the Paul Scherrer Institute, Villigen, Switzerland. In the diffractogram the most abundant phases found in the carbon-bearing aggregate, polycrystalline diamond, graphite, and iron metal are shown. (B) Diffraction image (Left) for a fragment of a carbon area in NWA 7983 (from an area that was dark in BEI), showing only diffraction spots typical of a monocrystalline diamond. This monocrystal must be at least $100\ \mu\text{m}$ (the size of the whole fragment removed along its longest dimension). We determined its unit-cell edge length, $a=3.569\ \text{\AA}$, typical of diamond. (C) Diffractogram (Left) and the diffraction image (Right) of another fragment of NWA 7983, this one from an area that was lighter in BEI. This sample was analyzed by the Rigaku-Oxford Diffraction Supernova kappa-geometry goniometer at the Department of Geoscience, University of Padova. In this fragment polycrystalline diamond, graphite, iron, cohenite, and a minor abundance of troilite are detected.

it was not possible to model the diffraction peaks of graphite, based on the peak broadening of its most intense peak it is likely that the graphite is also nanometric. In this study, an intimate association of micro- and nanodiamonds has been reported in natural samples, either terrestrial or extraterrestrial. Unfortunately, it was not possible to distinguish microdiamonds from nanodiamonds in either reflected light or BEI, and so our principal method of locating microdiamonds was a “hit-or-miss” approach of removing fragments from sections and X-raying them. This approach was time-consuming, thus limiting the number of areas that could be studied, and resulted in loss of textural context of the diamonds. In order to get an idea of the distribution, shapes, and relative abundance of microdiamonds in situ, we used micro-Raman imaging on several areas using 488-nm excitation (Fig. 9.1E and F). Raman mapping of these areas easily identifies larger diamond grains [$> \sim 45$ nm (Korepanov et al., 2014)] from the narrow, high intensity band at ~ 1332 cm^{-1} (37), although it does not allow definitive determination of their sizes (Osswald et al., 2009). These Raman maps show clearly that in a number of places the large diamond grains are elongated along the direction of the stripes seen in BEI and reflected light (parallel to external morphology of the carbon mass) and are concentrated along the stripes, that is, forming stripes of their own. We note that nanodiamonds are not easily identified in Raman spectra (Ferrari & Robertson, 2004; Osswald et al., 2009) and so the Raman images (Fig. 9.1E and F) are less useful for showing their distribution. Nevertheless, the XRD analyses showed clearly that nanodiamonds are present in both light and dark areas of the carbon masses.

Transmission Electron Microscopy

The same fragments of AhS209b and AhS 72 investigated by XRD were analyzed by transmission electron microscopy (TEM) with the main goal being to verify the crystallite size compared with the results from synchrotron micro XRD. The presence of diamond stacking faults (lonsdaleite), as predicted by micro XRD showing the typical shoulders at higher d-spacing with respect to the 2.06 Å peak of diamond, was confirmed by TEM. Sections of AhS 72 and AhS 209b suitable for TEM analyses were prepared by focused ion beam and investigated by a Philips200 CM transmission electron microscope. A typical bright-field image of the AhS 72 sample (Fig. 9.3,Left) shows diamond domains with size between about 20 and 150 nm. At the same time, electron diffraction images (Fig. 9.3,Right) indicate that nanodiamonds are associated with graphite (see the ring at about 3.35 Å) and lonsdaleite (see ring at about 2.18 Å), confirming the XRD results. In addition to these main phases, TEM analyses of the AhS 72 sample also revealed the presence of nanometric metallic iron (evident by XRD) and other phases including cohenite Fe_3C , iron sulphide, and Fe-Ni-P compounds. By XRD we determined the iron sulphide to be troilite, but unfortunately due to the

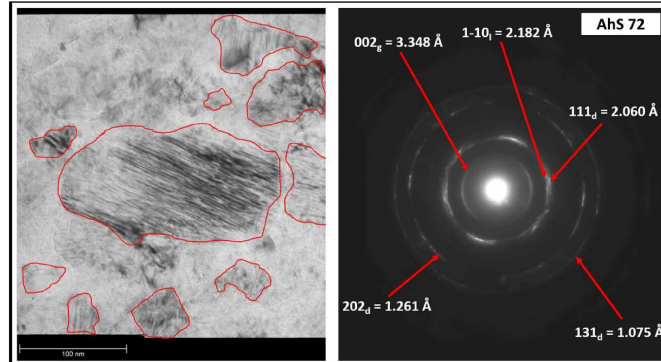


Figure 4.3. (Left) A typical bright-field image of the AhS 72 sample, which shows diamond domains with size ranging from 20 to 150 nm. The corresponding electron diffraction image (Right) indicates that nanodiamonds are associated with graphite (see the ring at about 3.35 Å) and diamond with stacking faults, that is, lonsdaleite (see ring at about 2.18 Å), confirming the XRD results. The diffraction line indicators are represented by the (hkl) planes of diamond (indicated with the subscript “d”) and graphite (indicated with the subscript “g”) and give the spacing in angstroms. These images were obtained with a Philips CM200 transmission electron microscope..

extremely small crystal size between 50 and 100 nm we were unable to determine the identity or stoichiometry of the Fe-Ni-P compounds, which could for example be schreibersite (Fe,Ni)P₃. Due to the nanometric size of the diamonds in this sample, we cannot state definitively whether these other phases are inclusions in diamonds or just coexist with diamonds in the carbon masses.

4.3 DISCUSSION

4.3.1 AhS 72 and AhS 209b

The results from synchrotron diffraction and TEM analyses of the AhS ureilites studied in this work show nanodiamonds associated with nanographite. In addition, they show metallic iron, troilite, cohenite, and nanometric grains of Fe-Ni-P (likely schreibersite) associated with the diamond phases. The diamond-metal-sulfide-carbide-phosphide association in these AhS stones is the same phase assemblage as that reported in AhS stone MS-170 (Nabiei et al., 2018), which argues that the diamond had a common origin in all three stones. However, AhS 72 and AhS 209b are highly shocked ureilites, based on shock features in their silicates (complete mosaicism of olivine). This strongly suggests that the diamonds formed as a result of the same shock event that affected the silicates. The association of metal, sulfide, carbide, and phosphide phases with diamonds in AhS 72 and AhS 209b is especially significant because Nabiei et al. (2018) argued that

these phases were definitive evidence of diamond formation at ≥ 21 GPa static pressure within a parent body with size comparable to Mercury or Mars. Nabiei et al. (2018) base this interpretation on the measured molar $(\text{Fe}+\text{Ni})/(\text{S}+\text{P})$ ratios of the bulk composition of multiphase (metal–sulfide–phosphide) inclusions in diamond, which were close to 3:1. They argue that this implies that the inclusions were trapped as crystals of the phase $(\text{Fe},\text{Ni})_3(\text{S},\text{P})$, which (for $\text{P}/[\text{P}+\text{S}] < 0.2$) is only stable at pressures above 21 GPa. However, this argument is flawed, because at temperatures above 1275 °C (or lower if S is present) the $(\text{Fe},\text{Ni})_3(\text{S},\text{P})$ phase melts (Minin et al., 2019; Stewart & Schmidt, 2007). This temperature is almost certainly much lower than temperatures in a Mars-sized body 4.55 Ga ago at depths equivalent to 21 GPa (Righter & Chabot, 2011). This means either that the interpretation that the inclusions were trapped as $(\text{Fe},\text{Ni})_3(\text{S},\text{P})$ solids is incorrect and their apparent stoichiometry is only a coincidence, or that the proposed formation in a Mars-sized body is incorrect, or both. In fact, the $(\text{Fe},\text{Ni})_3(\text{P},\text{S})$ phase can be formed simultaneously with diamonds by shock compression and quenching, as in shock melt veins in IIE iron meteorite Elga (Litasov et al., 2019). Therefore, the presence of these inclusions does not in any way require a static pressure (large parent body) origin. With respect to AhS 209b and AhS 72, based on the highly shocked nature of the silicates, and the association of nanodiamond, lonsdaleite, and nanographite, we argue that diamonds in these two ureilites most likely formed by a shock event (Decarli, 1995; DeCarli et al., 2002; DeCarli & Jamieson, 1961) with a peak pressure possibly as low as 15 GPa, based on mosaicism of olivine (Stöffler et al., 2018). The presence of the same phase assemblage (diamond–metal–sulfide–carbide–phosphide) in AhS stone MS-170 (13) as in the highly shocked AhS stones studied here strongly suggests that diamond had a common origin in all three samples. However, based on these samples alone, it cannot be ruled out that preexisting, large, defect-poor diamonds [formed, e.g., at high static pressures (Miyahara et al., 2015; Nabiei et al., 2018)] were reduced in grain size and acquired stacking faults during the shock event that affected the silicates, and that in MS-170 some of these preexisting diamonds happened to survive. Nevertheless, additional evidence provided by NWA 7983 (discussed below) leads to the conclusion that this possibility would be extremely unlikely.

4.3.2 NWA 7983

NWA 7983 is a crucial sample for understanding the origin of diamonds in ureilites because its silicates record a high degree of shock (again, complete mosaicism of olivine) and yet it contains large diamonds (i.e., single crystal diamonds up to at least 100 μm in size) in addition to the nanodiamonds that are accepted to be a common product of shock (Decarli, 1995; DeCarli et al., 2002; DeCarli & Jamieson, 1961). This discovery suggests the possibility that the large diamonds in this ureilite were also formed by the shock process, rather than simply having

fortuitously survived it. A first-order argument supporting this interpretation is the predominantly blade-shaped morphology of the carbon masses in which the diamonds are embedded along with graphite. This external morphology of the carbon areas is the same as that of millimeter-sized euhedral laminate (or tabular) graphite crystals that occur in very-low-shock-level ureilites and have been argued to represent the primary form of carbon in all ureilites (Berkley & Jones, 1982; Treiman & Berkley, 1994). If the diamonds in NWA 7983 were only remnants of larger diamonds that had formed at high static pressures during long residence times in a planetary mantle, the external shapes of the carbon areas would not be those of graphite crystals (even if graphite laths had been the precursor material) but would be those of typical diamonds formed deep within the Earth's mantle (Nestola et al., 2018). Instead, their shapes, and the prominent striped texture (Fig. 9.1) of both the nanodiamond aggregates and the larger diamonds within these blade-shaped regions, parallel to the long dimension of the laths which likely represents the trace of (0001) in original graphite (Berkley & Jones, 1982; Treiman & Berkley, 1994), strongly suggests that the diamonds are pseudomorphing original graphite crystals and formed in a rapid process that did not allow time for external graphite morphology to be replaced by diamond morphology. In fact, diamonds pseudomorphing original graphite forms is what is observed for diamonds formed in the Popigai impact crater (Koeberl et al., 1997; Ohfuji et al., 2015) in which aggregates of submicron-sized diamonds show external tabular shapes preserving the crystal habit of precursor graphite flakes (though we note that the primary graphite morphologies inferred for ureilites differ from those at Popigai). As emphasized above, our observations of NWA 7983 represent an astonishing intimate association of micro- and nanodiamonds reported in a natural sample. The nanodiamond aggregates in NWA 7983 are especially abundant and render this ureilite even more resistant to cutting and polishing than most ureilites, similar to industrially produced ultrahard nanodiamonds (Irifune et al., 2003; Isobe et al., 2013). As discussed by Decarli (1995), Decarli et al. (2002), and Decarli and Jamieson (1961), nanodiamonds of this type are the typical product of shock compression of disordered graphite, and nanodiamonds in ureilites and other meteorites are widely interpreted to be the product of impact shock (Garvie et al., 2014; Le Guillou et al., 2010; Lipschutz, 1964; Mostefaoui et al., 2002). However, the formation mechanism of the large diamonds observed in NWA 7983, and the question of whether they formed at the same time as the nanodiamonds, are the critical issues in this investigation, as Miyahara et al. (2015) and Nabiei et al. (2018) argue that such large sizes require long growth times under static high-pressure conditions. Hezel et al. (2008) reported diamonds up to $5\mu\text{m}$ in size (identified by in situ XRD) in a ureilite, and based on their close association with compressed graphite and secondary, polycrystalline graphite argued for formation of the diamonds by shock. The diamonds observed in this work are even larger and may require additional evidence to support formation

in a shock event, the principal objections being the extremely short duration of peak pressure conditions during a shock event (Bundy and Kasper, 1967; DeCarli et al., 2002; Irifune et al., 2003) and the kinetic/energetic limitations associated with direct transformation from graphite (DeCarli et al., 2002). We address both of these issues. First, although the effective duration of a typical laboratory shock experiment is on the order of a microsecond, and so does not allow time for the growth of diamonds beyond very small (less than micrometer) sizes (DeCarli and Jamieson, 1961), large natural impacts have a significantly longer duration of high-pressure conditions (DeCarli et al., 2002). The largest craters on asteroid 4 Vesta, with a diameter of 400 to 500 km, could have formed from a 25- to 30-km impactor, with peak shock pressure during the compression stage lasting for 4 to 5 s (Gillet and Goresy, 2013). During the major impact event of UPB disruption, which is the most likely event in the history of ureilites to explain the majority of their shock features (Goodrich et al., 2004; Herrin et al., 2010; Warren and Rubin, 2010), the duration of the compression stage could have been comparably long, based on the impact parameters of “Selective sampling during catastrophic disruption: Mapping the location of reaccumulated fragments in the original parent body” (2015) for catastrophic disruption of the UPB and equations of Gillet and Goresy (2013). Second, although the direct transformation of graphite to diamond may require higher pressures and/or longer duration of pressure than those of many shock events (DeCarli (1995), DeCarli et al. (2002), and Guillou et al. (2007)) the catalyzed formation of diamonds in metallic (Fe,Ni,Co)-C melts proceeds at notably lower pressures and higher reaction rates and has long been used in industrial production of diamonds (Bezrukov et al., 1975; Bundy et al., 1996; II et al., 2002; Strong and Hanneman, 1967; Trueb, 1968; Varfolomeeva, 1971). Catalysis by metallic melts (referred to as the solvent method or solvent-catalysis in some literature) is likely to have been a significant factor in formation of diamonds in ureilites. The millimeter-sized euhedral graphite crystals in ureilites of very low shock level are intimately associated with Fe,Ni metal. Such metal is a common interstitial component associated with carbon in most ureilites (Goodrich et al., 2013; Mittlefehldt et al., 1998). Goodrich et al. (2013) argued that the metal in ureilites represents Fe-Ni-C melt that was present at $T \geq 1150$ °C and remained after extraction of lower-temperature Fe,S-enriched melt during the igneous stage of ureilite formation. The presence in ureilite silicates of ~5- to 150- μm -diameter metallic spherules, consisting of cohenite (Fe_3C), metal, schreibersite (Fe_3P), and sulfide, constitute direct evidence for the presence of such melts at magmatic temperatures (Goodrich et al., 2013; Goodrich and Berkley, 1986). The impact disruption of the UPB occurred while the silicates were still hot, $\sim 1050 \pm 50$ °C (Herrin et al., 2010; Mittlefehldt et al., 1998). The temperature increase associated with this impact shock event, assuming a 5 km s^{-1} relative velocity, would have been on the order of 200 to 300 °C (Stöffler et al., 2018). Thus, grain boundary metal would have been remelted to create Fe-Ni-C liquids, and it seems inescapable

that they would have had a large effect on the growth rate of diamonds forming during the shock event. The importance of such metallic liquids in catalyzing the formation of diamonds from graphite in ureilites was previously suggested by Nakamuta et al. (2016) though not discussed for diamonds of such large sizes as those observed here. There is, in fact, a vast literature on the formation of diamonds via the catalytic method, because of the industrial importance of diamond. In general, the catalyzed formation of diamonds from graphite occurs in a very thin film of molten metal in contact with graphite (Bovenkerk et al., 1959; Bundy et al., 1996; Strong and Hanneman, 1967), with reported diamond growth rates ranging from 0.2 to 0.4 $\mu\text{m/s}$ at 5.4 GPa and 1127 °C (Strong and Hanneman, 1967) to 30 to 60 $\mu\text{m/s}$ (in the first 20 s) at 4.5 GPa and 1100 to 1200 °C (Bezrukov et al., 1975). The latter rates would easily permit formation of a 100- μm -sized diamond, as observed in NWA 7983, in the ~ 4 to 5 s estimate made above for the duration of peak pressure during the catastrophic disruption of the UPB. This evidence is sufficient to show that formation of large diamonds in ureilites during shock events is plausible and to cast reasonable doubt on the necessity for much longer growth times under static high-pressure conditions (Miyahara et al., 2015; Nabiei et al., 2018). Catalyzed formation of diamonds during a shock event can also account for simultaneous formation of micro- and nano-diamonds in ureilites. For example, using a technique of pulsed heating of a graphite-metal experimental charge in a static high-pressure apparatus at 8 to 14 GPa, which simulates natural impact processes (Bundy and Kasper, 1967; DeCarli et al., 2002) with respect to duration of peak pressures and temperatures, Varfolomeeva, 1971 reported formation of up to 10- μm -sized diamonds near the catalyst and nanodiamonds in other parts of the experimental charge. Catalysis of diamond formation from graphite via metallic melts may also explain other features of the diamonds in NWA 7983. For example, we hypothesize that the striped internal textures of the carbon areas, defined by stripes of concentrated (higher abundance of larger) diamonds and C-dominated (Fe,S-absent) chemistry (darker in BEI) alternating with stripes of dominantly nanodiamonds and C+Fe+S chemistry, could have formed if the metallic melts were injected between (0001) graphite platelets [assuming the long dimensions of the carbon masses to represent the trace of (0001) in original large graphite crystals]. Growth of larger diamonds then proceeded to form the largely Fe-free dark stripes adjacent to the metallic liquids, while the lighter stripes retain concentrations of residual Fe intermixed with nanodiamonds. In addition, Bezrukov et al. (1975) suggested that the growth of diamonds from metallic liquids proceeded through the intermediate step of carbide formation, which could explain the association of cohenite (Fe_3C) with diamonds observed in this work (Fig. A.2C). Another type of inclusion, chromite, reported by Nabiei et al. (2018) in ureilite diamonds, could also support catalytic formation of diamonds during a shock event. Nabiei et al. (2018) noted that the nearly pure (Al-Ti-Mg-free) compositions of the chromite required crystalliza-

tion from metallic melts (references 22 and 23 in Nabiei et al. (2018)). We agree with this interpretation, which is strongly supported by the presence of similarly pure chromite in the metallic metal–cohenite–sulfide–phosphide spherules in ureilite silicates mentioned above (Goodrich et al., 2013; Goodrich & Berkley, 1986). However, in contrast to Nabiei et al. (2018), who argued that the presence of such melts was inconsistent with the low-pressure igneous setting of ureilite formation, we note that the metallic spherules provide direct evidence that such melts were present in the primary ureilite silicate assemblage (Goodrich et al., 2013; Goodrich & Berkley, 1986) and so could have been remobilized to catalyze the formation of diamonds in an impact shock event.

4.3.3 *Additional evaluation of proposed evidence for high static pressure*

The 100- μm -sized single diamond crystal that we observed in NWA 7983 constitutes the first definite report of diamonds of this size in a ureilite. Nabiei et al. (2018) did not determine the sizes of the diamonds they studied in MS-170 (e.g., no microXRD was performed showing diffraction spots) but rather relied on the previous report by Miyahara et al. (2015) of large diamonds in this sample. In fact, the “large” diamonds reported by Miyahara et al. (2015) in MS-170 were not actually large single crystals but rather aggregates of many individual (unconnected) segments having almost the same crystallographic orientation. These aggregates were interpreted (Miyahara et al., 2015; Nabiei et al., 2018) to have originally been large single crystals. However, this is not the only possible interpretation. In fact, an aggregate of similarly oriented small crystals is what is expected for diamonds formed by shock compression of oriented graphite (Erskine and Nellis, 1991; Ohfuji et al., 2015; Ohfuji et al., 2017), as noted also by Nakamuta et al. (2016). Miyahara et al. (2015) stated that they did not observe the predicted crystallographic relationship between diamond and graphite, and used this as an argument against a shock origin. However, if originally large single graphite crystals had been internally recrystallized in a shock event to nanometric, randomly oriented grains (like those observed in the samples studied here), which is likely (Dremin and Breusov, 1993), their current orientations relative to the diamond are irrelevant. Instead, the orientation of the diamonds would have to be compared with the original orientation of the graphite precursors. By contrast, the presence of a truly single-crystal 100- μm -sized diamond in a highly shocked ureilite (NWA 7983) makes it more likely that such diamonds actually formed as a result of the shock process, rather than just having survived it. The shock state of silicates in MS-170 was not investigated by Miyahara et al. (2015) and Nabiei et al. (2018) but was classified as S₃ by Horstmann and Bischoff (2014), which implies shock pressures of 5 to 10 GPa (Stöffler et al., 2018), sufficient to produce diamonds (see Nakamuta et al., 2016). Critically, the external morphologies of the carbon masses in MS-170 are no different from those in NWA 7983 or other ureilites—that is, they

are elongated masses along silicate grain boundaries, suggesting that they were originally large, single crystals of graphite, as discussed above for all ureilites. This can be observed from inspection of figure 1 of Nabiei et al. (2018) and was confirmed by recent studies of our own on MS-170. This makes it extremely unlikely that the diamonds formed during long residence times at high pressures, because if they had then external diamond morphologies would have formed. In other words, there is no evidence that MS-170 is an unusual ureilite preserving diamonds formed in a planetary mantle. Finally, Miyahara et al. (2015) also reported the observation of sector zoning of nitrogen in diamond assemblages in MS-170 and argued that this required “sluggish growth” as in a static high-pressure setting. However, the evidence they present for sector zoning (e.g., figure 5 of Miyahara et al., 2015) is at best ambiguous. Heterogeneous nitrogen distribution is clearly shown, but its relationship to diamond crystal morphology is unclear, given that the diamond consists of several unconnected segments separated by areas of graphite (as discussed above) and no crystal orientation information is given. Furthermore, even if sector zoning of nitrogen is present in large ureilite diamonds, this would not require long, slow growth. For example, diamonds grown by the DeBeers Diamond Research Laboratory using an Fe-Ni metal catalyst for diamond growth developed strong sector zonation of nitrogen in 15 to 20 s, which is hardly “sluggish”. The distribution of nitrogen in large ureilite diamonds, and what it implies for their formation, warrants further investigation, but at this time there is no evidence that it supports a high static pressure.

4.4 CONCLUSIONS

In conclusion the results from combined micro XRD, TEM, SEM/electron micro probe analyzer (EMPA), and micro-Ramanspectroscopy of three highly shocked ureilites suggest that the most likely process by which both microdiamonds and nano-diamonds in ureilites formed is in a shock event characterized by a peak pressure possibly as low as 15 GPa, the shock level recorded by the silicates. Micrometer-sized diamonds can form from crystalline graphite in shock events when catalyzed by metallic Fe-Ni-C liquid, which was demonstrably present during the major shock events that occurred on the UPB, and do not require high static pressures and long growth times. None of the minor Fe-S-P phases associated with the diamonds in ureilites require high static pressures either, nor does sector zonation of nitrogen in diamonds. We find no compelling evidence that diamonds in ureilites formed in large planetary bodies or planetary embryos (Nabiei et al., 2018).

AUTHOR CONTRIBUTIONS

Author contributions: F.N. and C.A.G. designed research; F.N., C.A.G., M.M., A.B., O.C., F.E.B., A.M.F., and N.P.M.C. performed research; R.S.J., F.E.B., and M.D.F. contributed new reagents/analytic tools; F.N., C.A.G., M.M., A.B., O.C., M.C. Domeneghetti, M.C. Dalconi, M.A., A.M.F., M.L., and N.P.M.C. analyzed data; and F.N., C.A.G., M.M., A.B., R.S.J., O.C., F.E.B., M.C. Domeneghetti, M.C. Dalconi, M.A., A.M.F., K.D.L., M.D.F., M.L., N.P.M.C., P.J., and M.H.S. wrote the paper.

ACKNOWLEDGMENTS

We thank Marco van Gemeren for sample preparation and Kent Ross for assistance with SEM/EMPA. We are grateful to James Van Orman, Allan Treiman, and Maurizio Bellotto for helpful discussions. This work was supported by Programma Nazionale di Ricerche in Antartide (PNRA) 2018 grant PNRA18 00247-A to F. N. and NASA grants 80NSSC17K0165, NNX17AH09GSo3, and 80NSSC19K0507 to C.A.G. M.M., A.B., M.C. Domeneghetti, and M.A. were funded by the IMPACT project (R164WEJAHH); M.C. Domeneghetti was funded by the PNRA 2016 to L. Folco. This is Lunar and Planetary Institute (LPI) contribution 2393. LPI is operated by USRA under a cooperative agreement with the Science Mission Directorate of NASA.

REFERENCES

- Berkley, J. L. (1986). Four antarctic ureilites-petrology and observations on ureilite petrogenesis. *Meteoritics*, 21, 169–189.
- Berkley, J. L., & Jones, J. H. (1982). Primary igneous carbon in ureilites: Petrological implications. *Journal of Geophysical Research: Solid Earth*, 87(S01), A353–A364.
- Berkley, J. L., Taylor, G. J., Keil, K., Harlow, G. E., & Prinz, M. (1980). The nature and origin of ureilites. *Geochimica et Cosmochimica Acta*, 44(10), 1579–1597.
- Bezrukov, G., Butuzov, V., Vorzheikin, K., Korolev, D., & Laptev, V. (1975). Kinetic features of diamond crystallization. *Rost kristallov/growth of crystals* (pp. 74–77). Springer.
- Bovenkerk, H., Bundy, F., Hall, H., Strong, H., & Wentorf, R. (1959). Preparation of diamond. *Nature*, 184(4693), 1094–1098.
- Bundy, F., Bassett, W., Weathers, M., Hemley, R., Mao, H., & Goncharov, A. (1996). The pressure-temperature phase and transformation diagram for carbon. *Carbon*, 34(2), 141–153.
- Bundy, F., & Kasper, J. (1967). Hexagonal diamond—a new form of carbon. *The Journal of Chemical Physics*, 46(9), 3437–3446.

- Cloutis, E., Hudon, P., Romanek, C. S., Bishop, J. L., Reddy, V., Gaffey, M. J., & Hardersen, P. S. (2010). Spectral reflectance properties of ureilites. *Meteoritics & Planetary Science*, *45*(10-11), 1668–1694.
- Decarli, P. S. (1995). Shock wave synthesis of diamond and other phases. *MRS Online Proceedings Library Archive*, 383.
- DeCarli, P. S., Bowden, E., Jones, A. P., & Price, G. D. (2002). Laboratory impact experiments versus natural impact events. *Catastrophic events and mass extinctions: impacts and beyond*. Geological Society of America. <https://doi.org/10.1130/o-8137-2356-6.595>
- DeCarli, P. S., & Jamieson, J. C. (1961). Formation of diamond by explosive shock. *Science*, *133*(3467), 1821–1822.
- Delhez, R., De Keijser, T. H., & Mittemeijer, E. (1982). Determination of crystallite size and lattice distortions through x-ray diffraction line profile analysis. *Fresenius' Zeitschrift für analytische Chemie*, *312*(1), 1–16.
- Desch, S., O'Rourke, J., Schaefer, L., Sharp, T., & Schrader, D. (2019). Diamonds in ureilites from mars. *LPI*, (2132), 1646.
- Downes, H., Mittlefehldt, D. W., Kita, N. T., & Valley, J. W. (2008). Evidence from polymict ureilite meteorites for a disrupted and re-accreted single ureilite parent asteroid gardened by several distinct impactors. *Geochimica et Cosmochimica Acta*, *72*(19), 4825–4844.
- Dremin, A., & Breusov, O. (1993). Dynamic synthesis of superhard materials. *Shock waves in materials science* (pp. 17–34). Springer.
- Erskine, D., & Nellis, W. (1991). Shock-induced martensitic phase transformation of oriented graphite to diamond. *Nature*, *349*(6307), 317–319.
- Ferrari, A. C., & Robertson, J. (2004). Raman spectroscopy of amorphous, nanostructured, diamond-like carbon, and nanodiamond. *Philosophical Transactions of the Royal Society of London. Series A: Mathematical, Physical and Engineering Sciences*, *362*(1824), 2477–2512.
- Fukunaga, K., Matsuda, J.-i., Nagao, K., Miyamoto, M., & Ito, K. (1987). Noble-gas enrichment in vapour-growth diamonds and the origin of diamonds in ureilites. *Nature*, *328*(6126), 141–143.
- Garvie, L. A., Németh, P., & Buseck, P. R. (2014). Transformation of graphite to diamond via a topotactic mechanism. *American Mineralogist*, *99*(2-3), 531–538.
- Gillet, P., & Goresy, A. E. (2013). Shock events in the solar system: The message from minerals in terrestrial planets and asteroids. *Annual Review of Earth and Planetary Sciences*, *41*(1), 257–285. <https://doi.org/10.1146/annurev-earth-042711-105538>
- Goodrich, C. A., Ash, R. D., Van Orman, J. A., Domanik, K., & McDonough, W. F. (2013). Metallic phases and siderophile elements in main group ureilites: Implications for ureilite petrogenesis. *Geochimica et Cosmochimica Acta*, *112*, 340–373.

- Goodrich, C. A. (1992). Ureilites: A critical review. *Meteoritics*, 27(4), 327–352.
- Goodrich, C. A., & Berkley, J. L. (1986). Primary magmatic carbon in ureilites: Evidence from cohenite-bearing metallic spherules. *Geochimica et Cosmochimica Acta*, 50(5), 681–691.
- Goodrich, C. A., Hartmann, W. K., O'Brien, D. P., Weidenschilling, S. J., Wilson, L., Michel, P., & Jutzi, M. (2015). Origin and history of ureilitic material in the solar system: The view from asteroid 2008 tc₃ and the almahata sitta meteorite. *Meteoritics & planetary science*, 50(4), 782–809.
- Goodrich, C. A., Scott, E. R., & Fioretti, A. M. (2004). Ureilitic breccias: Clues to the petrologic structure and impact disruption of the ureilite parent asteroid. *Geochemistry*, 64(4), 283–327.
- Guillou, C. L., Brunet, F., Irifune, T., Ohfuji, H., & Rouzaud, J.-N. (2007). Nanodiamond nucleation below 2273 K at 15 GPa from carbons with different structural organizations. *Carbon*, 45(3), 636–648. <https://doi.org/https://doi.org/10.1016/j.carbon.2006.10.005>
- Herrin, J. S., Zolensky, M. E., Ito, M., Le, L., Mittlefehldt, D. W., Jenniskens, P., Ross, A. J., & Shaddad, M. H. (2010). Thermal and fragmentation history of ureilitic asteroids: Insights from the almahata sitta fall. *Meteoritics & Planetary Science*, 45(10–11), 1789–1803.
- Hezel, D. C., Dubrovinsky, L., Nasdala, L., Cauzid, J., Simionovici, A., Gellissen, M., & Schönbeck, T. (2008). In situ micro-Raman and X-ray diffraction study of diamonds and petrology of the new ureilite UAE 001 from the united arab emirates [eprint: <https://onlinelibrary.wiley.com/doi/pdf/10.1111/j.1945-5100.2008.tb01117.x>]. *Meteoritics & Planetary Science*, 43(7), 1127–1136. <https://doi.org/10.1111/j.1945-5100.2008.tb01117.x>
- Horstmann, M., & Bischoff, A. (2014). The almahata sitta polymict breccia and the late accretion of asteroid 2008 tc₃. *Geochemistry*, 74(2), 149–183.
- II, F., AA, C., & JM, D. (2002). Redox conditions of metal-carbon melts and natural diamond genesis. *Geochemical journal*, 36(3), 247–253.
- Irifune, T., Kurio, A., Sakamoto, S., Inoue, T., & Sumiya, H. (2003). Correction: Ultrahard polycrystalline diamond from graphite. *Nature*, 421(6925), 806–806.
- Isobe, F., Ohfuji, H., Sumiya, H., & Irifune, T. (2013). Nanolayered diamond sintered compact obtained by direct conversion from highly oriented graphite under high pressure and high temperature. *Journal of Nanomaterials*, 2013.
- Jenniskens, P., Shaddad, M., Numan, D., Elsir, S., Kudoda, A., Zolensky, M., Le, L., Robinson, G., Friedrich, J., Rumble, D., et al. (2009). The impact and recovery of asteroid 2008 TC 3. *Nature*, 458(7237), 485–488.
- Koeberl, C., Masaitis, V. L., Shafranovsky, G. I., Gilmour, I., Langenhorst, F., & Schrauder, M. (1997). Diamonds from the Popigai impact structure, Russia. *Geology*, 25(11), 967–970.

- Korepanov, V. I., Witek, H., Okajima, H., Ōsawa, E., & Hamaguchi, H.-o. (2014). Communication: Three-dimensional model for phonon confinement in small particles: Quantitative bandshape analysis of size-dependent raman spectra of nanodiamonds.
- Le Guillou, C., Rouzaud, J. N., Remusat, L., Jambon, A., & Bourrot-Denise, M. (2010). Structures, origin and evolution of various carbon phases in the ureilite Northwest Africa 4742 compared with laboratory-shocked graphite. *Geochimica et Cosmochimica Acta*, 74(14), 4167–4185. <https://doi.org/10.1016/j.gca.2010.03.038>
- Leoni, M., Gualtieri, A. F., & Roveri, N. (2004). Simultaneous refinement of structure and microstructure of layered materials. *Journal of applied crystallography*, 37(1), 166–173.
- Lipschutz, M. E. (1964). Origin of diamonds in the ureilites. *Science*, 143(3613), 1431–1434.
- Litasov, K. D., Teplyakova, S. N., Shatskiy, A., & Kuper, K. E. (2019). Fe-Ni-PS melt pockets in Elga IIE iron meteorite: Evidence for the origin at high-pressures up to 20 GPa. *Minerals*, 9(10), 616.
- Lorenz, C. A., Shiryayev, A. A., Vlasov, I. I., & Borisovsky, S. E. (2019). Metamorphism of four desert ureilites and luminescence spectroscopy of defects in ureilitic diamonds [eprint: <https://onlinelibrary.wiley.com/doi/pdf/10.1111/maps.13274>]. *Meteoritics & Planetary Science*, 54(6), 1197–1214. <https://doi.org/10.1111/maps.13274>
- Matsuda, J.-i., Fukunaga, K., & Ito, K. (1991). Noble gas studies in vapor-growth diamonds: Comparison with shock-produced diamonds and the origin of diamonds in ureilites. *Geochimica et Cosmochimica Acta*, 55(7), 2011–2023.
- Matsuda, J.-I., Kusumi, A., Yajima, H., & Syono, Y. (1995). Noble gas studies in diamonds synthesized by shock loading in the laboratory and their implications on the origin of diamonds in ureilites. *Geochimica et Cosmochimica Acta*, 59(23), 4939–4949.
- Minin, D. A., Shatskiy, A. F., Litasov, K. D., & Ohfuji, H. (2019). The Fe-Fe₂P phase diagram at 6 GPa. *High Pressure Research*, 39(1), 50–68.
- Mittlefehldt, D. W., McCoy, T. J., Goodrich, C. A., & Kracher, A. (1998). Non-chondritic meteorites from asteroidal bodies. *Reviews in Mineralogy and Geochemistry*.
- Miyahara, M., Ohtani, E., El Goresy, A., Lin, Y., Feng, L., Zhang, J.-C., Gillet, P., Nagase, T., Muto, J., & Nishijima, M. (2015). Unique large diamonds in a ureilite from Almahata Sitta 2008 TC₃ asteroid. *Geochimica et Cosmochimica Acta*, 163, 14–26.
- Mostefaoui, S., El Goresy, A., Hoppe, P., Gillet, P., & Ott, U. (2002). Mode of occurrence, textural settings and nitrogen-isotopic compositions of in

- situ diamonds and other carbon phases in the Bencubbin meteorite. *Earth and Planetary Science Letters*, 204(1-2), 89–100.
- Murri, M., Smith, R. L., McColl, K., Hart, M., Alvaro, M., Jones, A. P., Németh, P., Salzman, C. G., Corà, F., Domeneghetti, M. C., et al. (2019). Quantifying hexagonal stacking in diamond. *Scientific reports*, 9(1), 1–8.
- Nabiei, F., Badro, J., Dennenwaldt, T., Oveisi, E., Cantoni, M., Hébert, C., El Goresy, A., Barrat, J.-A., & Gillet, P. (2018). A large planetary body inferred from diamond inclusions in a ureilite meteorite. *Nature communications*, 9(1), 1–6.
- Nakamuta, Y., & Aoki, Y. (2000). Mineralogical evidence for the origin of diamond in ureilites [eprint: <https://onlinelibrary.wiley.com/doi/pdf/10.1111/j.1945-5100.2000.tb01430.x>]. *Meteoritics & Planetary Science*, 35(3), 487–493. <https://doi.org/10.1111/j.1945-5100.2000.tb01430.x>
- Nakamuta, Y., Kitajima, F., & Shimada, K. (2016). In situ observation, X-ray diffraction and Raman analyses of carbon minerals in ureilites: Origin and formation mechanisms of diamond in ureilites. *Journal of Mineralogical and Petrological Sciences*, 111(4), 252–269. <https://doi.org/10.2465/jmps.150906>
- Nestola, F., Korolev, N., Kopylova, M., Rotiroti, N., Pearson, D., Pamato, M., Alvaro, M., Peruzzo, L., Gurney, J., Moore, A., et al. (2018). CaSiO₃ perovskite in diamond indicates the recycling of oceanic crust into the lower mantle. *Nature*, 555(7695), 237–241.
- Ohfuji, H., Irifune, T., Litasov, K. D., Yamashita, T., Isobe, F., Afanasiev, V. P., & Pokhilenko, N. P. (2015). Natural occurrence of pure nano-polycrystalline diamond from impact crater. *Scientific reports*, 5, 14702.
- Ohfuji, H., Nakaya, M., Yelisseyev, A. P., Afanasiev, V. P., & Litasov, K. D. (2017). Mineralogical and crystallographic features of polycrystalline yakutite diamond. *Journal of mineralogical and petrological sciences*, 112(1), 46–51.
- Osswald, S., Mochalin, V., Havel, M., Yushin, G., & Gogotsi, Y. (2009). Phonon confinement effects in the raman spectrum of nanodiamond. *Physical Review B*, 80(7), 075419.
- Righter, K., & Chabot, N. L. (2011). Moderately and slightly siderophile element constraints on the depth and extent of melting in early mars. *Meteoritics & Planetary Science*, 46(2), 157–176.
- Ross, A. J., Steele, A., Fries, M. D., Kater, L., Downes, H., Jones, A. P., Smith, C. L., Jenniskens, P. M., Zolensky, M. E., & Shaddad, M. H. (2011). MicroRaman spectroscopy of diamond and graphite in Almahata Sitta and comparison with other ureilites. *Meteoritics & Planetary Science*, 46(3), 364–378.
- Ruzicka, A., Grossman, J., Bouvier, A., Herd, C. D., & Agee, C. B. (2015). The meteoritical bulletin, no. 102. *Meteoritics & Planetary Science*, 50(9), 1662–1662.
- Selective sampling during catastrophic disruption: Mapping the location of reaccumulated fragments in the original parent body [VIII Workshop on

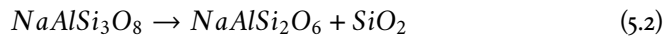
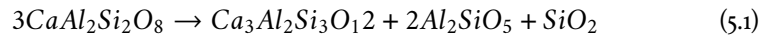
- Catastrophic Disruption in the Solar System]. (2015). *Planetary and Space Science*, 107, 24–28. <https://doi.org/https://doi.org/10.1016/j.pss.2014.08.005>
- Shaddad, M. H., Jenniskens, P., Numan, D., Kudoda, A. M., Elsir, S., Riyad, I. F., Ali, A. E., Alameen, M., Alameen, N. M., Eid, O., et al. (2010). The recovery of asteroid 2008 tc₃. *Meteoritics & Planetary Science*, 45(10-11), 1557–1589.
- Stewart, A., & Schmidt, M. (2007). Sulfur and phosphorus in the earth's core: The fe-p-s system at 23 gpa. *Geophysical research letters*, 34(13).
- Stöffler, D., Hamann, C., & Metzler, K. (2018). Shock metamorphism of planetary silicate rocks and sediments: Proposal for an updated classification system. *Meteoritics & Planetary Science*, 53(1), 5–49.
- Strong, H., & Hanneman, R. (1967). Crystallization of diamond and graphite. *The Journal of Chemical Physics*, 46(9), 3668–3676.
- Treiman, A. H., & Berkley, J. L. (1994). Igneous petrology of the new ureilites nova 001 and nullarbor 010. *Meteoritics*, 29(6), 843–848.
- Trueb, L. F. (1968). An electron-microscope study of shock-synthesized diamond. *Journal of Applied Physics*, 39(10), 4707–4716.
- Urey, H. C. (1956). Diamonds, meteorites, and the origin of the solar system. *The Astrophysical Journal*, 124, 623.
- Varfolomeeva, T. (1971). *Synthesis and investigation of polycrystalline diamond* (Doctoral dissertation). Institute for High Pressure Physics, USSR Academy of Sciences.
- Vdovykin, G. (1970). Ureilites. *Space Science Reviews*, 10(4), 483–510.
- Wacker, J. F. (1986). Noble gases in the diamond-free ureilite, alpha 78019: The roles of shock and nebular processes. *Geochimica et Cosmochimica Acta*, 50(4), 633–642.
- Warren, P. H., & Rubin, A. E. (2010). Pyroxene-selective impact smelting in ureilites. *Geochimica et Cosmochimica Acta*, 74(17), 5109–5133.

Part II Inclusions in metamorphic rocks: novel techniques and application to a case study

5 Crystal structure of quartz inclusions in garnet

5.1 INTRODUCTION

Quartz is by far one of the most common mineral inclusions in different types of rocks such as sandstones, granites, granodiorites, rhyolites and metamorphic rocks. The latter occurrence is often the result of reactions typical of subductions zones, for example (Ghent, 1976; Holland, 1980):



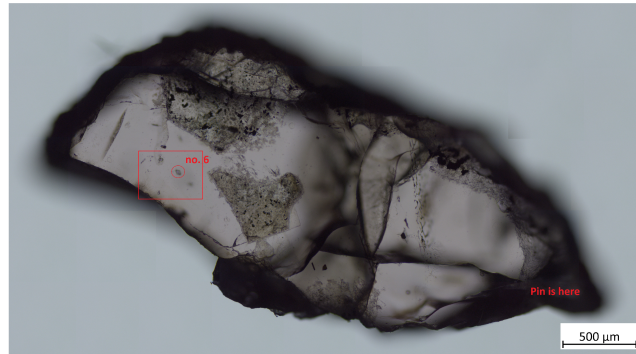
As a consequence, quartz can be trapped as an inclusion in garnets during the prograde metamorphism and the growth of the host crystal. This host-inclusion pair has recently emerged as a promising candidate for elastic geobarometry applications to back-calculate the pressure and temperature conditions at the entrapment of the inclusions mineral (e.g. Alvaro et al., 2020; Gonzalez et al., 2019; Mazzucchelli et al., 2019; Murri et al., 2018). Furthermore, the thermoelastic properties of quartz have been thoroughly characterized by means of different experimental, X-ray and neutron diffraction, Raman and Brillouin spectroscopy, and computational techniques, thus providing basis and reference data for elastic geobarometry. On the other hand, the crystal structure of mineral inclusions has rarely been characterized in situ (Ikuta et al., 2007). This is indeed an interesting case, since the included mineral, being entrapped inside another crystal, is not under hydrostatic stress conditions, as a result of the difference in the elastic properties of the two crystals and their mutual crystallographic orientations. Non-hydrostatic or deviatoric stress affects unit cell parameters (e.g. Bassett, 2006) and bond lengths and angles in crystal structures (e.g. Gatta et al., 2007). Such changes in the structures can modify the physical and thermodynamic properties of crystals, and thus their thermodynamic stability. It is then not surprising that both reconstructive phase transitions (Richter et al., 2016) and displacive-type symmetry-breaking phase transitions (Bismayer et al., 1982) under deviatoric stress have been reported at different temperatures and different mean stress with respect to the transitions points at hydrostatic pressure. Despite its importance,

characterization under non-hydrostatic stress conditions are often hindered by the fact that it is difficult to generate controlled deviatoric stress during experiments. Thus, they are usually performed under hydrostatic conditions. In particular, in the case of quartz the variation of the structure upon increasing hydrostatic pressure is well known. As in the case of thermal expansion, three mechanisms are responsible of the high pressure behavior of quartz (Jorgensen, 1978). First, the rigid rotation of linked tetrahedra is the most significant mechanism, accounting for for 13% of the total 16% in volume decrease for quartz (Glinnemann et al., 1992). It also causes the Si-O-Si bond angles and the O-O distances to decrease. In particular, Hazen et al. (1989) reported that the Si-O-Si angle decrease from 144° at room temperature and pressure to 124.2° at 12.5 GPa. Another compression mechanism is the distortion of tetrahedra, which increases with pressure, due to changes in bond angles while the bond length remains constant. The third mechanism is the shortening of bond lengths, where the larger of the two Si-O distances remains constant, while the shorter one decreases slightly (Glinnemann et al., 1992). Upon further pressure increase at room temperature, α -quartz transforms to an amorphous state, skipping the transitions to the high-pressure polymorphs coesite and stishovite (e.g. Hemley, 1987). Till now information on the effect of deviatoric stress on the structure of quartz were limited to Density Functional Theory (DFT) calculations. DFT shows that non-hydrostatic conditions affect mostly the internal angular deformation of the SiO₄ tetrahedra, while have little influence on the tilts and volume of the tetrahedra (Murri et al., 2019). Considering the ubiquity of quartz in rocks and the large amount of information available on its structure and properties, quartz inclusions in garnet represent an ideal starting point to characterize the structure of minerals under non-hydrostatic conditions and can potentially provide a better understanding of the stress conditions in phenomena occurring at depths, such as subduction and metamorphic events.

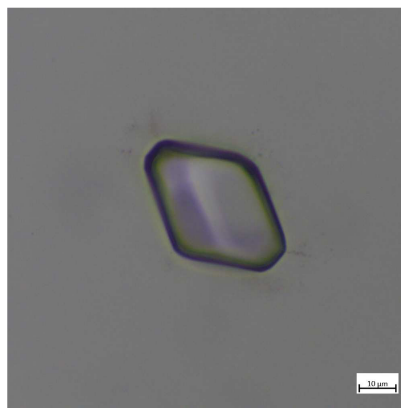
5.2 MATERIALS AND METHODS

5.2.1 Samples

The inclusion described in this thesis is a quartz crystal inside a garnet, TM90-1, from a fragment of an eclogite xenolith from the Mir kimberlite pipe, Yakutiya, Russia (Korsakov et al., 2009). The Mir pipe was identified as a relatively young kimberlite characterized by an eruption temperature of 1000 °C and very fast ascent rates (Korsakov et al., 2009). The garnet host is composed of pyrope (58 wt %), almandine (31 wt%) and grossular (10 wt %) and spessartine (1 wt%) (Korsakov et al., 2009). It contains up to 10 euhedral quartz inclusions. The largest inclusion, inc6, has been characterized by X-ray diffraction, micro-Raman spectroscopy and synchrotron radiation tomographic microscopy Alvaro et al. (2020) and Murri et al. (2018), while three smaller inclusions, inc5, 3 and 7, were measured by



(a)



(b)

Figure 5.1. (a) The sample TM90-1, the position of inc 6 and of the pin are marked in red. (b) Close-up of the quartz inclusion inc6.

micro-Raman spectroscopy and synchrotron radiation tomographic microscopy Alvaro et al. (2020). In particular, Alvaro et al. (2020) used the cell parameters measured from the inclusions to determine their strains relative to a free quartz, and thus to calculate the conditions of entrapment and/or equilibration, which were estimated to be 3 GPa and 850 °C, thus demonstrating that a quartz inclusion in a garnet host can be preserved when the rock enters the stability field of coesite.

Additionally, a quartz single crystal, labeled as QZPD01, was employed as a reference. The sample was obtained from the gem-quality Herkimer crystal described in Angel et al. (1997). The crystal shows a roughly cubic shape with an edge of 60 μm.

Table 5.1. Parameters used for data collection of the quartz free crystal.

I/SigI	25
$2\theta_{\max}$	100
Frame width (deg)	0.5
Exposure time (s) low angle	5
Exposure time (s) high angle	25
Detector distance (mm)	50
Redundancy	6
Voltage (kV)	50
Tube current (mA)	0.8

5.2.2 X-ray diffraction

X-ray diffraction data collection for both the free crystal and the inclusion was performed using a Rigaku XtaLab Supernova diffractometer, equipped with Mo microfocus source and a Dectris Pilatus 200kR detector. The free crystal was glued on a glass fiber and measured in air with the parameters listed in table 5.1.

For the data collection on the inclusion the sample was mounted on a brass pin with wax and the largest inclusion, inc6, was centered optically. Tomography measurements (Alvaro et al., 2020) show that inc6 is closer to one of the side of the garnet host, so this surface was set to face the detector in order to have the inclusion close to the instrument centre. The data collection for the inclusion was performed using the so called fixed phi mode, usually employed for diamond anvil cells (DAC) (Finger & King, 1978). In fact, as the access to the reciprocal space is limited due to the presence of body of the cell in typical high pressure experiment, only X-ray beams traveling in directions close to the perpendicular to the host surface will experience low absorption and thus will be measured. The exposure time was set to 70 s to provide a good diffracted intensity.

Data reduction was performed with the software CrysAlisPro (“CrysAlisPro Software system”, 2018). AVERAGE 2.3 was used to reject anomalous intensities from symmetry-equivalent reflections, while the software RFINE (Finger, 1975) was chosen for the refinements. The structure refinements were performed in space group $P_{32}21$ starting from the coordinates given by Donnay and Le Page (1978) using conventional independent atom model (IAM), and charged – atom scattering factors (Girani, 2019).

Table 5.2. Data quality of QZPD01 refinement.

2θ	R_w	R	Goodness of Fit
40	0.016	0.012	0.83
50	0.020	0.014	0.84
60	0.020	0.015	0.77
70	0.019	0.014	0.66
80	0.019	0.014	0.57
90	0.019	0.014	0.53
100	0.020	0.015	0.50

5.3 RESULTS AND DISCUSSION

5.3.1 Quartz in air

The crystal structure of the free quartz was refined at seven different resolutions from $2\theta_{max} = 100^\circ$ to 40° with steps of 10 to understand how the resolution affects the results of the refinement and guide the interpretation of the results from the quartz inclusion that does not allow data to be collected at high 2θ angles. Table 5.2 list the resulting R, R_w and Goodness of fit (G.o.F.) for the different resolutions. The values of R, R_w and G.o.F. are commonly use to asses the quality of the refinement. They are defined as follows:

$$R = \frac{\sum |Y_{obs} - Y_{calc}|}{\sum |Y_{obs}|} \quad (5.3)$$

$$R_w = \left[\frac{\sum w(Y_{obs}^2 - Y_{calc}^2)}{\sum Y_{obs}^2} \right]^{\frac{1}{2}} \quad (5.4)$$

$$\chi_w^2 = \left[\frac{\sum w(Y_{obs}^2 - Y_{calc}^2)}{(n - p)} \right]^{\frac{1}{2}} \quad (5.5)$$

where Y can be the structure factor F, the squared structure factor F^2 , or the intensity I, w is the weight, which results from the estimates of the precision of the measured quantity Y, (n-p) is the difference between the data and the parameters.

For the quartz in air the refined parameters were: scale factor, atomic coordinates, extinction, displacement parameters, and the twin component, which is below 1 %. The resulting Si-O₂ and Si-O₁ bond lengths show a similar trend with respect to resolution, remaining equal within the esd's down to $2\theta_{max} = 60^\circ$ (Fig.5.2a). At lower resolution, fewer data and correlation among the parameters affect the refinement. This is clear considering also the equivalent isotropic displacement parameters (B_{eq}) calculated from the anisotropic parameters. B_{eq}

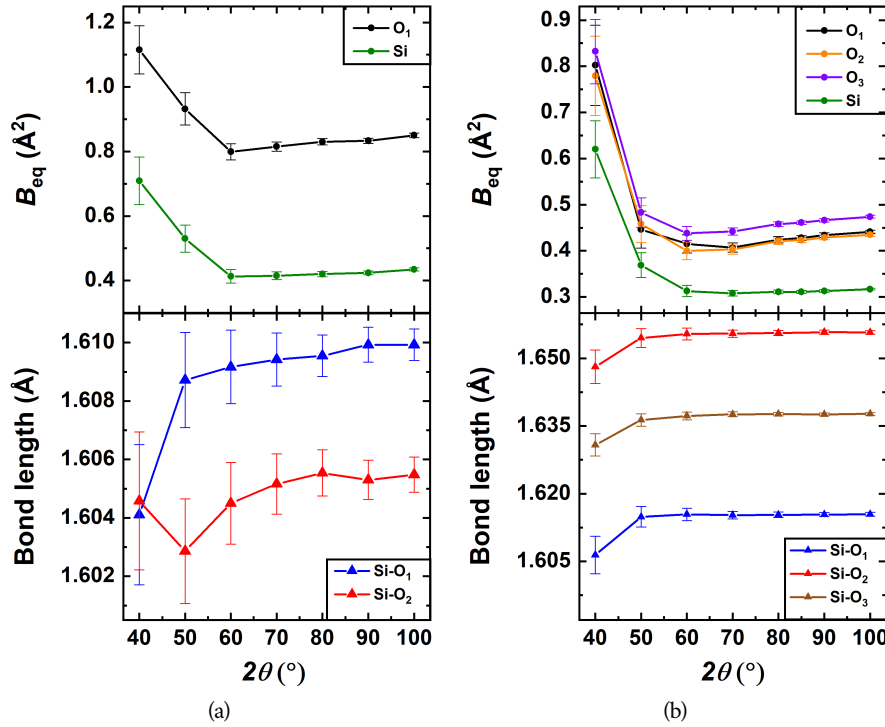


Figure 5.2. (a) Bond distances and B_{eq} vs resolution for quartz (b) Bond distances and B_{eq} vs resolution for olivine.

show the same behavior for silicon and oxygen and the strong variation upon decreasing resolution suggests that the displacement parameters correlate with the atomic coordinates causing the observed change in refined bond lengths of quartz at 40°.

In order to identify a $2\theta_{max}$ limit to reach with a XRD experiment with fixed phi mode, without affecting the precision of the measurements, data from the QZDP01 experiment can be compared with data from “San Carlos” olivine in Angel and Nestola (2016). As in the case of quartz, the data set from olivine was cut and refined at different resolutions. The refinement was performed with the same parameters as the quartz in air, using IAM model, charged-atom scattering factors and without extra electron in the bonds. The comparison of the two refinement clearly show analogies (Fig.5.2 and Table5.3). The bond lengths of quartz and olivine seem to have the same trend, even if the former are more scattered they follow a flat line within esd’s in the $2\theta_{max}$ range from 60° to 100°. The values of B_{eq} also show the same behavior, suggesting that the refinements performed up to $2\theta_{max} = 60^\circ$ for both quartz and olivine give the same values as experiment

Table 5.3. Bond lengths and displacement parameters for quartz and olive vs resolution.

Quartz			Olivine			
Bond lengths						
2θ (°)	Si-O ₁ (Å)	Si-O ₂ (Å)	Si-O ₁ (Å)	Si-O ₂ (Å)	Si-O ₃ (Å)	
40	1.604 (2)	1.605 (2)	1.648 (4)	1.631 (2)	1.606 (4)	
50	1.609 (2)	1.603 (2)	1.655 (2)	1.636 (1)	1.615 (2)	
60	1.609 (1)	1.604 (1)	1.655 (1)	1.6372 (9)	1.615 (1)	
70	1.6094 (9)	1.605 (1)	1.6554 (8)	1.6376 (6)	1.6153 (8)	
80	1.6095 (7)	1.6055 (8)	1.6556 (6)	1.6376 (4)	1.6153 (6)	
90	1.6099 (6)	1.6053 (7)	1.6558 (5)	1.6375 (3)	1.6154 (5)	
100	1.6099 (5)	1.6055 (6)	1.6557 (4)	1.6377 (3)	1.6155 (4)	
B _{eq}						
2θ (°)	Si (Å ²)	O ₁ (Å ²)	Si (Å ²)	O ₁ (Å ²)	O ₂ (Å ²)	O ₃ (Å ²)
40	0.71 (8)	1.11 (7)	0.62(6)	0.80 (9)	0.78 (9)	0.83 (7)
50	0.53 (4)	0.93 (5)	0.37 (3)	0.45 (4)	0.46 (4)	0.48 (3)
60	0.41 (2)	0.80 (2)	0.31 (1)	0.41 (2)	0.40 (2)	0.44 (1)
70	0.41 (1)	0.81 (1)	0.308 (6)	0.41 (1)	0.40 (1)	0.442 (8)
80	0.420 (8)	0.83 (1)	0.311 (4)	0.424 (7)	0.421 (7)	0.458 (5)
90	0.424 (6)	0.833 (8)	0.313 (3)	0.434 (5)	0.0.429 (5)	0.466 (4)
100	0.435 (5)	0.850 (7)	0.317 (2)	0.441 (4)	0.435 (4)	.474 (3)

performed at $2\theta_{max} = 100^\circ$, and are therefore independent of resolution.

5.3.2 Quartz inclusion

Because of the lower quantity and quality of the data, the refinement of the inclusion data was performed with “robust-resistant” weighting scheme, to exclude a few data that did not agree with the F’s calculated from the model, and isotropic displacement parameters, while the twin component and the extinction were not refined. Two different data sets were generated from the integration procedure with two DAC open angles: 40° (Inc6-440°) and 550° (Inc6-50°). To understand the effect of the confinement within the host, the bond distances and angles from the inclusion were compared with the ones from the QZPD01 free crystal refinement restricted to $2\theta=50^\circ$ with anisotropic B, extinction and twin fraction. The bond lengths in the two dataset, are the same within the esd’s, while the angles show a larger variation. This is not surprising, since compression mostly affects the Si-O-Si angle, while the Si-O change only slightly (e.g. Glinnemann et al., 1992). However, in order to exclude that these effects are not artifacts introduced by the

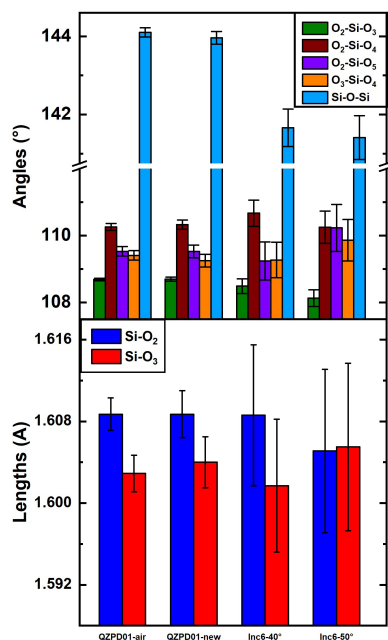


Figure 5.3. Comparison of the results from different refinement. See the main text for the explanation of the labels..

different refinement, the free quartz dataset restricted to $2\theta=50^\circ$ was refined with the same settings as in the inclusion refinement and the cell parameters for the original QZPD01. The new refinement was labeled as and named QZPD01-new. Also in this case the bond lengths are equal within esd's. On the other hand, the Si-O-Si angle is the same within esd's in refinements QZPD01 and QZPD01 with new parameters, but it is significantly smaller in all the inclusion data sets. The O-Si-O angles in the free crystal and in the inclusion show a different trend, since some angles increase and others decrease. This comparison suggest that the differences in bond distances and angles are due to the stress state of the inclusion. The results are summarized in Fig. 5.3 and Table 5.4.

As a further test, the experimental results can be compared with the DFT calculation by Murri et al. (2019). For the same strain conditions calculated from the unit cell parameter (Table 5.5), the Si-O-Si angle, which is the most affected angle by deviatoric stress, varies of 2.2° that is in good agreement with the value of $2.3^\circ(6)$ obtained from the inclusion data. In addition, the O₂-Si-O₃ and O₄-Si-O₅ angles show a variation of 0.25° and 0.20° in computational and experimental data respectively. The O₂-Si-O₅ and O₃-Si-O₄ angles also show the same pattern.

Table 5.4. Refinement results for free quartz and inc6. See the main text for the labels..

	QZPD01-50°	QZPD01-new	Inc6-40°	Inc6-50°
Lengths (Å)				
Si-O ₂	1.609 (2)	1.609 (2)	1.609(7)	1.605(8)
Si-O ₃	1.603 (2)	1.604 (2)	1.602 (6)	1.605 (8)
Angles (°)				
O ₂ -Si-O ₃	108.69(4)	108.70(6)	108.5 (2)	108.1 (2)
O ₂ -Si-O ₄	110.3 (1)	110.3 (1)	110.7 (4)	110.2 (5)
O ₂ -Si-O ₅	109.5 (1)	109.5 (2)	109.2 (6)	110.2 (7)
O ₃ -Si-O ₄	109.4 (1)	109.2 (2)	109.3 (5)	109.9 (6)
O ₃ -Si-O ₅	110.3 (1)	110.3 (1)	110.7 (4)	110.2 (5)
O ₄ -Si-O ₅	108.69 (4)	108.70(5)	108.5 (2)	108.1 (2)
Si-O-Si	144.1 (1)	144.0 (2)	141.7 (5)	141.4 (6)

Table 5.5. Unit cells of the free quartz and the inclusion.

	QZPD01	Inc6-40°
<i>a</i> (Å)	4.9094(1)	4.866(5)
<i>c</i> (Å)	5.4020(2)	5.359(13)
<i>V</i> (Å ³)	112.76(17)	109(1)

5.4 CONCLUSIONS AND FURTHER DEVELOPMENTS

The results reported in this chapter show that X-ray diffraction can be applied to investigate the structure and stress condition of mineral inclusions. However, the use of a laboratory diffractometer restricts the application of this procedure to large inclusions, which are quite rare in natural samples. In fact, a thickness of 1-2 mm of the host is required to preserve inclusion stress states (Campomenosi et al., 2018). Such a thickness together with the large X-ray absorption coefficient that a host mineral, such as garnet, might have, hinder the measurement of small inclusions. Considering that most of the inclusions have dimensions of the order of the micrometer or tens of micrometers, measurements on large inclusions only are not representative of natural systems. These problems might be solved employing a synchrotron source with shorter wavelength and higher intensity that would allow to measure smaller inclusions, despite the thickness and absorption of the samples. Moreover, shorter measurement on a synchrotron beamline would enable to measure a larger number of inclusions, thus providing more insight on the studied host-inclusions systems. For example, evaluating the reciprocal orientations of multiple inclusions with respect to the host can provide information on the growth conditions of the host-inclusion systems (Milani et al., 2016; Nestola et al., 2014). In light of the above, preliminary measurement on quartz standard free crystals and quartz inclusions in the TM90-1 garnet were performed on the high-pressure Indo-Italian beamline Xpress at Elettra, Trieste (Lotti et al., 2020). The measurements were mostly devoted to the development of a procedure for calibrating the detector parameters from the diffraction pattern of a single-crystal standard, the protocols to combine data from multiple collection runs to improve the reproducibility of the refined unit-cell parameters, including the refinement of the offsets of the sample crystal from the center of the goniometer. Taking into account the offset is important in the measurement of inclusions, since they cannot be optically-centered along the beam. Data were also collected from inc6 and two smaller inclusions that could not be measured on laboratory instruments. The development of these new procedures opens the possibility to measure large number of inclusions even if of small dimensions using synchrotron X-ray diffraction.

REFERENCES

- Alvaro, M., Mazzucchelli, M., Angel, R., Murri, M., Campomenosi, N., Scambelluri, M., Nestola, F., Korsakov, A., Tomilenko, A., Marone, F., & Morana, M. (2020). Fossil subduction recorded by quartz from the coesite stability field. *Geology*, 48(1), 24–28. <https://doi.org/10.1130/G46617.1>
- Angel, R. J., Allan, D. R., Miletich, R., & Finger, L. W. (1997). The use of quartz as an internal pressure standard in high-pressure crystallography. *Journal*

- of Applied Crystallography*, 30(4), 461–466. <https://doi.org/10.1107/S0021889897000861>
- Angel, R. J., & Nestola, F. (2016). A century of mineral structures: How well do we know them? *American Mineralogist*, 101(5), 1036–1045. <https://doi.org/10.2138/am-2016-5473>
- Bassett, W. A. (2006). Deviatoric stress: A nuisance or a gold mine? *Journal of Physics: Condensed Matter*, 18(25), S921–S931. <https://doi.org/10.1088/0953-8984/18/25/S01>
- Bismayer, U., Salje, E., & Joffrin, C. (1982). Reinvestigation of the stepwise character of the ferroelastic phase transition in lead phosphate-arsenate, $\text{Pb}_3(\text{PO}_4)_2 \cdot \text{Pb}_3(\text{AsO}_4)_2$. *Journal de Physique*, 43(9), 1379–1388. <https://doi.org/10.1051/jphys:019820043090137900>
- Campomenosi, N., Mazzucchelli, M. L., Mihailova, B., Scambelluri, M., Angel, R. J., Nestola, F., Reali, A., & Alvaro, M. (2018). How geometry and anisotropy affect residual strain in host-inclusion systems: Coupling experimental and numerical approaches [Publisher: De Gruyter Section: American Mineralogist]. *American Mineralogist*, 103(12), 2032–2035. <https://doi.org/10.2138/am-2018-6700CCBY>
- CrysAlisPro software system* (Version 1.171.40.19). (2018). Wroclaw, Poland, Rigaku Oxford Diffraction.
- Donnay, J., & Le Page, Y. (1978). The vicissitudes of the low-quartz crystal setting or the pitfalls of enantiomorphism. *Acta Crystallographica Section A: Crystal Physics, Diffraction, Theoretical and General Crystallography*, 34(4), 584–594.
- Finger, L. W. (1975). *A system of fortran iv computer programs for crystal structure computations* (Vol. 854). US Department of Commerce, National Bureau of Standards.
- Finger, L. W., & King, H. (1978). A revised method of operation of the single-crystal diamond cell and refinement of the structure of NaCl at 32 kbar. *American Mineralogist*, 63, 337–342.
- Gatta, G. D., Kantor, I., Boffa Ballaran, T., Dubrovinsky, L., & McCammon, C. (2007). Effect of non-hydrostatic conditions on the elastic behaviour of magnetite: An in situ single-crystal x-ray diffraction study. *Physics and Chemistry of Minerals*, 34(9), 627–635. <https://doi.org/10.1007/s00269-007-0177-3>
- Ghent, E. D. (1976). Plagioclase-garnet- Al_2SiO_5 -quartz; a potential geobarometer-geothermometer. *American Mineralogist*, 61(7-8), 710–714.
- Girani, A. (2019). *Structure determination of quartz inclusion in a host-inclusion system* (Bachelor). University of Pavia. Pavia, Italy.
- Glinnemann, J., King, H. E., Schulz, H., & Dacol, F. (1992). Crystal structures of the low-temperature quartz-type phases of SiO_2 and GeO_2 at elevated

- pressure. *Zeitschrift für Kristallographie - Crystalline Materials*, 198, 177–212.
- Gonzalez, J. P., Thomas, J. B., Baldwin, S. L., & Alvaro, M. (2019). Quartz-in-garnet and Ti-in-quartz thermobarometry: Methodology and first application to a quartzofeldspathic gneiss from eastern Papua New Guinea. *Journal of Metamorphic Geology*, 37(9), 1193–1208. <https://doi.org/10.1111/jmg.12508>
- Hazen, R. M., Finger, L. W., Hemley, R. J., & Mao, H. K. (1989). High-pressure crystal chemistry and amorphization of α -quartz. *Solid State Communications*, 72(5), 507–511. [https://doi.org/10.1016/0038-1098\(89\)90607-8](https://doi.org/10.1016/0038-1098(89)90607-8)
- Hemley, R. J. (1987). Pressure dependence of Raman spectra of SiO₂ polymorphs: α -quartz, coesite, and stishovite. In M. H. Manghnani & Y. Syono (Eds.), *Geophysical monograph series* (pp. 347–359). American Geophysical Union. <https://doi.org/10.1029/GM039p0347>
- Holland, T. J. (1980). The reaction albite = jadeite + quartz determined experimentally in the range 600–1200 c. *American Mineralogist*, 65(1-2), 129–134.
- Ikuta, D., Kawame, N., Banno, S., Hirajima, T., Ito, K., Rakovan, J. F., Downs, R. T., & Tamada, O. (2007). First in situ x-ray identification of coesite and retrograde quartz on a glass thin section of an ultrahigh-pressure metamorphic rock and their crystal structure details. *American Mineralogist*, 92(1), 57–63. <https://doi.org/10.2138/am.2007.2228>
- Jorgensen, J. D. (1978). Compression mechanisms in α -quartz structures—SiO₂ and GeO₂. *Journal of Applied Physics*, 49(11), 5473–5478. <https://doi.org/10.1063/1.324517>
- Korsakov, A. V., Perraki, M., Zhukov, V. P., Gussem, K. d., Vandenabeele, P., & Tomilenko, A. A. (2009). Is quartz a potential indicator of ultrahigh-pressure metamorphism? laser raman spectroscopy of quartz inclusions in ultrahigh-pressure garnets. *European Journal of Mineralogy*, 21(6), 1313–1323. <https://doi.org/10.1127/0935-1221/2009/0021-2006>
- Lotti, P., Milani, S., Merlini, M., Joseph, B., Alabarse, F., & Lausi, A. (2020). Single-crystal diffraction at the high-pressure Indo-Italian beamline Xpress at Elettra, Trieste. *Journal of Synchrotron Radiation*, 27(1), 222–229. <https://doi.org/10.1107/S1600577519015170>
- Mazzucchelli, M. L., Reali, A., Morganti, S., Angel, R. J., & Alvaro, M. (2019). Elastic geobarometry for anisotropic inclusions in cubic hosts. *Lithos*, 350–351, 105218. <https://doi.org/10.1016/j.lithos.2019.105218>
- Milani, S., Nestola, F., Angel, R., Nimis, P., & Harris, J. (2016). Crystallographic orientations of olivine inclusions in diamonds. *Lithos*, 265, 312–316. <https://doi.org/10.1016/j.lithos.2016.06.010>
- Murri, M., Alvaro, M., Angel, R. J., Prencipe, M., & Mihailova, B. D. (2019). The effects of non-hydrostatic stress on the structure and properties of alpha-quartz. *Physics and Chemistry of Minerals*. <https://doi.org/10.1007/s00269-018-01018-6>

- Murri, M., Mazzucchelli, M. L., Campomenosi, N., Korsakov, A. V., Prencipe, M., Mihailova, B. D., Scambelluri, M., Angel, R. J., & Alvaro, M. (2018). Raman elastic geobarometry for anisotropic mineral inclusions. *American Mineralogist*, *103*(11), 1869–1872. <https://doi.org/10.2138/am-2018-6625CCBY>
- Nestola, F., Nimis, P., Angel, R., Milani, S., Bruno, M., Prencipe, M., & Harris, J. (2014). Olivine with diamond-imposed morphology included in diamonds. Syngenesi or protogenesi? *International Geology Review*, *56*(13), 1658–1667. <https://doi.org/10.1080/00206814.2014.956153>
- Richter, B., Stünitz, H., & Heilbronner, R. (2016). Stresses and pressures at the quartz-to-coesite phase transformation in shear deformation experiments. *Journal of Geophysical Research: Solid Earth*, *121*(11), 8015–8033. <https://doi.org/10.1002/2016JB013084>

6 Quartz metastability at high pressure: what new can we learn from polarized Raman spectroscopy?

This chapter was published as an article in *Physics and Chemistry of Minerals* as:

Morana, M., Mihailova, B., Angel, R. J., and Alvaro, M. (2020). Quartz metastability at high pressure: What new can we learn from polarized Raman spectroscopy? *Physics and Chemistry of Minerals*, 47(8), 34. <https://doi.org/10.1007/s00269-020-01100-y>

ABSTRACT

The pressure dependence of the polarized Raman scattering of quartz was studied under hydrostatic conditions up to 9 GPa. We extended the available pressure calibrations, usually limited to the two most intense peaks, to a larger number of modes, providing polynomial functions that describe the relationship between pressure P and wavenumber shift $\Delta\omega$ for the 128-, 206-, 265-, 464-, 696-, 809-, 1080- and 1161- cm^{-1} modes. For the first time, the pressure behavior of the LO-TO splitting is characterized up to 9 GPa under hydrostatic conditions. The pressure-induced wavenumber changes and derived phonon compressibilities show that longitudinal and transverse modes can be used interchangeably for the calculation of strains through the Grüneisen tensor to derive the strains in crystals, such as mineral inclusions, under non-hydrostatic conditions. A careful examination of the linewidths as a function of pressure shows that they are sensitive to the metastability of the quartz structure with respect to the high-pressure silica polymorphs. It is proposed that strong multiphonon interactions contribute to the stability of the structure of quartz at ambient conditions.

6.1 INTRODUCTION

Quartz has attracted interest from many research fields, such as material science, geology and solid state physics, because of its application as an oscillator and piezoelectric material (Ballato, 2008), its abundance in the Earth's crust and its easily accessible α - β phase transition at high temperature. Recently quartz inclusions have been used in elastic geobarometry (e.g. Enami et al., 2007; Gonzalez et al., 2019; Murri et al., 2018). Elastic geobarometry exploits the difference in

elastic properties of host-inclusion pairs to back-calculate the entrapment pressures for the inclusions, P_{trap} , starting from their residual or remanent pressure, P_{inc} , measured when the host is at room conditions. For this application, Raman spectroscopy is a popular technique, since it is quick and allows small portions of the sample to be probed, thus providing information about the variation of the stress and strain inside the analyzed inclusions. Assuming that the inclusions are under hydrostatic pressure, the residual pressure can be determined from the shift of the Raman modes with respect to a free quartz crystal (e.g. Enami et al., 2007), applying a hydrostatic calibration such as the one provided by Schmidt and Ziemann (2000). The main issue with this approach is the assumption of hydrostaticity. In fact, due to the inherent elastic anisotropy of crystals, the inclusion-host boundary imposes deviatoric stress on any mineral trapped even in a cubic host, and, in particular for non-cubic mineral inclusions, the deviation from hydrostaticity may be considerable. Since the variation in the Raman peak positions of a crystal results from the strain imposed on it (e.g. Angel et al., 2019), an inclusion crystal will have different Raman shifts with respect to a crystal under hydrostatic pressure. Indeed, a recent experimental study by Bonazzi et al. (2019) has demonstrated that the values of P_{inc} and P_{trap} obtained from the hydrostatic calibration are not reliable when the strains imposed on the inclusions are significantly different from those of a crystal under hydrostatic conditions. For quartz inclusions, the strains can be calculated from the measured Raman shifts by using the phonon-mode Grüneisen tensor (Angel et al., 2019; Murri et al., 2019). The strains can then be used to determine the P_{inc} applying the ambient-pressure elastic tensor of quartz, such as the one provided by Wang et al. (2015). Considering this renewed interest in the response of the Raman spectrum of quartz to compression, a thorough and comprehensive characterization is needed. The most recent determination of the pressure dependence of the Raman wavenumbers of quartz by Schmidt and Ziemann (2000) is focused only on two modes (206- and 464- cm^{-1}) and restricted to 2.1 GPa. There is also evidence that quartz inclusions entrapped in garnet can be preserved in the coesite stability field (Alvaro et al., 2020) at pressures in excess of 2.5 GPa. Another aspect that has been neglected so far is the dependence of the polar modes wavenumbers on the orientation of the sample with respect to the direction of the incident and scattered light (Shapiro & Axe, 1972). While a free single crystal can be easily oriented, this is not the case for an inclusion, surrounded by the host. This might be an issue for the application of the method described above, since the Grüneisen parameters were calculated for the transverse optic (TO) E modes and not for the longitudinal optic (LO) E modes, that are measured experimentally in some orientations. The pressure dependence of the splitting of the E modes up to 5 GPa was investigated by Wong et al. (1986) by means of infrared spectroscopy, but using KBr as pressure transmitting medium, thus not providing hydrostatic conditions. The objective of our study was to re-examine the pressure evolu-

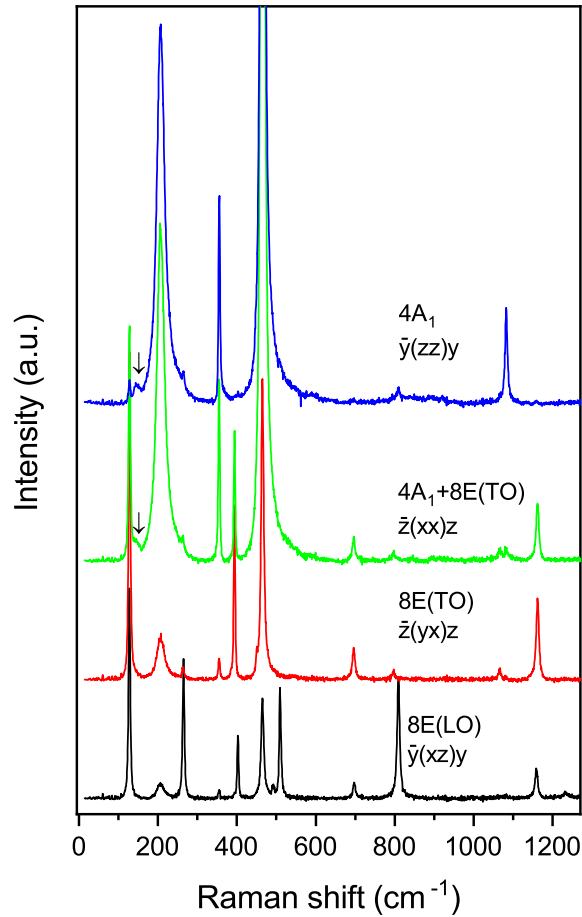


Figure 6.1. Polarized spectra at ambient conditions in the experimental scattering geometries. The arrows indicate a two-phonon band around 147 cm^{-1} .

tion of the quartz Raman active modes by polarized Raman spectroscopy under hydrostatic conditions in a pressure range covering the stability field of three polymorphs of SiO_2 .

6.2 MATERIAL AND METHODS

Oriented (010) and (001)-cuts from a gem-quality quartz were loaded in a Böhler-Almax diamond anvil cell (DAC), with a culet diameter of $600 \mu\text{m}$ and a stainless steel gasket, together with ruby chips to determine the pressure from the photoluminescence R1 line (Munro et al., 1985) with an accuracy of $\sim 0.1 \text{ GPa}$. A 16:4:1 methanol-ethanol-water mixture, which is hydrostatic up to 10.5 GPa (Angel et al.,

2007), was used as a pressure-transmitting medium. Polarized Raman spectra were collected at the Mineralogisch-Petrographisches Institut, Universität Hamburg, with a Horiba Jobin-Yvon T64000 triple-monochromator system equipped with a Symphony LN₂-cooled CCD detector, an Olympus BH41 microscope, and a Coherent Ar⁺ laser. The measurements were performed in backscattering geometry, with a 50x long-working-distance objective and an excitation wavelength of 514.532 nm. The spectrometer was aligned to the Raman peak position of a Si wafer at 520.5 cm⁻¹. The spectral resolution was approximately 2 cm⁻¹, while the instrumental precision in the peak positions was 0.35 cm⁻¹. In-situ pressure-dependent polarized spectra in $\bar{y}(zz)y$ and $\bar{y}(xz)y$ scattering geometry (Porto's notation with $z \parallel [001]$, $y \parallel [010]$, $y \perp x$ and z) were collected from the (010)-cut, whereas the $\bar{z}(xx)z$ and $\bar{z}(yx)z$ spectra were collected from the (001)-cut. In addition, at each pressure step the Raman spectra of the diamond anvils were measured, to estimate the degree of depolarization of Raman scattering due to stress-induced changes in the optical properties of the anvils (Mihailova et al., 2019), together with a background spectrum, which was then subtracted from the sample spectrum to remove the peaks from the pressure-transmitting medium. Data points were collected both on compression and decompression. The spectra were temperature reduced to account for the Bose-Einstein phonon population factor and fitted with pseudo-Voigt peak-shape functions (as no significant peak asymmetry was found) to determine the peak positions, full-widths at half-maximum (FWHM), and integrated intensities.

6.3 RESULTS AND DISCUSSION

Quartz has trigonal symmetry with space group $P3_221$ or $P3_121$ and 9 atoms per unit cell. The resulting $3N = 27$ degrees of freedom are divided into three acoustic vibrations ($A_2 + E$) and 24 optical vibrations of $4A_1 + 4A_2 + 8E$ symmetry. The non-degenerate A_1 modes are Raman active, the A_2 modes are infrared active, and the doubly degenerate E modes are both infrared and Raman active. Since A_2 and E modes are polar, they show transverse optic (TO) and longitudinal optic (LO) components. The group-theory analysis and allowed modes for the scattering geometries employed in this experiment are reported in Table 6.1 and reference spectra at ambient conditions are shown in Figure 6.1. In the geometries $\bar{y}(zz)y$ and $\bar{z}(xx)z$ another spectral feature centred around 147 cm⁻¹ is clearly visible; this is a two-phonon excitation that triggers the α to β quartz phase transition (Scott, 1968). According to Etchepare et al. (1974), Si-O bond stretching modes are localized in the regions 700-800 cm⁻¹ and 1050-1100 cm⁻¹, the bending of O-Si-O angles in the region 350-500 cm⁻¹, and the bending of Si-O-Si bond angles and twisting below 300 cm⁻¹. It is well known (e.g. Asell & Nicol, 1968) that modes that show a strong temperature dependence, such as the 128-, 206- and 464-cm⁻¹ modes, are also the ones that exhibit a strong pressure dependence,

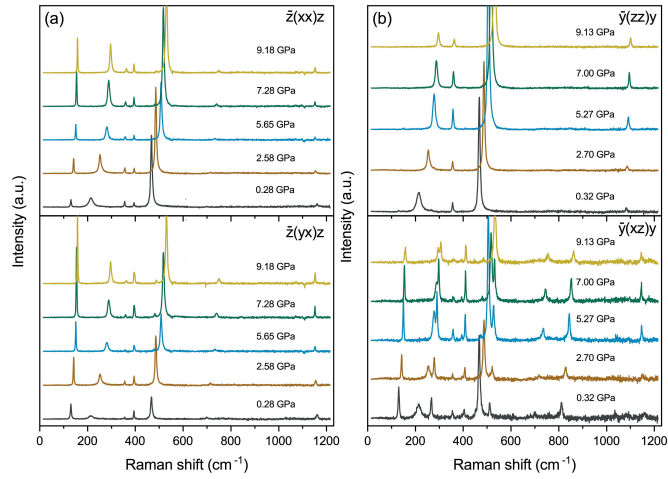


Figure 6.2. Selected spectra at high pressure in the experimental scattering geometries..

while Hemley (1987) reported that several sets of *E*-symmetry modes show a weak pressure dependence. Selected spectra are reported in Figure 6.2 to show the pressure evolution of the Raman-active phonon modes in quartz.

Table 6.1. Mode symmetry, selection rules and reference peak positions at ambient conditions; uncertainties in the wavenumbers are from the spectral fitting. The peak assignment is after Etchepare et al. (1974) as well as based on the atomic vector displacements derived from DFT simulations (Murri et al., 2019). Note that the polar doubly degenerate E modes marked by asterisk interact with Raman-inactive polar A_2 modes and, as a result, the corresponding E(TO) components observed in $\bar{z}(xy)z$ transform into A_2 when the angle between the phonon wavevector and the c axis changes to 90° , while the E(LO) components observed in $\bar{y}(xz)y$ are inherently related to A_2 (Shapiro & Axe, 1972).

Symmetry	Acoustic	Optic	Raman activity	IR activity
A_1	0	4	$\alpha_{xx} = \alpha_{yy}, \alpha_{zz}$	-
A_2	1	4	-	μ_z
E	1	8	$(\alpha_{xx}^x = -\alpha_{yy}^x, \alpha_{yz}^y), (\alpha_{xy}^y, \alpha_{xz}^x)$	μ_x, μ_y

Reference data at ambient conditions				
Scattering geometry	Modes	Wavenumber (cm^{-1})	Dominant type of atomic vibration	
$\bar{y}(zz)y$	A_1	207.62(6)	Rotation of SiO_4 tetrahedra	
		355.69(6)	SiO_4 bending	
		465.015(6)	Ring <i>O_{bridge}</i> -breathing mode	
		1082.3(2)	SiO_4 stretching	
$\bar{z}(xy)z$	$E(TO)$	128.351(7)	Rotation of SiO_4 tetrahedra	
		263.8(2)	O-Si-O & Si-O-Si bending	
		394.08(1)	SiO_4 bending	
		450.3(2)	SiO_4 bending	
		695.9(1)	Si-O stretching & O-Si-O bending, with Si vibrations \parallel to \mathbf{c} axis	
		796.0(6)	Si-O stretching & O-Si-O bending, with Si vibrations \perp to \mathbf{c} axis	
		1065.5(5)	Anti-symmetrical SiO_4 stretching with weak Si vibrations \perp to \mathbf{c} axis	
		1161.46(6)	Symmetrical SiO_4 stretching with weak Si vibrations \parallel to \mathbf{c} axis	
$\bar{y}(xz)y$	$E(LO)$	128.099(8)	See corresponding E(TO) modes	
		265.02(1)		
		402.80(3)		
		509.67(2)*		
		697.3(2)		
		809.18(2)		
		1233.0(5)*		
1158.3(1)				
$\bar{z}(xx)z$	$A_1 + E(TO)$	Same values within uncertainties		

Table 6.2. Pressure dependence of the peak positions and FWHMs of the four A_1 modes. Reported uncertainties are from the spectral fitting..

Pressure (GPa)	ω_{206} (cm ⁻¹)	FWHM ₂₀₆ (cm ⁻¹)	ω_{355} (cm ⁻¹)	FWHM ₃₅₅ (cm ⁻¹)	ω_{464} (cm ⁻¹)	FWHM ₄₆₄ (cm ⁻¹)	ω_{1080} (cm ⁻¹)	FWHM ₁₀₈₀ (cm ⁻¹)
0.16 (8)	209.2 (2)	23.6 (6)	355.5 (2)	5.3 (5)	465.42 (2)	8.74 (6)	1080.9 ^a	- ^a
0.20 (8)	209.3 (1)	23.3 (3)	355.5 (1)	5.5 (2)	465.59 (1)	8.5 (3)	1081.8 (5)	11 (1)
0.32 (8)	214.06 (9)	21.6 (2)	355.7 (1)	5.5 (2)	467.27 (1)	8.39 (3)	1082.8 (4)	6.9 (7)
0.60 (8)	220.94 (9)	20.6 (2)	355.4 (1)	5.8 (3)	469.86 (1)	8.47 (3)	1082.6 (4)	8.8 (9)
1.27 (8)	233.52 (6)	15.4 (2)	355.14 (8)	5.1 (2)	475.230 (8)	8.02 (2)	1083.7 (3)	6.7 (6)
2.70 (8)	254.27 (5)	12.8 (2)	355.68(8)	5.3 (2)	486.648 (8)	7.80 (2)	1085.9 (3)	9.6 (7)
2.50 (8)	252.38 (4)	12.3 (1)	355.65 (7)	5.2 (2)	485.463 (7)	7.87 (2)	1085.8 (3)	9.3 (6)
1.80 (9)	242.16 (6)	13.8 (2)	355.35 (8)	5.4 (2)	479.631 (8)	7.99 (2)	1085.0 (3)	8.1 (7)
2.15 (9)	246.73 (4)	12.4 (1)	355.63 (7)	5.2 (2)	482.150 (7)	7.95 (2)	1085.3 (3)	8.0 (6)
2.39 (9)	250.80 (6)	12.5 (2)	355.73 (9)	5.1 (2)	484.566 (9)	7.68 (2)	1085.6 (4)	11.5 (9)
3.26 (9)	261.14 (7)	13.0 (3)	356.0 (1)	5.8 (3)	491.174 (9)	7.88 (3)	1087.5 (3)	9.6 (8)
3.1 (1)	259.16 (5)	12.5 (1)	356.17 (8)	5.2 (2)	489.954 (7)	7.87 (2)	1086.7 (3)	9.8 (7)
4.0 (1)	268.29 (5)	13.0 (1)	356.47 (7)	5.3 (1)	496.361 (6)	7.53 (2)	1088.7 (2)	9.0 (5)
4.5 (1)	272.13 (5)	12.8 (1)	356.62 (7)	5.1 (2)	499.490 (7)	7.75 (2)	1089.7 (2)	9.4 (4)
5.3 (1)	278.11 (5)	12.4 (1)	357.31 (7)	5.5 (2)	505.067 (7)	7.93 (2)	1091.2 (2)	7.3 (4)
5.9 (1)	282.17 (5)	11.9 (1)	357.901 (6)	5.9 (2)	509.497 (7)	8.49 (2)	1092.7 (2)	6.7 (3)
7.0 (1)	287.82 (4)	10.8 (1)	359.259 (5)	6.0 (2)	516.732 (5)	8.83 (2)	1095.1 (1)	6.0 (2)
7.6 (1)	290.94 (3)	9.92 (9)	360.45 (5)	5.9 (1)	521.087 (4)	8.81 (1)	1097.09 (9)	5.6 (1)
8.1 (1)	293.46 (3)	8.95 (9)	361.47 (4)	6.0 (1)	525.003 (3)	8.63 (1)	1098.3 (8)	5.6 (1)
8.6 (1)	295.52 (3)	7.99 (8)	362.48 (5)	5.7 (1)	528.441 (4)	8.40 (1)	1099.41 (7)	5.7 (1)
9.1 (1)	296.29 (5)	8.8 (2)	362.589 (8)	6.0 (3)	531.342 (6)	8.93 (2)	1100.4 (1)	6.1 (2)
5.7 (1)	280.89 (5)	12.7 (1)	357.66 (8)	6.9(2)	508.396 (7)	8.97 (2)	1092.2 (2)	8.1 (4)
3.58 (9)	264.52 (4)	13.3 (1)	355.86 (7)	5.8 (2)	493.679 (6)	8.03 (2)	1087.8 (2)	9.6 (5)
0 ^b	206.7 (1)	25.7 (4)	355.4 (1)	6.6 (3)	464.68 (2)	9.28 (4)	1081.1 (7)	10 (2)

^aDue to low intensity, the peak could not be properly fitted;

^b Open cell.

Table 6.3. Pressure dependence of the peak positions and FWHMs of four selected E modes. Reported uncertainties are from the spectral fitting..

Pressure (GPa)	ω_{128} (cm ⁻¹)	FWHM ₁₂₈ (cm ⁻¹)	ω_{1161} (cm ⁻¹)	FWHM ₁₁₁₆₁ (cm ⁻¹)	Pressure ^a (GPa)	ω_{265} (cm ⁻¹)	FWHM ₂₆₅ (cm ⁻¹)	ω_{809} (cm ⁻¹)	FWHM ₈₀₉ (cm ⁻¹)
1.19 (8)	134.90 (1)	3.98 (3)	1157.2 (1)	8.4 (3)	0.16 (8)	264.9 (4)	8 (1)	808.5 (9)	- ^b
0.48 (8)	130.25 (3)	4.73 (9)	1160.5 (2)	9.6 (5)	0.20 (8)	265.1 (1)	6.0 (3)	809.3 (2)	8.7 (5)
0.28 (8)	129.05 (5)	4.9 (1)	1160.5 (3)	10.7 (7)	0.32 (8)	266.4 (1)	6.6 (4)	811.1 (2)	10.0 (6)
0.99 (8)	133.85 (3)	4.29 (7)	1158.2 (3)	8.1 (7)	0.60 (8)	268.0 (1)	6.4 (3)	813.2 (3)	11.9 (7)
1.43 (9)	136.51 (2)	4.02 (6)	1157.3 (3)	9.6 (8)	1.27 (8)	271.52 (9)	5.4 (2)	818.1 (2)	7.4 (5)
1.67 (9)	137.67 (2)	3.88 (5)	1156.6 (3)	8.7 (6)	2.70 (8)	278.62 (8)	5.9 (2)	828.2 (2)	13.1 (7)
2.15 (9)	139.68 (2)	3.87 (5)	1155.4 (3)	8.8 (6)	2.50 (8)	277.65 (6)	5.7 (2)	826.9 (1)	8.6 (4)
2.58 (9)	141.70 (1)	3.64 (4)	1154.5 (2)	7.6 (3)	1.80 (9)	274.0 (1)	5.5 (3)	821.6 (3)	10.0 (9)
3.10 (9)	143.37 (2)	3.58 (5)	1154.0 (3)	7.0 (5)	2.15 (9)	275.76 (7)	5.6 (2)	824.8 (2)	8.3 (5)
0.71 (9)	132.32 (5)	4.4 (1)	1159.3 (5)	14 (1)	2.39 (9)	277.26 (8)	5.4 (2)	825.6 (3)	12.3 (7)
4.37 (9)	147.26 (1)	3.59 (3)	1152.5 (2)	5.6 (3)	3.26 (9)	281.31 (9)	5.7 (3)	831.5 (2)	8.5 (6)
4.97 (8)	148.90 (1)	3.56 (3)	1152.0 (2)	4.5 (2)	3.1 (1)	280.60 (6)	5.6 (2)	830.6 (2)	11.2 (4)
5.6 (1)	150.84 (1)	3.40 (4)	1152.2 (2)	4.4 (3)	4.0 (1)	284.59 (4)	5.1 (1)	836.1 (1)	8.5 (3)
6.0 (1)	151.37 (1)	3.40 (3)	1152.1 (2)	4.5 (2)	4.5 (1)	286.50 (4)	5.1 (1)	838.6 (1)	8.8 (3)
6.8 (1)	153.41 (1)	3.20 (4)	1152.0 (2)	3.8 (2)	5.3 (1)	290.15 (4)	5.1 (1)	843.3 (1)	8.3 (2)
7.2 (1)	153.836 (4)	3.37 (2)	1151.9 (1)	3.7 (1)	5.9 (1)	292.98 (6)	5.2 (2)	846.4 (1)	9.1 (3)
9.2 (1)	157.980 (7)	3.26 (2)	1152.1 (1)	4.0 (1)	7.0 (1)	297.47 (5)	4.7 (2)	851.7 (1)	7.4 (3)
3.7 (2)	144.95 (1)	3.38 (3)	1153.3 (2)	5.7 (3)	7.6 (1)	300.42 (5)	4.7 (2)	855.4 (1)	7.9 (3)
1.6 (1)	136.55 (2)	4.03 (5)	1157.0 (4)	9.8 (7)	8.1 (1)	302.66 (4)	4.9 (1)	858.1 (1)	8.0 (2)
0.87 (8)	133.07 (2)	4.40 (5)	1159.0 (3)	9.5 (6)	8.6 (1)	304.94 (5)	5.0 (1)	860.5 (1)	8.2 (2)
0 ^c	128.46 (4)	5.2 (2)	1159.6 (7)	9 (1)	9.1 (1)	305.9 (2)	8.4 (6)	861.6 (3)	9.1 (7)
					5.7 (1)	291.72 (9)	6.9 (2)	845.0 (1)	9.0 (4)
					3.58 (9)	282.27 (5)	6.4 (1)	833.7 (1)	7.8 (3)
					0 ^c	263.4 (4)	7 (1)	807.5 (4)	7 (1)

^aData collected in two runs, see the Material and methods section for details.

^bDue to low intensity, the peak could not be properly fitted;

^cOpen cell.

The experimentally-determined phonon wavenumbers and FWHMs are reported in the Table 6.2. They are in good agreement with experimental results at lower pressure (Schmidt & Ziemann, 2000) as well as with the calculated pressure trends (Murri et al., 2019), see Figure 6.3. The agreement with the peak positions reported by Schmidt and Ziemann (2000) is excellent, as in the case of the FWHM of the 206-cm⁻¹ mode. The deviation between the experimental and calculated shifts for the 206-cm⁻¹ mode is not surprising, since Density Functional Theory (DFT) does not take into account the complex multiphonon interaction in which this mode is involved, as described below. The FWHMs of the 464-cm⁻¹ mode from the experiments define the same trend, and the slight difference is compatible with the different peak fitting function, a Pearson IV, employed by Schmidt and Ziemann (2000). The use of a symmetric pseudo-Voigt peak function does not affect the peak positions at room temperature, since the asymmetry of this mode only becomes significant at elevated temperatures (Schmidt & Ziemann, 2000). The pressure variation of the 206-cm⁻¹ and 464-cm⁻¹ modes calculated from the phonon-mode Grüneisen tensor (Angel et al., 2019; Murri et al., 2019) and the variation of cell parameters from Scheidl et al. (2016) shows a good agreement with the experimental data up to 2 GPa. The same level of agreement is generally found for all of the modes. The pressure dependence of the peak positions ω_i and FWHMs of the four A_1 modes and selected E modes is depicted in Figure 6.4 and 6.5, respectively. Polynomial functions were used to fit the data points ω_i vs P, see Table 6.4, and then to calculate the phonon compressibility $\beta_\omega = \frac{1}{\omega_0} \frac{\partial \omega}{\partial P}$ of each mode (Fig.6.6). Phonon compressibilities represent the response of atomic dynamics to the applied pressure and their values confirm that the modes more sensitive to temperature are also the more sensitive to pressure. In particular, the phonon compressibility of the 206-cm⁻¹ mode considerably decreases with pressure up to 6 GPa. Similar behavior is shown by the other rotational mode at 128 cm⁻¹. The rest of phonons exhibit a relatively small change in compressibility, but it is worth noting that the stretching mode near 1161 cm⁻¹ starts from a negative compressibility and is thus soft, as can also be seen in Fig.6.5d. The rate of its softening decreases with increasing pressure and the phonon compressibility approaches zero. The A_1 mode at 355 cm⁻¹ shows a very slightly negative compressibility at low pressures.

Quartz is employed as a pressure sensor in diamond anvil cells through the wavenumber change with pressure of the Raman peaks, but this approach is limited to the restricted number of modes reported by Schmidt and Ziemann (2000). We therefore report in Table 6.5 the relationship between pressure P and wavenumber shift $\Delta\omega$ relative to the line position at 0.0001 GPa as a polynomial function. This relationship can be expressed as a quadratic function for the 128-, 265-, 464-, 696-, 809-, 1080- and 1161-cm⁻¹ modes, only the 206-cm⁻¹ mode requires a polynomial function of order higher than two.

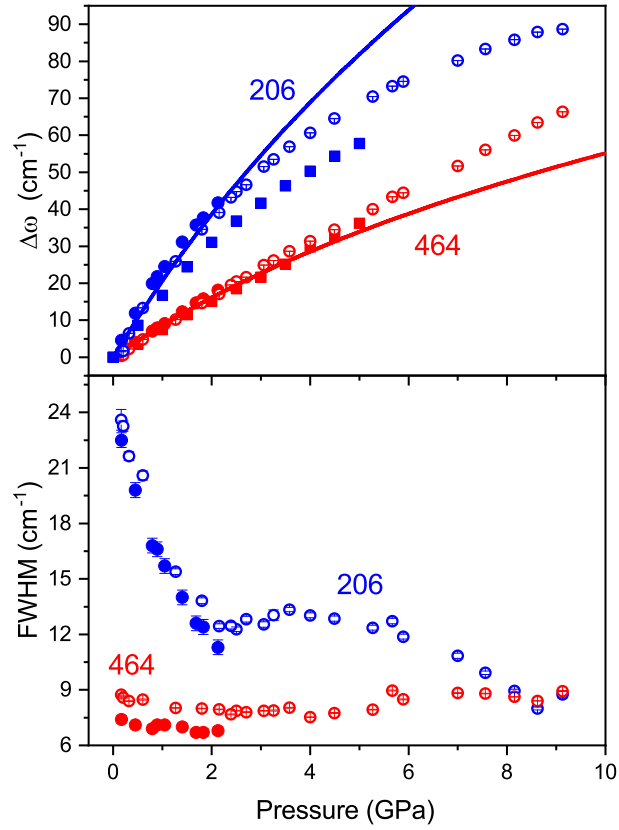


Figure 6.3. Comparison between the measured pressure dependencies of the phonon wavenumbers and FWHMs (this study, open circles) with experimental data from Schmidt and Ziemann (2000) (filled circles), simulated $\Delta\omega$ by DFT calculations at 0 K (squares) and predictions of the mode Grüneisen tensors (lines) (Murri et al., 2019). Uncertainties on peak positions and pressures for data from the current work are generally smaller than the symbol size. This also applies to subsequent figures unless the error bars are visible. A realistic estimate of the true precision can be obtained from the scatter of consecutive data points. .

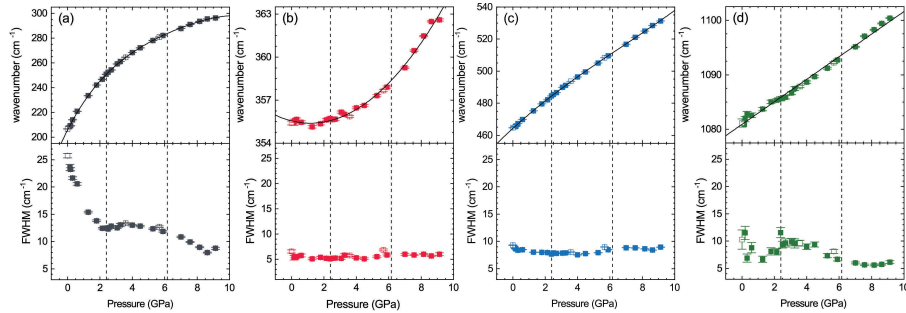


Figure 6.4. Pressure dependence of the peak positions and FWHMs of the four A_1 modes. Dashed lines indicate the pressures of the equilibrium phase boundaries between quartz and coesite (Bose & Ganguly, 1995) and coesite and stishovite (Zhang et al., 1996). Open symbols are data points collected on decompression. .

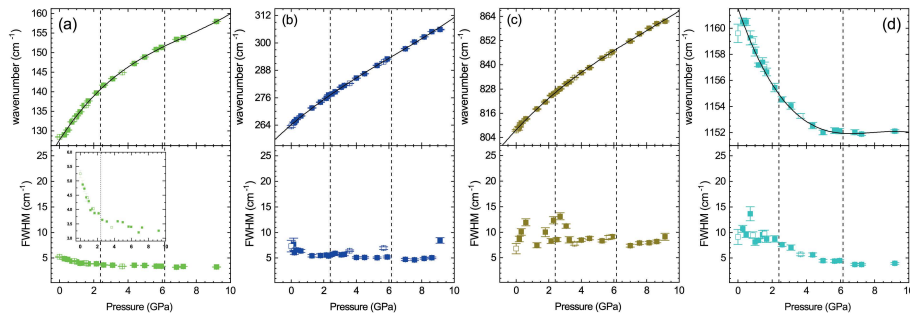


Figure 6.5. Pressure dependence of the peak positions and FWHMs of selected E modes. Dashed lines indicate the pressures of the equilibrium phase boundaries between quartz and coesite (Bose & Ganguly, 1995) and coesite and stishovite (Zhang et al., 1996). Open symbols are data points collected on decompression..

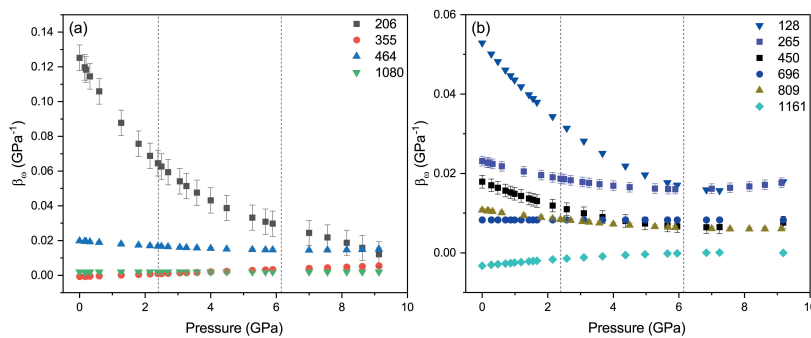


Figure 6.6. Phonon compressibilities of the four A_1 modes and well resolved E modes. Dashed lines indicate the pressures of the equilibrium phase boundaries between quartz and coesite (Bose & Ganguly, 1995) and coesite and stishovite (Zhang et al., 1996).

Table 6.4. Coefficients of the function $\omega_i(P)$.

$\omega(P) = \omega_0 + \omega'P + \omega''P^2 + \omega'''P^3 + \omega''''P^4$				
ω_0	ω'	ω''	ω'''	ω''''
<i>A</i> ₁ modes				
205.8(3)	25.8(6)	-3.6(3)	0.30(6)	-0.011(3)
355.56(9)	-0.28(5)	0.12(1)	0	0
464.2(2)	9.2(2)	-0.36(5)	0.017(4)	0
1080.9(2)	2.07(4)	0	0	0
<i>E</i> modes				
127.7(2)	6.8(2)	-0.64(5)	0.029(3)	0
264.0(2)	6.1(2)	-0.30(6)	0.016(4)	0
394.2(1)	0.18(3)	0	0	0
404.3(1)	0.79(2)	0	0	0
448.8(5)	8.0(5)	-0.7(1)	0.035(7)	0
697.9(5)	5.80(8)	0	0	0
807.7(2)	8.7(2)	-0.47(7)	0.019(5)	0
1158.9(3)	-4.0(3)	0.40(7)	-0.013(5)	0
1161.5(3)	-3.8(3)	0.49(6)	-0.021(4)	0

Table 6.5. Pressure calibrations for the modes at 128, 206, 265, 464, 696, 809, 1080, 1161 cm^{-1} .

$P(\text{GPa}) = A\Delta\omega + B\Delta\omega^2 + C\Delta\omega^3$			
Mode	A	B	C
128 ^a	0.125 (7)	0.0059 (3)	0
206 ^a	0.060 (4)	-0.0006(1)	0.0000125 (10)
265 ^a	0.191 (2)	0.00071 (8)	0
464 ^a	0.118 (1)	0.00029 (3)	0
696 ^a	0.135 (4)	0.00063 (10)	0
809 ^a	0.128 (2)	0.00080 (5)	0
1080 ^a	0.72(2)	-0.013(1)	0
1161 ^b	-0.20 (3)	0.030(5)	0

^aPressure range: 0-9 GPa;

^b Pressure range: 0-4 GPa.

The phonon decay and hence the peak FWHM should not change with pressure in the absence of structural transformations because pressure, in contrast to temperature, is not expected to influence the phonon-phonon interactions, which is the main source of phonon decay at non-zero temperatures in insulating materials. This is indeed the case for most of the phonons (e.g. Fig.6.4b-d and Fig.6.5b-c). However, the FWHM of the 206- cm^{-1} mode displays a peculiarly strong pressure dependence with two kinks at 2.5 and 6 GPa (Fig. 6.4). This mode is the fundamental phonon mode involved in the α - β phase transition. Approaching the phase transition temperature, it experiences softening and damping due to coupling with the two-phonon excitation at 147 cm^{-1} , which is the true soft mode driving the α - β phase transition (Scott, 1968). Applying pressure, on the contrary, the 206- cm^{-1} mode hardens and its width decreases. Jayaraman et al. (1987) suggested that the change in the line width is determined by the interaction with the two-phonon excitation, in analogy to the strong anharmonic interaction observed by Scott (1968) at high temperatures, where the 206- cm^{-1} mode softens with increasing temperature due to coupling with the two-phonon excitation around 147 cm^{-1} . Between ambient pressure and 2.5 GPa, the line width of the 206- cm^{-1} mode rapidly sharpens, indicating strong suppression of the phonon-phonon interaction. It is worth noting that the same behavior is observed for the width of the mode at 128 cm^{-1} , that is related to rotation of SiO_4 tetrahedra, i.e. the same type of atomic vibration as the 206- cm^{-1} mode. The pressure of 2.5 GPa is the point at which, at room temperature, quartz becomes metastable with respect to coesite, that is, where the framework topology of quartz is less stable. Due to the type of atomic vibrations involved, rotational modes should be very sensitive to stability or instability of the framework topology. Thinking the other way around, from higher to lower pressure, the strong increase of

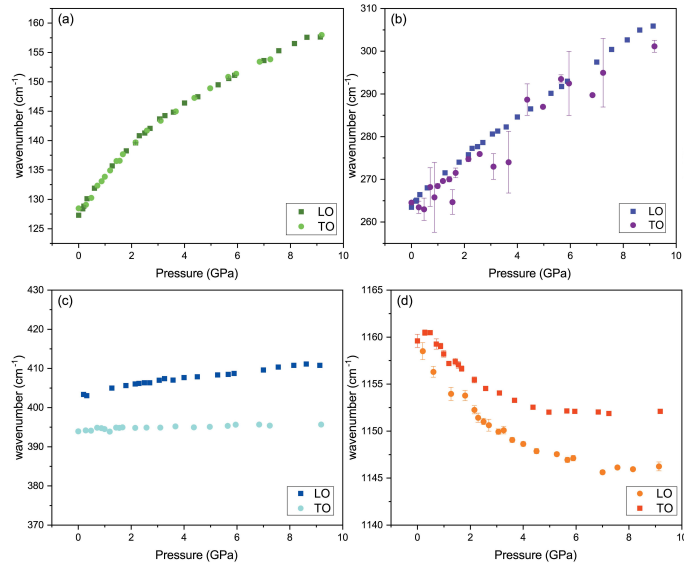


Figure 6.7. LO-TO splitting of the 128- (LO+TO) (a), 264- (TO) and 265- (LO) (b), 394- (TO) and 403- (LO) (c), and 1161- (TO) and 1159-cm⁻¹ (LO) modes (d).

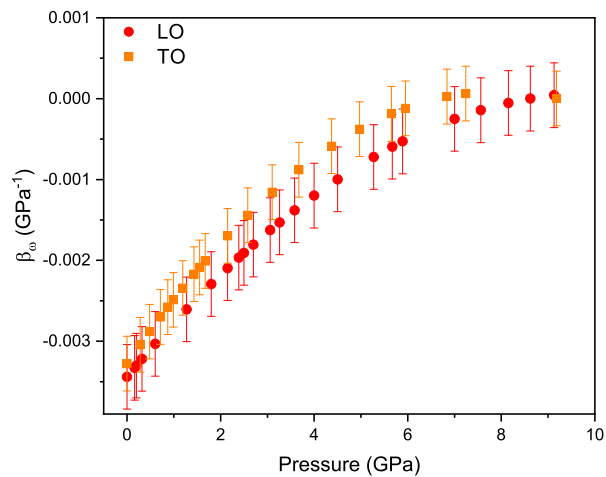


Figure 6.8. Phonon compressibilities of the 1161- (TO) and 1159-cm⁻¹ (LO) modes.

the FWHM on pressure decrease from 2.5 GPa to ambient P indicates that the Si-O framework topology typical of quartz is stabilized due to the multiphonon interactions involving SiO₄ rotational modes. Between 2.5 and 6 GPa the FWHM of the 206-cm⁻¹ mode remains constant although still relatively large (13 cm⁻¹ vs 5 cm⁻¹ for the neighboring A₁ mode at 355 cm⁻¹) and then, above 6 GPa, continues to slightly decrease with further pressure increase. Above 6 GPa quartz becomes metastable also with respect to stishovite, that is, the four-fold coordination of Si becomes metastable with respect to the six-fold Si coordination. Destabilization of the coordination is expected to influence the Si-O bond stretching vibrations. Indeed, the FWHM of the SiO₄ stretching mode near 1161 cm⁻¹ decreases when the pressure increases from 2.5 to 6 GPa, i.e. in the range where the FWHM of the SiO₄ rotation mode remains constant. Again, considering the ongoing phenomena from higher to lower pressures, it is clear that the phonon-phonon interactions comprising stretching modes contribute to the stabilization of the tetrahedral Si coordination at lower pressures. Hence, the anomalous pressure behavior of the FWHM of the SiO₄ rotation and stretching modes experimentally demonstrates the key importance of multiphonon interactions for the stability and therefore natural abundance of quartz at ambient conditions. Other possible explanations for the FWHM decrease at high pressures, such as pressure-induced mobilization of bulk point and/or topological defects, are ruled out because all of the observed changes in the FWHM are fully reversible.

As previously mentioned, the polar *E* modes of quartz split in longitudinal and transverse optical vibrations. For some of these modes, such as the 128-cm⁻¹ mode, the splitting is negligible and does not vary with pressure (Fig. 6.7a). Other modes, for example the 394- (TO) and 403-cm⁻¹ (LO) and the 1159 (LO) and 1161-cm⁻¹ (LO), have slightly larger splittings. The phonon compressibilities of the 1159-cm⁻¹ (TLO) and 1161-cm⁻¹ (TO) components in Fig. 6.8 show the same response upon compression. From the analysis of the wavenumber shifts together with the phonon compressibility of LO and TO components, it is clear that their atomic dynamics displays the same response to the application of pressure. As a consequence, the Grüneisen components obtained from DFT calculations for the TO modes can also be used for the LO components to derive the strains in crystals under non-hydrostatic conditions, as proposed by Angel et al., 2019 and Murri et al., 2019. Because of its ubiquity in natural samples, quartz inclusions have been widely studied, but little attention has been focused so far on the effect of the orientation of the inclusions that can lead to additional changes in the wavenumbers for the polar *E* modes, which depend on the angle between the phonon wavevector and the *c* axis (Shapiro & Axe, 1972). As a consequence, identifying the actual LO-TO component accessible in the available orientations of the measured inclusions is a necessary prerequisite for the application of this approach. In elastic geobarometry applications, a reference data set of polar-

ized Raman spectra is thus a useful guide to interpret correctly experimental results from mineral inclusions. Furthermore, improved $P(\omega)$ calibration curves constructed over a wider pressure range and for a larger number of modes can improve the precision in predicting the residual pressure, better constraining the pressure behavior of Raman active modes in the lower pressure range of interest for mineral inclusions.

6.4 CONCLUSIONS

In this contribution we report a complete data set of quartz Raman spectra under hydrostatic conditions up to 9 GPa, and several main conclusions can be drawn from our results. First, the stability of alpha-quartz at ambient conditions with respect to other silica polymorphs seems to result from strong multiphonon interactions. Second the measured pressure dependence of all of the Raman shifts of quartz is predicted by the phonon-mode Grüneisen tensors up to 2 GPa, thereby validating the parameter values reported for the Raman modes of quartz by Murri et al. (2019). Finally, the LO and TO components of the polar E modes show the same phonon compressibility. This is quite significant for the practical use of Raman geobarometry, because it experimentally supports the application of the Grüneisen-tensor approach (Angel et al., 2019; Murri et al., 2019) to both LO and TO modes and verifies that the orientation of quartz inclusions with respect to the surface of the host does not bias the strain-induced shifts of the Raman peaks originating from E modes.

ACKNOWLEDGEMENTS

We thank Lukas Panitz and Dr. Naemi Waesermann, University of Hamburg, for help in collecting the Raman data. This work was financially supported by the European Research Council (ERC) under the European Union's Horizon 2020 research and innovation program grant agreement 714936 to M. Alvaro.

REFERENCES

- Alvaro, M., Mazzucchelli, M., Angel, R., Murri, M., Campomenosi, N., Scambelluri, M., Nestola, F., Korsakov, A., Tomilenko, A., Marone, F., & Morana, M. (2020). Fossil subduction recorded by quartz from the coesite stability field. *Geology*, 48(1), 24–28. <https://doi.org/10.1130/G46617.1>
- Angel, R. J., Bujak, M., Zhao, J., Gatta, G. D., & Jacobsen, S. D. (2007). Effective hydrostatic limits of pressure media for high-pressure crystallographic studies. *Journal of Applied Crystallography*, 40(1), 26–32. <https://doi.org/10.1107/S0021889806045523>

- Angel, R. J., Murri, M., Mihailova, B., & Alvaro, M. (2019). Stress, strain and Raman shifts. *Zeitschrift für Kristallographie - Crystalline Materials*, 234(2), 129–140. <https://doi.org/10.1515/zkri-2018-2112>
- Asell, J. F., & Nicol, M. (1968). Raman spectrum of α quartz at high pressures. *The Journal of Chemical Physics*, 49(12), 5395–5399. <https://doi.org/10.1063/1.1670064>
- Ballato, A. (2008). Basic material quartz and related innovations. *Piezoelectricity* (pp. 9–35). Springer Berlin Heidelberg.
- Bonazzi, M., Tumiati, S., Thomas, J. B., Angel, R. J., & Alvaro, M. (2019). Assessment of the reliability of elastic geobarometry with quartz inclusions. *Lithos*, 350–351, 105201. <https://doi.org/10.1016/j.lithos.2019.105201>
- Bose, K., & Ganguly, J. (1995). Quartz-coesite transition revisited: Reversed experimental determination at 500–1200 °C and retrieved thermochemical properties. *American Mineralogist*, 80(3), 231–238. <https://doi.org/10.2138/am-1995-3-405>
- Enami, M., Nishiyama, T., & Mouri, T. (2007). Laser raman microspectrometry of metamorphic quartz: A simple method for comparison of metamorphic pressures. *American Mineralogist*, 92(8), 1303–1315. <https://doi.org/10.2138/am.2007.2438>
- Etchepare, J., Merian, M., & Smetankine, L. (1974). Vibrational normal modes of SiO₂. I. α and β quartz. *The Journal of Chemical Physics*, 60(5), 1873–1876. <https://doi.org/10.1063/1.1681287>
- Gonzalez, J. P., Thomas, J. B., Baldwin, S. L., & Alvaro, M. (2019). Quartz-in-garnet and Ti-in-quartz thermobarometry: Methodology and first application to a quartzofeldspathic gneiss from eastern Papua New Guinea. *Journal of Metamorphic Geology*, 37(9), 1193–1208. <https://doi.org/10.1111/jmg.12508>
- Hemley, R. J. (1987). Pressure dependence of Raman spectra of SiO₂ polymorphs: α -quartz, coesite, and stishovite. In M. H. Manghnani & Y. Syono (Eds.), *Geophysical monograph series* (pp. 347–359). American Geophysical Union. <https://doi.org/10.1029/GM039p0347>
- Jayaraman, A., Wood, D. L., & Maines, R. G. (1987). High-pressure Raman study of the vibrational modes in AlPO₄ and SiO₂ (α -quartz). *Physical Review B*, 35(16), 8316–8321. <https://doi.org/10.1103/PhysRevB.35.8316>
- Mihailova, B., Waesermann, N., Stangarone, C., Angel, R. J., Prencipe, M., & Alvaro, M. (2019). The pressure-induced phase transition(s) of ZrSiO₄: Revised. *Physics and Chemistry of Minerals*, 46(8), 807–814. <https://doi.org/10.1007/s00269-019-01041-1>
- Munro, R. G., Piermarini, G. J., Block, S., & Holzapfel, W. B. (1985). Model line-shape analysis for the ruby R lines used for pressure measurement. *Journal of Applied Physics*, 57(2), 165. <https://doi.org/10.1063/1.334837>
- Murri, M., Alvaro, M., Angel, R. J., Prencipe, M., & Mihailova, B. D. (2019). The effects of non-hydrostatic stress on the structure and properties of alpha-

- quartz. *Physics and Chemistry of Minerals*. <https://doi.org/10.1007/s00269-018-01018-6>
- Murri, M., Mazzucchelli, M. L., Campomenosi, N., Korsakov, A. V., Prencipe, M., Mihailova, B. D., Scambelluri, M., Angel, R. J., & Alvaro, M. (2018). Raman elastic geobarometry for anisotropic mineral inclusions. *American Mineralogist*, *103*(11), 1869–1872. <https://doi.org/10.2138/am-2018-6625CCBY>
- Scheidl, K. S., Kurnosov, A., Trots, D. M., Boffa Ballaran, T., Angel, R. J., & Miletich, R. (2016). Extending the single-crystal quartz pressure gauge up to hydrostatic pressure of 19 GPa. *Journal of Applied Crystallography*, *49*(6), 2129–2137. <https://doi.org/10.1107/S1600576716015351>
- Schmidt, C., & Ziemann, M. A. (2000). In-situ Raman spectroscopy of quartz: A pressure sensor for hydrothermal diamond-anvil cell experiments at elevated temperatures. *American Mineralogist*, *85*(11), 1725–1734. <https://doi.org/10.2138/am-2000-11-1216>
- Scott, J. F. (1968). Evidence of coupling between one- and two-phonon excitations in quartz. *Physical Review Letters*, *21*(13), 907–910. <https://doi.org/10.1103/PhysRevLett.21.907>
- Shapiro, S. M., & Axe, J. D. (1972). Raman scattering from polar phonons. *Physical Review B*, *6*(6), 2420–2427. <https://doi.org/10.1103/PhysRevB.6.2420>
- Wang, J., Mao, Z., Jiang, F., & Duffy, T. S. (2015). Elasticity of single-crystal quartz to 10 GPa. *Physics and Chemistry of Minerals*, *42*(3), 203–212. <https://doi.org/10.1007/s00269-014-0711-z>
- Wong, P. T. T., Baudais, F. L., & Moffatt, D. J. (1986). Hydrostatic pressure effects on TO–LO splitting and softening of infrared active phonons in α -quartz. *The Journal of Chemical Physics*, *84*(2), 671–674. <https://doi.org/10.1063/1.450563>
- Zhang, J., Li, B., Utsumi, W., & Liebermann, R. (1996). In situ X-ray observations of the coesite-stishovite transition: Reversed phase boundary and kinetics. *Physics and Chemistry of Minerals*, *23*(1). <https://doi.org/10.1007/BF00202987>

7 Raman scattering of a free quartz crystal at high temperature

7.1 INTRODUCTION

At ambient pressure, quartz undergoes a well known phase transition at 573 °C from the low-temperature α -phase to the high temperature β -phase. The two phases crystallize in the chiral space groups $P3_121$ and $P3_221$, and $P6_222$ and $P6_422$, respectively (e.g. Donnay & Le Page, 1978). Following the approach of Grimm and Dorner (1975), the crystal structure of quartz can be seen as made of rigid unit of SiO_4 tetrahedra linked at the corners (Fig 7.1). This assumption is justified by the fact that the tetrahedral sp^3 σ bonds are strong, while the relative orientations of SiO_4 tetrahedra are determined by weaker forces. As a consequence, the α -phase can be derived from the high-temperature phase by a slight rotation of the tetrahedra around their two-fold axis that determines the lattice strains. The rotation angle ϕ can then be taken as the microscopic order parameter, ranging from 0 to $\approx 16.3^\circ$ in the β and α -phase at room temperature, respectively. In particular, Grimm and Dorner (1975) identified three interdependent effects. First, rotation of rigid tetrahedra reduce the lattice parameters only through a spontaneous macroscopic strain that scales with ϕ^2 . In fact, higher order contributions to the variation in lattice parameters are negligible, since they vary with $\cos \phi$ (Megaw, 1973) that can be expanded as:

$$\cos \phi = 1 - \frac{1}{2}\phi^2 + \frac{1}{24}\phi^4 - \dots \quad (7.1)$$

giving a fourth order term that is only $\sim 1\%$ of the second order one. Second, the rotations of the tetrahedra reduce the Si-O-Si angle, while increasing the Si-O bond length. Finally, the tetrahedra undergo shearing deformation that cause an increase in the c unit cell parameter. Carpenter et al. (1998) carried a semi-quantitative analysis of these three effects and suggested that their macroscopic consequence are similar in magnitude, but the shearing of the tetrahedra shows a non-linear strain behavior. In particular the variation of the ratio c/a with temperature shows the typical evolution of excess properties induced by a phase transition. In fact, c/a should be smaller in α -quartz than in β , if the tetrahedra were rigid, while it increases upon cooling as a result of the deformation of the

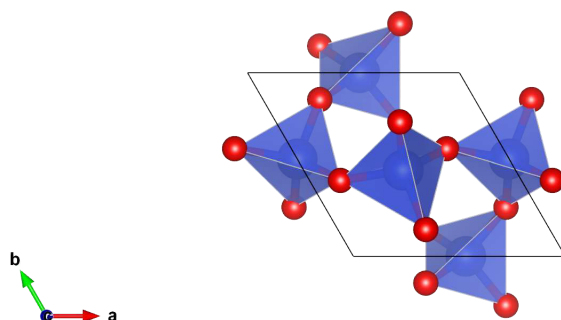


Figure 7.1. Crystal structure of quartz (S.G. $P3_121$).

tetrahedra (Fig. 14a in Carpenter et al., 1998).

7.2 MATERIALS AND METHODS

Polarized Raman spectra were collected with a Horiba Jobin-Yvon T64000 triple-monochromator system equipped with a Symphony LN₂-cooled CCD detector (Horiba Jobin Yvon, Villeneuve d'Ascq, France), an Olympus BH41 microscope, and a Coherent Ar⁺ laser. The measurements were performed in backscattering geometry, with a 50x super long working distance objective and an excitation wavelength of 514.532 nm. The spectrometer was calibrated to the T_{2g} mode at 520.5 cm^{-1} of a Si wafer. The spectral resolution was approximately 2 cm^{-1} , while the instrumental precision in the peak positions was 0.35 cm^{-1} . The data collection was conducted on heating from room temperature to 1400 K with a rate of temperature change of 50 K min^{-1} , using a Linkam TS1200 stage equipped with a T95 controller (Linkam, Tadworth, UK). This setup allows to collect spectra from ambient temperature to 1200 °C with heating rates from 1 to 200 °C/min and a data sampling rate of 20/s. The stage has a type S Pt-10% Rh/Pt thermocouple, a light aperture of 1.7 mm and a temperature stability of 1 °C. The sample is held in a cup of dimensions 10mm diameter x 5mm deep (“T95 Specifications”; “TS1200 features”). To prevent thermal gradient across the crystal, the sample was kept for 5 minutes at the desired experimental temperature before the data collection was started. The acquisition time was set to obtain a satisfactory signal-to-noise ratio, and thus the spectra were collected for 30 s averaging over a minimum of 5 accumulations in the wavenumber range $15\text{--}1615\text{ cm}^{-1}$.

To assess temperature stability and the absence of temperature gradients, data

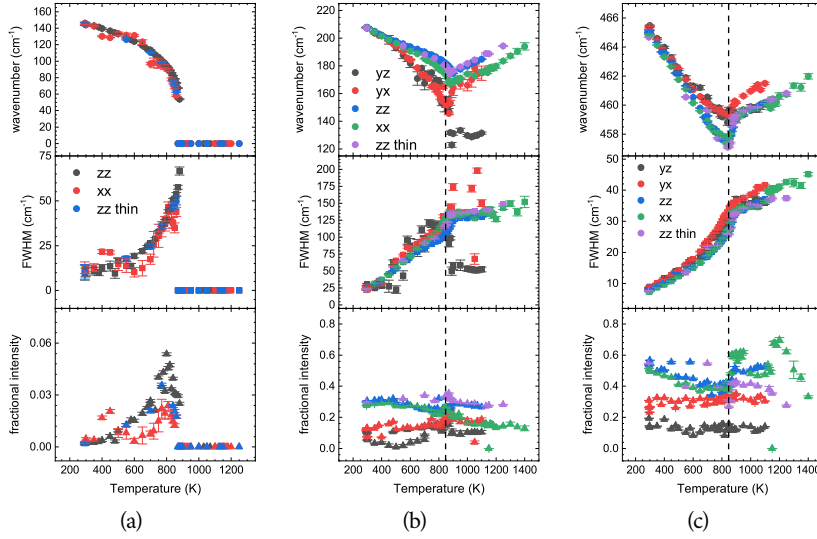


Figure 7.2. Temperature dependence of the peak positions of: the 147-cm^{-1} two-phonon band (a) in the scattering geometries $\bar{z}(xx)z$, and the $\bar{y}(zz)y$ for the thickest and the thinnest sample (zz thin); the 206-cm^{-1} (b) and the 464-cm^{-1} (c) in the scattering geometries $\bar{z}(xx)z$, $\bar{z}(yx)z$, $\bar{y}(xz)y$, and $\bar{y}(zz)y$ for the thickest and the thinnest sample (zz thin). Data from the geometries $\bar{z}(yx)z$, $\bar{y}(xz)y$, and $\bar{y}(zz)y$ for the thickest sample are from (Murri et al., 2019). Dashed lines indicate the α - β transition temperature .

from Murri et al. (2019), collected on a 1 mm-thick quartz crystal, were compared with spectra from oriented (010)- and (001)-cuts of lower thickness (Table 7.2 and 7.3 respectively). The results are summarized in Figure 7.2. There is in general a very good agreement in the data from samples of different thickness and orientation. The slight differences might be related to two main reasons:

- The A_1 modes are formally allowed only in parallel polarized spectra, but the 206-cm^{-1} (b) and the 464-cm^{-1} modes, which are the two A_1 modes with the highest intensity, appear also in cross polarized spectra, probably because of depolarization of the incident and scattered light (Scott & Porto, 1967). The residual components are indeed of low intensity, thus affecting the quality of the fit.
- On the data from Murri et al. (2019) a baseline correction was carried out before the temperature reduction (M. Murri, personal communication, July 27, 2020), while the data presented in this thesis were only temperature reduced, as described below. This difference in the data treatment might affect the results from the 206-cm^{-1} mode, particularly sensitive to temperature as described in Section 7.3.

To account for the Bose–Einstein occupation factor, the intensity of the measured spectra was temperature-corrected using the relation $I =$

$I_{measured}/[(\exp^{\hbar\omega/k_B T} - 1)^{-1} + 1]$, where \hbar , ω , k_B , and T are the reduced Planck constant, phonon wavenumber, Boltzmann constant, and temperature, respectively. The spectra were then normalized to the acquisition time. Pseudo-Voigt functions ($PV = qL + (1 - q)G$, where L and G are Lorentzian and Gaussian peak-shape functions) were used to fit the spectra and determine the Raman peak positions ω , full widths at half maximum (FWHMs), and integrated intensities I . The A_1 mode at 464 cm^{-1} shows a pronounced asymmetry upon increasing temperature (e.g. Schmidt & Ziemann, 2000), which cannot be taken into account by Pseudo-Voigt functions. As consequence, an additional peak was introduced, following the fitting procedure described by Murri et al. (2019).

7.3 RAMAN SCATTERING AT HIGH TEMPERATURE

Low-quartz has D_3 group and 9 atoms per unit cell, thus $3N = 27$ degrees of freedom. Excluding the three acoustic vibrations, the representation of the optic vibrations is:

$$\Gamma^{op} = 4A_1 + 4A_2 + 8E \quad (7.2)$$

The A_1 modes are Raman active, while the A_2 modes are infrared active, while the doubly degenerate E modes are both infrared and Raman active and thus show transverse optic (TO) and longitudinal optic (LO) components. Moving to β -quartz the group changes to D_6 and the optical vibrations are given by:

$$\Gamma^{op} = A_1 + 2A_2 + 2B_2 + 3B_1 + 4E_1 + 4E_2 \quad (7.3)$$

where the A_1 and E_2 modes are Raman active, the A_2 is infrared active, the B_1 and B_2 modes are silent, and the E_1 modes are both Raman and infrared active and thus transverse optic (TO) and longitudinal optic (LO) components. As in the case of α -quartz, the lowest E_1 mode is expected to show negligible splitting, while the other three modes exhibit larger splitting (Fries & Claus, 1973). The relation of the symmetry species of the factor groups is given in the correlation diagram, Table 7.1 (Bates & Quist, 1972). When performing polarized Raman spectroscopy, polarization selection rules also apply. In α -quartz, in back-scattering geometry the E(LO) components are allowed in the geometries $\bar{x}(yy)x$, $\bar{x}(yz)x$, and $\bar{y}(xz)y$ (Porto's notation), while the E(TO) components are allowed in the geometries $\bar{y}(xx)y$, $\bar{z}(xx)z$, $\bar{z}(xy)z$, and $\bar{z}(yy)z$ (Kroumova et al., 2003; Scott & Porto, 1967). Additionally, the polar nature of these modes induces a dependence on the angle between θ between the phonon wavevector and the c axis. Shapiro and Axe (1972) identified two different types of behavior as θ changes from 0° to 90° . The first group includes modes, such as the 394- and 364-cm^{-1} (A_2), and 797- and 810-cm^{-1} , that change its character from transverse to longitudinal, but remaining A_2 or E at $\theta = 0$ and $\theta = 90$. The second group includes modes, such as the 550- (A_2) and 510-cm^{-1} extremes as occurs, for example, that do not

Table 7.1. Correlation diagram for α - and β -quartz.

	α -quartz (D_3)	β -quartz (D_6)	
		A ₁	$x^2 + y^2, zz$
$x^2 + y^2, z^2$	A ₁	A ₂	z
z	A ₂	B ₁	
		B ₂	
		E ₁	$(x, y); (yz, xz)$
$(x, y)(x^2 - y^2, xy); (yz, xz)$	E	E ₂	$(x^2 - y^2, xy)$

change the transverse or longitudinal character, while changing its transformation properties from A_2 to E . This behavior is the result of two competing forces. In the first group the long-range electromagnetic forces dominate over the anisotropic short-range forces maintaining the transverse or longitudinal character, whereas in the second group the anisotropic short-range forces prevail (Loudon, 1964). In β -quartz, back-scattering geometry allows only the detection of E_1 (TO) modes in cross polarized spectra, and E_2 modes in parallel polarized spectra, while the E_1 (TO) components are accessible through the right-angle scattering geometry (Bates & Quist, 1972; Fries & Claus, 1973; Kroumova et al., 2003).

From the correlation diagram and the representations, only one A_1 out of four is allowed to persist in the β -phase. This mode is the 464-cm^{-1} mode, because of the high symmetry of the atomic motions (Etchepare et al., 1974). The 464-cm^{-1} mode shows a discontinuity both in the wave-number shift and in the FWHM at the phase transition (Fig. 7.4 a). The peak position decreases almost linearly up to 810 K, then a discontinuity at 860 K is clearly evident. The temperature dependence of the FWHM shows the same behavior. The fact that the spectral changes induced by the phase transition appear approximately 10 degrees higher than the transition temperature was already reported by Salje et al. (1992), who state that the direct coupling between the order parameter, Q , and the intensity, A , and frequency shift, $\Delta(\omega^2)$, is of the fourth order: $-\Delta A \propto \Delta(\omega^2) \propto Q^4$.

However, Figure 7.3, which shows spectra at selected temperatures in the $\bar{z}(xx)z$ scattering geometry, suggests that the 464-cm^{-1} mode is not the only A_1

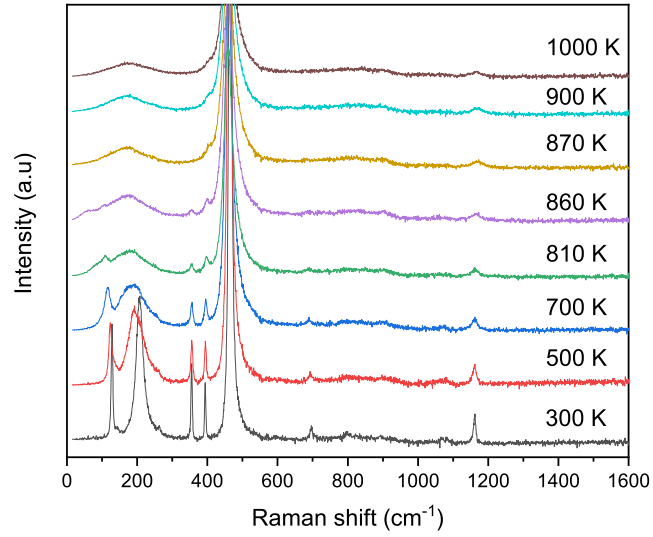


Figure 7.3. Selected spectra upon increasing temperature in the $\bar{z}(xx)z$ scattering geometry.

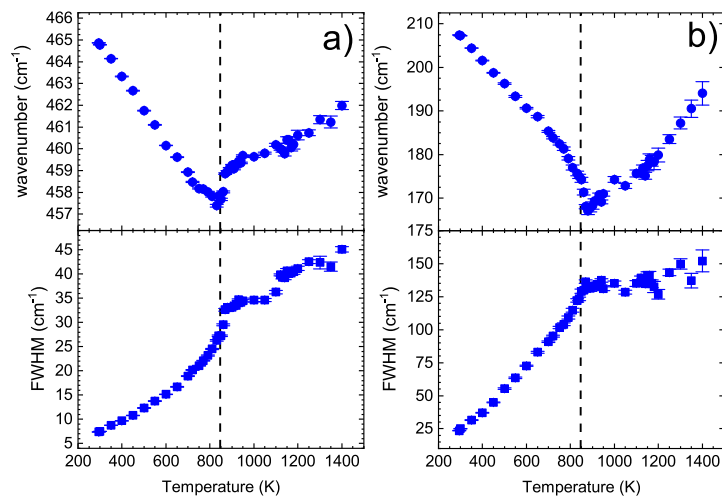


Figure 7.4. Temperature dependence of the peak positions and FWHMs of the 464- cm^{-1} (a) and 206- cm^{-1} (b) modes in the $\bar{z}(xx)z$ scattering geometry. Dashed lines indicate the α - β transition temperature.

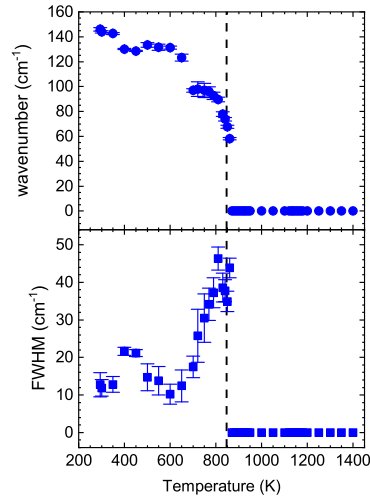


Figure 7.5. Temperature dependence of the peak positions and FWHMs of the two-phonon excitation around 147 cm^{-1} in the $\bar{z}(xx)z$ scattering geometry. Dashed lines indicate the α - β transition temperature.

that persists in the β -phase. In fact, the 206-cm^{-1} A_1 mode is present after the transition from the α to the β phase. This mode is the most sensitive to temperature: in the temperature range from 300 to 860 K its peak position changes from 207.27 to 171.3 cm^{-1} , while its FWHM largely increases from 25.1 to 130 cm^{-1} , as shown in figure 7.4b. Because of this huge temperature dependence, this mode has often been considered as the soft-mode driving the phase transition. However, the phonon wave-number of a soft-mode is expected to decrease to zero as the transition temperature is approached (Cochran, 1960; Ginzburg, 1960), while this mode only softens, which therefore implies there are some higher-order interactions in the real material that are not accounted for in the theory. Indeed, the huge temperature dependence and anomalous broadening of this mode is related to another spectral feature centered around 147 cm^{-1} at ambient conditions Fig7.5 that is a two-phonon excitation (Scott, 1968, 1974) whose phonon wave-number tends to zero approaching the phase transition. Scott (1968) suggested that these two spectral features could interact via Fermi resonance, which is possible when a one quantum vibrational level for one mode lies very near the energy of a two-quantum vibrational level for another mode. If the levels have the same symmetry, there is an anharmonic interaction between the levels that cause a level repulsion and thus a "no-crossing" rule. In the interpretation by Scott (1968), the soft mode is the the band at higher wavenumber at low temperatures, while is the band at low wavenumber at high temperatures. At room and intermediate temperatures, the fundamental A_1 mode and the A_1 -symmetry two-phonon band

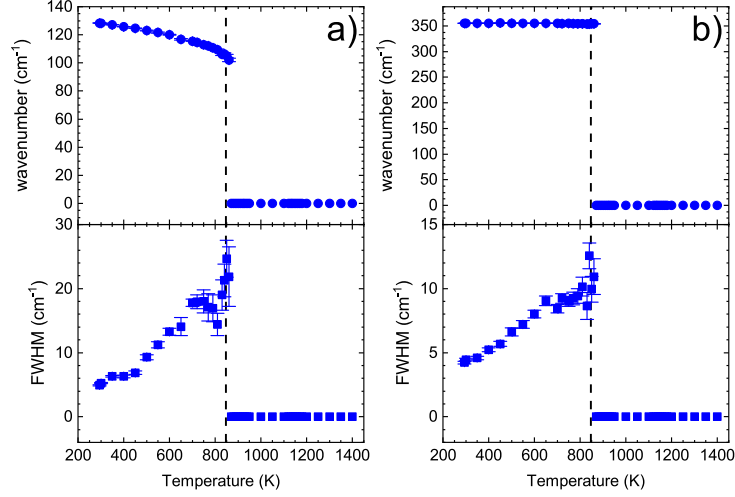


Figure 7.6. Temperature dependence of the peak positions and FWHMs of the mode around 128 cm^{-1} (a) and 355 cm^{-1} (b) in the $\bar{z}(xx)z$ scattering geometry. The E_1 mode in β -quartz corresponding to the E mode at 128 cm^{-1} is not allowed by polarization selection rule in this scattering geometry. Dashed lines indicate the α - β transition temperature.

are mixed. Above the transition temperature, the excitation has predominately a second-order character and thus does not violate selection rules. This interpretation is also supported by inelastic neutron scattering data (Axe & Shirane, 1970). The other modes in quartz obey the selection rules and the remaining two A_1 modes disappear at the phase transition (Fig 7.6b and Table 7.3).

7.4 RAMAN SHIFTS AND GRÜNEISEN TENSOR COMPONENTS AT HIGH TEMPERATURE

The relationship between by the wavenumber ω and the strain ε is given by:

$$\frac{-\Delta\omega^m}{\omega_0^m} = \gamma^m : \varepsilon \quad (7.4)$$

where $\frac{-\Delta\omega^m}{\omega_0^m}$ is the fractional change in the wavenumber for a mode m and γ^m is the second-rank symmetric mode Grüneisen tensor. Equation 7.4 can also be expressed in Voigt notation as:

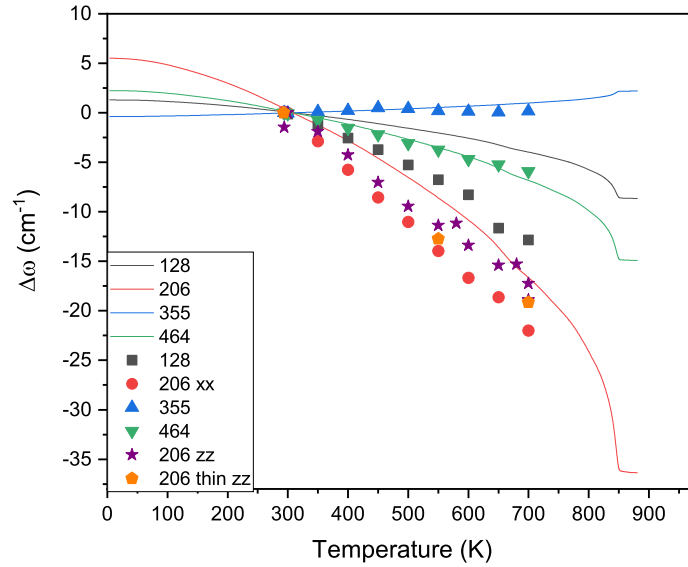
$$\frac{-\Delta\omega^m}{\omega_0^m} = \gamma_1^m \varepsilon_1 + \gamma_2^m \varepsilon_2 + \gamma_3^m \varepsilon_3 + \gamma_4^m \varepsilon_4 + \gamma_5^m \varepsilon_5 + \gamma_6^m \varepsilon_6 \quad (7.5)$$

In the case of quartz, trigonal symmetry reduces Equation 7.5 to:

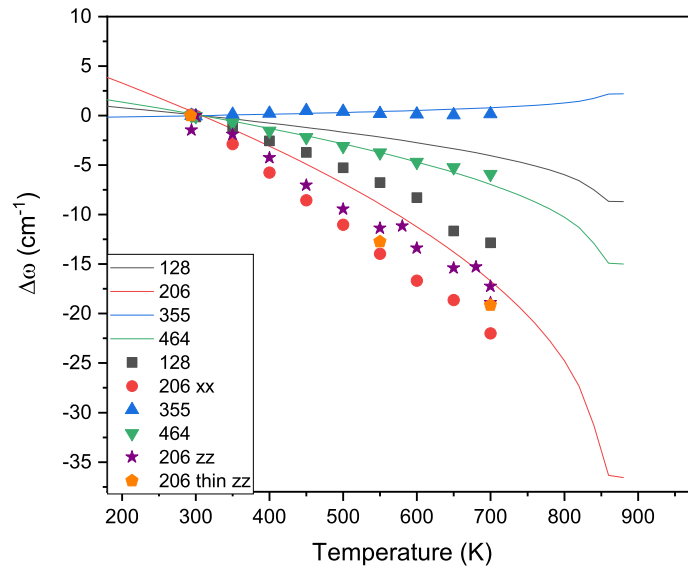
$$\frac{-\Delta\omega^m}{\omega_0^m} = 2\gamma_1^m \varepsilon_1 + \gamma_3^m \varepsilon_3 \quad (7.6)$$

Murri et al. (2019) determined the Grüneisen tensor components from Density Functional Theory (DFT) calculations, obtaining two sets of components employing as reference wavenumbers ω_0 from experiments at 300K and DFT calculations at 0 K (see Table 2 in Murri et al., 2019, for details). The Grüneisen tensor components were tested against experimental wavenumber shifts as a function of temperature using the unit cell parameters determined by Carpenter et al. (1998), identifying three groups of modes (Fig. 8 in Murri et al., 2019). The first group includes modes that have a very good agreement with the trends predicted by the Grüneisen components, which are greater than 0.5. The 464-, 696- 796- cm^{-1} modes are in this first group. The second group has smaller Grüneisen components, around 0.05, and a slightly worse agreement, as the mode at 1161 cm^{-1} . The third group is characterized by modes with Grüneisen components greater than 1, low frequency and poor agreement with the predicted trends also at room temperature, such as the mode at 206 cm^{-1} .

In Figure 7.7 this approach is replicated on the modes at 128, 206, 355, and 464 cm^{-1} , using the unit-cell parameters from Carpenter et al. (1998) and those calculated from the equation of state of quartz by Angel et al. (2017) (Table 8.3) following the procedure described in Alvaro et al. (2020). The reported modes follow the classification described by Murri et al. (2019). In fact, the modes at 128 and 206 cm^{-1} have Grüneisen tensor components greater than 1 and shows a poor agreement with the predictions, whereas the other two modes have Grüneisen tensor components around 0.5 and show a good agreement (Table 2 in Murri et al., 2019). The wavenumber shift from Murri et al. (2019) for the 206- cm^{-1} mode might have a slightly better agreement with the predicted trends, because the subtraction of the baseline from the high temperature spectra might lead to underestimate the temperature effect on this modes. However, a poor agreement with DFT results is expected for this mode because of the complex multi-phonon interactions described above, which cannot be accounted for by *ab initio* calculations.



(a)



(b)

Figure 7.7. Experimental wavenumber changes of the Raman modes at 128, 206, 355, 464 cm^{-1} as a function of temperature; for the 206- cm^{-1} mode data from Murri et al. (2019) and from a thinner quartz cut are reported. Predicted trends calculated from Grüneisen tensor components from Murri et al. (2019) are shown as solid lines. The trend are calculated from unit-cell parameters from Carpenter et al. (1998) (a) and the equation of state of quartz by Angel et al. (2017) (b).

Table 7.2. Temperature dependence of peak positions and FWHM for the 128-, 206-, 355 and 464-cm⁻¹ modes and the 147-cm⁻¹ two-phonon band in the $\bar{z}(xx)z$ scattering geometry. Reported uncertainties are from spectral fitting..

T K	ω cm ⁻¹	FWHM cm ⁻¹								
294	128.37 (3)	4.91 (9)	146 (1)	13 (3)	207.41 (5)	23.5 (1)	355.18 (5)	4.2 (1)	464.859 (6)	7.375 (2)
300	128.24 (3)	5.26 (9)	144.0 (8)	12 (2)	207.27 (5)	25.1 (1)	355.12 (5)	4.5 (1)	464.775 (7)	7.49 (2)
350	127.15 (4)	6.3 (1)	142.7 (8)	13 (2)	204.41 (7)	31.6 (2)	355.31 (5)	4.6 (1)	464.137 (8)	8.76 (2)
400	125.82 (6)	6.3 (2)	130.2 (6)	22 (1)	201.55 (8)	37.1 (2)	355.40 (6)	5.2 (1)	463.322 (10)	9.70 (3)
450	124.65 (8)	6.9 (3)	128.6 (4)	21.1 (9)	198.8 (1)	44.8 (3)	355.67 (7)	5.7 (2)	462.67 (1)	10.79 (4)
500	123.1 (2)	9.3 (4)	133 (2)	15 (3)	196.3 (2)	55.5 (5)	355.6 (1)	6.6 (3)	461.75 (2)	12.34 (6)
550	121.6 (4)	11.2 (5)	132 (2)	14 (4)	193.3 (2)	63.6 (5)	355.4 (1)	7.2 (3)	461.11 (2)	13.74 (6)
600	120.1 (3)	13.3 (5)	131 (1)	10 (3)	190.6 (2)	72.7 (5)	355.3 (1)	8.0 (3)	460.16 (2)	15.16 (6)
650	116.7 (6)	14 (1)	123 (3)	12 (4)	188.7 (2)	82.9 (7)	355.2 (1)	9.0 (4)	459.61 (2)	16.69 (7)
700	115.5 (2)	17.8 (6)	97 (2)	17 (3)	185.3 (2)	90.9 (7)	355.4 (1)	8.4 (3)	458.93 (2)	18.92 (7)
720	114.5 (7)	18 (1)	98 (6)	26 (7)	183.8 (3)	95.2 (8)	354.8 (2)	9.2 (4)	458.47 (3)	20.17 (8)
750	112.9 (6)	18 (2)	97 (6)	30 (6)	182.4 (3)	101.7 (8)	355.0 (2)	9.0 (4)	458.17 (3)	21.10 (8)
770	112.2 (4)	17 (2)	96 (3)	34 (4)	181.3 (4)	104 (1)	354.8 (2)	9.2 (5)	458.16 (3)	22.08 (9)
790	110.9 (4)	17 (2)	93 (3)	37 (4)	179.1 (4)	109 (1)	354.5 (2)	9.4 (6)	458.01 (3)	23.2 (1)
810	109.3 (5)	14 (2)	90 (2)	46 (3)	177.0 (6)	115 (1)	354.5 (3)	10.1 (7)	457.83 (4)	24.5 (1)
830	106.2 (9)	19 (2)	78 (2)	39 (4)	175.6 (5)	122 (1)	354.0 (3)	9 (1)	457.40 (5)	26.3 (2)
840	106.2 (9)	21 (2)	74 (1)	38 (3)	174.9 (5)	123 (1)	353.9 (4)	13 (1)	457.83 (4)	27.2 (1)
850	105 (1)	25 (3)	68 (1)	35 (3)	174.2 (5)	129 (1)	354.8 (4)	10 (1)	457.68 (5)	27.2 (2)
860	102 (1)	22 (4)	58.2 (9)	44 (3)	171.3 (7)	130 (2)	354.3 (6)	11 (1)	458.02 (4)	29.5 (2)
870	0	0	0	0	168.0 (5)	136 (1)	0	0	458.87 (3)	32.6 (3)

Table 7.2 continued from previous page

880	o	o	o	o	167.1 (9)	133 (2)	o	o	458.95 (5)	33.1 (3)
890	o	o	o	o	167.7 (9)	131 (2)	o	o	459.11 (4)	33.0 (3)
900	o	o	o	o	168.2 (8)	133 (2)	o	o	459.24 (4)	33.1 (3)
910	o	o	o	o	169.3 (5)	133 (1)	o	o	459.08 (5)	33.5 (2)
920	o	o	o	o	169.4 (5)	134 (1)	o	o	459.27 (4)	33.5 (3)
930	o	o	o	o	170.7 (5)	133 (1)	o	o	459.42 (5)	34.8 (1)
940	o	o	o	o	169.1 (5)	137 (1)	o	o	459.36 (3)	34.1 (3)
950	o	o	o	o	171.0 (5)	131 (1)	o	o	459.69 (4)	34.5 (2)
1000	o	o	o	o	174.2 (6)	135 (2)	o	o	459.64 (5)	34.6 (4)
1050	o	o	o	o	172.8 (5)	128 (1)	o	o	459.80 (5)	34.6 (3)
1100	o	o	o	o	175.6 (8)	135 (2)	o	o	460.19 (7)	36.3 (4)
1120	o	o	o	o	175.7 (6)	139 (1)	o	o	460.00 (7)	39.8 (2)
1130	o	o	o	o	176.9 (7)	136 (2)	o	o	459.94 (8)	39.3 (3)
1140	o	o	o	o	175.1 (8)	135 (2)	o	o	459.8 (1)	39.2 (4)
1150	o	o	o	o	177 (1)	141 (3)	o	o	460.4 (1)	40.7 (5)
1160	o	o	o	o	179 (1)	141 (3)	o	o	460.4 (1)	40.1 (4)
1170	o	o	o	o	178 (1)	135 (3)	o	o	460.1 (2)	40.2 (5)
1180	o	o	o	o	178 (2)	132 (4)	o	o	460.2 (2)	40.6 (6)
1200	o	o	o	o	180 (1)	127 (4)	o	o	460.6 (2)	41.2 (4)
1250	o	o	o	o	183 (1)	143 (2)	o	o	460.7 (1)	42.6 (4)
1300	o	o	o	o	187 (1)	150 (4)	o	o	461.3 (2)	42 (1)
1350	o	o	o	o	190 (2)	137 (5)	o	o	461.2 (3)	41.5 (9)
1400	o	o	o	o	194 (3)	152 (8)	o	o	462.0 (2)	45.1 (5)

Table 7.3. Temperature dependence of peak positions and FWHM for the 147-cm^{-1} two-phonon band, the 206-, 355 and 464- and 1080-cm^{-1} modes in the $\bar{y}(zz)y$ scattering geometry. Reported uncertainties are from spectral fitting.

T K	ω cm^{-1}	FWHM cm^{-1}								
293	145 (2)	10 (4)	207.33 (6)	23.6 (2)	355.39 (6)	4.7 (1)	464.68 (1)	7.73 (3)	1082.0 (3)	7.5 (5)
550	126.2 (5)	18 (1)	194.6 (2)	65.2 (6)	356.6 (1)	7.9 (3)	460.56 (3)	13.62 (8)	1079.3 (6)	12 (1)
700	110.7 (5)	25 (1)	188.2 (3)	92.1 (1)	357.4 (2)	10.3 (5)	459.66 (4)	21.9 (1)	1077.3 (9)	19 (2)
770	97.8 (5)	36 (1)	185.7 (3)	98.2 (8)	357.6 (1)	10.4 (4)	457.71 (5)	22.3 (1)	1077 (1)	23 (2)
840	76.7 (7)	47 (2)	180.8 (3)	114.6 (9)	357.4 (2)	11.5 (6)	457.11 (6)	25.9 (2)	1072 (2)	33 (4)
850	70.8 (7)	47 (2)	179.6 (3)	118.1 (9)	357.6 (3)	12.5 (7)	457.13 (6)	25.9 (2)	1073 (2)	34 (4)
860	62.9 (9)	50 (2)	178.2 (3)	122.5 (1)	357.5 (3)	12.2 (7)	457.40 (6)	27.7 (2)	1073 (2)	36 (5)
870	o	o	175.0 (3)	133 (1)	o	o	458.58 (8)	31.0 (5)	o	o
875	o	o	174.3 (4)	131 (1)	o	o	458.78 (4)	31.6 (2)	o	o
880	o	o	175.8 (4)	135 (1)	o	o	459.13 (4)	32.4 (2)	o	o
885	o	o	175.3 (4)	133 (1)	o	o	459.01 (4)	32.3 (2)	o	o
890	o	o	175.9 (4)	133 (1)	o	o	459.24 (4)	32.7 (2)	o	o
900	o	o	176.6 (4)	136 (1)	o	o	459.32 (4)	32.9 (2)	o	o
950	o	o	179.1 (4)	136 (1)	o	o	459.59 (5)	34.2 (2)	o	o
1000	o	o	181.7 (4)	137 (1)	o	o	459.85 (5)	35.4 (2)	o	o
1050	o	o	184.2 (4)	138 (1)	o	o	459.86 (5)	35.1 (2)	o	o
1130	o	o	189.0 (4)	140 (2)	o	o	460.33 (8)	36.8 (4)	o	o
1150	o	o	188.6 (4)	139 (1)	o	o	460.41 (6)	37.3 (2)	o	o
1250	o	o	194.3 (4)	148 (1)	o	o	460.82 (8)	37.4 (2)	o	o

Table 7.4. Strains calculated from unit-cell parameters from Carpenter et al. (1998) (A) and from the equation of state of quartz by Angel et al. (2017) (B). The calculated strains show a good agreement, generally between 1 and 3 σ of the uncertainties on the unit-cell parameters reported by Carpenter et al. (1998). A worse agreement is expected below 200K, because of order parameter saturation, as described in Alvaro et al. (2020)..

A			B		
T (K)	ε_1	ε_3	T	ε_1	ε_3
25	-0.00268	-0.00134	25	-0.00342	-0.00263
50	-0.00262	-0.00132	50	-0.00315	-0.00242
75	-0.00250	-0.00128	75	-0.00287	-0.00220
100	-0.00234	-0.00121	100	-0.00259	-0.00198
125	-0.00215	-0.00113	125	-0.00230	-0.00176
150	-0.00192	-0.00102	150	-0.00201	-0.00153
175	-0.00168	-0.00090	175	-0.00171	-0.00130
200	-0.00142	-0.00078	200	-0.00141	-0.00107
225	-0.00113	-0.00062	250	-0.00077	-0.00058
250	-0.00083	-0.00046	298	-0.00014	-0.00010
308	0.00000	0.00000	300	-0.00011	-0.00008
383	0.00105	0.00055	308	0.00000	0.00000
434	0.00189	0.00102	320	0.00017	0.00012
484	0.00279	0.00154	340	0.00045	0.00033
524	0.00354	0.00198	346	0.00053	0.00040
564	0.00432	0.00243	360	0.00073	0.00055
605	0.00519	0.00293	380	0.00103	0.00077
645	0.00616	0.00349	400	0.00133	0.00099
670	0.00709	0.00410	420	0.00164	0.00121
700	0.00777	0.00449	440	0.00196	0.00144
720	0.00832	0.00479	460	0.00229	0.00168
739	0.00891	0.00516	480	0.00262	0.00192
761	0.00957	0.00553	500	0.00297	0.00217
781	0.01029	0.00595	520	0.00333	0.00242
816	0.01210	0.00700	540	0.00370	0.00269
824	0.01270	0.00736	560	0.00409	0.00295
832	0.01343	0.00778	580	0.00449	0.00323
841	0.01454	0.00841	600	0.00491	0.00352
848	0.01667	0.00952	620	0.00535	0.00381
851	0.01692	0.00975	640	0.00581	0.00412
853	0.01694	0.00976	660	0.00629	0.00444
855	0.01695	0.00976	680	0.00681	0.00478
857	0.01697	0.00976	700	0.00736	0.00513

Table 7.4 continued from previous page

859	0.01697	0.00978	720	0.00796	0.00551
861	0.01699	0.00976	740	0.00861	0.00591
866	0.01701	0.00977	760	0.00933	0.00634
871	0.01703	0.00977	780	0.01014	0.00682
876	0.01704	0.00977	800	0.01111	0.00736
881	0.01706	0.00976	820	0.01234	0.00800
			840	0.01430	0.00889
			860	0.01701	0.00980
			880	0.01711	0.00986

REFERENCES

- Alvaro, M., Mazzucchelli, M., Angel, R., Murri, M., Campomenosi, N., Scambelluri, M., Nestola, F., Korsakov, A., Tomilenko, A., Marone, F., & Morana, M. (2020). Fossil subduction recorded by quartz from the coesite stability field. *Geology*, *48*(1), 24–28. <https://doi.org/10.1130/G46617.1>
- Angel, R. J., Alvaro, M., Miletich, R., & Nestola, F. (2017). A simple and generalised p–t–v EoS for continuous phase transitions, implemented in EosFit and applied to quartz. *Contributions to Mineralogy and Petrology*, *172*(5), 29. <https://doi.org/10.1007/s00410-017-1349-x>
- Axe, J. D., & Shirane, G. (1970). Study of the alpha-beta quartz phase transformation by inelastic neutron scattering. *Physical Review B*, *1*(1), 342–348. <https://doi.org/10.1103/PhysRevB.1.342>
- Bates, J. B., & Quist, A. S. (1972). Polarized raman spectra of β -quartz. *The Journal of Chemical Physics*, *56*(4), 1528–1533. <https://doi.org/10.1063/1.1677402>
- Carpenter, M. A., Salje, E. K. H., Graeme-Barber, A., Wruck, B., Dove, M. T., & Knight, K. S. (1998). Calibration of excess thermodynamic properties and elastic constant variations associated with the $\alpha \leftrightarrow \beta$ phase transition in quartz. *American Mineralogist*, *83*(1), 2–22. <https://doi.org/10.2138/am-1998-1-201>
- Cochran, W. (1960). Crystal stability and the theory of ferroelectricity. *Advances in Physics*, *9*(36), 387–423. <https://doi.org/10.1080/00018736000101229>
- Donnay, J., & Le Page, Y. (1978). The vicissitudes of the low-quartz crystal setting or the pitfalls of enantiomorphism. *Acta Crystallographica Section A: Crystal Physics, Diffraction, Theoretical and General Crystallography*, *34*(4), 584–594.
- Etchepare, J., Merian, M., & Smetankine, L. (1974). Vibrational normal modes of SiO₂. I. α and β quartz. *The Journal of Chemical Physics*, *60*(5), 1873–1876. <https://doi.org/10.1063/1.1681287>
- Fries, J., & Claus, R. (1973). Phonon and polariton spectra of β -quartz [eprint: <https://onlinelibrary.wiley.com/doi/pdf/10.1002/jrs.1250010106>]. *Journal of Raman Spectroscopy*, *1*(1), 71–81. <https://doi.org/10.1002/jrs.1250010106>
- Ginzburg, V. (1960). Some remarks on phase transitions of the second kind and the microscopic theory of ferroelectric materials [Fiz. Tverd. Tela, 2, 2031 (1960)]. *Sov. Phys. Solid State*, *1*, 1824.
- Grimm, H., & Dorner, B. (1975). On the mechanism of the $\alpha - \beta$ phase transformation of quartz. *Journal of Physics and Chemistry of Solids*, *36*(5), 407–413. [https://doi.org/10.1016/0022-3697\(75\)90066-9](https://doi.org/10.1016/0022-3697(75)90066-9)
- Kroumova, E., Aroyo, M. I., Perez-Mato, J. M., Kirov, A., Capillas, C., Ivantchev, S., & Wondratschek, H. (2003). Bilbao crystallographic server : Useful databases and tools for phase-transition studies. *Phase Transitions*, *76*(1), 155–170. <https://doi.org/10.1080/0141159031000076110>

- Loudon, R. (1964). The raman effect in crystals. *Advances in Physics*, 13(52), 423–482. <https://doi.org/10.1080/00018736400101051>
- Megaw, H. (1973). Crystal structures. *A working approach, Studies in physics and chemistry*, 10.
- Murri, M., Alvaro, M., Angel, R. J., Prencipe, M., & Mihailova, B. D. (2019). The effects of non-hydrostatic stress on the structure and properties of alpha-quartz. *Physics and Chemistry of Minerals*. <https://doi.org/10.1007/s00269-018-01018-6>
- Salje, E. K. H., Ridgwell, A., Guttler, B., Wruck, B., Dove, M. T., & Dolino, G. (1992). On the displacive character of the phase transition in quartz: A hard-mode spectroscopy study. *Journal of Physics: Condensed Matter*, 4(2), 571–577. <https://doi.org/10.1088/0953-8984/4/2/025>
- Schmidt, C., & Ziemann, M. A. (2000). In-situ Raman spectroscopy of quartz: A pressure sensor for hydrothermal diamond-anvil cell experiments at elevated temperatures. *American Mineralogist*, 85(11), 1725–1734. <https://doi.org/10.2138/am-2000-11-1216>
- Scott, J. F. (1968). Evidence of coupling between one- and two-phonon excitations in quartz. *Physical Review Letters*, 21(13), 907–910. <https://doi.org/10.1103/PhysRevLett.21.907>
- Scott, J. F. (1974). Soft-mode spectroscopy: Experimental studies of structural phase transitions. *Reviews of Modern Physics*, 46(1), 83–128. <https://doi.org/10.1103/RevModPhys.46.83>
- Scott, J. F., & Porto, S. P. S. (1967). Longitudinal and transverse optical lattice vibrations in quartz. *Physical Review*, 161(3), 903–910. <https://doi.org/10.1103/PhysRev.161.903>
- Shapiro, S. M., & Axe, J. D. (1972). Raman scattering from polar phonons. *Physical Review B*, 6(6), 2420–2427. <https://doi.org/10.1103/PhysRevB.6.2420>
- T95 specifications [Linkam scientific]. Retrieved August 12, 2020, from <https://www.linkam.co.uk/t95-specifications>
- TS1200 features [Linkam scientific]. Retrieved August 13, 2020, from <https://www.linkam.co.uk/ts1200>

8 Raman scattering from a quartz inclusion at high temperature

8.1 INTRODUCTION

Quartz has long been studied in different fields because of its structure and properties, such as piezoelectricity (Curie & Curie, 1880) and its polymorphism as a function of pressure and temperature. In fact, it has many possible technological applications being used in resonators, transducers, sensors, processors, and actuators. In Earth science quartz plays an important role, being one of the most common minerals in the crust. As a consequence, the structure and thermoelastic properties of quartz have been thoroughly characterized (e.g. Glinnemann et al., 1992; Hazen et al., 1989; Jorgensen, 1978; Scheidl et al., 2016; Wang et al., 2015). In particular, the α - β phase transition occurs at a temperature, 574 °C, and, being relatively easy to access, has drawn much attention over time, including a lively debate on its nature (e.g. Dove et al., 1999; Salje et al., 1992). Notably, it was also one of the first phase transitions characterized by Raman spectroscopy (Raman & Nedungadi, 1940). In the geological field there is a renewed attention to quartz for its application in elastic geobarometry that allows using the difference in the elastic properties between the host and the inclusion to determine the conditions at which the entrapment occurred. In this context, Raman spectroscopy is often the technique of choice. In fact, in situ Raman spectroscopy can probe small volumes of the samples, thus allowing to: characterize inclusions of dimensions down to a few microns; changes of stress and strain in the inclusion volume in the case of faceted inclusions, whose edges and corners act as stress concentrators (Campomenosi et al., 2018; Mazzucchelli et al., 2018; Murri et al., 2018); and the strain state in the host crystals (Campomenosi et al., 2020). However, there are still few experimental validations of this approach, mainly due to the complexity of performing controlled experiments on host-inclusions systems. A notable example and a major step for the validation of the approach was provided by Bonazzi et al. (2019), who synthesized quartz inclusions in almandine garnet at known pressure and temperature conditions in a piston-cylinder press and were able to back-calculate the entrapment conditions using elastic geobarometry. This study also showed that the determination of inclusion pressures from Raman spectra must be carefully performed taking into account the deviatoric stress developed

in the inclusions. In fact, the change in the Raman peak positions of an inclusion with respect to a free crystal is determined by the strains imposed on it by the host and can be calculated using the phonon-mode Grüneisen tensors proposed by Angel et al. (2019) and Murri et al. (2018). Conversely, the calculation of the entrapments condition performed by hydrostatic calibrations of the Raman shifts of quartz with pressure leads to significant errors in back-calculated entrapment pressures, as shown by Bonazzi et al. (2019). In this chapter, an heating experiment on a natural host-inclusion system, a quartz inclusion in garnet, is described in order to further explore the applicability of elastic geobarometry.

8.2 MATERIALS AND METHODS

A cut from a thin section from the Blåhø garnet-kyanite gneiss microdiamond-bearing garnet-kyanite gneiss in the Blåhø nappe, Fjortoft, Nordøyane archipelago, Norway, was selected for the measurements (Dobrzhinetskaya et al., 1995; Larsen et al., 1998; Liu & Massonne, 2019). The sample dimensions were 400x340x300 μm . The host mineral is garnet, with composition py: 0.33, alm: 0.60, gr: 0.05, sps: 0.02 (Gilio et al., submitted). It contains a large quartz inclusion (60x40 μm), two smaller zircon inclusions, distant approximately 80 and 120 μm , and rutile exolutions.

Polarized Raman spectra were collected with a Horiba Jobin-Yvon T64000 triple-monochromator system equipped with a Symphony LN₂-cooled CCD detector, an Olympus BH41 microscope, and a Coherent Ar⁺ laser. The measurements were performed in backscattering geometry, with a 50x super long working distance objective and an excitation wavelength of 514.532 nm. The spectral resolution was approximately 2 cm^{-1} , while the instrumental precision in the peak positions was 0.35 cm^{-1} . The data collection was conducted on heating from room temperature with a rate of temperature change of 50 K min^{-1} , using a Linkam TS1200 EV-1015 stage, for details on the stage see chapter 7. Spectra were acquired at the center of the inclusion, in the host close to the host-inclusion boundary and away from the inclusion. To account for the Bose-Einstein occupation factor, the intensity of the measured spectra was temperature-corrected using the relation $I = I_{\text{measured}} / [(\exp^{\hbar\omega/k_B T} - 1)^{-1} + 1]$, where \hbar , ω , k_B , and T are the reduced Planck constant, phonon wavenumber, Boltzmann constant, and temperature, respectively. The spectra collected from the host away from the inclusion were subtracted from the inclusion spectra, since the peak positions of the garnet host did not change over the sample. Pseudo-Voigt functions ($PV = qL + (1 - q)G$, where L and G are Lorentzian and Gaussian peak-shape functions) were used to fit the spectra and determine the Raman peak positions ω , full widths at half maximum (FWHMs), and integrated intensities I.

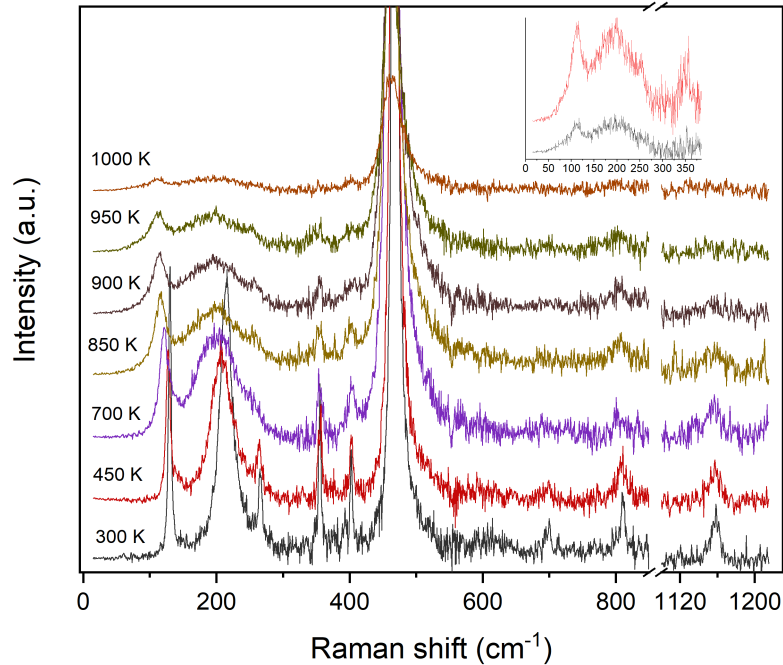


Figure 8.1. Example Raman spectra from the quartz inclusion at various temperatures obtained subtracting the host spectra.

8.3 RESULTS

The major effect of the confinement of the quartz crystal in the host during the heating is the absence of the α - β phase transition. Selected spectra of the quartz inclusion at increasing temperature are reported in figure 8.1 and the inset on the low frequency region of the spectra at 950 and 1000 K clearly shows how the A_1 mode at 355 cm^{-1} persists up to 1000 K. In fact, the 4 A_1 modes of α -quartz transform in one A_1 mode, the mode around 464 cm^{-1} , and three silent B_1 modes. It is well known that the A_1 mode at 206 cm^{-1} does not obey the selection rules (Scott, 1968) and is still present in the β phase, while the other two A_1 modes, at 355 and 1080 cm^{-1} , indeed disappear above the transition temperature (e.g. Bates and Quist, 1972). The absence of the phase transition is not surprising, since the stress imposed on the sample is expected to shift the transition point to higher temperature. In particular, under hydrostatic conditions, the transition temperature increases of approximately $26^\circ\text{C}/100\text{ MPa}$ (Shen et al., 1993 and references therein, Table 8.2). Using the equations of state of the host (Table 8.1) and the inclusion (Table 8.2) it is possible to calculate where the transition point would lie for an inclusion showing a certain remnant pressure P_{inc} when the host is at

Table 8.1. Equation of state parameters for the three garnet endmembers almandine, grossular and pyrope. The model for compression is a Birch-Murnaghan equation of the 3rd order, while the model for the thermal expansion is a Mie-Grüneisen-Debye equation.

	Almandine	Grossular	Pyrope
V_0 (cm ⁻³ /mol)	115.250	125.350	113.130
K_0 (GPa)	175.0	166.9	169.9
K_0'	5.25	5.26	4.43
K_0'' (GPa ⁻¹)	-0.0383	-0.0404	-0.0265
Debye temperature (K)	550	759	650
Atoms per formula unit	20	20	20
γ_0	0.941	1.160	1.190
q	-	0.55	0
α_0 (K ⁻¹)	1.974×10^{-5}	2.040×10^{-5}	2.464×10^{-5}

room temperature and pressure. This pressure can be used to calculate a pressure of entrapment P_{trap} at a given temperature of entrapment T_{trap} , then from the entrapment conditions P_{inc} can be back-calculated at different temperatures. The starting P_{inc} was estimated using three different methods: calculating the strains from the shifts and the quartz elastic tensor, as described in Bonazzi et al. (2019); using the newly developed software *EntraPT* (Mazzucchelli et al., in press); applying a wavenumber shift versus pressure equation obtained from high pressure experiments.

8.3.1 Determination of P_{inc}

As described in Bonazzi et al. (2019), from the Raman shift calculated with respect to a free crystal the strains in the inclusion can be derived from the Grüneisen tensor using the software *Strainman* (Angel et al., 2019). The strains can then be transformed into stress using the elastic tensor of quartz, such as the one provided by Wang et al. (2015), and the pressure is calculated as the mean normal stress. Three calculations were performed starting with different combinations of modes, labeled as 4, 3a and 3b. This approach is summarized in table 8.3, the uncertainties on the pressure are calculated as

$$\delta(\sigma_i^{rel}) = \sum_{j=1}^6 \left(\left(\left(\frac{\delta(C_{ij})}{C_{ij}} \right)^2 + \left(\frac{\delta(\varepsilon_j^{rel})}{\varepsilon_j^{rel}} \right)^2 \right)^{1/2} |C_{ij}\varepsilon_j^{rel}| \right) \quad (8.1)$$

$$\delta(P_{inc}) = \frac{(\delta(\sigma_1^{rel}) + \delta(\sigma_2^{rel}) + \delta(\sigma_3^{rel}))}{3} \quad (8.2)$$

Table 8.2. Equation of state parameters for quartz from (Angel et al., 2017a). The reported properties are not elastic properties of α -quartz but of the so-called bare phase, as defined in Angel et al. (2017a) and Carpenter et al. (1998).

Properties of the bare phase at 298 K, 1 bar	Curved boundary model
V_0	1.0462
K_0 (GPa)	64.3
K_0'	5.07
α_0 (K^{-1})	-0.47×10^{-5}
dK_0/dT (GPa K^{-1})	0.016
Transition parameters	
T_0 (K)	847
dT_{tr}/dP_{tr} (K GPa^{-1})	270
dT_{tr}^2/dP_{tr}^2 (K GPa^{-2})	-10

Table 8.3. Pressure calculated from Raman shift and strains through the Grüneisen tensor. Different combinations of modes are reported, used modes are marked with a star.

	E 128) (cm^{-1})	A_1 206 (cm^{-1})	A_1 355 (cm^{-1})	A_1 464 (cm^{-1})	$\varepsilon_1+\varepsilon_2$	ε_3	P (GPa)
Inc	130.08 (6)	214.7 (1)	355.1 (1)	467.39 (2)			
Ref	128.25 (3)	207.27 (5)	355.12 (5)	464.775 (7)			
4	★	★	★	★	-0.00688(331)	-0.00144(172)	0.30 (14)
3a	★	★	★		-0.00898 (546)	-0.00035 (285)	0.33 (23)
3b	★		★	★	-0.00297 (417)	-0.00331 (208)	0.25 (17)

Table 8.4. Pressure using *EntraPT*. Different combinations of modes are reported, see Table 8.3 for the labels.

Label	P (GPa)
4	0.302 (44)
3a	0.329 (72)
3b	0.246 (58)

Table 8.5. Pressure in GPa from hydrostatic calibrations. Uncertainties were estimated to be of 0.05 GPa by Schmidt and Ziemann (2000), while the uncertainties for Morana et al. (2020) were calculated from the uncertainties on the polynomial coefficients and the instrumental precision in the peak positions of 0.35 cm⁻¹.

Mode	Morana et al. (2020)	Thomas and Spear (2018) and Schmidt and Ziemann (2000)	Morana et al. (2020) up to 2.5 GPa
128	0.25 (13)	0.26	
206	0.41 (6)	0.26	0.32 (4)
464	0.31 (11)	0.29	

A similar approach was used in *EntraPT*, where the calculation was performed starting from the strains, selecting almandine as the host and using the elastic tensor from Wang et al. (2015). The results are reported in Table 8.4.

Finally, the pressure was calculated applying an hydrostatic calibration to the shifts. For the 128-cm⁻¹ mode the equations from Thomas and Spear (2018) and from Morana et al. (2020) were used, for the 206- and 464-cm⁻¹ modes the equations from Schmidt and Ziemann (2000) and Morana et al. (2020) (2,3). The results are reported in table 8.5. Since the results, from Morana et al. (2020) for the 464-cm⁻¹ mode appears overestimated, the data were refitted only up to 2.5 GPa, as in Schmidt and Ziemann (2000), obtaining a more consistent result:

$$P(\text{GPa}) = 0.040(3)\Delta\omega + 0.00038(7)\Delta\omega^2 \quad (8.3)$$

The discrepancy is probably due to the different pressure range: the equation reported by Schmidt and Ziemann (2000) does not take into account and thus cannot reproduce the behavior at higher pressures (Fig. 8.2). As Schmidt and Ziemann (2000) pointed out, also the equation by Liu and Mernagh (1992), which can be used for pressures up to 18.5 GPa, gives pressures for the same frequency shift that are higher by approximately 0.1 GPa.

All the calculations point to a pressure of 0.25 or 0.30 GPa that are the same within uncertainties.

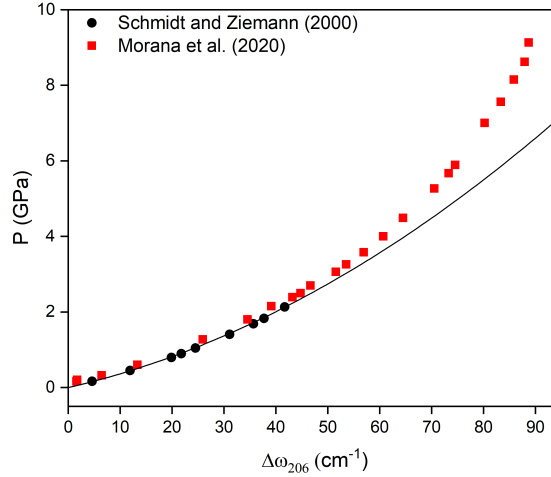


Figure 8.2. Comparison of the pressure range employed in Schmidt and Ziemann (2000) and Morana et al. (2020). The hydrostatic calibration reported by Schmidt and Ziemann (2000) is drawn as a solid line.

Table 8.6. P_{trap} calculated with *EosFitPinc* (Angel et al., 2017b) for almandine, grossular and pyrope using a P_{inc} of 0.3 GPa and T_{trap} of 1000 K.

garnet	P_{trap} (GPa)
Almandine	1.369
Grossular	1.278
Pyrope	1.183

8.3.2 Calculation of the temperature dependence of P_{inc}

Assuming a P_{inc} of 0.30 GPa, a P_{trap} can be calculated at a given T_{trap} (Angel et al., 2017b). A T_{trap} of 1000 K yields the P_{trap} reported in table 8.6 for the three garnet endmembers. The equations of state listed in this chapter are currently in development, since they provide a better fit to recent elasticity data than equations previously published, but the P-V-T relationships are very similar (e.g. Milani et al., 2017). Using different equations of state does not significantly affect the results, due to their similarity.

From the entrapment conditions, P_{inc} can be back calculated at a given temperature to estimate the increase of P_{inc} with temperature and identify the $\alpha - \beta$ transition temperature. This calculation was performed for almandine and pyrope, while grossular gives an intermediate results between the other two endmembers, as suggested by its thermoelastic properties and resulting P_{trap} (Table 8.1 and

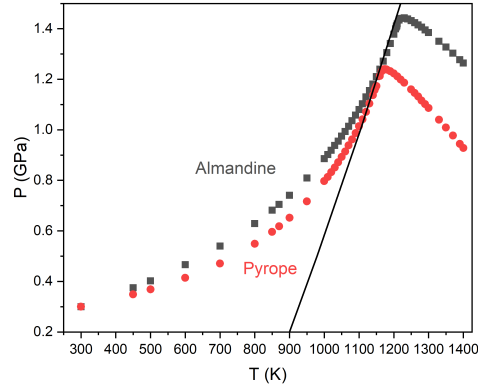


Figure 8.3. P-T diagram for quartz calculated with almandine and pyrope as the host; the solid line represents the α - β phase transition boundary .

8.6). The results are summarized in Table 8.7 and Figure 8.3. From this calculation the phase transition is predicted to occur in the inclusion at 1209 and 1150 K for almandine and pyrope respectively, thus approximately 360 and 300 K above the transition temperature at room pressure.

Table 8.7. P_{inc} variation with temperature.

Almandine		Pyrope	
T (K)	P_{inc} (GPa)	T (K)	P_{inc} (GPa)
300	0.300	300	0.30
450	0.375	450	0.349
500	0.402	500	0.369
600	0.466	600	0.414
700	0.54	700	0.471
800	0.629	800	0.549
850	0.682	850	0.596
870	0.705	870	0.618
900	0.741	900	0.652
950	0.809	950	0.717
1000	0.886	1000	0.797
1010	0.902	1010	0.813
1020	0.919	1020	0.832
1030	0.938	1030	0.851
1040	0.955	1040	0.871
1050	0.975	1050	0.893
1060	0.993	1060	0.914

Table 8.7 continued from previous page

1070	1.014	1070	0.938
1080	1.036	1080	0.962
1090	1.058	1090	0.987
1100	1.08	1100	1.014
1110	1.103	1110	1.041
1120	1.13	1120	1.071
1130	1.155	1130	1.104
1140	1.181	1140	1.137
1150	1.21	1145	1.157
1160	1.24	1147	1.164
1170	1.271	1149	1.171
1180	1.305	1150	1.173
1190	1.341	1160	1.213
1200	1.378	1165	1.231
1205	1.399	1170	1.239
1207	1.407	1175	1.24
1208	1.411	1178	1.239
1209	1.411	1180	1.238
1210	1.419	1190	1.232
1215	1.434	1200	1.223
1220	1.441	1210	1.211
1230	1.443	1220	1.199
1240	1.439	1230	1.186
1250	1.432	1250	1.16
1260	1.424	1260	1.146
1270	1.415	1270	1.132
1280	1.406	1280	1.116
1290	1.395	1290	1.102
1300	1.385	1300	1.086
1330	1.35	1330	1.04
1350	1.327	1350	1.009
1370	1.303	1370	0.977
1390	1.277	1390	0.944
1400	1.264	1400	0.928

8.3.3 *Temperature dependence of Raman peak positions and widths*

The absence of the phase transition confirmed by the temperature dependence of the peak position and FWHMs, as shown in Figure 8.4 and Table 8.9, where the data from the free quartz crystal are also reported for comparison. All Raman

Mode	Free	Inclusion
206	-0.0551(4)	-0.035(2)
464	-0.0144(2)	-0.0120(8)

Table 8.8. Slopes $d\omega/dT$ from the linear fits up to 800 K for the free and trapped quartz.

modes of the inclusion, except the A_1 mode at 355 cm^{-1} that is a hard mode and thus less sensitive to pressure and temperature (e.g. Hemley, 1987; Salje et al., 1992), have higher wavenumbers than the modes from the free quartz at the same temperature, confirming that the inclusion remains under pressure over the entire temperature range of the measurements. From the variation of the peak positions with respect to temperature for the modes at 464 and 206 cm^{-1} (Fig. 8.5) it is clear that we can identify different regimes. The first regime is characterized by linear variation for both the free crystal and the inclusion peak positions, since they are both in the α -phase. However the linear trends of the 464- and 206-cm^{-1} modes have a different slope, as reported in Table 8.8, accounting for the confinement of the inclusion. As it can be expected, being more sensitive to the effect of pressure and temperature, the difference is larger for the 206-cm^{-1} mode.

Approaching the transition, the data from the free quartz show the expected behavior: a minimum in the peak position that corresponds to a maximum in the FWHM. In the case of the quartz inclusion the peak positions are instead clustered around a constant value. The variation of the peak position is clearly associated with a change in the FWHM. In fact, in the same temperature range where the peak positions of the free quartz deviate from the linear trend, the FWHM of the inclusion deviate from the FWHM of the free quartz, which show, in particular for the 464-cm^{-1} mode, an excess in the temperature region corresponding to the reorganization of the structure from the α to the β phase. This excess is missing in the FWHM of the inclusion, thus confirming that the phase transition does not occur in the host-inclusion system. In fact, while the pre-transition and transitions effects are clearly visible in the free quartz data, this is not the case for the inclusion data.

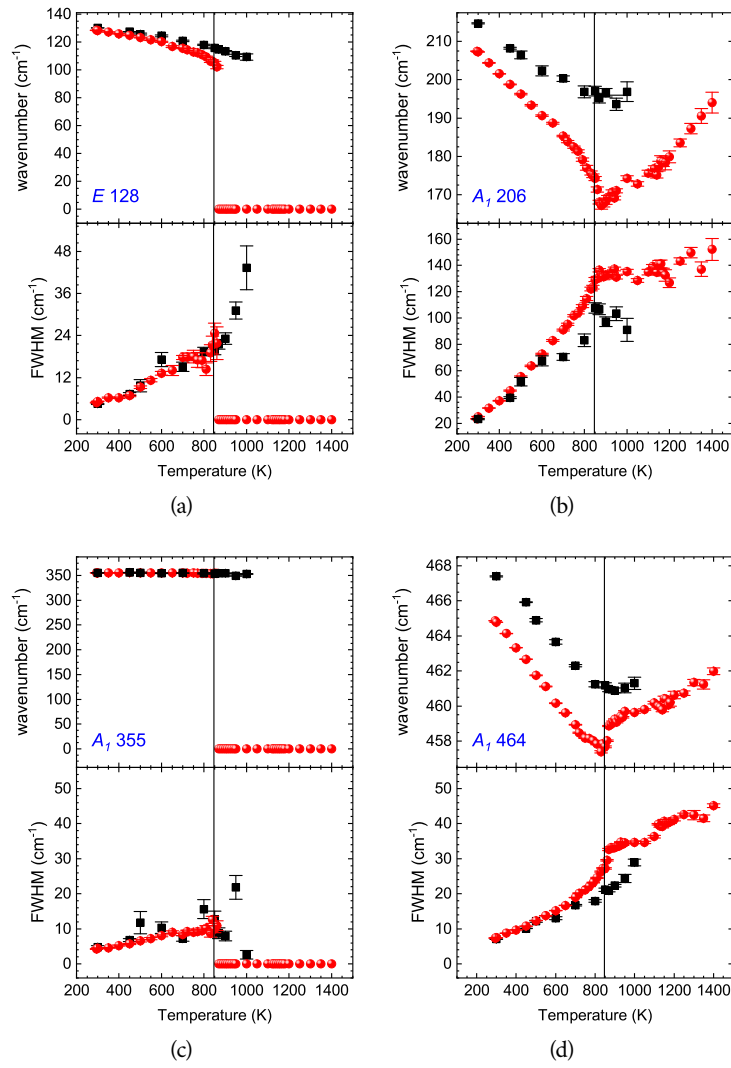
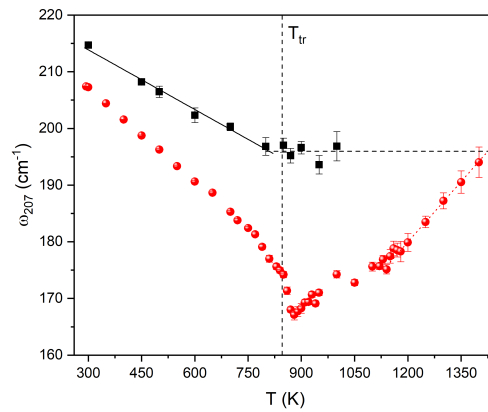
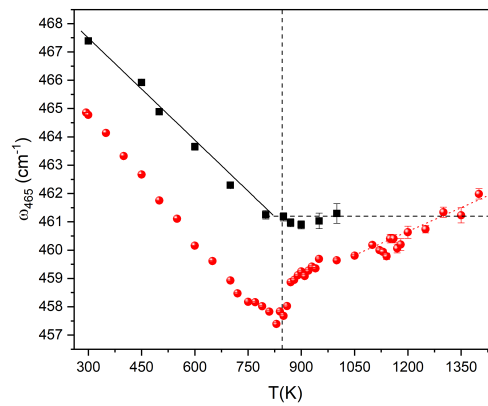


Figure 8.4. Temperature dependence of the peak positions and FWHMs of selected modes for a free (red) and trapped quartz (black) .



(a)



(b)

Figure 8.5. Temperature dependence of the peak positions of the 206- and 464-cm⁻¹ modes in free (red) and trapped quartz (black).

Table 8.9. Temperature dependence of the peak positions and FWHMs of selected modes for the quartz inclusion and a free quartz crystals. Uncertainties are from spectral fitting.

Inclusion								
T (K)	128 ω (cm ⁻¹)	FWHM (cm ⁻¹)	206 ω (cm ⁻¹)	FWHM (cm ⁻¹)	355 ω (cm ⁻¹)	FWHM (cm ⁻¹)	464 ω (cm ⁻¹)	FWHM (cm ⁻¹)
300	130.08 (6)	4.5 (2)	214.7 (1)	23.2 (4)	355.1 (1)	4.8 (4)	467.39 (2)	7.08 (6)
450	127.4 (1)	7.3 (4)	208.2 (2)	39.5 (7)	355.7 (2)	6.9 (4)	465.92 (3)	10.12 (9)
500	125.7 (6)	10 (1)	206 (1)	52 (3)	355 (1)	12 (3)	464.89 (9)	12.2 (3)
600	124.4 (7)	17 (2)	202 (1)	67 (4)	354.5 (6)	10 (1)	463.6 (1)	13.1 (4)
700	120.9 (5)	15 (1)	200.3 (7)	70 (2)	355.1 (3)	7.2 (8)	462.29 (7)	16.7 (2)
800	117.9 (4)	19 (1)	197 (2)	83 (5)	354.3 (9)	16 (3)	461.2 (1)	17.9 (4)
850	115.7 (4)	19 (1)	197 (1)	108 (4)	354.1 (8)	13 (2)	461.2 (1)	21.1 (4)
870	114.5 (5)	21 (1)	195 (1)	107 (4)	354.5 (5)	9 (1)	461.0 (1)	20.9 (4)
900	113.4 (5)	23 (1)	197 (1)	97 (4)	354.6 (6)	8 (1)	460.9 (1)	22.3 (3)
950	110.3 (8)	31 (2)	194 (1)	103 (5)	350 (1)	22 (3)	461.0 (3)	24 (1)
1000	109 (2)	43 (6)	197 (3)	91 (9)	352.9 (7)	3 (1)	461.3 (3)	28.9 (9)
Free crystal								
T (K)	128 ω (cm ⁻¹)	FWHM (cm ⁻¹)	206 ω (cm ⁻¹)	FWHM (cm ⁻¹)	355 ω (cm ⁻¹)	FWHM (cm ⁻¹)	464 ω (cm ⁻¹)	FWHM (cm ⁻¹)
294	128.37 (3)	4.91 (9)	207.41 (5)	23.4 (1)	355.18 (5)	4.2 (1)	464.859 (6)	7.37 (2)
300	128.25 (3)	5.26 (7)	207.27 (5)	25.1 (1)	355.12 (5)	4.5 (1)	464.775 (7)	7.49 (2)
350	127.15 (4)	6.3 (1)	204.41 (7)	31.6 (2)	355.31 (5)	4.6 (1)	464.137 (7)	8.76 (5)
400	125.82 (6)	6.3 (2)	201.55 (8)	37.1 (1)	355.40 (6)	5.2 (1)	463.322 (10)	9.70 (3)
450	124.65 (8)	6.9 (3)	198.7 (1)	44.8 (3)	355.67 (7)	5.7 (2)	462.67 (1)	10.79 (4)

Table 8.9 continued from previous page

500	123.1 (2)	9.3 (4)	196.3 (2)	55.5 (5)	355.6 (1)	6.6 (3)	461.75 (2)	12.34 (6)
550	121.6 (5)	11.2 (5)	193.3 (2)	63.6 (5)	355.4 (1)	7.2 (3)	461.11 (2)	13.74 (6)
600	120.1 (3)	13.3 (5)	190.6 (2)	72.7 (5)	355.3 (1)	8.0 (3)	460.16 (2)	15.16 (6)
650	116.7 (6)	14 (1)	188.7 (2)	82.9 (7)	355.2 (1)	9.0 (4)	459.61 (2)	16.69 (7)
700	115.5 (2)	17.8 (6)	185.3 (2)	90.9 (7)	355.4 (1)	8.4 (3)	458.93 (2)	18.92 (7)
720	114.5 (7)	18 (1)	183.8 (3)	95.2 (8)	354.8 (2)	9.2 (4)	458.47 (3)	20.17 (8)
750	112.9 (6)	18 (1)	182.4 (3)	101.7 (8)	355.0 (2)	9.0 (4)	458.17 (3)	21.10 (8)
770	112.2 (4)	17 (2)	181.3 (4)	104 (1)	354.8 (2)	9.2 (5)	458.16 (3)	22.08 (9)
790	110.9 (4)	17 (2)	179.1 (4)	109 (1)	354.5 (2)	9.4 (6)	458.01 (3)	23.2 (1)
810	109.3 (5)	14 (1)	177.0 (6)	115 (1)	354.5 (3)	10.1 (7)	457.83 (4)	24.5 (1)
830	106.2 (9)	19 (2)	175.6 (5)	122 (1)	354.0 (4)	9 (1)	457.39 (5)	26.3 (2)
840	106.2 (9)	21 (2)	174.9 (5)	123 (1)	353.9 (4)	13 (1)	457.83 (4)	27.2 (1)
850	105 (1)	25 (3)	174.2 (6)	129 (1)	354.8 (4)	10 (1)	457.68 (5)	27.2 (2)
860	102 (1)	22 (5)	171.3 (7)	130 (2)	354.3 (6)	11 (1)	458.02 (4)	29.5 (2)
870	0	0	168.1 (5)	136 (1)	0	0	458.87 (3)	32.6 (3)
880	0	0	167.1(9)	133 (2)	0	0	458.95 (5)	33.1 (3)
890	0	0	167.7 (9)	131 (2)	0	0	459.11 (4)	33.0 (3)
900	0	0	168.2 (8)	133 (2)	0	0	459.24 (4)	33.1 (3)
910	0	0	169.3 (8)	133 (1)	0	0	459.08 (5)	33.5 (2)
920	0	0	169.4 (5)	134 (1)	0	0	459.27 (4)	33.5 (3)
930	0	0	170.7 (5)	133 (1)	0	0	459.42 (4)	34.8 (1)
940	0	0	169.1 (5)	137 (1)	0	0	459.36 (3)	34.1 (3)
950	0	0	171.0 (5)	131 (1)	0	0	459.69 (4)	34.5 (3)
1000	0	0	174.2 (6)	135 (2)	0	0	459.64 (5)	34.6 (4)
1050	0	0	172.8 (5)	128 (1)	0	0	459.80 (5)	34.6 (3)

Table 8.9 continued from previous page

1100	o	o	175.6 (8)	135 (2)	o	o	460.19 (5)	36.3 (3)
1120	o	o	175.7 (6)	139 (1)	o	o	460.00 (7)	39.8 (2)
1130	o	o	176.9 (7)	136 (2)	o	o	459.94 (8)	39.3 (4)
1140	o	o	175.1 (8)	135 (3)	o	o	459.8 (1)	39.2 (3)
1150	o	o	177 (1)	141 (3)	o	o	460.4 (1)	40.7 (5)
1160	o	o	179 (1)	141 (3)	o	o	460.4 (1)	40.1 (4)
1170	o	o	178 (1)	135 (3)	o	o	460.1 (1)	40.2 (5)
1180	o	o	178 (1)	132 (4)	o	o	460.2 (2)	40.6 (6)
1200	o	o	180 (2)	127 (4)	o	o	460.6 (2)	41.2 (4)
1250	o	o	183 (1)	143 (2)	o	o	460.7 (1)	42.6 (4)
1300	o	o	187 (1)	150 (4)	o	o	461.3 (2)	42 (1)
1350	o	o	190 (1)	137 (5)	o	o	461.2 (3)	41.5 (9)
1400	o	o	194 (1)	152 (8)	o	o	462.0 (2)	45.1 (5)

8.4 DISCUSSION

In principle it is possible to describe the variation of the wavenumber shift of a mode i with pressure and temperature as:

$$\Delta\omega_i = (\Delta\omega_P)_i + (\Delta\omega_T)_i + (\Delta\omega_{PT})_i \quad (8.4)$$

where $(\Delta\omega_P)_i$ is the temperature-independent pressure contribution, $(\Delta\omega_T)_i$ is the pressure-independent temperature contribution, and $(\Delta\omega_{PT})_i$ is a cross-term (Gillet et al., 1990; Schmidt & Ziemann, 2000). Assuming that the cross term is negligible, $\Delta\omega_i$ is given by the sum of the pressure and temperature contribution. Thus, in the limit of isotropic stress, $\Delta\omega_i$ can be obtained by adding the $(\Delta\omega_T)_i$ calculated from a function describing the trends in the free quartz data and the $(\Delta\omega_P)_i$ from a $(\Delta\omega_P)_i$ vs pressure curve from hydrostatic experiments. The predictions of the model can then be compared with the experimental data to understand whether it is able to reproduce the observed trends. The data from the free quartz for the 128-, 206-, and 464-cm⁻¹ modes were fitted with a polynomial up to 860 and 880 K for the 128- and 206-, 464-cm⁻¹ modes respectively, while the pressure contribution was calculated from the equations reported in Morana et al. (2020). The results are summarized in Table 8.10 and Figure 8.6, where the predicted $\Delta\omega_i$ are plotted alongside the inclusion data.

From the graphs, it is clear that the predictions are able to reproduce the data only up to a relatively low temperature, approximately 600 K. The worst agreement is shown by the 206-cm⁻¹ mode. This is not surprising, since this mode is the most sensitive to both temperature and pressure, and the cross term is significantly different from zero (Schmidt & Ziemann, 2000). The difference between the prediction and the experimental data might be due to the fact that the model used for the temperature contribution includes pre-transition effects, that are not present in the first region of the inclusion data, when they show a linear trend. In order to exclude the pre-transition effects, $(\Delta\omega_T)_{464}$ was fitted with a line only up to 600 K:

$$(\Delta\omega_T)_{464} = 4.5(1) - 0.015(3)T \quad (8.5)$$

A new model was then calculated with the new temperature contribution, as reported in Table 8.11 and Figure 8.7, for the 464-cm⁻¹ mode. The agreement between the prediction and the experimental data is slightly better, but the model is still not able to reproduce the experimental trends above 600 K.

Table 8.10. Calculated $(\Delta\omega)_i$ for the 128-, 206-, and 464-cm⁻¹ modes.

T (K)	P_{inc} (GPa)	$(\Delta\omega_P)_{128}$	$(\Delta\omega_T)_{128}$	$(\Delta\omega)_{128}$	$(\Delta\omega_P)_{206}$	$(\Delta\omega_T)_{206}$	$(\Delta\omega)_{206}$	$(\Delta\omega_P)_{464}$	$(\Delta\omega_T)_{464}$	$(\Delta\omega)_{464}$
Almandine										
300	0.300	1.983	-0.067	1.917	7.424	-0.617	6.807	2.728	-0.039	2.689
450	0.375	2.462	-3.507	-1.045	9.184	-9.283	-0.099	3.4	-2.245	1.155
500	0.402	2.632	-5.146	-2.514	9.809	-12.416	-2.607	3.641	-2.921	0.72
600	0.466	3.033	-8.312	-5.28	11.271	-17.98	-6.71	4.211	-4.49	-0.28
700	0.54	3.49	-11.826	-8.336	12.929	-23.266	-10.338	4.866	-6.14	-1.274
800	0.629	4.031	-17.788	-13.757	14.877	-30.991	-16.114	5.649	-7.035	-1.387
850	0.682	4.349	-22.815	-18.466	16.014	-37.22	-21.207	6.112	-6.758	-0.645
870	0.705				16.502	-40.398	-23.896	6.313	-6.437	-0.124
Grossular										
300	0.300	1.983	-0.067	1.917	7.424	-0.617	6.807	2.728	-0.039	2.689
450	0.370	2.430	-3.507	-1.077	9.068	-9.283	-0.215	3.356	-2.245	1.110
500	0.394	2.582	-5.146	-2.564	9.624	-12.416	-2.791	3.57	-2.921	0.649
600	0.450	2.933	-8.312	-5.379	10.908	-17.98	-7.073	4.069	-4.49	-0.422
700	0.517	3.349	-11.826	-8.477	12.417	-23.266	-10.849	4.663	-6.14	-1.478
800	0.601	3.862	-17.788	-13.926	14.269	-30.991	-16.721	5.403	-7.035	-1.632
850	0.652	4.17	-22.815	-18.646	15.372	-37.22	-21.848	5.85	-6.758	-0.907
870	0.673				15.822	-40.398	-24.576	6.034	-6.437	-0.403
Pyrope										
300	0.300	1.983	-0.067	1.917	7.424	-0.617	6.807	2.728	-0.039	2.689
450	0.349	2.296	-3.507	-1.211	8.578	-9.283	-0.705	3.168	-2.245	0.922

Table 8.10 continued from previous page

500	0.369	2.424	-5.146	-2.722	9.045	-12.416	-3.371	3.347	-2.921	0.426
600	0.414	2.708	-8.312	-5.605	10.085	-17.98	-7.895	3.748	-4.49	-0.742
700	0.471	3.064	-11.826	-8.762	11.384	-23.266	-11.882	4.255	-6.14	-1.885
800	0.549	3.545	-17.788	-14.243	13.128	-30.991	-17.863	4.945	-7.035	-2.09
850	0.596	3.832	-22.815	-18.984	14.16	-37.22	-23.06	5.359	-6.758	-1.399
870	0.618				14.639	-40.398	-25.759	5.552	-6.437	-0.885

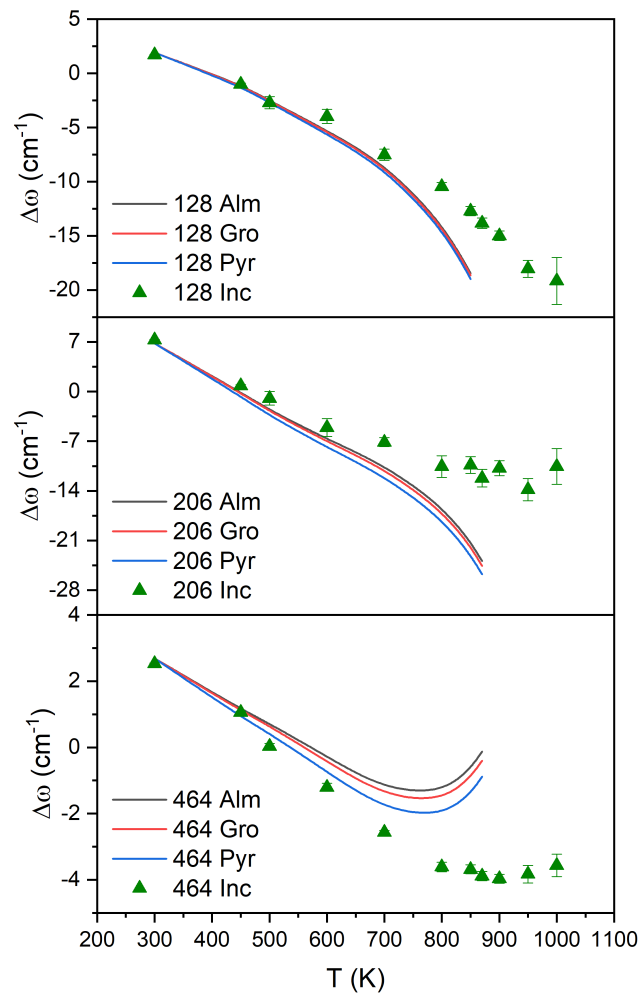
Figure 8.6. Comparison between the calculated $\Delta\omega_i$ and the inclusion data.

Table 8.11. Calculated $(\Delta\omega)_{464}$ with a linear temperature contribution.

T (K)	P_{inc} (GPa)	$(\Delta\omega_P)_{464}$	$(\Delta\omega_T)_{464}$	$(\Delta\omega)_{464}$
Almandine				
300	0.300	2.728	-0.027	2.701
450	0.375	3.400	-2.307	1.094
500	0.402	3.641	-3.067	0.575
600	0.466	4.211	-4.587	-0.376
700	0.540	4.866	-6.107	-1.241
800	0.629	5.649	-7.627	-1.978
850	0.682	6.112	-8.387	-2.274
870	0.705	6.313	-8.691	-2.378
900	0.741	6.626	-9.147	-2.520
950	0.809	7.216	-9.907	-2.690
1000	0.886	7.880	-10.667	-2.786
Grossular				
300	0.300	2.728	-0.027	2.701
450	0.370	3.356	-2.307	1.049
500	0.394	3.570	-3.067	0.503
600	0.450	4.069	-4.587	-0.518
700	0.517	4.663	-6.107	-1.444
800	0.601	5.403	-7.627	-2.224
850	0.652	5.850	-8.387	-2.537
870	0.673	6.034	-8.691	-2.657
900	0.708	6.339	-9.147	-2.807

Table 8.11 continued from previous page

950	0.775	6.922	-9.907	-2.985
1000	0.852	7.588	-10.667	-3.079
Pyrope				
300	0.300	2.728	-0.027	2.701
450	0.349	3.168	-2.307	0.861
500	0.369	3.347	-3.067	0.280
600	0.414	3.748	-4.587	-0.838
700	0.471	4.255	-6.107	-1.852
800	0.549	4.945	-7.627	-2.682
850	0.596	5.359	-8.387	-3.028
870	0.618	5.552	-8.691	-3.139
900	0.652	5.850	-9.147	-3.297
950	0.717	6.418	-9.907	-3.489
1000	0.797	7.112	-10.667	-3.554

8.5 CONCLUSIONS

From the above discussion, it is clear that models based on isotropic stress are not able to reproduce the experimental data from the inclusion. The disagreement could be due to different effects. One first effect to consider is the dependence of $(\partial\omega/\partial P)$ upon temperature. However, Schmidt and Ziemann (2000) could determine a constant isotherm slope, at least for the 464-cm^{-1} mode and for temperature between 100 and $560\text{ }^{\circ}\text{C}$, quasi-linear up 1.1 GPa. Additionally, to obtain the measured shift at 800 K would require a $(\partial\omega/\partial P)$ of approximately $6\text{ cm}^{-1}/\text{GPa}$, while the experimentally determined slope by Schmidt and Ziemann (2000) is $9.0(5)\text{ cm}^{-1}/\text{GPa}$ (Fig 8.8).

Another possible cause of disagreement between the model and the experimental data might be the composition of the garnet. However, the difference between the P_{inc} and the resulting shifts for different endmembers is small. Additionally, temperature-induced changes in the host can be excluded. In fact, up to 1000 K the most intense peak of garnet, the A_{1g} mode at $\sim 920\text{ cm}^{-1}$, shows the expected behavior (Fig. 8.9a), with the peak position decreasing linearly upon heating (Gillet et al., 1992).

When heating from 1000 to 1050 K, the sample unexpectedly jumped and it was not possible to continue the measurement. The sample was cooled down to room temperature and heated again, but in this second run the sample jumped at 1150 K and broke into pieces; it was possible to recover only a fragment of the garnet host. The spectra at room temperature for run 1 and 2 show that the host-inclusion system was not altered by the first heating, while the recovered garnet after run 2 has a distinctly different spectrum (Fig. 8.9b). The additional peaks are attributed to nanocrystalline hematite, that was reported to form in almandine upon heating (Zboril et al., 2004). In the recovered fragment, the most intense peak in the garnet host is shifted from $920.05(3)\text{ cm}^{-1}$ to $918.07(7)\text{ cm}^{-1}$, reflecting the oxidation of Fe^{+2} to Fe^{+3} . Similar macroscopic effects such as jumping are observed in single crystals and are called dynamic effects (for a recent review see Naumov et al., 2020). In particular, the thermosalient effect is defined as the propensity of a crystal to jump, sometimes to heights of several times its size, when heated over a phase transition, and it is usually accompanied by a large and anisotropic change in the cell volume (Panda et al., 2014; Sahoo et al., 2013; Skoko et al., 2010). Jumping has never been reported so far for an host-inclusions system, where it might be the result of the difference in elastic properties upon heating of the two members of the pair, in particular, when the quartz inclusion approaches the phase transition, that is hindered by the confinement within the host, resulting in the jump and breakage of the system. Furthermore, a too high heating rate would not justify the disagreement between the model and the experimental data. The fact that the isotropic model is not able to reproduce the data trends suggests that the anisotropy of the system has to be taken into account. In fact, the quartz

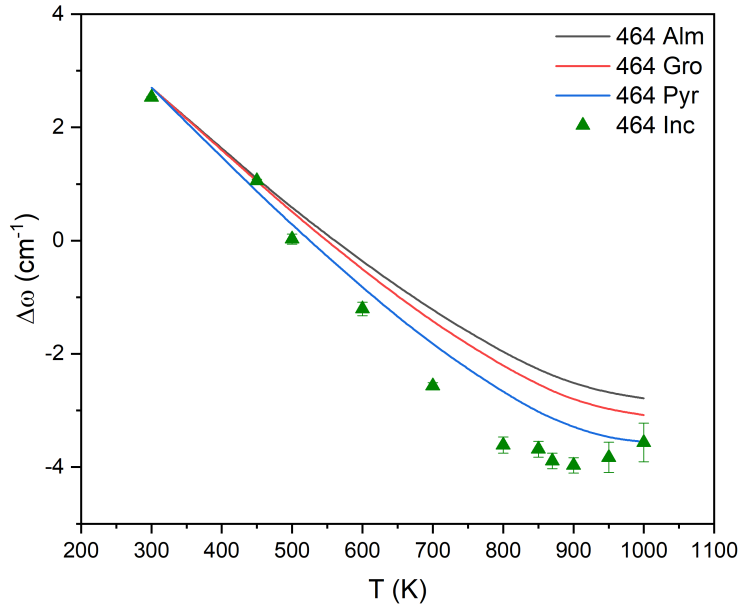


Figure 8.7. Comparison between the calculated $\Delta\omega_{464}$ not including pre-transition effects and the inclusion data.

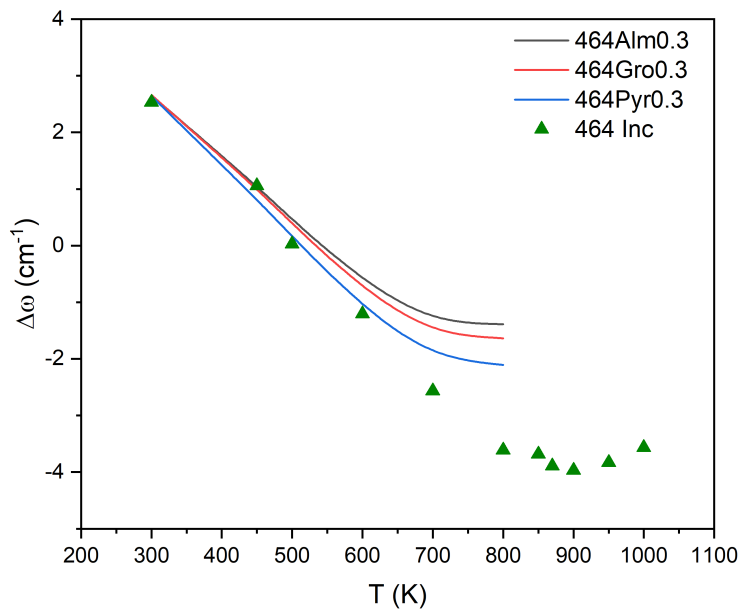


Figure 8.8. Comparison between the $\Delta\omega_i$ calculated with the isotherm slope from Schmidt and Ziemann (2000) and the inclusion data.

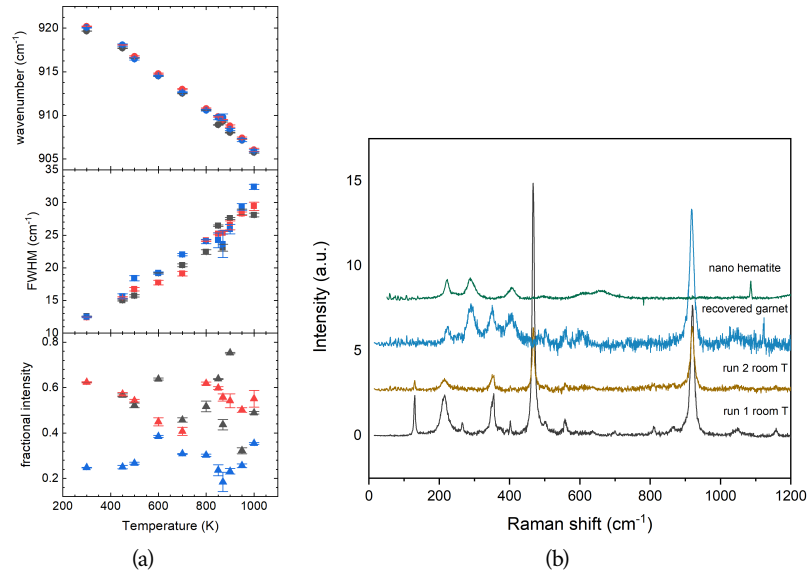


Figure 8.9. (a) Temperature dependence of peak positions, widths and fractional intensities of the A_{1g} mode of garnet at $\sim 920 \text{ cm}^{-1}$ (b) Spectra at room temperature before run 1 and run 2 and spectrum of the recovered garnet fragment after run 2. A spectrum of nanocrystalline hematite is reported for reference.

inclusion is subject to isotropic strains imposed by the host garnet and being elastically anisotropic develops deviatoric stresses. Furthermore, the shift of the α - β phase transition to higher temperature under high pressure appears to be sensitive to the stress state. Uniaxial compression perpendicular and parallel to the c axis raises the temperature of $10.6(4)^\circ\text{C}/100 \text{ MPa}$ and $5.0(4)^\circ\text{C}/\text{kb}$, respectively (Coe & Paterson, 1969), whereas it increases of approximately of $26^\circ\text{C}/100 \text{ MPa}$ (Shen et al., 1993) under hydrostatic conditions. Thus, to answer to these open questions a new anisotropic model must be developed and this study could be compared with the characterizations of different inclusions, such as zircon, that have phase transitions or undergo melting at higher temperatures.

REFERENCES

- Angel, R. J., Alvaro, M., Miletich, R., & Nestola, F. (2017a). A simple and generalised p - t - v EoS for continuous phase transitions, implemented in EoSFit and applied to quartz. *Contributions to Mineralogy and Petrology*, 172(5), 29. <https://doi.org/10.1007/s00410-017-1349-x>

- Angel, R. J., Mazzucchelli, M. L., Alvaro, M., & Nestola, F. (2017b). EosFit-Pinc: A simple GUI for host-inclusion elastic thermobarometry. *American Mineralogist*, 102(9), 1957–1960.
- Angel, R. J., Murri, M., Mihailova, B., & Alvaro, M. (2019). Stress, strain and Raman shifts. *Zeitschrift für Kristallographie - Crystalline Materials*, 234(2), 129–140. <https://doi.org/10.1515/zkri-2018-2112>
- Bates, J. B., & Quist, A. S. (1972). Polarized raman spectra of β -quartz. *The Journal of Chemical Physics*, 56(4), 1528–1533. <https://doi.org/10.1063/1.1677402>
- Bonazzi, M., Tumiati, S., Thomas, J. B., Angel, R. J., & Alvaro, M. (2019). Assessment of the reliability of elastic geobarometry with quartz inclusions. *Lithos*, 350–351, 105201. <https://doi.org/10.1016/j.lithos.2019.105201>
- Campomenosi, N., Mazzucchelli, M. L., Mihailova, B. D., Angel, R. J., & Alvaro, M. (2020). Using polarized raman spectroscopy to study the stress gradient in mineral systems with anomalous birefringence. *Contributions to Mineralogy and Petrology*, 175(2), 16. <https://doi.org/10.1007/s00410-019-1651-x>
- Campomenosi, N., Mazzucchelli, M. L., Mihailova, B., Scambelluri, M., Angel, R. J., Nestola, F., Reali, A., & Alvaro, M. (2018). How geometry and anisotropy affect residual strain in host-inclusion systems: Coupling experimental and numerical approaches [Publisher: De Gruyter Section: American Mineralogist]. *American Mineralogist*, 103(12), 2032–2035. <https://doi.org/10.2138/am-2018-6700CCBY>
- Carpenter, M. A., Salje, E. K. H., Graeme-Barber, A., Wruck, B., Dove, M. T., & Knight, K. S. (1998). Calibration of excess thermodynamic properties and elastic constant variations associated with the $\alpha \leftrightarrow \beta$ phase transition in quartz. *American Mineralogist*, 83(1), 2–22. <https://doi.org/10.2138/am-1998-1-201>
- Coe, R. S., & Paterson, M. S. (1969). The $\alpha - \beta$ inversion in quartz: A coherent phase transition under nonhydrostatic stress. *Journal of Geophysical Research*, 74(20), 4921–4948. <https://doi.org/10.1029/JB074i020p04921>
- Curie, J., & Curie, P. (1880). Développement par compression de l'électricité polaire dans les cristaux hémihédres à faces inclinées. *Bulletin de minéralogie*, 3(4), 90–93.
- Dobrzhinetskaya, L. F., Eide, E. A., Larsen, R. B., Sturt, B. A., Trønnes, R. G., Smith, D. C., Taylor, W. R., & Posukhova, T. V. (1995). Microdiamond in high-grade metamorphic rocks of the western gneiss region, norway. *Geology*, 23(7), 597–600.
- Dove, M. T., Gambhir, M., & Heine, V. (1999). Anatomy of a structural phase transition: Theoretical analysis of the displacive phase transition in quartz and other silicates. *Physics and Chemistry of Minerals*, 26(4). <https://doi.org/10.1007/s002690050194>

- Gilio, M., Scambelluri, M., Angel, R. J., & Alvaro, M. (submitted). The contribution of elastic geobarometry to the controversy of HP vs. UHP metamorphism. *Earth and Planetary Science Letters*.
- Gillet, P., Cléac'h, A. L., & Madon, M. (1990). High-temperature Raman spectroscopy of SiO₂ and GeO₂ polymorphs: Anharmonicity and thermodynamic properties at high-temperatures. *Journal of Geophysical Research: Solid Earth*, 95, 21635–21655. <https://doi.org/10.1029/JB095iB13p21635>
- Gillet, P., Fiquet, G., Malézieux, J. M., & Geiger, C. A. (1992). High-pressure and high-temperature Raman spectroscopy of end-member garnets: Pyrope, grossular and andradite. *European Journal of Mineralogy*, 4(4), 651–664. <https://doi.org/10.1127/ejm/4/4/0651>
- Glinnemann, J., King, H. E., Schulz, H., & Dacol, F. (1992). Crystal structures of the low-temperature quartz-type phases of SiO₂ and GeO₂ at elevated pressure. *Zeitschrift für Kristallographie - Crystalline Materials*, 198, 177–212.
- Hazen, R. M., Finger, L. W., Hemley, R. J., & Mao, H. K. (1989). High-pressure crystal chemistry and amorphization of α -quartz. *Solid State Communications*, 72(5), 507–511. [https://doi.org/10.1016/0038-1098\(89\)90607-8](https://doi.org/10.1016/0038-1098(89)90607-8)
- Hemley, R. J. (1987). Pressure dependence of Raman spectra of SiO₂ polymorphs: α -quartz, coesite, and stishovite. In M. H. Manghnani & Y. Syono (Eds.), *Geophysical monograph series* (pp. 347–359). American Geophysical Union. <https://doi.org/10.1029/GM039p0347>
- Jorgensen, J. D. (1978). Compression mechanisms in α -quartz structures—SiO₂ and GeO₂. *Journal of Applied Physics*, 49(11), 5473–5478. <https://doi.org/10.1063/1.324517>
- Larsen, R. B., Eide, E. A., & Burke, E. A. (1998). Evolution of metamorphic volatiles during exhumation of microdiamond-bearing granulites in the western gneiss region, Norway. *Contributions to Mineralogy and Petrology*, 133(1–2), 106–121.
- Liu, L.-G., & Mernagh, T. P. (1992). High-pressure Raman study of the α -quartz forms of SiO₂ and GeO₂ at room temperature. *High Temperatures. High Pressures (Print)*, 24(1), 13–21.
- Liu, P., & Massonne, H.-J. (2019). An anticlockwise P–T–t path at high-pressure, high-temperature conditions for a migmatitic gneiss from the island of fjørtoft, Western Gneiss Region, Norway, indicates two burial events during the Caledonian orogeny. *Journal of Metamorphic Geology*, 37(4), 567–588.
- Mazzucchelli, M. L., Burnley, P., Angel, R. J., Morganti, S., Domeneghetti, M. C., Nestola, F., & Alvaro, M. (2018). Elastic geothermobarometry: Corrections for the geometry of the host-inclusion system [Publisher: GeoScience-World]. *Geology*, 46(3), 231–234. <https://doi.org/10.1130/G39807.1>

- Mazzucchelli, M. L., Angel, R. J., & Alvaro, M. (in press). EntraPT: An online platform for elastic geobarometry. *American Mineralogist*. <https://doi.org/10.2138/am-2021-7693CCBYNCND>
- Milani, S., Angel, R. J., Scandolo, L., Mazzucchelli, M. L., Ballaran, T. B., Klemme, S., Domeneghetti, M. C., Miletich, R., Scheidl, K. S., Derzsi, M., Tokár, K., Prencipe, M., Alvaro, M., & Nestola, F. (2017). Thermo-elastic behavior of grossular garnet at high pressures and temperatures [Publisher: GeoScienceWorld]. *American Mineralogist*, 102(4), 851–859. <https://doi.org/10.2138/am-2017-5855>
- Morana, M., Mihailova, B., Angel, R. J., & Alvaro, M. (2020). Quartz metastability at high pressure: What new can we learn from polarized Raman spectroscopy? *Physics and Chemistry of Minerals*, 47(8), 34. <https://doi.org/10.1007/s00269-020-01100-y>
- Murri, M., Mazzucchelli, M. L., Campomenosi, N., Korsakov, A. V., Prencipe, M., Mihailova, B. D., Scambelluri, M., Angel, R. J., & Alvaro, M. (2018). Raman elastic geobarometry for anisotropic mineral inclusions. *American Mineralogist*, 103(11), 1869–1872. <https://doi.org/10.2138/am-2018-6625CCBY>
- Naumov, P., Karothu, D. P., Ahmed, E., Catalano, L., Commins, P., Mahmoud Halabi, J., Al Handawi, M., & Li, L. (2020). The rise of the dynamic crystals [Published online]. *Journal of the American Chemical Society*. <https://doi.org/10.1021/jacs.0c05440>
- Panda, M. K., Runčevski, T., Sahoo, S. C., Belik, A. A., Nath, N. K., Dinnebier, R. E., & Naumov, P. (2014). Colossal positive and negative thermal expansion and thermosalient effect in a pentamorphic organometallic martensite. *Nature communications*, 5(1), 1–8.
- Raman, C. V., & Nedungadi, T. M. K. (1940). The $\alpha - \beta$ transformation of quartz [Number: 3665 Publisher: Nature Publishing Group]. *Nature*, 145(3665), 147–147. <https://doi.org/10.1038/145147a0>
- Sahoo, S. C., Panda, M. K., Nath, N. K., & Naumov, P. (2013). Biomimetic crystalline actuators: Structure–kinematic aspects of the self-actuation and motility of thermosalient crystals. *Journal of the American Chemical Society*, 135(33), 12241–12251.
- Salje, E. K. H., Ridgwell, A., Guttler, B., Wruck, B., Dove, M. T., & Dolino, G. (1992). On the displacive character of the phase transition in quartz: A hard-mode spectroscopy study. *Journal of Physics: Condensed Matter*, 4(2), 571–577. <https://doi.org/10.1088/0953-8984/4/2/025>
- Scheidl, K. S., Kurnosov, A., Trots, D. M., Boffa Ballaran, T., Angel, R. J., & Miletich, R. (2016). Extending the single-crystal quartz pressure gauge up to hydrostatic pressure of 19 GPa. *Journal of Applied Crystallography*, 49(6), 2129–2137. <https://doi.org/10.1107/S1600576716015351>
- Schmidt, C., & Ziemann, M. A. (2000). In-situ Raman spectroscopy of quartz: A pressure sensor for hydrothermal diamond-anvil cell experiments

- at elevated temperatures. *American Mineralogist*, 85(11), 1725–1734. <https://doi.org/10.2138/am-2000-11-1216>
- Scott, J. F. (1968). Evidence of coupling between one- and two-phonon excitations in quartz. *Physical Review Letters*, 21(13), 907–910. <https://doi.org/10.1103/PhysRevLett.21.907>
- Shen, A. H., Bassett, W. A., & Chou, I.-M. (1993). The $\alpha - \beta$ quartz transition at high temperatures and pressures in a diamond-anvil cell by laser interferometry. *American Mineralogist*, 78(7), 694–698.
- Skoko, Z., Zamir, S., Naumov, P., & Bernstein, J. (2010). The thermosalient phenomenon. “jumping crystals” and crystal chemistry of the anticholinergic agent oxitropium bromide. *Journal of the American Chemical Society*, 132(40), 14191–14202.
- Thomas, J. B., & Spear, F. S. (2018). Experimental study of quartz inclusions in garnet at pressures up to 3.0 gpa: Evaluating validity of the quartz-in-garnet inclusion elastic thermobarometer. *Contributions to Mineralogy and Petrology*, 173(5), 42.
- Wang, J., Mao, Z., Jiang, F., & Duffy, T. S. (2015). Elasticity of single-crystal quartz to 10 GPa. *Physics and Chemistry of Minerals*, 42(3), 203–212. <https://doi.org/10.1007/s00269-014-0711-z>
- Zboril, R., Mashlan, M., Machala, L., Walla, J., Barcova, K., & Martinec, P. (2004). Characterization and thermal behaviour of garnets from almandine—pyrope series at 1200°C (M. E. Elzain, A. A. Yousif, A. D. al Rawas, & A. M. Gismelseed, Eds.). *Hyperfine Interactions*, 156/157, 403–410. https://doi.org/10.1007/978-1-4020-2852-6_61

9 Fossil subduction recorded by quartz from the coesite stability field

This chapter was published as an article in *Geology* as:

Alvaro, M., Mazzucchelli, M., Angel, R., Murri, M., Campomenosi, N., Scambelluri, M., Nestola, F., Korsakov, A., Tomilenko, A., Marone, F., and Morana, M. (2020). Fossil subduction recorded by quartz from the coesite stability field. *Geology*, 48(1), 24–28.
<https://doi.org/10.1130/G46617.1>

ABSTRACT

Metamorphic rocks are the records of plate tectonic processes whose reconstruction relies on correct estimates of the pressures and temperatures (P-T) experienced by these rocks through time. Unlike chemical geothermobarometry, elastic geobarometry does not rely on chemical equilibrium between minerals, so it has the potential to provide information on overstepping of reaction boundaries and to identify other examples of non-equilibrium behavior in rocks. Here we introduce a method that exploits the anisotropy in elastic properties of minerals to determine the unique P and T of entrapment from a single inclusion in a mineral host. We apply it to preserved quartz inclusions in garnet from eclogite xenoliths hosted in Yakutian kimberlites (Russia). Our results demonstrate that quartz trapped in garnet can be preserved when the rock reaches the stability field of coesite (the high-pressure and high temperature polymorph of quartz) at 3 GPa and 850 °C. This supports a metamorphic origin for these xenoliths and sheds light on the mechanisms of craton accretion from a subducted crustal protolith. Furthermore, we show that interpreting P and T conditions reached by a rock from the simple phase identification of key inclusion minerals can be misleading.

9.1 INTRODUCTION

The mechanisms attending the downward transport of crustal material into the mantle and its return back to Earth's surface (exhumation) are still a matter of vigorous debate. Chemical information only allows the interpretation of the

measurements on mineral and rock composition in terms of pressure (P) for perfectly lithostatic systems under ideal chemical equilibrium. However, significant overstepping of reaction boundaries Spear et al., 2016 as well as the presence of non-lithostatic stresses might prevent the correct interpretation of P, and in turn depths, reached by crustal rocks during subduction and metamorphism. Host-inclusion geobarometry provides an alternative and complementary method to determine pressures and temperatures (P-T) attained during the history of rocks (Angel et al., 2014; Angel et al., 2015; Zhang, 1998). A mineral trapped as an inclusion within another host mineral is not free to expand or contract as would a free crystal but is constrained by the host mineral. This results in the development of stress in the inclusion that differs from the external stress or pressure applied to the host mineral, both while it is in the earth and afterwards when we examine the rock at room pressure in the laboratory. The stress state of the inclusion arises from the change in P and T from the time of its entrapment, so measurement of the stress state of the still-entrapped inclusion while in the laboratory enables the conditions of entrapment to be calculated, provided no plastic or brittle deformation occurred upon exhumation after entrapment. However, the current state of the art is based upon the assumption that both the host and the inclusion are elastically isotropic. But, no mineral is isotropic in elastic properties and this may cause errors in calculated P and T. This also means that a measurement of a single inclusion pressure while the host is at room pressure provides only one constraint on the entrapment conditions. As a consequence, one can only calculate a line in P-T space (the entrapment isomeke) which represents possible entrapment conditions of the inclusion (Angel et al., 2014; Rosenfeld and Chase, 1961). Here we describe how the anisotropy of mineral inclusions can be exploited to determine unique P-T conditions last recorded by the rock. The basic idea behind this approach is that an anisotropic inclusion will exhibit different stresses and strain along different crystallographic directions. By measuring these strains from a single inclusion, we obtain two or three independent data which, in combination with the known P-T variation of the unit-cell parameters of the inclusion mineral and the host, enable both the P and T of entrapment or elastic equilibration of the inclusion to be determined.

9.2 ECLOGITE XENOLITH FROM THE MIR PIPE (YAKUTIA)

The Mir pipe (Yakutian kimberlites, Russia) is a relatively young kimberlite (360 Ma) for which eruption temperatures of ~ 1000 °C and very fast ascent rates or short residence time (< 0.1 m.y.) have been estimated (Korsakov et al., 2009; Zhukov and Korsakov, 2015). The Mir pipe kimberlite carried to the surface eclogite xenoliths made of omphacite, garnet, and rutile (Taylor et al., 2003; Tomilenko et al., 2005; Zhukov and Korsakov, 2015). The major and trace element bulk composition of these eclogite xenoliths suggests that they may be derived from subducted

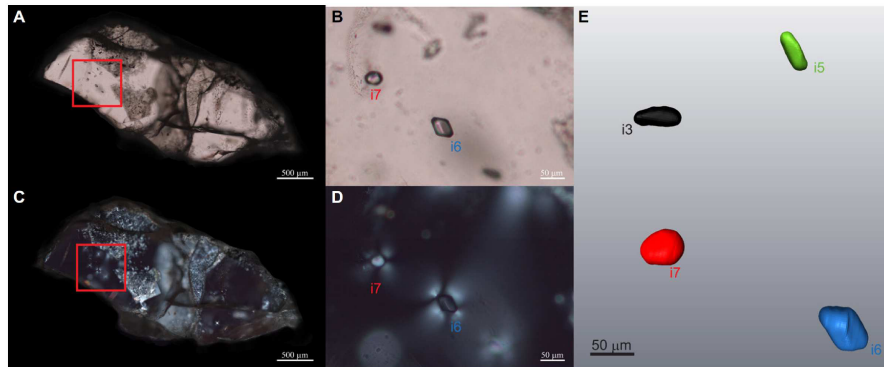


Figure 9.1. (A) Microphotography of a thin section (parallel polarized light) of eclogite xenolith from the Mir pipe (Yakutian kimberlites, Russia), where location of inclusions within the garnet host are highlighted (red box). (B) High-magnification microphotography of two inclusions highlighting the high degree of preservation of quartz crystals, absence of cracks, and back-transformation features. (C,D) In cross-polarized light images (same areas as shown in A and B), birefringence haloes around selected inclusions show the presence of significant residual stresses in the inclusions. (E) Reconstructed three-dimensional microtomography of the same cluster of inclusions as in B and D (colored) and the host (gray background), which demonstrates the absence of cracks and shows that only one inclusion (i6, blue) has a very complex shape, far from a sphere or ellipsoid, for which dedicated finite element model (FEM) calculation on its specific shape is mandatory.

oceanic crust (Shimizu and Sobolev, 1995; Taylor et al., 2003). The studied xenolith contains coarse homogeneous garnet hosting relatively large primary quartz inclusions (Fig. 9.1). Previous models show that the short eruption time prevents any significant resetting of inclusion pressures by plastic flow of the garnet during upward transport from the mantle (Zhong et al., 2018). This is confirmed by the estimated residual pressures of 1.0–1.2 GPa for the quartz inclusions, which are significantly higher than 0.1–0.6 GPa reported on other quartz inclusions in garnets from coesite-grade and diamond-grade ultrahigh-pressure (UHP) rocks (see Korsakov et al., 2009). The relatively large sizes and high pressures of the inclusions and the homogeneous composition of the garnet host, coupled with the fast kimberlite ascent which may have been insufficient to reset the rock-forming minerals, make these eclogites an ideal case to test and prove the potential of anisotropic elastic geobarometry.

9.3 DETERMINATION OF INCLUSION STRAINS

The birefringence haloes around the four selected inclusions (see Fig. 9.1) indicate the presence of significant residual stresses in the inclusions (Campomenosi et al.,

Table 9.1. Strains calculated for inclusions i3, i5, i6 and i7 (see figure 1) from micro-Raman measurements, together with single-crystal x-ray diffraction data on inclusion i6 before and after subtracting the anisotropic relaxation.

Inclusion label	$\epsilon_1 + \epsilon_2$	ϵ_3	ϵ_V	χ^2
Relaxed				
i6, X-ray*	-0.0182(2)	-0.0091(3)	-0.027(3)	
i6, MRS	-0.018(3)	-0.009(2)	-0.0264(11)	0.47
i5, MRS	-0.021(3)	-0.009(2)	-0.030(2)	0.46
i3, MRS	-0.021(5)	-0.009(4)	-0.030(2)	0.40
i7, MRS	-0.020(4)	-0.008(3)	-0.029(2)	0.25
Unrelaxed				
i6, X-ray*	-0.0237(4)	-0.0122(6)	-0.0359(7)	
i6, MRS	-0.023(4)	-0.012(3)	-0.036(4)	
i5, MRS	-0.026(4)	-0.012(3)	-0.039(4)	
i3, MRS	-0.026(6)	-0.012(5)	-0.039(7)	
i7, MRS	-0.026(6)	-0.011(4)	-0.038(6)	

MRS—micro-Raman spectroscopy. Estimated standard deviations are given in parentheses. For inclusions i6 and i5, strains have been determined from four Raman bands at 128, 260, 464, and 696 cm^{-1} , whereas for inclusions i3 and i7, the Raman band at 696 cm^{-1} has been excluded because of the poor quality of the profile and the consequent large uncertainties in the fitting results. Single-crystal X-ray diffraction data on i6 are taken from Murri et al. (2018)

2018; Howell et al., 2010; Korsakov et al., 2007; Korsakov et al., 2009). The upshift of the Raman bands (Fig. 9.2A) at various positions across the inclusion confirms that the inclusion is under significant residual strain. Quantitative values of the strains have been determined from the wavenumber shifts of the Raman bands at 128, 206, 464, and 696 cm^{-1} by using the mode Grüneisen tensors of quartz (Angel et al., 2019; Bonazzi et al., 2019; Murri et al., 2019; Murri et al., 2018). The strains determined in this way from several inclusions in the same garnet are identical within estimated standard deviations, and agree with the measurements by single-crystal X-ray diffraction (Table A.1).

The residual strains as determined by X-ray diffraction and by micro-Raman spectroscopy (MRS) cannot be directly used to back-calculate the residual pressure at entrapment conditions because they are the product of two processes: the contrast in the elastic properties of the host and inclusion over P and T that leads to the inclusions exhibiting an excess pressure, and the mutual elastic relaxation of the system driven by this excess pressure (Angel et al., 2014). Before calculating

entrapment conditions by using the equations of state of the host and inclusion minerals, the residual strains must be corrected for elastic relaxation (Angel et al., 2017). Correction for elastic relaxation of a spherical inclusion in an elastically isotropic system depends only on the elastic properties of the host and inclusion (Angel et al., 2017; Zhang, 1998). For faceted or complex-shaped inclusions, and for all elastically anisotropic inclusions, the final stress state depends on both the geometry of the system and the elastic anisotropy of the inclusion-host pair (Campomenosi et al., 2018; Eshelby, 1957; Mazzucchelli et al., 2018; Mazzucchelli et al., 2019; Zhukov and Korsakov, 2015). Therefore, for all of these cases, the elastic relaxation must be calculated numerically (Mazzucchelli et al., 2018; Mazzucchelli et al., 2019) using the exact shape of the inclusion and its full elastic properties together with those for the host. We determined the three-dimensional (3-D) model of the entire sample (see Fig. 9.1E) from X-ray microtomography measurements at the TOMCAT (Tomographic Microscopy and Coherent Radiology Experiments) beamline of the Swiss Light Source (SLS; Paul Scherrer Institut) (Stampanoni et al., 2006). From these images, we created a meshed 3-D model in order to perform finite element (FE) analyses that allow us to calculate the amount of elastic relaxation that has occurred (Mazzucchelli et al., 2018). Because of the anisotropy of quartz, the amount of elastic relaxation is different in different directions. Only after correction for the elastic relaxation can we demonstrate that the measured quartz inclusions were subject to isotropic strain (Table A.1; Fig. 9.2B) as a consequence of the change of the dimensions of the cubic host mineral with P and T. The corrected strains of all four inclusions are identical within the estimated uncertainties, consistent with them having been trapped under the same conditions and having experienced the same post-entrapment history.

9.4 CALCULATION OF UNIQUE PRESSURE AND TEMPERATURE OF ELASTIC EQUILIBRATION

Once the measured inclusion pressure or strain (as appropriate) has been corrected for the effects of mutual relaxation, the determination of possible entrapment conditions is a purely thermodynamic calculation. In the isotropic model (Angel et al., 2014; Angel et al., 2015; Angel et al., 2017), entrapment conditions are calculated as the conditions under which there are no stress gradients across the host and inclusion, which leads to an entrapment isomeke, which is a line in P-T space along which there would have been no strain gradients in the system. We exploit the anisotropy of quartz and the known variation with P and T of its unit-cell parameters (for details see the Data Repository) to calculate a line of possible entrapment conditions from each of the corrected strains calculated along a and c crystallographic axes (Table A.1). The intersection of these two lines (e.g., crossing point of dashed and solid lines in Fig. 9.2C) provides a unique P and

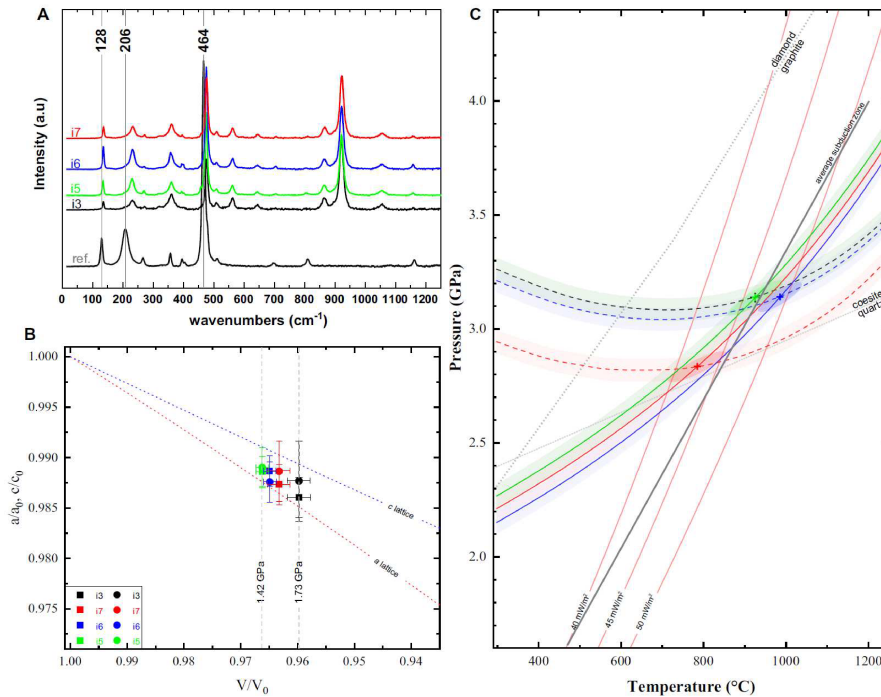


Figure 9.2. (A) Raman spectra measured on four inclusions of eclogite xenolith from the Mir pipe (Yakutian kimberlites, Russia) while still trapped in the host. a.u.—arbitrary units. (B) Residual strains (a/a_0 and c/c_0) on inclusions along a and c lattice (squares and circles, respectively) after correcting for anisotropic elastic relaxation are isotropic within estimated standard deviations. Dashed lines represent hydrostatic equations of state for a and c lattice for quartz. Two boundary values of inclusion pressure are given at corresponding V/V_0 value. (C) Plot with a and c lattice strains for quartz inclusions trapped in garnet as a function of temperature calculated as described in the Data Repository (see footnote 1). Dashed line is strain along c axis and solid line is strain along a axis. Shaded areas represent uncertainties on measurements. Intersection between lattice isomekes represents the unique condition of garnet elastic equilibration at the pressure and temperature that occurred under hydrostatic conditions. Ellipsoids represent correlation of uncertainties for the calculation of intersection between strains. Color coding is as in Figure 1.

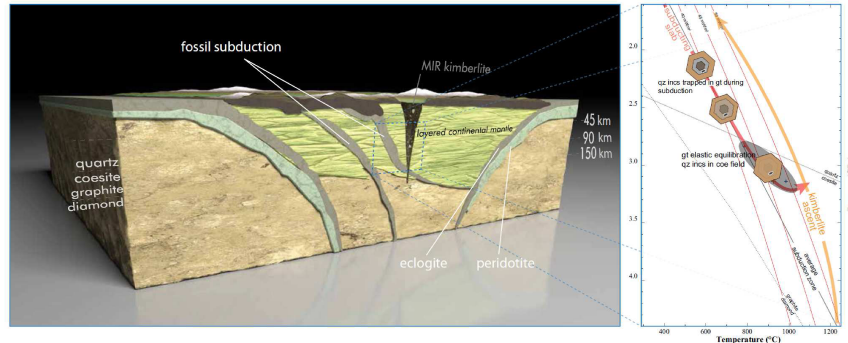


Figure 9.3. Schematic view of the area of Mir pipe (Yakutian kimberlites, Russia) and process from fossil subduction to elastic equilibration of garnet and subsequent exhumation during kimberlite ascent. Image not to scale. Abbreviations and color coding as in Figure 2..

T of entrapment and /or equilibration for each inclusion, three of which are very similar and cluster around 3 GPa, close to the mantle geotherms corresponding to surface heat flow of 40–50 mW/m² considered appropriate for these eclogites (Litasov et al., 2003).

9.5 ECLOGITE XENOLITHS: MAGMATIC OR METAMORPHIC?

We show that the quartz inclusions in the garnet of the eclogite xenoliths from the Mir kimberlite record P-T conditions of elastic equilibration within the coesite stability field at pressures lower than the stability field of diamond (Fig. 9.2C). We can exclude the possibility that the inclusions were originally trapped as coesite and then inverted to quartz because the inclusions are perfect single crystals and do not exhibit the palisade texture typical of quartz inclusions inverted from coesite (Kotková et al., 2011; Schertl et al., 1991). Neither is there evidence (Fig. 9.1) of cracks that would have allowed access of fluids to catalyze the otherwise very slow inversion from coesite. Fluid infiltration would also be required to remove silica from the inclusion to allow the pressure to drop below the pressure of the coesite-quartz equilibrium phase boundary, at which the pressure of an isolated inclusion consisting of a mixture of coesite and quartz should be buffered (Ferrero and Angel, 2018). The absence of coesite from this fragment of xenolith, which consists mostly of garnet and clinopyroxene instead, indicates that the garnet grew at relatively low P-T along the prograde subduction path of a crustal protolith, which produced minor quartz that became entrapped as inclusions. Subduction then proceeded toward UHP conditions to mantle depths of ~100 km and the pressures in the quartz inclusions, much softer than the garnet host crystals, will lag behind

the external pressures by ~ 1.5 GPa (Angel et al., 2015). Therefore, at rock pressures of 3.5 GPa, the quartz experiences only 2.0 GPa, well within its stability field, and would not transform to coesite. A significant period of residence of the studied garnet at high temperatures would be consistent with the complete absence of compositional zoning and gradients in the eclogitic garnet host (Shimizu and Sobolev, 1995). We suggest that at the same time that the compositional gradients in the garnet were eliminated by diffusion, the pressure difference between the quartz inclusions and the garnet host drove plastic flow that relaxed the stress difference while maintaining the isolation of the inclusions so that no fluids were available to catalyze the quartz to coesite. Similar resetting of inclusion pressures in garnets has also been documented in metamorphic settings (Ferrero and Angel, 2018). Subsequent eruption of the kimberlite would have been sufficiently rapid to prevent further significant resetting of the inclusion stress state (Zhong et al., 2018). Therefore, the remanent pressures that we measured on these inclusions reflect resetting at mantle pressures and temperatures following subduction (see Figs. ref2 and 9.3). We note that the resetting temperature and pressure cluster around a mantle geotherm associated with surface heat flow of 45 mW/m², appropriate for ambient conditions at the time of the kimberlite eruption, so they may indicate that the xenolith was incorporated at the time of eruption (Litasov et al., 2003). On the other hand, the measured remanent inclusion pressures definitely exclude the possibility that the studied mantle eclogite xenoliths are the product of direct high-pressure magma crystallization at mantle depths, as already supported by geochemical evidence for other xenoliths (Aulbach et al., 2017; Griffin and O'Reilly, 2007). Direct crystallization at depth would result in either coesite inclusions, or inclusions whose remanent pressures would indicate entrapment within the stability field of quartz. This example illustrates that the anisotropic behavior of quartz is not just a complication that may invalidate an isotropic analysis of inclusion data, but actually provides additional information that can be used in certain circumstances to provide P and T estimates that are completely independent of chemical equilibrium in the rock. The same principles and methodology can certainly be applied to any other uniaxial mineral trapped in almost isotropic host minerals such as garnets.

ACKNOWLEDGMENTS

This project received funding from the European Research Council under the European Union's Horizon 2020 research and innovation program grant agreement 714936 (ERC-STG TRUE DEPTHS) to M. Alvaro. Alvaro and Scambelluri have been supported by the Ministero dell'Istruzione dell'Università e della Ricerca (MIUR) Progetti di Ricerca di Interesse Nazionale (PRIN) Bando PRIN 2017 - Prot. 2017ZE49E7_005. We acknowledge the Paul Scherrer Institut, Villigen, Switzerland, for provision of synchrotron radiation beamtime at the TOMCAT beamline

of the Swiss Light Source. We thank Catherine Mottram, Jay Thomas, and one anonymous reviewer.

REFERENCES

- Angel, R. J., Mazzucchelli, M. L., Alvaro, M., Nimis, P., & Nestola, F. (2014). Geobarometry from host-inclusion systems: the role of elastic relaxation. *Am. Miner.*, *99*, 2146.
- Angel, R. J., Nimis, P., Mazzucchelli, M. L., Alvaro, M., & Nestola, F. (2015). How large are departures from lithostatic pressure? Constraints from host-inclusion elasticity. *J. Metamorph. Geol.*, *33*, 801.
- Angel, R. J., Mazzucchelli, M. L., Alvaro, M., & Nestola, F. (2017). EosFit-Pinc: A simple GUI for host-inclusion elastic thermobarometry. *American Mineralogist*, *102*(9), 1957–1960.
- Angel, R. J., Murri, M., Mihailova, B., & Alvaro, M. (2019). Stress, strain and Raman shifts. *Zeitschrift für Kristallographie - Crystalline Materials*, *234*(2), 129–140. <https://doi.org/10.1515/zkri-2018-2112>
- Aulbach, S., Jacob, D., Cartigny, P., Stern, R., Simonetti, S., Wörner, G., & Viljoen, K. (2017). Eclogite xenoliths from orapa: Ocean crust recycling, mantle metasomatism and carbon cycling at the western zimbabwe craton margin. *Geochimica et Cosmochimica Acta*, *213*, 574–592.
- Bonazzi, M., Tumiati, S., Thomas, J. B., Angel, R. J., & Alvaro, M. (2019). Assessment of the reliability of elastic geobarometry with quartz inclusions. *Lithos*, *350–351*, 105201. <https://doi.org/10.1016/j.lithos.2019.105201>
- Campomenosi, N., Mazzucchelli, M. L., Mihailova, B., Scambelluri, M., Angel, R. J., Nestola, F., Reali, A., & Alvaro, M. (2018). How geometry and anisotropy affect residual strain in host-inclusion systems: Coupling experimental and numerical approaches [Publisher: De Gruyter Section: American Mineralogist]. *American Mineralogist*, *103*(12), 2032–2035. <https://doi.org/10.2138/am-2018-6700CCBY>
- Eshelby, J. D. (1957). The determination of the elastic field of an ellipsoidal inclusion, and related problems. *Proceedings of the royal society of London. Series A. Mathematical and physical sciences*, *241*(1226), 376–396.
- Ferrero, S., & Angel, R. J. (2018). Micropetrology: Are inclusions grains of truth? *Journal of Petrology*, *59*(9), 1671–1700.
- Griffin, W. L., & O'Reilly, S. Y. (2007). Cratonic lithospheric mantle: Is anything subducted? *Episodes*, *30*(1), 43–53.
- Howell, D., Wood, I., Dobson, D., Jones, A., Nasdala, L., & Harris, J. (2010). Quantifying strain birefringence halos around inclusions in diamond. *Contributions to Mineralogy and Petrology*, *160*(5), 705–717.
- Korsakov, A. V., Hutsebaut, D., Theunissen, K., Vandenabeele, P., & Stepanov, A. S. (2007). Raman mapping of coesite inclusions in garnet from the kokchetav

- massif (northern kazakhstan). *Spectrochimica Acta Part A: Molecular and Biomolecular Spectroscopy*, 68(4), 1046–1052.
- Korsakov, A. V., Perraki, M., Zhukov, V. P., Gussem, K. d., Vandenabeele, P., & Tomilenko, A. A. (2009). Is quartz a potential indicator of ultrahigh-pressure metamorphism? laser raman spectroscopy of quartz inclusions in ultrahigh-pressure garnets. *European Journal of Mineralogy*, 21(6), 1313–1323. <https://doi.org/10.1127/0935-1221/2009/0021-2006>
- Kotková, J., O'Brien, P. J., & Ziemann, M. A. (2011). Diamond and coesite discovered in saxony-type granulite: Solution to the variscan garnet peridotite enigma. *Geology*, 39(7), 667–670.
- Litasov, K. D., Malkovets, V. G., Kostrovitsky, S. I., & Taylor, L. A. (2003). Petrogenesis of ilmenite-bearing symplectite xenoliths from vitim alkaline basalts and yakutian kimberlites, russia. *International Geology Review*, 45(11), 976–997.
- Mazzucchelli, M. L., Burnley, P., Angel, R. J., Morganti, S., Domeneghetti, M. C., Nestola, F., & Alvaro, M. (2018). Elastic geothermobarometry: Corrections for the geometry of the host-inclusion system [Publisher: GeoScience-World]. *Geology*, 46(3), 231–234. <https://doi.org/10.1130/G39807.1>
- Mazzucchelli, M., Reali, A., Morganti, S., Angel, R., & Alvaro, M. (2019). Elastic geobarometry for anisotropic inclusions in cubic hosts. *Lithos*, 350, 105218.
- Murri, M., Alvaro, M., Angel, R. J., Prencipe, M., & Mihailova, B. D. (2019). The effects of non-hydrostatic stress on the structure and properties of alpha-quartz. *Physics and Chemistry of Minerals*. <https://doi.org/10.1007/s00269-018-01018-6>
- Murri, M., Mazzucchelli, M. L., Campomenosi, N., Korsakov, A. V., Prencipe, M., Mihailova, B. D., Scambelluri, M., Angel, R. J., & Alvaro, M. (2018). Raman elastic geobarometry for anisotropic mineral inclusions. *American Mineralogist*, 103(11), 1869–1872. <https://doi.org/10.2138/am-2018-6625CCBY>
- Rosenfeld, J. L., & Chase, A. B. (1961). Pressure and temperature of crystallization from elastic effects around solid inclusions in minerals? *American Journal of Science*, 259(7), 519–541. <https://doi.org/10.2475/ajs.259.7.519>
- Schertl, H.-P., Schreyer, W., & Chopin, C. (1991). The pyrope-coesite rocks and their country rocks at parigi, dora maira massif, western alps: Detailed petrography, mineral chemistry and pt-path. *Contributions to Mineralogy and Petrology*, 108(1-2), 1–21.
- Shimizu, N., & Sobolev, N. (1995). Young peridotitic diamonds from the mir kimberlite pipe. *Nature*, 375(6530), 394–397.
- Spear, F. S., Pattison, D. R., & Cheney, J. T. (2016). The metamorphism of metamorphic petrology. *The web of geological sciences: Advances, impacts, and interactions II*. Geological Society of America. [https://doi.org/10.1130/2016.2523\(02\)](https://doi.org/10.1130/2016.2523(02))

- Taylor, L. A., Snyder, G. A., Keller, R., Remley, D. A., Anand, M., Wiesli, R., Valley, J., & Sobolev, N. V. (2003). Petrogenesis of group a eclogites and websterites: Evidence from the obnazhennaya kimberlite, yakutia. *Contributions to Mineralogy and Petrology*, 145(4), 424–443.
- Tomilenko, A., Kovyazin, S., & Pokhilenko, N. (2005). Primary crystalline and fluid inclusions in garnet from diamondiferous eclogite from kimberlite pipes mir and udachnaya, yakutiya, russia. in. “*ECROFI XVIII. European current research on fluid inclusions*”, Siena, Italy.
- Zhang, Y. (1998). Mechanical and phase equilibria in inclusion–host systems. *Earth and Planetary Science Letters*, 157(3-4), 209–222.
- Zhong, X., Moulas, E., & Tajčmanová, L. (2018). Tiny timekeepers witnessing high-rate exhumation processes. *Scientific reports*, 8(1), 1–9.
- Zhukov, V., & Korsakov, A. (2015). Evolution of host-inclusion systems: A visco-elastic model. *Journal of Metamorphic Geology*, 33(8), 815–828.

In this thesis mineral inclusions are characterized by means of various non-destructive techniques that allow to extract a plethora of information from the host-inclusion system without compromising its integrity. Inclusions have the potential to shed light on different geological problems: from their composition we can infer the conditions of the environment in which they grew; the mutual crystallographic orientations of the host and the inclusions allow to identify whether the inclusion grew before or together with the host, or conditions of epitaxial growth; from the stress state of the inclusions we can determine the pressure and temperature conditions of the entrapment.

The work on magnetic inclusion in diamonds shows that even rare inclusions can play an important role in understanding the environment of formation of diamond and that a multi-analytical approach can exploit all the properties of the included minerals. In fact, as shown in Chapters 2 and 3 magnetic properties can help in the identification of the composition of the inclusions and thus of the environment in which the host-inclusion system grew. The use of X-ray tomography allows to identify epigenetic inclusions, such as hematite. Furthermore, the combination of different techniques can provide a unique identification also in complex cases, highlighting the importance of a multi-analytical approach. In particular, X-ray tomography played an important role not only in the locating all the inclusions in the samples, but also in determining their formation mechanism, and the identification of the phases.

The determination of the stress state of the inclusions and the influence of such stress on the structure and properties is addressed in the second part of this thesis. Chapter 5 demonstrates that it is possible to characterize the crystal structure of inclusions in situ. This study not only paves the way to a systematic analysis of the structures of mineral inclusions, but it also allows to use host-inclusions system as model systems to study the effect of non-hydrostatic stress on crystal structures, a problem still to explore in mineralogy and material sciences. Chapters 6 and 7 demonstrate the fundamental importance of a thorough characterization of the free minerals in order to correctly interpret the results from inclusions. In particular, in Chapter 6 the characterization of the response of quartz Raman scattering to compression allowed to verify experimentally the validity of the approach based on the phonon-mode Grüneisen tensor to calculate the pressure

in the inclusions. Furthermore, the investigation of the splitting of E modes shows that both LO and TO modes have the same phonon compressibility, supporting the application of the Grüneisen-tensor approach (Angel et al., 2019; Murri et al., 2019) to the two components, and that the orientation of quartz inclusions with respect to the surface of the host does not bias the strain-induced shifts of the Raman peaks from E modes. It also characterized in full details the strong multiphonon interactions that can contribute to the stability of alpha-quartz at ambient conditions and provide new pressure calibrations for a larger number of modes and in a wider pressure range than previously reported (Schmidt & Ziemann, 2000). The reexamination of the temperature dependence of quartz Raman scattering at high temperature provided a complete data set and reference to understand how the spectrum of quartz change as function of temperature and approaching the α - β phase transition. It provides a good description of the behavior of the spectral features involved in the transition, affected by multiphonon interactions (Scott, 1968). Thanks to this information, it is possible to interpret the complex results from the in-situ heating experiment on a quartz in garnet host-inclusion pair described in Chapter 8. This experiment show that the quartz inclusion does not undergo the α - β phase transition. This observation is supported not only by a detailed characterization of the Raman peak positions and widths, which are compared with the ones from the heating experiment on the free crystal, but also by calculations based on the thermoelastic properties of the host and the inclusion. The comparison of the free and trapped crystal data clearly shows a different response to heating. In fact, the free quartz data can be interpreted in terms of three regimes: a first region where only simple thermal expansion occurs, a second region showing pre-transition effects and the the actual transition, a last regime that is related to the high symmetry phase. The data from the inclusion cannot be reconciled with this picture and thus require further investigation. The applied models cannot reproduce the experimental data and it can be shown that the disagreement between the data and the prediction is due to the elastic anisotropy of quartz. In fact, a quartz trapped in garnet, which is cubic, will be subject to isotropic strains imposed by the host. Since it is elastically anisotropic, the inclusion will develop deviatoric (non-hydrostatic) stresses that are not taken into account by the models used so far to reproduce the experimental data. Thus, as a further development a new model tacking into account elastic anisotropy will be developed.

REFERENCES

- Angel, R. J., Murri, M., Mihailova, B., & Alvaro, M. (2019). Stress, strain and Raman shifts. *Zeitschrift für Kristallographie - Crystalline Materials*, 234(2), 129–140. <https://doi.org/10.1515/zkri-2018-2112>

- Murri, M., Alvaro, M., Angel, R. J., Prencipe, M., & Mihailova, B. D. (2019). The effects of non-hydrostatic stress on the structure and properties of alpha-quartz. *Physics and Chemistry of Minerals*. <https://doi.org/10.1007/s00269-018-01018-6>
- Schmidt, C., & Ziemann, M. A. (2000). In-situ Raman spectroscopy of quartz: A pressure sensor for hydrothermal diamond-anvil cell experiments at elevated temperatures. *American Mineralogist*, *85*(11), 1725–1734. <https://doi.org/10.2138/am-2000-11-1216>
- Scott, J. F. (1968). Evidence of coupling between one- and two-phonon excitations in quartz. *Physical Review Letters*, *21*(13), 907–910. <https://doi.org/10.1103/PhysRevLett.21.907>

Appendices

1 Spiridonovite, $(\text{Cu}_{1-x}\text{Ag}_x)_2\text{Te}$ ($x \approx 0.4$), a new telluride from the Good Hope Mine, Vulcan, Colorado (U.S.A.)

This chapter was published as an article in *Minerals* as:

Morana M. and Bindi L. (2020). Spiridonovite, $(\text{Cu}_{1-x}\text{Ag}_x)_2\text{Te}$ ($x \approx 0.4$), a New Telluride from the Good Hope Mine, Vulcan, Colorado (U.S.A.). *Minerals*, 9(3), 194
<https://doi.org/10.3390/min9030194>

This article is an open access article distributed under the terms and conditions of the Creative Commons Attribution (CC BY) license. .

ABSTRACT

Here we describe a new mineral in the Cu-Ag-Te system, spiridonovite. The specimen was discovered in a fragment from the cameronite [ideally, $\text{Cu}_{5-x}(\text{Cu},\text{Ag})_{3+x}\text{Te}_{10}$] holotype material from the Good Hope mine, Vulcan, Colorado (U.S.A.). It occurs as black grains of subhedral to anhedral morphology, with a maximum size up to $65 \mu\text{m}$, and shows black streaks. No cleavage is observed and the Vickers hardness (VHN_{100}) is $158 \text{ kg} \cdot \text{mm}^{-2}$. Reflectance percentages in air for R_{\min} and R_{\max} are 38.1, 38.9 (471.1 nm), 36.5, 37.3 (548.3 nm), 35.8, 36.5 (586.6 nm), 34.7, 35.4 (652.3 nm). Spiridonovite has formula $(\text{Cu}_{1.24}\text{Ag}_{0.75})\text{S}_{1.99}\text{Te}_{1.01}$, ideally $(\text{Cu}_{1-x}\text{Ag}_x)_2\text{Te}$ ($x \approx 0.4$). The mineral is trigonal and belongs to the space group $P - 3c1$, with the following unit-cell parameters: $a = 4.630(2) \text{ \AA}$, $c = 22.551(9) \text{ \AA}$, $V = 418.7(4) \text{ \AA}^3$, and $Z = 6$. The crystal structure has been solved and refined to $R_1 = 0.0256$. It can be described as a rhombohedrally-compressed antiferite structure, with a rough ccp arrangement of Te atoms. It consists of two Te sites and three M (metal) sites, occupied by Cu and Ag, and is characterized by the presence of edge-sharing tetrahedra, where the four-fold coordinated M atoms lie. The mineral and its name have been approved by the Commission of New Minerals, Nomenclature and Classification of the International Mineralogical Association (No. 2018-136).

A.1 INTRODUCTION

Spiridonovite is a new member of the Cu-Ag-Te system, together with rickardite, $(\text{Cu}_{3-x}\text{Te}_2)$ (Ford, 1903), vulcanite (CuTe) (Cameron & Threadgold, 1961), weissite

(Cu_{2-x}Te) (Bindi et al., 2013), cameronite [$\text{Cu}_{5-x}(\text{Cu,Ag})_{3+x}\text{Te}_{10}$] (Bindi & Pinch, 2014), and henryite [$(\text{Cu,Ag})_{3+x}\text{Te}_2$] (Bindi, 2014). The new mineral species was discovered in a fragment from the cameronite holotype material, sample R-934, from the Good Hope mine ($38^\circ 20' 35'' \text{N}$, $107^\circ 0' 26'' \text{W}$), Vulcan, Colorado (U.S.A.) obtained in 1974 by the late William W. Pinch on exchange from the Smithsonian Institution, Washington D.C. (U.S.A.) (Bindi & Pinch, 2014). The Good Hope mine was active from 1898 to 1904, and intermittently through 1930. The mineralization is hosted in mafic intrusive rock, schist and felsic volcanic rock (Hartley, 1983). Precious metals and tellurides are localized in quartz veins and successive supergene alteration of tellurides (altaite, galena, and goldfieldite) formed native Te and Cu-tellurides (e.g., rickardite, vulcanite, weissite), like spiridonovite. The new mineral has been named after Ernst M. Spiridonov (b. 1938), Professor at the Department of Mineralogy, Moscow State University, Russia. He studied gold deposits of the Urals, Transbaikalia, Kamchatka, Uzbekistan, Armenia, and Bulgaria in the last fifty years and discovered 20 new mineral species, most of them ore minerals. The new mineral and mineral name have been approved by the Commission on New Minerals, Nomenclature and Classification of the International Mineralogical Association (No. 2018-136). The holotype material is deposited in the collections of the Museo di Storia Naturale, Università degli Studi di Firenze, Via La Pira 4, I-50121, Firenze, Italy, catalogue number 3295/I.

A.2 DESCRIPTION AND PHYSICAL PROPERTIES

Spiridonovite occurs as very rare crystals closely associated to rickardite, vulcanite, cameronite and native tellurium (Figure A.1); its maximum grain size is about $65 \mu\text{m}$. The mineral shows a subhedral to anhedral grain morphology without inclusions or intergrowths with other minerals. Spiridonovite crystals are black, show metallic luster and black streak, and are not fluorescent. Mohs hardness, estimated from the Vickers measurements, is ~ 3 . Micro-indentation measurements, carried out with a CORE micro-indentation system, give a mean value of $158 \text{ kg} \cdot \text{mm}^{-2}$ (range 145–170).

Tenacity is brittle, and cleavage is not observed. Parting is not observed, and fractures are irregular. The density could not be determined due to the small grain size. The calculated density is $4.6 \text{ g} \cdot \text{cm}^3$, using the empirical formula and X-ray single-crystal data (see below). In plane-polarize incident light, the mineral is dark bluish black, with moderate bireflectance (slightly higher than cameronite) and very weak pleochroism from light grey to a slightly greenish grey. Under crossed polars, spiridonovite shows very weak anisotropism with greyish to light-blue rotation tint. Internal reflections are absent, and there is no optical evidence of growth zonation. Reflectance values were measured in air using a MPM-200 Zeiss microphotometer equipped with a MSP-20 system processor on a Zeiss Axioplan ore microscope (Zeiss, Jena, Germany). The filament temperature

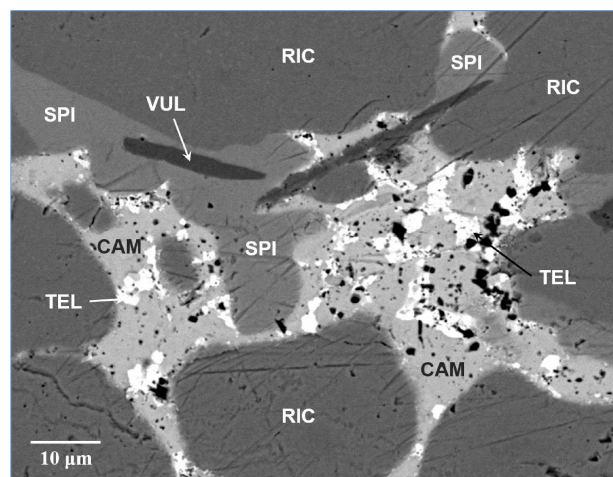


Figure A.1. Scanning Electron Microscopy-BackScattered Electron (SEM-BSE) image of spiridonovite (SPI) associated with cameronite (CAM), rickardite (RIC), vulcanite (VUL) and tellurium (TEL).

Table A.1. Reflectance values for spiridonovite..

R_{max}	R_{min}	λ (nm)
38.9	38.1	471.1
37.3	36.5	548.3
36.5	35.8	586.6
35.4	34.7	652.3

was approximately 3350 K. An interference filter was adjusted, in turn, to select four wavelengths for measurement (471.1, 548.3, 586.6, and 652.3 nm). Readings were taken for specimen and standard (SiC) maintained under the same focus conditions. The diameter of the circular measuring area was 0.05 mm. Reflectance values are reported in Table [A.1](#).

A.3 CHEMICAL DATA

A preliminary chemical analysis using EDS performed on the crystal fragment used for the structural study did not indicate the presence of elements ($Z > 9$) other than Cu, Ag and Te. However, given the minor elements found in cameronite (Bindi & Pinch, [2014](#)), we analyzed also Bi, Pb, Zn, Fe, Sb, As, S, Se at the electron microprobe. Analyses ($n=5$) were carried out using a JEOL 8200 microprobe (WDS mode, 25 kV, 20 nA, 1 μm beam size, counting times 20 s for peak and 10 s

Table A.2. Analytical data in wt.% for spiridonovite..

Constituent	Mean	Range	Stand. dev. (σ)	Standard
Ag	27.83	25.88–28.09	0.19	Ag metal
Cu	27.12	26.02–27.94	0.16	Cu metal
Bi	0.01	0.00–0.03	0.03	synthetic Bi ₂ S ₃
Pb	0.02	0.00–0.03	0.02	galena
Zn	0.01	0.00–0.02	0.02	synthetic ZnS
Fe	0.02	0.00–0.04	0.04	pyrite
Sb	0.01	0.00–0.02	0.02	synthetic Sb ₂ Te ₃
As	0.02	0.00–0.03	0.03	synthetic As ₂ S ₃
S	0.01	0.00–0.02	0.02	pyrite
Se	0.02	0.00–0.04	0.03	synthetic PtSe ₂
Te	44.35	42.63–45.81	0.29	synthetic Sb ₂ Te ₃
Total	99.42 99.	15–100.55		

for background. JEOL, Tokyo, Japan). For the WDS analyzes the following lines were used: $SK\alpha$, $FeK\alpha$, $CuK\alpha$, $ZnK\alpha$, $AsL\alpha$, $SeL\alpha$, $AgL\alpha$, $SbL\beta$, $TeL\alpha$, $PbM\alpha$, $BiM\beta$. The crystal fragment was found to be homogeneous within analytical error. Analytical data are given in Table A.2.

The empirical formula based on 3 atoms per formula unit is $(Cu_{1.24}Ag_{0.75})_{\Sigma 1.99}Te_{1.01}$, which is in excellent agreement with that derived from the structure refinement, i.e. $(Cu_{1.19}Ag_{0.81})_{\Sigma 2.00}Te$. The simplified formula is $(Cu,Ag)_2Te$. The ideal formula is $(Cu_{1-x}Ag_x)_2Te$ ($x \approx 0.4$). $(Cu_{0.6}Ag_{0.4})_2Te$ requires Cu 26.28, Ag 29.74, Te 43.98, Total 100. Silver is an essential constituent in spiridonovite with the intrinsic role to stabilize the crystal structure.

A.4 X-RAY CRYSTALLOGRAPHY

X-ray powder diffraction data (Table A.3) were collected on a fragment hand-picked from the polished section with an Oxford Diffraction Excalibur PX Ultra diffractometer fitted with a 165 mm diagonal Onyx CCD detector and using copper radiation ($CuK\alpha$, $\lambda = 1.54138 \text{ \AA}$)

Single-crystal X-ray studies were carried out using an Oxford Diffraction Xcalibur diffractometer equipped with an Oxford Diffraction CCD detector, with graphite-monochromatized $MoK\alpha$ radiation ($\lambda = 0.71073 \text{ \AA}$). Crystal data and details of the intensity data collection and refinement are reported in Table A.4.

Single-crystal X-ray diffraction intensity data were integrated and corrected for standard Lorentz polarization factors with the CrysAlisPro package ("CrysAlis RED", 2006). The program ABSPACK in CrysAlis RED ("ABSPACK in CrysAlis

Table A.3. Observed and calculated X-ray powder diffraction data (d in Å) for spiridonovite; calculated diffraction pattern obtained with the atom coordinates and occupancies reported in Table A.5 (only reflections with $I_{rel} \geq 4$ are listed).

h	k	l	d_{obs}	I_{est}	d_{calc}	I_{calc}
0	1	2	3.78	60	3.778	67
0	0	6	3.76	20	3.759	23
1	0	4	-	-	3.268	8
1	1	0	2.317	100	2.315	100
0	1	8	2.305	85	2.306	99
2	0	2	-	-	1.9739	10
1	1	6	1.973	15	1.9711	21
1	0	10	-	-	1.9656	9
2	0	8	1.635	30	1.6338	30
1	2	2	-	-	1.502	8
0	1	14	-	-	1.4947	4
3	0	0	1.338	10	1.3366	14
1	2	8	1.333	25	1.3348	27
1	0	16	1.328	10	1.3297	13
2	2	0	-	-	1.1575	8
0	2	16	-	-	1.153	8
3	1	8	1.033	5	1.0345	11
2	1	16	-	-	1.0321	11
0	4	8	-	-	0.9445	5
1	3	16	-	-	0.873	9
1	1	24	-	-	0.8706	10

Table A.4. Crystal and experimental data for spiridonovite.

Crystal size (μm)	$0.040 \times 0.050 \times 0.060$
Cell setting	Trigonal
Space group	$P\bar{3}c1$ (#165)
a, c (\AA)	4.630(2), 22.551(9)
V (\AA^3)	418.7(4)
Z	6
Temperature (K)	293(2)
$2\theta_{max}$ ($^\circ$)	64.30
Measured reflections	2155
Unique reflections	435
Reflections with $F_o > 4\sigma(F_o)$	103
R_{int}	0.0312
R_σ	0.0270
Range of h, k, l	-5 - 5; -6 - 6; -32 - 32
$R_1 [F_o > 4\sigma(F_o)]$	0.0256
R_1 (all data)	0.0304
wR (on F^2)	0.0696
Goof	0.991
No. least-squares parameters	18
Max. and min. resid. peak ($e \text{\AA}^{-3}$)	0.38; -0.24

Table A.5. Atoms, site-occupancy factors (s.o.f.), Wyckoff positions, atom coordinates and isotropic displacement parameters (\AA^2) for spiridonovite.

atom	s.o.f	Wyckoff	x/a	y/b	z/c	U_{eq}
M1	Cu _{0.60(1)} Ag _{0.40}	4c	0	0	0.37419(7)	0.0623(5)
M2	Cu _{0.64(1)} Ag _{0.36}	4d	$\frac{1}{3}$	$\frac{2}{3}$	0.79165(7)	0.0628(4)
M3	Cu _{0.55(1)} Ag _{0.45}	4d	$\frac{1}{3}$	$\frac{2}{3}$	0.04146(7)	0.0634(4)
Te1	Te _{1.00}	2b	0	0	0	0.0646(5)
Te2	Te _{1.00}	4d	$\frac{1}{3}$	$\frac{2}{3}$	0.66635(3)	0.0700(5)

Table A.6. Selected bond distances (\AA) for spiridonovite.

M1-	Te1	2.837(2)	M2-	Te2	2.826(2)	M3-	Te2	2.816(2)
	Te2	2.825(1) (×3)		Te2	2.836(1) (×3)		Te1	2.832(1) (×3)

RED", 2006) was used for the absorption correction. A total of 435 unique reflections were collected. Systematic absences were consistent with the space groups $P-3c1$ and $P3c1$. The statistical tests on the distribution of $|E|$ values ($|E^2-1| = 0.977$) indicated the presence of an inversion center and so the $P-3c1$ space group was chosen. The structure was solved and refined using the program Shelx-97 (Sheldrick, 2008). The site occupation factor (s.o.f.) at the cation sites was allowed to vary (Cu vs. Ag for the M positions and Te vs. structural vacancy for the anionic positions) using scattering curves for neutral atoms taken from the International Tables for X-ray Crystallography (Wilson, 1992). The Te sites were found fully occupied by tellurium and then fixed in the subsequent refinement cycles. Final atomic coordinates and equivalent isotropic displacement parameters are given in Table A.5, whereas selected bond distances are shown in Table A.6.

A.5 RESULTS AND DISCUSSION

From a chemical point of view, spiridonovite is close to weissite (Cu_{2-x}Te). However, while weissite can be Ag-free, the presence of Ag in spiridonovite enlarges the coordination polyhedra, creating a different topology with respect to that of weissite, and stabilizing the structure. Indeed, spiridonovite can be seen as a rhombohedrally-compressed antiferroite structure, with a rough ccp arrangement of Te atoms, which exhibit a cubic arrangement. On the contrary, Te atoms exhibit a highly distorted hcp arrangement in weissite, thus producing short Cu-Cu distances and partially occupied Cu sites. Weissite has a complex structure with 24 independent Cu and 12 Te atoms showing significantly different crystal-chemical environments (Bindi et al., 2013), while the crystal structure of

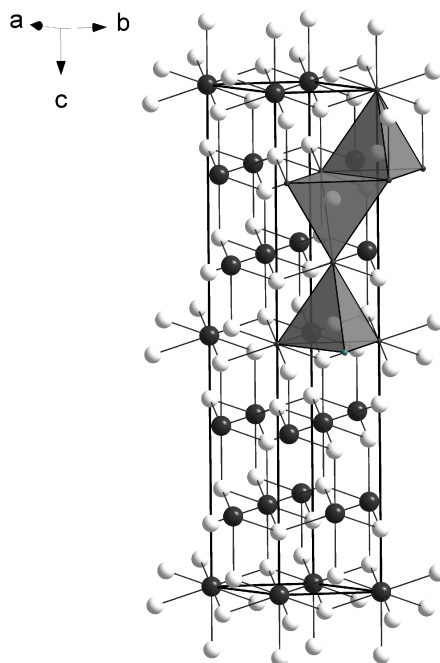


Figure A.2. The crystal structure of spiridonovite. M (Cu,Ag) sites and Te atoms are given as white and black circles, respectively. The tetrahedral coordination of the M sites is shown as isolated polyhedra. The unit cell and the orientation of the structure are outlined.

spiridonovite is far simpler and comprises two Te sites and three M sites, which are occupied by Cu and minor Ag, as reported in Table A.5. The M atoms have four-fold coordination, creating an arrangement of edge-sharing tetrahedra on (110), similarly to what reported for the crystal structure of empressite (AgTe), that shows sheets of edge-sharing AgTe_4 tetrahedra (Bindi et al., 2004). The main difference between the two structures is the environment of tellurium atoms: in empressite there are Te_3 groups, a rare feature in mineral crystal structures, so far reported only in empressite and krennerite Pertlik, 1984. The spiridonovite structure is shown in Figure A.2.

The presence of Ag affects the bond distances (in the range 2.82-2.84 Å; Table 6) that are larger than those reported for Cu tellurides, such as vulcanite (CuTe) (Cameron & Threadgold, 1961), rickardite ($\text{Cu}_{3-x}\text{Te}_2$) (Ford, 1903), cameronite ($\text{Cu}_{5-x}(\text{Cu,Ag})_{3+x}\text{Te}_{10}$) [Bindi and Pinch, 2014], weissite (Cu_{2-x}Te) (Bindi et al., 2013), and henryite ($(\text{Cu,Ag})_{3+x}\text{Te}_2$) Bindi, 2014. Conversely, they are smaller than those observed in Ag-tellurides, such as empressite (AgTe) (Bindi et al., 2004) and hessite (Ag_2Te) (van der Lee & de Boer, 1993). No short metal-metal contacts are

Table A.7. Bond valence sums (v.u.) for spiridonovite.

	M1	M2	M3	Σ Te
Te1	$0.265 \times 2 \rightarrow$		$0.277 \times 3 \downarrow \times 6 \rightarrow$	2.192
		0.267		
Te2	$0.274 \times 3 \downarrow \times 3 \rightarrow$		0.286	2.148
		$0.260 \times 3 \times \downarrow \times 4 \rightarrow$		
	1.087	1.047	1.117	

Table A.8. Minerals belonging to the Cu-Ag-Te system.

Mineral	Formula	Space Group	Cell Values (Å)	V(Å ³)	Z
cameronite [4]	$\text{Cu}_{5-x}(\text{Cu,Ag})_{3+x}\text{Te}_{10}$ (x = 0.43)	<i>C2/c</i>	$a = 17.906(1)$ $b = 17.927(1)$ $c = 21.230(2)$ $\beta = 98.081(8)^\circ$	6747.2(8)	14
empressite [11]	AgTe	<i>Pmnb</i>	$a = 8.882(1)$ $b = 20.100(5)$ $c = 4.614(1)$	823.7(3)	16
henryite [5]	$(\text{Cu,Ag})_{3+x}\text{Te}_2$ (x = 0.40)	<i>Fd-3c</i>	$a = 12.1987(5)$ $a = 8.164(1)$ $b = 4.468(1)$	1815.3(2)	16
hessite [15]	Ag ₂ Te	<i>P2₁/c</i>	$c = 8.977(1)$ $\beta = 124.16(1)^\circ$ $a = 16.58(3)$	271.0(1)	4
krennerite [12]	$(\text{Au}_{1-x}\text{Ag}_x)\text{Te}_2$ (x = 0.2)	<i>Pma2</i>	$b = 8.849(3)$ $c = 4.464(3)$ $a = 3.9727(4)$	654(1)	8
rickardite [14]	$\text{Cu}_{3-x}\text{Te}_2$	<i>Pmmn</i>	$b = 4.0020(5)$ $c = 6.1066(3)$ $a = 3.155(1)$	97.1(1)	2
vulcanite [13]	CuTe	<i>Pmmn</i>	$b = 4.092(1)$ $c = 6.956(1)$ $a = 8.3124(7)$	89.80(3)	2
weissite [3]	Cu_{2-x}Te (x = 0.21)	<i>P3m1</i>	$c = 21.546(1)$	1289.3(2)	24

observed. Bond valence sums (Table A.7), calculated according to the parameters given by Brese and O’Keeffe (1991), and taking into account the refined occupancies (Table A.5), confirm the validity of the structural model.

All the minerals belonging to the Cu-Ag-Te system are shown in Table A.8, together with some crystallographic detail. If we consider a tripled parameter for spiridonovite, we get the cell: $a = 13.89$ and $c = 22.55$ Å. Such a metric has some analogy with that of the β^{III} synthetic compound of the Cu-Te system (Baranova et al., 1974), which exhibits a hexagonal symmetry and $a = 12.54$ and $c = 21.71$ Å. The cell enlargement observed for spiridonovite could be due to the presence of Ag replacing Cu. However, as demonstrated by Pashinkin and Fedorov (2003), the β^{III} synthetic phase is actually an intermetallic compound, with short Cu-Cu and Te-Te contacts, and thus different from spiridonovite. Cameronite ($\text{Cu}_{5-x}(\text{Cu},\text{Ag})_{3+x}\text{Te}_{10}$ [Bindi and Pinch, 2014]) and weissite (Cu_{2-x}Te) (Bindi et al., 2013) have a similar intermetallic nature, showing short bond distances between the metals, characterized by the presence of typical “interpenetrated tetrahedra” due to the short Cu-Cu, Te-Te, and Cu-Te distances.

REFERENCES

- ABSPACK in *CrysAlis RED* (Version Version 1.171.31.2). (2006). Abingdon, Oxfordshire, England., Oxford Diffraction Ltd,
- Baranova, R., Avilov, A., & Pinsker, Z. (1974). Determination of the crystal structure of the hexagonal phase beta III in the Cu-Te system by electron diffraction. *Sov. Phys. Crystallogr.*, 18(6), 736–740.
- Bindi, L., Carbone, C., Belmonte, D., Cabella, R., & Bracco, R. (2013). Weissite from Gambatesa mine, Val Graveglia, Liguria, Italy: Occurrence, composition and determination of the crystal structure. *Mineralogical Magazine*, 77(4), 475–483.
- Bindi, L. (2014). Chemical and structural characterization of henryite, $(\text{Cu},\text{Ag})_{3+x}\text{Te}_2$ ($x \sim 0.40$): A new structure type in the (Ag)–Cu–Te system. *Solid State Sciences*, 38, 108–111. <https://doi.org/10.1016/j.solidstatesciences.2014.10.008>
- Bindi, L., & Pinch, W. W. (2014). Cameronite, $\text{Cu}_{5-x}(\text{Cu},\text{Ag})_{3+x}\text{Te}_{10}$ ($x = 0.43$), from the Good Hope Mine, Vulcan, Colorado: Crystal structure and revision of the chemical formula. *The Canadian Mineralogist*, 52(3), 423–432. <https://doi.org/10.3749/canmin.52.3.423>
- Bindi, L., Spry, P. G., & Cipriani, C. (2004). Empressite, AgTe, from the Empress-Josephine mine, Colorado, U.S.A.: Composition, physical properties, and determination of the crystal structure. *American Mineralogist*, 89(7), 1043–1047. <https://doi.org/10.2138/am-2004-0715>
- Brese, N. E., & O’Keeffe, M. (1991). Bond-valence parameters for solids. *Acta Crystallographica Section B Structural Science*, 47(2), 192–197. <https://doi.org/10.1107/S0108768190011041>

- Cameron, E. N., & Threadgold, I. M. (1961). Vulcanite, a new copper telluride from Colorado, with notes on certain associated minerals. *American Mineralogist: Journal of Earth and Planetary Materials*, 46(3-4 Part 1), 258–268.
- CrysAlis RED (Version Version 1.171.31.2). (2006). Abingdon, Oxfordshire, England., Oxford Diffraction Ltd,
- Ford, W. (1903). Rickardite, a new mineral. *American Journal of Science*, 15(85), 69.
- Hartley, T. (1983). Geology and mineralization of the Vulcan-Good Hope Massive Sulfide Deposit, Gunnison County, Colorado. *Gunnison gold belt and powderhorn carbonatite field trip guidebook: Dregs* (Handfield, R.C., editor, pp. 19–27).
- Pashinkin, A., & Fedorov, V. (2003). Phase equilibria in the Cu–Te system. *Inorganic Materials*, 39(6), 539–554.
- Pertlik, F. (1984). Crystal chemistry of natural tellurides II: Redetermination of the crystal structure of krennerite, $(\text{Au}_{1-x}\text{Ag}: x)\text{Te}_2$ with $x \sim 0.2$. *Tschermaks Mineralogische und Petrographische Mitteilungen*, 33(4), 253–262.
- Sheldrick, G. M. (2008). A short history of SHELX. *Acta Crystallographica Section A Foundations of Crystallography*, 64(1), 112–122. <https://doi.org/10.1107/S0108767307043930>
- van der Lee, A., & de Boer, J. L. (1993). Redetermination of the structure of hessite, Ag_2Te -III. *Acta Crystallographica Section C Crystal Structure Communications*, 49(8), 1444–1446. <https://doi.org/10.1107/S0108270193003294>
- Wilson, A. J. C. (1992). *International Tables for Crystallography: Mathematical, physical, and chemical tables* (Vol. 3). International Union of Crystallography.

2 Exploring the role of halide mixing in lead-free BZA_2SnX_4 two dimensional hybrid perovskites

This chapter was published as an article in *Journal of Material Chemistry A* as:

Pisanu A., Coduri M., Morana M., Ciftci Y.O., Rizzo A., Listorti A., Gaboardi M., Bindi L., Queloiz V. I. E., Milanese C., Grnacini G. and Malavasi L. (2020). Spiridonovite, Exploring the role of halide mixing in lead-free BZA_2SnX_4 two dimensional hybrid perovskites. *Journal of Material Chemistry A*, 8, 1875
<https://doi.org/10.1039/C9TA11923J>

ABSTRACT

The role of halide substitution in a lead-free 2D hybrid perovskite is investigated on the BZA_2SnX_4 (BZA=benzylammonium; X=Cl, Br and I) system, by reporting the synthesis and the structural analysis by means of single-crystal X-ray diffraction data of the two novel compositions BZA_2SnBr_4 and BZA_2SnCl_4 . In addition, the mixed composition $BZA_2Sn(BrxI_{1-x})_4$ ($0 \leq x \leq 1$) has been prepared by mechanochemical synthesis confirming the existence of a wide solid solubility between the two end-members. The absorption and emission spectra revealed a wide tuning of the band-gap by changing the halide, covering more than 300 nm in the visible range. Combined experimental and DFT calculations provide a complete picture of the electronic and structural properties of the BZA_2SnX_4 system, revealing a strong influence of the halide on the orientation for the benzylammonium cation, on the hydrogen bonding system within the perovskite network, and on the distortion of the octahedra.

B.1 INTRODUCTION

The field of organic–inorganic hybrid halide perovskites has recently moved towards two-dimensional (2D) systems, which provide an impressive space for material engineering and tailoring of desired functions with concomitant excellent photophysical properties (Gangadharan & Ma, 2019; Gao, Nazeeruddin, et al., 2018; Grancini & Nazeeruddin, 2019; Mao et al., 2018; Wang et al., 2019; Wang et al., 2018). Among the several classes of 2D perovskites, recently and deeply reviewed in Gao, Nazeeruddin, et al. (2018), the one comprising (100)-oriented 2D materials

is by far the most abundant and explored. They consist of alternating organic–inorganic layers with corner-sharing $[\text{MX}_6]^{4-}$ units and organic spacers between them. They can form Ruddlesden–Popper (RP) and Dion–Jacobson phases depending on the nature of the A site organic group(s) (Gao, Nazeeruddin, et al., 2018). Further, among the RP phases, the $n=1$ members, with general formula A_2PbX_4 (A= monovalent organic cation; X =halide) have received significant attention for their optoelectronic properties and material robustness. Calabrese et al., 1991; Gao, Nazeeruddin, et al., 2018; Kamminga et al., 2016; Li et al., 2017; Mao et al., 2016; Smith et al., 2014 However, the plethora of organic spacers and the extension of the homologous series ($n > 1$), allow for a huge variety of materials to be engineered for tailored applications, including the solid solubility of mixed organic cations on the A-site of the 2D perovskite (Gao, Nazeeruddin, et al., 2018). On the opposite, the exploration of halide mixing approach on 2D hybrid perovskites has been very limited to date, with few examples related to the optimization of quantum yield of white-light emission (Dohner et al., 2014; Gao, Nazeeruddin, et al., 2018; Yang et al., 2018). This is quite surprising, considering the success of this approach on 3D materials and 0D nanocrystals (Calabrese et al., 1991; Hong et al., 2019; Karmakar et al., 2019). Finally, another poorly explored area of research on 2D hybrid perovskites is the preparation and characterization of lead-free systems. The few examples available confirm the known (on 3D perovskites) tunability of band-gap and optical properties induced by tin or germanium replacement (Cheng et al., 2018; Mao et al., 2018). Based on the above considerations, we explored the role of halide mixing on a tin-based 2D hybrid perovskite, namely BZA_2SnX_4 (BZA=benzylammonium; X= Cl, Br and I). In particular, we afforded the preparation of the novel Br/I mixed system in order to define the possible existence and extension of such solid solution, as well as the preparation of $\text{BZA}_2\text{SnCl}_4$. We highlight that among the compounds of this series, only BZA_2SnI_4 is actually known in the current literature (Mao et al., 2016). Mao et al. (2016) explored the synthesis of the $\text{BZA}_2\text{Pb}_{1-x}\text{Sn}_x\text{I}_4$ solid solution, showing a significant reduction of the band-gap by progressively replacing Sn for Pb, with an anomalous (non Vegard) trend with metal mixing (Mao et al., 2016). In the same work, the crystal and electronic structures were provided, showing, for example, that the inorganic layers in the compounds adopt a staggered motif (Mao et al., 2016). Due to the peculiar structural properties of 2D halide perovskite, it is of significant interest to investigate the evolution of the crystal and optical properties as a function of the halide substitution, being the two BZA groups coordinating two adjacent halides.

B.2 RESULTS AND DISCUSSION

Samples of the $\text{BZA}_2\text{Sn}(\text{Br}_x\text{I}_{1-x})_4$ series have been prepared in form of polycrystalline powders by high energy ball-milling. This approach, very scarcely

Table B.1. Atomic coordinates in the structure of BZA₂SnI₄ resolved from single crystal X-ray diffraction.

		<i>x</i>	<i>y</i>	<i>z</i>	<i>msf</i> (Å ²)	<i>s.o.f.</i>
Sn	Sn1	0.5	0	0.5	0.03688(13)	1
I	I1	0.28824(4)	0.29076(4)	0.49275(2)	0.04951(13)	1
I	I2	0.54468(5)	0.02018(5)	0.39134(2)	0.05508(14)	1
N	N1	.5804(6)	00.4342(7)	0.4134(2)	0.0616(13)	1
C	C1	0.4755(11)	0.5499(9)	0.3934(3)	0.076(2)	1
C	C2	0.4428(7)	0.5136(7)	0.3438(3)	0.0547(14)	1
C	C3	0.3334(7)	0.4091(10)	0.3330(3)	0.076(2)	1
C	C4	0.2993(9)	0.3781(14)	0.2872(4)	0.099(3)	1
C	C5	0.3741(12)	0.4491(11)	0.2522(3)	0.089(3)	1
C	C6	0.4825(11)	0.5524(11)	0.2625(3)	0.084(2)	1
C	C7	0.5162(9)	0.5835(9)	0.3081(3)	0.0721(19)	1
H	H1NA	0.5471	0.3395	0.4080	0.092	1
H	H1NB	0.5884	0.4490	0.4439	0.092	1
H	H1NC	0.6680	0.4455	0.4001	0.092	1
H	H1A	0.3851	0.5492	0.4112	0.091	1
H	H1B	0.5179	0.6522	0.3955	0.091	1
H	H3	0.2826	0.3595	0.3568	0.092	1
H	H4	0.2250	0.3084	0.2802	0.119	1
H	H5	0.3515	0.4273	0.2214	0.107	1
H	H6	0.5333	0.6016	0.2387	0.101	1
H	H7	0.5905	0.6535	0.3148	0.087	1

applied to 2D hybrid perovskites, is becoming of wider interest because it is green, scalable, and can easily allow the synthesis of hybrid perovskites as well as allinorganic perovskites for photovoltaics. Besides, stoichiometric BZA₂SnX₄ compounds (X=Cl, Br, and I) were grown as single crystals for a more accurate determination of their crystal structure. The crystal structure of BZA₂SnI₄ was re-investigated, and agrees with the previous determination provided in Mao et al. (2016). The compound shows an orthorhombic unit cell (space group, s.g., *Pbca*) with lattice parameters of $a = 9.1105(1)$ Å, $b = 8.6776(1)$ Å, and $c = 28.754(6)$ Å (Mao et al., 2016). The determination of the crystal structures of the novel compounds BZA₂SnBr₄ and BZA₂SnCl₄ by single crystal X-ray diffraction revealed that they are orthorhombic (s.g. *Cmc2₁*), with lattice parameters $a = 33.2806(1)$ Å, $b = 8.1046(4)$ Å, and $c = 8.1036(4)$ Å for BZA₂SnBr₄, and $a = 33.505(3)$ Å, $b = 7.7784(6)$ Å, and $c = 7.7678(5)$ Å for BZA₂SnCl₄ (Tables 1–3).

Although the *Pbca* and *Cmc2₁* space groups have different settings (mainly due

Table B.2. Atomic coordinates in the structure of BZA₂SnBr₄ resolved from single crystal X-ray diffraction.

		<i>x</i>	<i>y</i>	<i>z</i>	<i>msf</i> (Å ²)	<i>s.o.f.</i>
Sn	Sn1	0.5	0.2503(2)	0.5221(5)	0.0411(2)	1
Br	Br1	0.5	0.4385(3)	0.2085(3)	0.0594(7)	1
Br	Br2	0.5	-0.0623(3)	0.3325(2)	0.0524(6)	1
Br	Br3	0.41079(3)	0.2505(4)	0.5218(8)	0.0738(3)	1
N	N1	0.4224(3)	0.1703(19)	0.0996(14)	0.067(3)	1
C	C1	0.4012(3)	0.291(3)	-0.003(3)	0.080(5)	1
C	C2	0.3569(2)	0.258(3)	0.011(3)	0.081(3)	1
C	C3	0.3352(7)	0.136(3)	-0.068(4)	0.122(10)	1
C	C4	0.2938(7)	0.129(4)	-0.047(6)	0.185(16)	1
C	C5	0.2748(4)	0.238(4)	0.060(6)	0.190(15)	1
C	C6	0.2968(6)	0.357(3)	0.143(5)	0.159(13)	1
C	C7	0.3380(6)	0.364(3)	0.119(4)	0.111(10)	1
H	H1NA	0.4488	0.1880	0.0930	0.101	1
H	H2NB	0.4145	0.1805	0.2040	0.101	1
H	H3NC	0.41689	0.0689	0.0640	0.101	1
H	H1A	0.4097	0.2814	-0.1169	0.096	1
H	H1B	0.4071	0.4022	0.0347	0.096	1
H	H3	0.3482	0.0584	-0.1338	0.146	1
H	H4	0.2788	0.0521	-0.1051	0.222	1
H	H5	0.2472	0.2302	0.0757	0.228	1
H	H6	0.2841	0.4312	0.2131	0.191	1
H	H7	0.3531	0.4414	0.1773	0.134	1

Table B.3. Atomic coordinates in the structure of BZA₂SnCl₄ resolved from single crystal X-ray diffraction.

		<i>x</i>	<i>y</i>	<i>z</i>	<i>msf</i> (Å ²)	<i>s.o.f.</i>
Sn	Sn1	0.5	0.25148(18)	0.5294(6)	0.0454(2)	1
Cl	Cl1A	0.5	0.4088(18)	0.234(3)	0.070(4)	0.5
Cl	Cl1B	0.5	0.4675(18)	0.181(3)	0.070(4)	0.5
Cl	Cl2A	0.5	-0.0346(13)	0.3622(12)	0.0384(15)	0.5
Cl	Cl2B	0.5	-0.1143(12)	0.3355(14)	0.0384(15)	0.5
Cl	Cl3	0.41561(7)	0.2558(7)	0.5318(18)	0.0800(7)	1
N	N1	0.4254(3)	0.1832(17)	0.1179(13)	0.057(2)	1
C	C1	0.4033(3)	0.269(2)	-0.0205(16)	0.065(4)	1
C	C2	0.35900(19)	0.2689(16)	0.0268(16)	0.064(2)	1
C	C3	0.3378(5)	0.143(2)	-0.060(2)	0.096(6)	1
C	C4	0.2971(4)	0.131(2)	-0.034(3)	0.117(7)	1
C	C5	0.2783(3)	0.240(3)	0.079(3)	0.142(11)	1
C	C6	0.2993(4)	0.362(3)	0.171(3)	0.126(8)	1
C	C7	0.3400(4)	0.374(2)	0.143(2)	0.085(5)	1
H	H1NA	0.4200	0.2343	0.2178	0.085	1
H	H1NB	0.4514	0.1898	0.0967	0.085	1
H	H1NC	0.4181	0.0733	0.1232	0.085	1
H	H1A	0.4073	0.2090	-0.1284	0.079	1
H	H1B	0.412689	0.38639	-0.0338	0.079	1
H	H3	0.3507	0.0683	-0.1342	0.115	1
H	H4	0.048658	0.282381	-0.093367	0.140	1
H	H5	0.2509	0.2318	0.0945	0.171	1
H	H6	0.2866	0.4344	0.2485	0.151	1
H	H7	0.3548	0.4545	0.2036	0.102	1

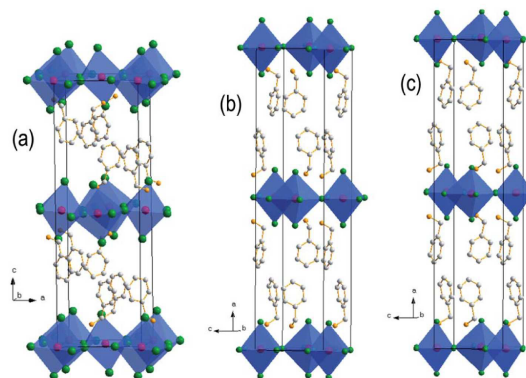


Figure B.1. Room temperature sketch as determined from single crystal diffraction for (a) BZA_2SnI_4 , (b) $\text{BZA}_2\text{SnBr}_4$, and (c) $\text{BZA}_2\text{SnCl}_4$. Sn atoms are depicted in red, halide in green, C in white and N in yellow.

to the different Bravais lattice), we use that of BZA_2SnI_4 for sake of clarity and data representation taking into account that $a_I = c_{\text{Br,Cl}}$, $b_I = b_{\text{Br,Cl}}$, and $c_I = a_{\text{Br,Cl}}$ (the subscripts I, Br, and Cl indicate the halogen of the different compounds). A sketch of the three structures is reported in Fig. [B.1](#).

As it can be appreciated from the lattice parameters data reported above and in Fig. [B.1](#) the change from iodide to bromide induces an expansion of the c -axis of the crystal structure, passing from about 28 Å in BZA_2SnI_4 to about 33 Å in $\text{BZA}_2\text{SnBr}_4$, and a reduction of the in-plane parameters (due to the relative ion size of Br^- and I^-). Such elongated structure is also found for the chloride member, with even a slight further expansion of the c -axis with respect to $\text{BZA}_2\text{SnBr}_4$. The out-of-plane elongation is essentially due to the change in the staggering of the two benzylammonium cations which move apart the two halides passing from an interlayer halide–halide distance of 9.31 Å (I–I) through 11.44 Å (Br–Br), to 11.76 Å (Cl–Cl). The tilt of the organic molecule with respect to the long cell axis increases from $\sim 9^\circ$ for $\text{BZA}_2\text{SnBr}_4$ and $\text{BZA}_2\text{SnCl}_4$, up to 17.4° for BZA_2SnI_4 , thus facilitating the staggering of the organic cations with consequence shrinking of the long cell axis. The protonated ammonium ion connects to the apical halides through hydrogen bonding showing a significant reduction of the donor–acceptor distance passing from about 3.6 Å for BZA_2SnI_4 to about 3.5 Å for $\text{BZA}_2\text{SnBr}_4$ down to 3.2 Å for $\text{BZA}_2\text{SnCl}_4$. The role of hydrogen bonding in driving electronic and structural properties of hybrid perovskites is well known and discussed in many recent papers (El-Mellouhi et al., [2016](#); Lee et al., [2016](#); Svane et al., [2017](#); Tan et al., [2017](#); Zheng et al., [2017](#)). The list of interatomic distances and angles of interest is given in Tables [B.4](#) and [B.5](#).

The distortion inside the inorganic framework was evaluated by looking at

Table B.4. Octahedral interatomic distances in the structure of BZA₂SnX₄.

	BZA ₂ SnI ₄	BZA ₂ SnBr ₄	BZA ₂ SnCl ₄
apical	3.1557(9) Å (x 2)	2.977(1) Å (x 2)	2.823(3) Å (x 2)
equatorial	3.200(3) Å (x 2)	2.965(4) Å (x 1)	3.015(11) Å (x 1)
		2.964(4) Å (x 1)	2.966(11) Å (x 1)
	3.183(2) Å (x2)	2.940(4) Å (x 1)	2.743(10) Å (x 1)
		2.942(4) Å (x 1)	2.690(11) Å (x 1)

Table B.5. Sn-X-Sn bond angles within the inorganic layer in the structure of BZA₂SnX₄.

	BZA ₂ SnI ₄	BZA ₂ SnBr ₄	BZA ₂ SnCl ₄
Sn-X ₁ -Sn	160.57(2)°	151.9(1)°	151.1(4)°
Sn-X ₂ -Sn	-	152.4(1)°	144.3(4)°

the Sn-X-Sn angle and the Sn-X bond distances. For BZA₂SnI₄ the Sn-I-Sn angle is 160.6°, in agreement with previous determinations, while the distortion index of the bond length has been found to be 0.0049, which compares to 152° and 0.0039 for BZA₂SnBr₄. As for BZA₂SnCl₄, the equatorial site split leads to an alternation of wide (154°) and narrow (144°) Sn-X-Sn angles, indicating a greater distortion between the octahedra moving towards the smaller halide (Lufaso & Woodward, 2004; Mao et al., 2016). Interestingly, the octahedral distances evolve significantly with the nature of the halide: the apical bond length contracts moving from I (3.16 Å) through Br (2.98 Å) and Cl (2.82 Å), in keeping with the halide ionic radii. A similar behavior is observed for the average of equatorial bonds, which decreases from 3.192(10) Å for I to 2.964(14) Å for Br and 2.85(16) Å for Cl. Therefore, the octahedra become more distorted moving to Cl. A possible Cl-site splitting is discussed in the “Experimental methods”. The in-plane lattice parameters follow, on the other hand, a trend reflecting the different size of the halide, with a continuous decrease of the a and b axes going from BZA₂SnI₄ to BZA₂SnCl₄. The orthorhombic distortion of the unit cell is relevant for the iodide-containing perovskite while it becomes significantly smaller for the other two compositions. After having elucidated the specific crystal structure of line compounds, providing the information on the novel BZA₂SnBr₄ and BZA₂SnCl₄ materials, we afforded the investigation of the polycrystalline samples of the possible BZA₂Sn(Br_xI_{1-x})₄ solid solution. The synthesized samples are reported in Fig. B.2a, as obtained from the ball-milling synthesis, showing a progressive change of color from brilliant yellow of BZA₂SnBr₄ to dark red of BZA₂SnI₄. Their powder X-ray diffraction (XRD) patterns are shown in Fig. B.2b. The elemental analysis on selected specimens by energy dispersive spectroscopy (EDS)

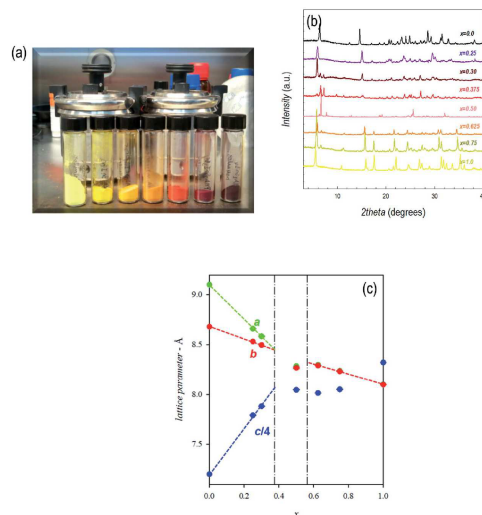


Figure B.2. (a) Photo of some of the samples synthesized by ball-milling; (b) room temperature XRD patterns of the samples of the $BZA_2Sn(Br_xI_{1-x})_4$ system; (c) lattice parameters of the samples reported in (b) keeping the setting of the I-member for simplicity.

is reported in the Table [B.6](#), indicating a good correlation between nominal and effective stoichiometries with only a slight, but systematic, enrichment in Br in the mixed I/Br samples.

From the analysis of the diffraction patterns of Fig. [B.2b](#), we found that single-phase materials do not exist in the complete compositional range of Br/I halide mixing. In the $\sim 0.40 < x < \sim 0.55$ compositional region we observed peaks pertaining to a new phase, that will be discussed later on this chapter. The XRD patterns of the single-phase samples of the $BZA_2Sn(Br_xI_{1-x})_4$ solid solution shown in Fig. 2b were refined in order to determine the lattice parameters, which are reported

Table B.6. Elemental composition of some selected samples probed by EDX, where x refers to $BZA_2Sn(Br_xI_{1-x})_4$ composition and X/Sn indicates the halide to Sn ratio, which is 4 for a full 2D composition. E.s.d. for the measurements is around 5%.

nominal x	exp x	exp X/Sn
1.000	-	3.90
0.75	0.753	4.10
0.625	0.636	4.14
0.250	0.275	4.09
0	-	3.96

Table B.7. Lattice parameters in Å of the BZA₂Sn(Br_xI_{1-x})₄ solid solution from powder X-ray diffraction in the same setting.

x	a	b	c
1	8.1007(6)	8.0993(8)	33.287(3)
0.75	8.2367(9)	8.2318(9)	32.207(5)
0.625	8.297(2)	8.290(1)	32.056(5)
0.5	8.285(8)	8.268(8)	32.184(7)
0.3	8.584(4)	8.496(3)	31.524(8)
0.25	8.660(3)	8.532(3)	31.166(9)
0	9.101(1)	8.680(1)	28.802(3)

in Fig. B.2c and listed in Table B.7.

Looking at the a , b parameters, we note a progressive linear contraction passing from BZA₂SnI₄ to BZA₂SnBr₄, accompanied by a reduction of their relative difference. Let us remember that in BZA₂SnBr₄ we observed $a = 8.1046(4)$ Å and $b = 8.1036(4)$ Å, i.e. an extremely small orthorhombic distortion (as a matter of fact, in Fig. A.2c, such a difference is so small that is graphically covered by the marker). Below $x = 0.625$, the two parameters have always a very small orthorhombic distortion, which starts to be significant from $x = 0.3$, i.e. in the iodide-rich samples. This behavior correlates to the reduced octahedral distortion of BZA₂SnBr₄ (see above) which clearly manifests already for mixed halide compositions of the Br-rich side. Also, the linear dependence of lattice parameters with x helped us to estimate the compositional region where the 2D perovskite is likely absent, indicated by vertical dashed lines in Fig. B.2c. An interesting behavior is shown by the trend of the c -axis. As we reported above, there is a lengthening of nearly 5 Å when moving from iodide to bromide, which is due to the different orientation of the benzylammonium cations between the inorganic layers. The expansion of the c -axis from BZA₂SnI₄ up to $x = 0.3$ is linear (see Fig. A.2c) and becomes flatter in the Br-rich side of the solid solution, until the final value of 33.2806(1) Å is attained for BZA₂SnBr₄. There are several factors that play a role when moving from $x = 0$ to $x = 1$, such as the change of the staggering mode of organic cations, the distortion of the octahedra and the hydrogen bonding between the halide and the amine group. The interplay of such effects, clearly more effective in the Br-rich mixed compositions, defines the trend of the c -axis. Interestingly, an anomalous trend in the lattice parameters has been very recently observed in the BZA₂Pb(Br_xCl_{1-x})₄ system (Jung, 2019). Thermal properties of the BZA₂Sn(Br_xI_{1-x})₄ solid solution have been determined by thermogravimetry (TGA) and Differential Scanning Calorimetry (DSC). TGA curves show a general stability of the phases up to about 150 °C ; after that a significant

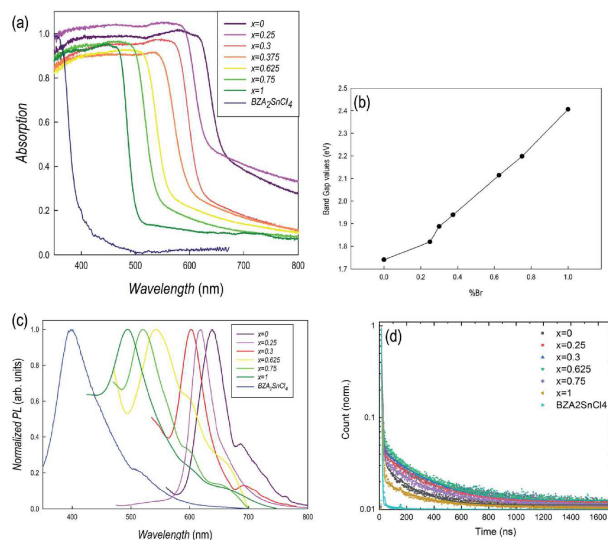


Figure B.3. (a) Absorption spectra of the $\text{BZA}_2\text{Sn}(\text{Br}_x\text{I}_{1-x})_4$ system; (b) trend of the band-gap as a function of x ; (c) PL measurements for the samples of the of the $\text{BZA}_2\text{Sn}(\text{Br}_x\text{I}_{1-x})_4$ system; (d) PL decay at the peak emission upon excitation at 375 nm.

weight loss is found with an apparent slightly greater temperature stability for $\text{BZA}_2\text{SnBr}_4$. DSC measurements in the $80^\circ\text{C} < T < 100^\circ\text{C}$ interval do not show any thermal event suggesting phase transition in the system. The samples are fully stable after six months of storage under inert atmosphere in the glove-box, as confirmed by UV-Vis spectra and diffraction measurements. On the other hand, we performed an aging test on the BZA_2SnI_4 sample (selected as representative) by exposing it to laboratory air (RH around 40%) and collecting UV-Vis spectra and diffraction patterns after 1, 5 and 10 days. The same test has been performed on the lead-based analogue, i.e. BZA_2PbI_4 . The BZA_2SnI_4 sample shows a clear change of diffraction as well as optical properties under air already after 24 hours. It is worth noticing that the absorbance significantly red-shifts during aging and that a vacuum treatment after 10 days of air-exposure partially relieves the initial situation suggesting a certain level of reversibility of the air-induced effects. On the other hand, BZA_2PbI_4 sample is fully stable up to 10 days, indicating a positive effect of a large organic cation towards moisture stability. The optical properties of the samples reported above have been investigated by absorption and steady-state photoluminescence (PL) spectroscopies. Fig. B.3a reports the absorption spectra of the single-phase mixed samples of the $\text{BZA}_2\text{Sn}(\text{Br}_x\text{I}_{1-x})_4$ system together with the $\text{BZA}_2\text{SnCl}_4$ sample, while Fig. B.3b shows the trend of the band-gap determined from the Tauc plots of the spectra for the single-phase samples of the $\text{BZA}_2\text{Sn}(\text{Br}_x\text{I}_{1-x})_4$ solid solution.

A clear blue-shift is observed in the spectra by moving from BZA_2SnI_4 to BZA_2SnBr_4 , with a linear increase of the band-gap from 1.74 eV to 2.41 eV (Jung, 2019; Mao et al., 2016). The analogous lead-based 2D hybrid perovskites, namely BZA_2PbI_4 to BZA_2PbBr_4 , exhibit band-gaps of about 2.20 eV and 2.90 eV, respectively, thus confirming the usual ~ 0.6 – 0.7 eV difference between Pb and Sn systems found in 3D perovskites (Frost et al., 2014; Mosconi et al., 2015). This is interesting considering the different local environment of 3D and 2D hybrid perovskites. However, DFT calculations performed on similar systems revealed that, in general, the valence band maximum (VBM) is dominated by metal s-orbitals and halide orbitals, while the conduction band minimum (CBM) is dominated by empty metal p-orbitals. This indicates that, qualitatively, the electronic structure is similar to that of the 3D perovskites, which is in agreement with the “rigid” shift of about 0.5 eV observed when passing from Pb to Sn systems. The band-gap of BZA_2PbCl_4 is found at about 3.04 eV which again is in line with the expected variations moving from bromide to chloride (Mancini et al., 2015). Steady-state PL (Fig. B.4c) reveals a quite narrow emission by all the samples (around 40 nm) with a progressive blue-shift by moving from iodide to chloride anion, covering in the whole nearly 300 nm from I to Cl. There is also slight increase of emission peak width by replacing I with Br and Cl. Fig. B.3d reports the PL decay upon excitation at 375 nm. The decay show only marginal difference among the samples, with a first fast component followed by a slower decay which is completed in the first microsecond time window. The fast component can be assigned to rapid electron–hole recombination while the longer living tail to trap-mediated recombination. Notably, for the Cl sample only a fast decay is observed while the second component is vanished out.

Further insight into the electronic structure of the present samples has been obtained by DFT calculations. For the structural optimization, the structure determined experimentally was used as the starting geometry. The theoretical ground-state structure was obtained from this, by full geometry optimization, that is, the atom positions and cell parameters were fully relaxed. Geometry optimization of BZA_2SnX_4 in orthorhombic structure ($Pbca$) for $X = I$ and $Cmc2_1$ for $X = Br, Cl$ was performed using the DMol3 program in the spin unrestricted approach (see computational details in the Experimental section). The calculated structural parameters and the related experimental data correspond to experimental values with an error range of 0.08–5.5%, which confirms the validity of our calculation. The calculated electronic band structure of BZA_2SnX_4 ($X = I, Br, \text{ and } Cl$) along high symmetry points of the first Brillouin zone are plotted in Fig. B.4, where the labeled k-points are present as $G(0, 0, 0)$, $Z(0, 0, 0.5)$, $T(-0.5, 0, 0.5)$, $Y(-0.5, 0, 0)$, $S(-0.5, 0.5, 0)$, $X(0, 0.5, 0)$, $U(0, 0.5, 0.5)$, and $R(-0.5, 0.5, 0.5)$. The maximum of the valence band (VBM) and the minimum of the conduction band (CBM) occur at G for BZA_2SnI_4 and Y the point in the Brillouin zone for BZA_2SnX_4 . All of the BZA_2SnX_4 structures were found to have direct band gaps

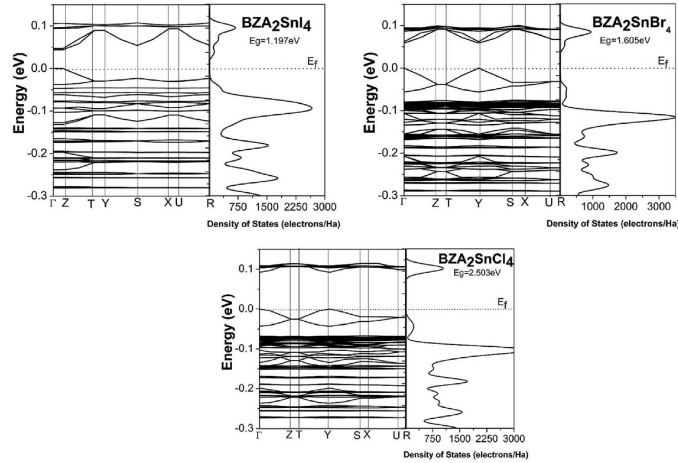


Figure B.4. DFT calculations of electronic band structures for BZA_2SnX_4 ($X = I, Br, \text{ and } Cl$).

which are consistent with the observed steepness of the absorption edges in the spectra. The calculated energy gaps are 1.197 eV, 1.605 eV, and 2.503 eV which are underestimated compared to the experimental value of 1.7 eV, 2.4 eV, and 3.04 eV. This value of the energy gap demonstrates that the material belongs to the semiconductor family. When we go from Cl to I, the band gap decreases due to increasing electronic charge density and lattice constants. Therefore, from Cl to I, number of atom and number of electrons in the crystals increases. As a result, the valence band shifts up to Fermi level due to the occupation of electrons in the position near Fermi level, result in a decrease in the energy gap between valence and conduction bands. Such an underestimation of the calculated band gaps is an intrinsic property of the ab initio method and is related to the DFT limitations, namely, not taking into account the discontinuity in the exchange-correlation potential. Our obtained band gap value for BZA_2SnI_4 (1.197 eV) is in good agreement with other DFT result (1.33 eV) by Mao et al. (2018). The total electronic density of states (TDOS) and partial density of states (PDOS) using the calculated lattice constants of BZA_2SnX_4 are given in Fig. B.5. The properties observed in the PDOS spectra of the BZA_2SnX_4 are similar to each others. From the PDOS of BZA_2SnX_4 it is possible to see the distribution of various electronic states in the valence and in the conduction band. In the lower valence band region, s-states of N are dominant and with less contribution of s-states of C. The s-states of H and p-states of N can overlap with the p-states of C in the energy range between -0.45 Ha and -0.3 Ha and can form covalent bonds. The d- and p-states for Sn and C atoms, respectively, are dominantly contributing to the valence band in the

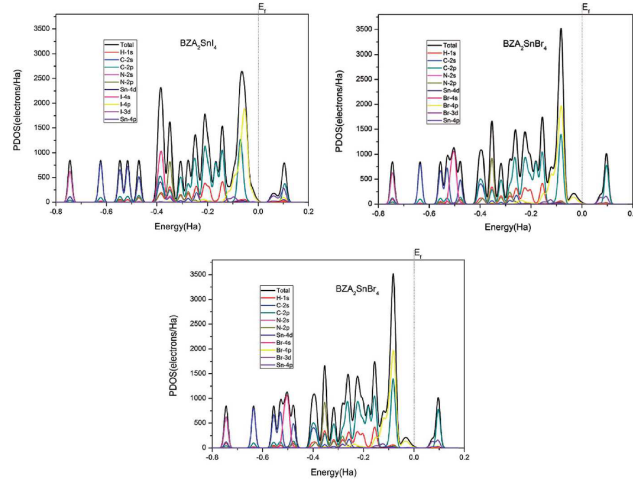


Figure B.5. DFT calculations of total and partial density of states (PDOS) for BZA_2SnX_4 ($X= I, Br, \text{ and } Cl$).

range between -0.3 Ha and -0.22 Ha. Both s - and p -states of H and Sn atoms also contribute to the VB. The p -states of C and s -states of H are distributed energetically in the same range and thus they can effectively overlap and form very strong covalent bonds. Although the p -state of C for X is energetically degenerate with that of Sn, in the whole valence band, the spatial separation of these two atoms makes no covalent bonding between Sn and X. The d -state of Sn is well localized which leads to ionic bonding between Sn and X. Below the Fermi level, VBM is dominated by X p -orbitals and less C p -orbitals. The conduction bands are derived largely from the C p - and Sn p -states. Moreover, to Cl from I, the hybridism interaction between C and Sn atoms increased because of the smaller electronegativity of I, which shifts the C p states to high energy, as can be seen from Fig. B.5. This result is in agreement with the band gap increase from I to Cl and may be attributed to the hybridization of C p - and Sn p -states near the Fermi level. Notably, it is found that C p -states have a relatively high value, which indicates that the electron transits directly from the Sn p - to C p -states. This result suggests a high mobility and a low resistivity in BZA_2SnX_4 .

To further improve the understanding of the bonding interactions, we also computed a charge density analysis. From the illustration in Fig. B.6 it is clear that C, H, and N atoms in the organic linker form a BZA_2SnX_4 structural subunit. As a result, the C–C, C–H, and C–N bonding interactions are dominantly covalent in character. Moreover, there is a substantial charge density distributed between C atoms, and between C, H and N atoms, indicating the presence of covalent bonding. From Fig. B.6 it can be seen that the charges are spherically distributed

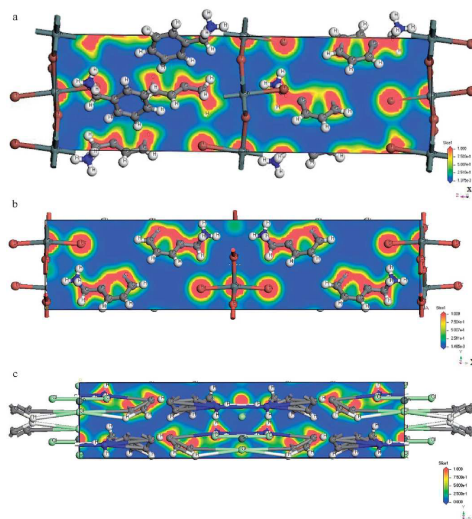


Figure B.6. Calculated charge density for BZA_2SnX_4 ($X= I, Br, \text{ and } Cl$) within the $[110]$ plane.

at the X and Sn sites, which is characteristic of systems having ionic interactions. Additionally, there is no noticeable charge density distributed between X and Sn atoms which clearly demonstrate the presence of ionic bonding.

Concerning the hydrogen bonding, it can be seen from the unit cell of Fig. B.7 that the three H atoms of the $-NH_3^+$ group in BZA are attracted toward the surrounding halogen atoms of the perovskite cage in BZA_2SnX_4 , forming at least three X/H(-N) intermolecular contacts. This is evidence of the occurrence of intermolecular contacts; two of these contacts are short and equivalent, with $d(X-H(-N)) = 1.036 \text{ \AA}$, 1.038 \AA and 1.051 \AA . These are hydrogen bonds since each of these three intermolecular distances is significantly smaller than the sum of the van der Waals radii of the Sn and H atoms, 3.62 \AA ($Sn = 2.42 \text{ \AA}$ and $H = 1.20 \text{ \AA}$) (Desiraju et al., 2013; Desiraju & Steiner, 2001; Munshi & Guru Row, 2005). This result indicates that there is big penetration between the non-covalently bound X and H atoms involved in hydrogen bond formation in this system, making the entire structure compact and stable (Desiraju et al., 2013; Munshi & Guru Row, 2005).

The H atoms of the $-CH_3$ group of the BZA also form intermolecular contacts with the X atoms of the perovskite cage. C-H bond lengths are 1.093 \AA , 1.097 \AA and 1.091 \AA for BZA_2SnX_4 . Each of these contact distances is slightly smaller than the sum of the van der Waals radii of the H (1.2 \AA) and X (2.04 , 1.86 and 1.82 \AA) atoms, 3.24 \AA . This means that the hydrogen bonds formed between the H atoms of the $-CH_3$ group and the Sn atoms of the perovskite cage may have a

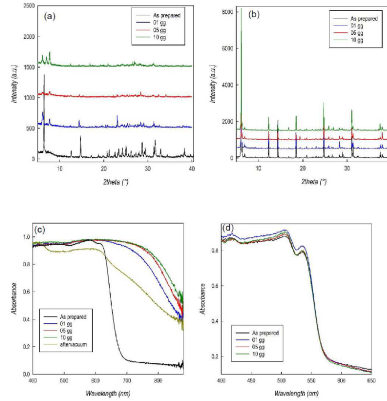


Figure B.7. XRD patterns of BZA₂SnI₄ (a) and BZA₂PbI₄ (b) as a function of time under laboratory-air exposure and UV-Vis spectra of BZA₂SnI₄ (c) and BZA₂PbI₄ (d) as a function of time under laboratory-air exposure.

relevance. The X/H(-N) hydrogen bonds are stronger than the X/H(-C) hydrogen bonds in BZA₂SnX₄ because of shorter bond lengths. However, from the angle of approach for hydrogen bond formation, it can be concluded that the X/H(-C) hydrogen bonds are more directional than the X/H(-N) hydrogen bonds. It is generally believed that the more linear (directional) non-covalent interactions are stronger than others. This means that the -NH₃⁺ and -CH₃ groups of the BZA are strongly competitive with each other in forming hydrogen bonded interactions with the X cage in BZA₂SnX₄.

B.2.1 New 1D perovskite

The XRD patterns of the solid solutions of Fig. 2 showed clear evidence of another phase especially in the $\sim 0.40 < x < \sim 0.55$ compositional range. In particular, this occurred for all the replica of the 50% I/Br samples, while attempts to obtain the new phase pure in Br or I, either via ball milling or by solution, failed. This suggests that the coexistence of mixed halides is crucial for its formations. In order to unveil the nature of the phase formed, we applied solution synthesis to grow single crystals of the BZA₂Sn(Br_xI_{1-x})₄ solid solution with $x = 0.50$. A pool of crystals with different color shades was obtained, suggesting the presence of crystal with various halide ratios. The structural analysis of several fragments indicated that they possess a monoclinic symmetry with similar lattice parameters. The crystal structure analysis carried out on a selected fragment led to the discovery of a new 1D tin-based hybrid perovskite, namely BZA₃Sn(Br_{0.3}I_{0.7})₅. This is consistent with the increase of the X/Sn ratio evidenced by elemental analysis (Table B.6). A sketch of the structure of this novel compound is reported in Fig. B.8a and the

atomic coordinates are given in Table B.8.

Table B.8. Atomic coordinates in the structure of $\text{BZA}_3\text{Sn}(\text{Br}_{0.3}\text{I}_{0.7})_5$ resolved from single crystal X-ray diffraction.

		<i>x</i>	<i>y</i>	<i>z</i>	<i>m.s.f.</i> (\AA^2)	<i>s.o.f.</i>
Sn	Sn1	0.47938(3)	0.51806(4)	0.33246(2)	0.03654(12)	1
I	I1	0.27258(3)	0.50385(6)	0.27551(2)	0.05074(18)	0.705(8)
Br	Br1					0.295(8)
I	I2	0.45932(3)	0.72741(5)	0.42358(2)	0.05239(16)	0.927(8)
Br	Br2					0.073(8)
I	I3	0.49802(4)	0.81420(6)	0.26269(2)	0.04739(19)	0.314(7)
Br	Br3					0.686(7)
I	I4	0.46490(4)	0.23012(5)	0.39661(2)	0.05487(17)	0.853(8)
Br	Br4					0.147(8)
I	I5	0.27135(3)	0.99076(6)	0.12891(2)	0.05781(18)	0.986(8)
Br	Br5					0.014(8)
N	N1	0.3457(5)	0.5863(8)	0.1577(2)	0.0731(19)	1
C	C1A	0.2937(7)	0.5070(11)	0.0342(3)	0.085(2)	1
C	C1B	0.2582(10)	0.5466(15)	-0.0181(4)	0.120(3)	1
C	C1C	0.1679(10)	0.6071(16)	-0.0294(6)	0.127(4)	1
C	C1D	0.1097(10)	0.6179(18)	0.0032(5)	0.139(4)	1
C	C1E	0.1508(9)	0.5715(16)	0.0542(5)	0.114(3)	1
C	C1F	0.2423(5)	0.5138(8)	0.0708(3)	0.0633(17)	1
C	C1G	0.2817(10)	0.4691(13)	0.1250(4)	0.108(3)	1
N	N2	0.3153(5)	1.0857(8)	0.2671(3)	0.0641(15)	1
C	C2A	0.1629(6)	1.0987(11)	0.3357(3)	0.071(2)	1
C	C2B	0.0728(7)	1.1210(13)	0.3411(4)	0.085(3)	1
C	C2C	-0.0020(6)	1.0438(12)	0.3091(4)	0.080(2)	1
C	C2D	0.0126(6)	0.9447(12)	0.2716(4)	0.084(3)	1
C	C2E	0.1025(6)	0.9206(10)	0.2664(3)	0.072(2)	1
C	C2F	0.1796(5)	0.9947(8)	0.2999(3)	0.0540(15)	1
C	C2G	0.2796(6)	0.9619(9)	0.2963(4)	0.067(2)	1
N	N3	0.6571(5)	0.4662(9)	0.4902(3)	0.0707(18)	1
C	C3A	0.8157(6)	0.4753(11)	0.5982(3)	0.068(2)	1
C	C3B	0.9041(7)	0.4287(14)	0.6289(3)	0.086(3)	1
C	C3C	0.9836(6)	0.4588(13)	0.6127(4)	0.083(3)	1
C	C3D	0.9773(6)	0.5376(13)	0.5660(4)	0.082(3)	1
C	C3E	0.8895(6)	0.5831(11)	0.5351(3)	0.068(2)	1
C	C3F	0.8080(5)	0.5525(9)	0.5513(3)	0.0555(16)	1
C	C3G	0.7133(6)	0.6009(11)	0.5176(3)	0.071(2)	1
H	H1NA	0.3300	0.6824	0.1445	0.11	1

H	H1NB	0.4057	0.5652	0.1578	0.11	1
H	H1NC	0.3400	0.5822	0.1906	0.11	1
H	H1A	0.3568	0.4735	0.0454	0.102	1
H	H1B	0.2922	0.5325	-0.0432	0.144	1
H	H1C	0.1433	0.6454	-0.0635	0.153	1
H	H1D	0.0472	0.6538	-0.0080	0.167	1
H	H1E	0.1151	0.5795	0.0786	0.137	1
H	H1G1	0.3167	0.3711	0.1259	0.13	1
H	H1G2	0.2295	0.4487	0.1407	0.13	1
H	H2NA	0.2825	1.0789	0.2329	0.096	1
H	H2NB	0.3777	1.0728	0.2714	0.096	1
H	H2NC	0.3046	1.1802	0.2792	0.096	1
H	H2A	0.2135	1.1556	0.3569	0.085	1
H	H2B	0.0629	1.1892	0.3669	0.102	1
H	H2C	-0.0633	1.0588	0.3128	0.096	1
H	H2D	-0.0389	0.8927	0.2493	0.1	1
H	H2E	0.1118	0.8540	0.2401	0.086	1
H	H2G1	0.3218	0.9541	0.3317	0.08	1
H	H2G2	0.2807	0.8611	0.2789	0.08	1
H	H3NA	0.6868	0.4234	0.4680	0.106	1
H	H3NB	0.5996	0.4997	0.4723	0.106	1
H	H3NC	0.6511	0.3943	0.5138	0.106	1
H	H3A	0.7613	0.4543	0.6092	0.081	1
H	H3B	0.9092	0.3768	0.6607	0.103	1
H	H3C	1.0429	0.4258	0.6332	0.1	1
H	H3D	1.0321	0.5598	0.5555	0.098	1
H	H3E	0.8848	0.6345	0.5032	0.082	1
H	H3G1	0.6779	0.6529	0.5393	0.085	1
H	H3G2	0.7223	0.6765	0.4916	0.085	1

The 1D hybrid perovskite crystallizes in the $P2_1/c$ space group with $a=14.5383(4)$ Å, $b=8.46698(19)$ Å, $c=26.2932(6)$ Å, and $\beta=105.410(3)^\circ$. The new phase is characterized by Sn-halide corner-sharing octahedra forming 1D nanowires in a zig-zag fashion, surrounded by benzylammonium cations. This arrangement is qualitatively similar to that of IPA₃SnI₅ (IPA = isopropylammonium) (Stoumpos et al., 2017) where the smaller organic cation allowed to preserve an orthorhombic unit cell. A similar connectivity was observed in dimethylethylenediamine lead bromide (Yuan et al., 2017) and foreseen for Cs₃PbI₅ Xiao et al., 2018 while many other 1D perovskites show unusual hexagonal symmetry for perovskites, with the octahedra sharing faces (e.g. MAMnBr₃ Daub et al., 2018) or alternating faces and corner connectivity (GASnI₃ GA = guanidinium). The structure refinement

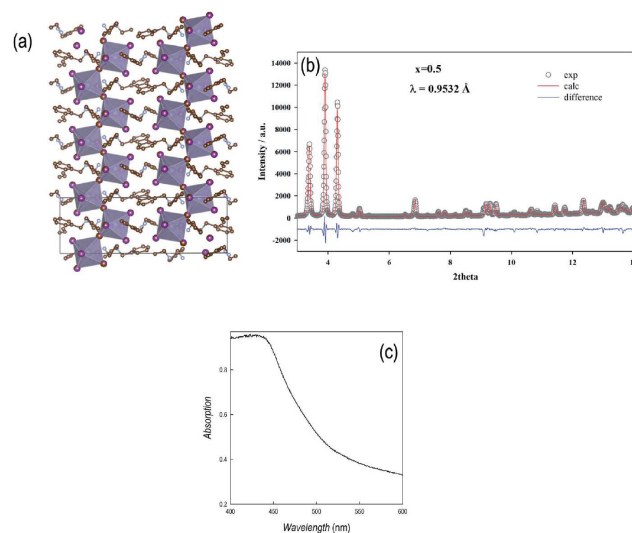


Figure B.8. (a) Sketch of the crystal structure of $\text{BZA}_3\text{Sn}(\text{Br}_{0.3}\text{I}_{0.7})_5$ along the b -axis; (b) refinement of powder pattern of $\text{BZA}_3\text{Sn}(\text{Br}_{0.3}\text{I}_{0.7})_5$; (c) absorption spectra of the sample.

of $\text{BZA}_3\text{Sn}(\text{Br}_{0.3}\text{I}_{0.7})_5$ indicates excess of iodine from nominal $x = 0.50$ composition. In order to confirm the formation of the 1D perovskite in the samples produced through ball-milling, a sample with nominal composition $x = 0.5$ was investigated by synchrotron powder diffraction, using a rotating-capillary-stage which allowed to reduce significantly preferred orientations. The refinement (Fig. B.8b) performed using the structural model obtained by single-crystal analysis confirmed the goodness of the structural solution. Table B.9 reports the lattice parameters of the 1D perovskite whenever observed in the solid solution, together with the overall nominal composition x . In general, the lattice parameters of the 1D perovskites were observed to scale monotonically with the nominal Br/I concentration. As an example, the nominal composition $x = 0.5$ showed significantly smaller lattice parameters compared to the single crystal, suggesting Br-enrichment. The lattice contraction occurs nearly isotropically, suggesting it is driven by simple steric effects related to halide substitution. This result further suggests that $\text{BZA}_3\text{Sn}(\text{Br}_{0.3}\text{I}_{0.7})_5$ can be potentially formed with different Br/I composition. As a matter of fact, the tendency in forming 1D perovskites of various I/Br ratios has been observed in the present work when the samples were synthesized by solution chemistry, possibly as a consequence of a reduced reactivity of tin leading to a BZA/Sn stoichiometry more close to 3 : 1. The use of mechanochemical synthesis allowed a proper control of reagents amount thus providing the set of 2D perovskites presented above. Finally, the absorption spectrum of the sample reported in Fig. B.3b is shown in Fig. B.8c, corresponding to a

Table B.9. Comparison of lattice parameters (Å) of BZA₃Sn(Br_{0.3}I_{0.7})₅ obtained with different nominal composition.

x	X-ray data collection	<i>a</i>	<i>b</i>	<i>c</i>	β
0.30 ^a	Single crystal	14.5383(4)	8.46698(19)	26.2932(6)	105.410(3)
0.30 ^b	Powder- synchrotron	14.490(3)	8.4356(8)	26.295(4)	104.93(2)
0.375	Powder- lab	14.473(8)	8.444(6)	26.23(1)	105.0(1)
0.50	Powder- synchrotron	14.455(2)	8.3984(9)	26.214(3)	104.86(1)
0.625 ^b	Powder -synchrotron	14.418(4)	8.423(6)	26.103(6)	104.54(4)

^a Value estimated by refinement of I/Br site occupation. ^b Minority phase.

band-gap of 2.05 eV, which is intermediate between those of the pure I and Br 2D end-members.

B.3 CONCLUSIONS

We reported a detailed investigation of the lead-free 2D BZA₂SnX₄ (X = I, Br, and Cl) system as a function of the halide nature by preparing, by means of mechanochemistry, two novel compositions, i.e. BZA₂SnBr₄ and BZA₂SnCl₄, as well as the BZA₂Sn(Br_xI_{1-x})₄ solid solution. From a structural point of view, the progressive replacement of the halide from iodide to chloride leads to an expansion of the c-axis due to the change in the staggering of the two benzylammonium cations and to a contraction of the in-plane lattice parameters reflecting the different size of the halide. The optical properties show a linear shift in the band-gap throughout the I/Br mixed compositions and, together with the BZA₂SnCl₄ sample, the samples cover an optical region extending from about 400 nm to about 700 nm, with PL data showing narrow emission in the whole range. During the study of the 2D BZA₂SnX₄ system we also identified a novel lead-free 1D perovskite showing as well a possible mixed I/Br composition, namely the BZA₂Sn(Br_xI_{1-x})₄ compound. A full computational investigation of the three stoichiometric samples, i.e. BZA₂SnX₄ (X =I, Br, and Cl), has been performed by means of DFT calculation providing a complete description of their electronic structure. In conclusion, the data reported extend the actual knowledge on lead-free two-dimensional perovskites, also highlighting the correlation between the staggering of the organic cation as a function of the halide, providing a novel system with emission extending in a wide visible region.

B.4 EXPERIMENTAL SECTION

B.4.1 *Materials preparation*

Samples of general formula $\text{BZA}_2\text{Sn}(\text{Br}_x\text{I}_{1-x})_4$ (1 g) were prepared by a one-step fully-dry mechanochemical approach via ball-milling. For the synthesis, a proper stoichiometric amount of the reactants, e.g. benzylammonium iodide and bromide (BZAI, BZABr) and tin iodide and bromide (SnI_2 , SnBr_2) powders, is transferred to a tungsten carbide (WC) milling bowl with 30.5 mm diameter WC balls. The bowl is tightly closed and mounted into the planetary ball milling machine (Fritsch, Pulverisette 7, Premium Line), the speed was set to 400 rpm and the reaction time was 6 h. In the planetary ball miller, the jar performs two movements: a rotation around its own axis and a rotation around the center of the main disk. After the milling, uniformly colored powders were obtained. For a perfect conservation of the samples, the reaction was set up in a N_2 glove box (to prevent the oxidation of Sn(II) to Sn(IV)), sealed and removed from the glove box, placed in the planetary mill for the reaction and again collected in the glove box, without annealing or other further purifications. The single crystals of BZASnI_4 and BZASnBr_4 were prepared according to a general and original procedure that our group developed previously (Mancini et al., 2015). In a typical synthesis a proper amount of Sn(II) acetate is dissolved in a large excess of the desired HX acid under continuous stirring and nitrogen atmosphere. Hypophosphoric acid is added to the solution and inert atmosphere is maintained in the reaction environment in order to prevent Sn oxidation. Then, the solution is heated to 100 °C and the corresponding BZA solution is added in equimolar amount. The solution is then cooled down to ca. 50 °C at 1 °C/5 min, until the formation of a needle-shaped precipitate, which is immediately filtered and dried under vacuum overnight. For the synthesis of $\text{BZA}_2\text{SnCl}_4$, the procedure was slightly different because the slow cooling of the solution didn't lead to any precipitation. The white product was obtained quenching the 100 °C solution in an iced-water bath and then treated as previously reported.

B.4.2 *Optical spectroscopy*

Absorbance was measured with a UV/Vis/NIR spectroscopy (PerkinElmer Lambda 950S) and steady-state PL emission was measured with a Fluorescence spectrometer (PerkinElmer LS55) and an Edinburgh FLS920 spectrometer equipped with a Peltier-cooled Hamamatsu R928 photomultiplier tube (185– 850 nm). An Edinburgh Xe900 450 W Xenon arc lamp was used as exciting light source. Corrected spectra were obtained via a calibration curve supplied with the instrument (lamp power in the steady state PL experiments 0.6 mW cm^{-2} , spot area 0.5 cm^2).

B.4.3 X-ray diffraction measurements

XRD measurements on powdered samples were performed using a Bruker D8 Advance in Bragg–Brentano geometry under Cu K α radiation. Single crystal data collections for BZA₂SnCl₄ and BZA₃Sn(I_{0.7}Br_{0.3}) were performed using a Rigaku Oxford Diffraction SuperNova diffractometer equipped with a Dectris PILATUS3 R 200K-A detector and a micro-focus sealed X-ray tube ($\lambda=0.71073$ Å). X-ray diffraction intensity data were integrated and corrected for standard Lorentz polarization factors with the CrysAlisPro package, while ABSPACK in CrysAlis RED was used for the absorption correction (“ABSPACK in CrysAlis RED”, 2006; “CrysAlis RED”, 2006). The structure was solved and refined using the program Shelx-2013 (Sheldrick, 2008). Synchrotron powder diffraction data ($\lambda=0.9532$ Å) were collected on the high-resolution MCX beamline at the Elettra synchrotron light source (Trieste, Italy) Rebuffi et al., 2014. Standard 0.3 mm diameter borosilicate capillaries were filled with powders under argon atmosphere (<0.5 ppm O₂ and H₂O), capped with vacuum grease, and finally sealed using a butane torch. Diffraction patterns were acquired in Debye geometry on the 4-circle Huber goniometer by spinning capillaries at 3000 rpm. For BZA₂SnCl₄ isotropic full-matrix least-squares cycles were initially run assuming the atom sites as fully occupied, although unusually high values of the isotropic displacement factor for the Cl1 and Cl2 atoms strongly suggested disorder at those sites. For this reason, we split Cl1 and Cl2 into two positions (Cl1a/Cl1b and Cl2a/Cl2b) with the site-occupancy left free to be refined. The site scattering at the split positions was identically distributed between the ‘a’ and ‘b’ positions and thus fixed in the subsequent cycles of the refinement. The anisotropic model of the structure led to R₁=0.0952. At this stage, considering the similarity in the *b* and *c* parameters (~ 7.75 Å), we hypothesized the presence of a twinning simulating a four-fold symmetry axis (four-twinned components) according to the matrix $|-100/001/010|$. Twinning is quite common in perovskite-type materials when the distortion from the cubic aristotype is evident (Rothmann et al., 2017; Wang et al., 1990). The introduction of the twin law lowered the R₁ index to 0.0638 for 2012 observed reflections [$F_o > 4\sigma(F_o)$] and 107 refined parameters. Further trials using a different refinement program by introducing an additional twin law (merohedral twinning) and higher tensors to describe the displacement parameters for Cl1 and Cl2 did not improve the overall quality of the refinement (Petříček et al., 2014).

B.4.4 EDX analysis

Elemental analyses of the powders were performed by Energy Dispersive X-ray Analysis (EDX) by a X-max 50 mm² probe (Oxford Instrument) connected to a EVO MA10 scanning electron microscope (SEM). The powders were dispersed on graphite bi-adhesive supports fixed on Al stubs inside a glove box under Ar

atmosphere. The stubs were inserted in a home – made sample holder that was sealed in the glove box and in which the low vacuum was made by a rotary pump. In this way, the samples were transferred in the SEM chamber avoiding the exposition to air. Subsequently, the sample holder was open and the measurements performed under ultra-high vacuum at a working distance of 8.5 mm and with an electron generation voltage of 20 kV.

ACKNOWLEDGEMENTS

The authors gratefully acknowledge the project PERSEO- “PERrovskite-based Solar cells: towards high Efficiency and long-term stability” (Bando PRIN 2015-Italian Ministry of University and Scientific Research (MIUR) Decreto Direttoriale 4 novembre 2015 no. 2488, project number 2015LECAJ) for funding. Marta Morana is supported by the European Research Council (ERC) under the European Union’s Horizon 2020 Research and Innovation Programme (grant agreement 714936) for the project TRUE DEPTHS to M. Alvaro.

REFERENCES

- ABSPACK in CrysAlis RED* (Version Version 1.171.31.2). (2006). Abingdon, Oxfordshire, England., Oxford Diffraction Ltd,
- Calabrese, J., Jones, N., Harlow, R., Herron, N., Thorn, D., & Wang, Y. (1991). Preparation and characterization of layered lead halide compounds. *Journal of the American Chemical Society*, 113(6), 2328–2330.
- Cheng, P., Wu, T., Liu, J., Deng, W.-Q., & Han, K. (2018). Lead-free, two-dimensional mixed Germanium and Tin perovskites. *The Journal of Physical Chemistry Letters*, 9(10), 2518–2522.
- CrysAlis RED* (Version Version 1.171.31.2). (2006). Abingdon, Oxfordshire, England., Oxford Diffraction Ltd,
- Daub, M., Ketterer, I., & Hillebrecht, H. (2018). Syntheses, crystal structures, and optical properties of the hexagonal perovskites variants ABX_3 (B= Ni, A= Gu, FA, MA, X= Cl, Br; B= Mn, A= MA, X= Br). *Zeitschrift für anorganische und allgemeine Chemie*, 644(5), 280–287.
- Desiraju, G. R., Ho, P. S., Kloo, L., Legon, A. C., Marquardt, R., Metrangolo, P., Politzer, P., Resnati, G., & Rissanen, K. (2013). Definition of the halogen bond (IUPAC recommendations 2013). *Pure Appl. Chem*, 85(8), 1711–1713.
- Desiraju, G. R., & Steiner, T. (2001). *The weak hydrogen bond: In structural chemistry and biology* (Vol. 9). International Union of Crystal.
- Dohner, E. R., Jaffe, A., Bradshaw, L. R., & Karunadasa, H. I. (2014). Intrinsic white-light emission from layered hybrid perovskites. *Journal of the American Chemical Society*, 136(38), 13154–13157.

- El-Mellouhi, F., Marzouk, A., Bentría, E. T., Rashkeev, S. N., Kais, S., & Alharbi, F. H. (2016). Hydrogen bonding and stability of hybrid organic–inorganic perovskites. *ChemSusChem*, *9*(18), 2648–2655.
- Frost, J. M., Butler, K. T., Brivio, F., Hendon, C. H., Van Schilfgaarde, M., & Walsh, A. (2014). Atomistic origins of high-performance in hybrid halide perovskite solar cells. *Nano letters*, *14*(5), 2584–2590.
- Gangadharan, D. T., & Ma, D. (2019). Searching for stability at lower dimensions: Current trends and future prospects of layered perovskite solar cells. *Energy & Environmental Science*, *12*(10), 2860–2889.
- Gao, P., Nazeeruddin, M. K. et al. (2018). Dimensionality engineering of hybrid halide perovskite light absorbers. *Nature communications*, *9*(1), 1–14.
- Grancini, G., & Nazeeruddin, M. K. (2019). Dimensional tailoring of hybrid perovskites for photovoltaics. *Nature Reviews Materials*, *4*(1), 4. <https://doi.org/10.1038/s41578-018-0065-0>
- Hong, Z., Tan, D., John, R. A., Tay, Y. K. E., Ho, Y. K. T., Zhao, X., Sum, T. C., Mathews, N., Garcia, F., & Soo, H. S. (2019). Completely solvent-free protocols to access phase-pure, metastable metal halide perovskites and functional photodetectors from the precursor salts. *iScience*, *16*, 312–325.
- Jung, M.-H. (2019). White-light emission from the structural distortion induced by control of halide composition of two-dimensional perovskites ((c6h5ch2nh3)2pbbr4-x cl x). *Inorganic Chemistry*, *58*(10), 6748–6757.
- Kamminga, M. E., Fang, H.-H., Filip, M. R., Giustino, F., Baas, J., Blake, G. R., Loi, M. A., & Palstra, T. T. M. (2016). Confinement effects in low-dimensional lead iodide perovskite hybrids [Publisher: American Chemical Society]. *Chemistry of Materials*, *28*(13), 4554–4562. <https://doi.org/10.1021/acs.chemmater.6b00809>
- Karmakar, A., Dodd, M. S., Zhang, X., Oakley, M. S., Klobukowski, M., & Michaelis, V. K. (2019). Mechanochemical synthesis of 0d and 3d cesium lead mixed halide perovskites. *Chemical Communications*, *55*(35), 5079–5082.
- Lee, J. H., Lee, J.-H., Kong, E.-H., & Jang, H. M. (2016). The nature of hydrogen-bonding interaction in the prototypic hybrid halide perovskite, tetragonal CH₃NH₃PbI₃. *Scientific reports*, *6*, 21687.
- Li, X.-N., Li, P.-F., Liao, W.-Q., Ge, J.-Z., Wu, D.-H., & Ye, H.-Y. (2017). Phase-transition and photoluminescence properties of a hybrid layered perovskite: Bis [(cyclohexylmethyl) ammonium] tetrabromidolead (ii). *European Journal of Inorganic Chemistry*, *2017*(5), 938–942.
- Lufaso, M. W., & Woodward, P. M. (2004). Jahn–teller distortions, cation ordering and octahedral tilting in perovskites. *Acta Crystallographica Section B: Structural Science*, *60*(1), 10–20.
- Mancini, A., Quadrelli, P., Milanese, C., Patrini, M., Guizzetti, G., & Malavasi, L. (2015). CH₃NH₃Sn_xPb_{1-x}Br₃ hybrid perovskite solid solution: Synthesis, structure, and optical properties. *Inorganic chemistry*, *54*(18), 8893–8895.

- Mao, L., Stoumpos, C. C., & Kanatzidis, M. G. (2018). Two-dimensional hybrid halide perovskites: Principles and promises. *Journal of the American Chemical Society*, *141*(3), 1171–1190.
- Mao, L., Tsai, H., Nie, W., Ma, L., Im, J., Stoumpos, C. C., Malliakas, C. D., Hao, F., Wasielewski, M. R., Mohite, A. D., et al. (2016). Role of organic counterion in lead- and tin-based two-dimensional semiconducting iodide perovskites and application in planar solar cells. *Chemistry of Materials*, *28*(21), 7781–7792.
- Mosconi, E., Umari, P., & De Angelis, F. (2015). Electronic and optical properties of mixed Sn–Pb organohalide perovskites: A first principles investigation. *Journal of Materials Chemistry A*, *3*(17), 9208–9215.
- Munshi, P., & Guru Row, T. N. (2005). Exploring the lower limit in hydrogen bonds: Analysis of weak C–H ···O and C–H ··· π interactions in substituted coumarins from charge density analysis. *The Journal of Physical Chemistry A*, *109*(4), 659–672.
- Petříček, V., Dušek, M., & Palatinus, L. (2014). Crystallographic computing system JANA2006: General features. *Zeitschrift für Kristallographie - Crystalline Materials*, *229*(5). <https://doi.org/10.1515/zkri-2014-1737>
- Rebuffi, L., Plaisier, J. R., Abdellatif, M., Lausi, A., & Scardi, P. (2014). Mcx: A synchrotron radiation beamline for x-ray diffraction line profile analysis. *Zeitschrift für anorganische und allgemeine Chemie*, *640*(15), 3100–3106.
- Rothmann, M. U., Li, W., Zhu, Y., Bach, U., Spiccia, L., Etheridge, J., & Cheng, Y.-B. (2017). Direct observation of intrinsic twin domains in tetragonal $\text{CH}_3\text{NH}_3\text{PbI}_3$. *Nature communications*, *8*(1), 1–8.
- Sheldrick, G. M. (2008). A short history of SHELX. *Acta Crystallographica Section A Foundations of Crystallography*, *64*(1), 112–122. <https://doi.org/10.1107/S0108767307043930>
- Smith, I. C., Hoke, E. T., Solis-Ibarra, D., McGehee, M. D., & Karunadasa, H. I. (2014). A layered hybrid perovskite solar-cell absorber with enhanced moisture stability. *Angewandte Chemie*, *126*(42), 11414–11417.
- Stoumpos, C. C., Mao, L., Malliakas, C. D., & Kanatzidis, M. G. (2017). Structure–band gap relationships in hexagonal polytypes and low-dimensional structures of hybrid tin iodide perovskites. *Inorganic chemistry*, *56*(1), 56–73.
- Svane, K. L., Forse, A. C., Grey, C. P., Kieslich, G., Cheetham, A. K., Walsh, A., & Butler, K. T. (2017). How strong is the hydrogen bond in hybrid perovskites? *The journal of physical chemistry letters*, *8*(24), 6154–6159.
- Tan, L. Z., Zheng, F., & Rappe, A. M. (2017). Intermolecular interactions in hybrid perovskites understood from a combined density functional theory and effective hamiltonian approach. *ACS Energy Letters*, *2*(4), 937–942.

- Wang, J., Dong, J., Lu, F., Sun, C., Zhang, Q., & Wang, N. (2019). Two-dimensional lead-free halide perovskite materials and devices. *Journal of Materials Chemistry A*, 7(41), 23563–23576.
- Wang, N., Liu, W., & Zhang, Q. (2018). Perovskite-based nanocrystals: Synthesis and applications beyond solar cells. *Small Methods*, 2(6), 1700380.
- Wang, Y., Guyot, F., Yeganeh-Haeri, A., & Liebermann, R. C. (1990). Twinning in MgSiO₃ perovskite. *Science*, 248(4954), 468–471.
- Xiao, Z., Zhou, Y., Hosono, H., Kamiya, T., & Padture, N. P. (2018). Bandgap optimization of perovskite semiconductors for photovoltaic applications. *Chemistry—A European Journal*, 24(10), 2305–2316.
- Yang, S., Lin, Z., Wang, J., Chen, Y., Liu, Z., Yang, E., Zhang, J., & Ling, Q. (2018). High color rendering index white-light emission from uv-driven leds based on single luminescent materials: Two-dimensional perovskites (C₆H₅C₂H₄NH₃)₂PbBr_xCl_{4-x}. *ACS applied materials & interfaces*, 10(18), 15980–15987.
- Yuan, Z., Zhou, C., Tian, Y., Shu, Y., Messier, J., Wang, J. C., Van De Burgt, L. J., Kountouriotis, K., Xin, Y., Holt, E., et al. (2017). One-dimensional organic lead halide perovskites with efficient bluish white-light emission. *Nature communications*, 8, 14051.
- Zheng, Z., Egger, D. A., Bredas, J.-L., Kronik, L., & Coropceanu, V. (2017). Effect of solid-state polarization on charge-transfer excitations and transport levels at organic interfaces from a screened range-separated hybrid functional. *The Journal of Physical Chemistry Letters*, 8(14), 3277–3283.